NASA TECHNICAL NOTE

NASA TN D-8143

A STUDY OF A SECTOR SPECTROPHOTOMETER AND AURORAL $O^+(^2P-^2D)$ EMISSIONS

Gary R. Swenson

George C. Marshall Space Flight Center
Marshall Space Flight Center, Ala. 35812

NATIONAL AERONAUTICS AND SPACE ADMINISTRATION • WASHINGTON, D. C. • JANUARY 1976

TECHNICAL

1. REPORT NO.
NASA TN D-8143

2. GOVERNMENT ACCESSION NO.

4. TITLE AND SUBTITLE
A Study of a Sector Spectrophotometer and Auroral $O^+(^2P\text{-}^2D)$ Emissions

5. REPORT DATE
January 1976

6. PERFORMING ORGANIZATION CODE
M160

7. AUTHOR(S)
Gary R. Swenson

8. PERFORMING ORGANIZATION REPORT #

9. PERFORMING ORGANIZATION NAME AND ADDRESS
George C. Marshall Space Flight Center
Marshall Space Flight Center, Alabama 35812

10. WORK UNIT NO.

11. CONTRACT OR GRANT NO.

13. TYPE OF REPORT & PERIOD COVERED
Technical Note

12. SPONSORING AGENCY NAME AND ADDRESS
National Aeronautics and Space Administration
Washington, D.C. 20546

14. SPONSORING AGENCY CODE

15. SUPPLEMENTARY NOTES
Financial support was provided by NSF GA-28690X2 (National Science Foundation) for instrumental and expedition work performed at the University of Michigan. Work at Marshall was supported by OMSF and OSS-SRT funds.

16. ABSTRACT

This study is an investigation of the metastable $O^+(^2P\text{-}^2D)$ auroral emission. The neighboring OH contaminants and low intensity levels of the emission itself necessitated the evolution of an instrument capable of separating the emission from the contaminants and having a high sensitivity in the wavelength region of interest. A new type of scanning photometer was developed during the study, and its properties are discussed in this report.

The evolution of the scanning photometer involved theoretical and laboratory examination of transmission characteristics of all-dielectric, Fabry-Perot type filters. The photometer scanning principle employed a spatially moving field stop in the aperture plane of the instrument, creating an angular exposure of the filter to the detector. The moving field stop was accomplished by rotating a disk containing a spiral slit behind a spatially fixed, sector shaped, masking disk. The spatial scanning scheme accomplished a nearly constant peak transmittance and bandpass for large tilt angles. This advantage, coupled with the throughput advantage of the large Fabry-Perot type filter elements, offered a unique tool for examination of low light level emissions in contaminated backgrounds.

An instrument was built and tested in the laboratory for verification of the theoretical concept. Another instrument, employing a multi-spiral configuration, was then prepared with its instrument design oriented to the development of a ground based system for the measurement of $O^+(^2P\text{-}^2D)$ auroral emissions.

The theoretical aspects of auroral electron interaction with atomic oxygen and the resultant $O^+(^2P\text{-}^2D)$ emissions were examined in conjunction with N_2^+1NEG emissions. The fact that N_2 and O are differentially distributed in the thermosphere, and that $O^+(^2P)$ is quenched, lead to an investigation of the ratio of these two emissions as an emission signature relevant to the precipitating auroral electrons.

Ground based measurements of $O^+(^2P\text{-}^2D)$ auroral emission intensities were made in College, Alaska, (64.9°N, 148°N) using the spatial scanning photometer (sector spectrophotometer). Simultaneous measurements of $N_2^+1NEG_{1,0}$ emission intensity were made in the same field of view using a tilting photometer. Time histories of the ratio of these two emissions made in the magnetic zenith during auroral breakup periods are given. Theories of I_{7319}/I_{4278} of previous investigators were presented. These previous theories are not in agreement with the ground based measurements.

A rocket measurement of $N_2^+1NEG_{0,0}$ and $O^+(^2P\text{-}^2D)$ emission in aurora was examined in detail and was found to agree with the ground based measurements. Theoretical examination resulted in the deduction of the electron impact efficiency generating $O^+(^2P)$ and also suggests a large source of $O^+(^2P)$ at low altitude. A possible source is charge exchange of $N^+(^1S)$ with OI (^3P). These new theories are different from those previously deduced by other investigators.

17. KEY WORDS

18. DISTRIBUTION STATEMENT
Category: 46

19. SECURITY CLASSIF. (of this report)	20. SECURITY CLASSIF. (of this page)	21. NO. OF PAGES	22. PRICE
Unclassified	Unclassified	192	$7.00

MSFC - Form 3292 (Rev December 1972)

For sale by the National Technical Information Service, Springfield, Virginia 22161

TABLE OF CONTENTS

TABLE OF CONTENTS (Continued)

TABLE OF CONTENTS (Concluded)

LIST OF ILLUSTRATIONS

LIST OF ILLUSTRATIONS (Continued)

LIST OF ILLUSTRATIONS (Continued)

LIST OF ILLUSTRATIONS (Continued)

LIST OF ILLUSTRATIONS (Concluded)

LIST OF TABLES

LIST OF SYMBOLS

Symbol	Definition
a	Slope of wavelength versus tilt angle squared (tilt angle in radians).
A	Area of cone of intercept.
A_1	Area of interference filter exposed to source at normal incidence.
A_2	Area of aperture stop of field stop.
A_λ	Einstein transition probability for emission at wavelength.
$A^3\Sigma_u^+$	Lower state of N_2 1PG band transition.
BG	Background of instrument signal due to noise in detectors and continuum observed in instrument.
$B^3\pi g$	Upper state of N_2 1PG band transition.
$B^2\Sigma_u^+$	Upper state of N_2^+1NEG band transition.
C	Cryolite, Chapters II, III, and Appendix A.
C	Chapman type ionization profile, Appendix F.
C_{14}	Carbon fourteen.
$C_\sigma(E)$	Parameterization of several cross section ratios, for production of $O^+(^2P)$, through charge exchange of $N^+(^1S)$, Chapter VIII.
CF	Calibration factor for spectrophotometer, 7319Å data.
e	Electronic charge.
ev	Energy, electron volts.
E_0	Most probable energy as employed in electron energy distribution functions, Chapter VI.
EFF	$O^+(^2P)$ metastable production efficiency by electron impact, i.e., $\sigma_{O^{+2}P}(E)/\sigma_{O^+}(E)$

LIST OF SYMBOLS (Continued)

Symbol	Definition
f	Focal length of objective lens adjacent to a Fabry-Perot type interference generator.
F	Reflectivity parameter, Appendix A.
$F(E)$	Flux of primary electrons through a given altitude, Chapter VII.
F_K	Reflectivity parameter generalized for a K index spacer.
G	General Function, G( ).
H_{N2}	Scale height for molecular nitrogen.
h	Planck's constant.
$IO^+(^2P\text{-}^2D)$	Intensity of O^+ emissions originating from the $O^+(^2P\text{-}^2D)$ transition.
$I1NEG_{i,j}$	Intensity of N_2^+ first negative bands or band (i,j) as specified in text.
$I1PG_{i,j}$	Intensity of N_2 first positive bands or band (i,j) as specified in text.
I_λ	Intensity of atomic or molecular emissions whose emitting wavelength or band head is indicated by wavelength λ, in raleighs.
$I(i)$	Initial light intensity, Appendix A.
$I(t)$	Intensity of transmitted light, Appendix A.
L	Instrumental throughput, Chapter II.
L	Total loss of $O^+(^2P)$ in continuity, Chapter VI.
m	Electron mass, Chapter VI.
m	Order of interference for plane parallel plates, Appendix A.
n	Number of rotations a spiral disk makes in a scan, Chapters II, IV, and V.

LIST OF SYMBOLS (Continued)

Symbol	Definition
n	Order of the spacer of an all-dielectric filter, Appendix A.
n[ ]	Population or number density of constituent in bracket. Altitude dependence is implied in atmospheric applications.
N_A	Aperture finesse, $\Delta\lambda_{max}/\delta\lambda_A$.
N_B	Aperture breadth finesse, $\Delta\lambda_{max}/\delta\lambda_B$.
N_C	Aperture curvature finesse, $\Delta\lambda_{max}/\delta\lambda_C$.
N_I	Total instrument finesse, $\Delta\lambda_{max}/\delta\lambda_I$.
N_2	Molecular nitrogen gas.
$N_2\,1PG_{i,j}$	N_2 first positive band system. For a particular band, i and j refer to the upper and lower vibrational state respectively. The (1,0), λ8912Å; (5,3), λ7387Å; and (6,4), λ7274Å bands are referred to in this report.
$N_2^+1NEG_{i,j}$	N_2^+ first negative system. For a particular band, i and j refer to the upper and lower vibrational state respectively. The (0,0),λ3914Å; and (1,0), λ4278Å; bands are referred to in this report.
O	Atomic oxygen in the neutral state.
OI	Atomic oxygen in the neutral state.
OI(^{1}D)	OI in the ^{1}D state.
OI(^{1}D-^{3}P)	Spontaneous cascade of OI from the ^{1}D to the ^{3}P state, λ6300Å.
OII	Atomic oxygen in the singly ionized state.
O^+	Atomic oxygen in the singly ionized state.
O^+(^{2}D)	O^+ in the ^{2}D state.
O^+(^{2}P)	O^+ in the ^{2}P state.

LIST OF SYMBOLS (Continued)

Symbol	Definition
$O^+(^2P\text{-}^2D)$	Spontaneous cascade of O^+ from the ^2P state to the ^2D state. Emissions correspond to 7319Å and 7330Å wavelengths.
OH $P_{i,j}$	Hydroxyl compounds producing emissions from the earth's mesosphere where P refers to the P branch and i,j the upper and low states involved in a particular transition.
M	Monoenergetic type ionization profile, Appendix F.
P	Effective slope parameter of wavelength versus angle of tilt squared. Subscripts z and c refer to particular slopes produced by zinc sulfide and cryolite respectively, Chapter II, Appendix A.
P	Production rate of an excited state, Chapter VI.
P	N_2 proportional ionization profile, Chapter VIII and Appendix F.
$P_{\perp,\parallel}$	P defined in terms of the perpendicular and parallel polarized components, Appendix A.
$P_{i,j}$	Refers to OH P branch emission for OH transitions of upper level i to lower level j.
Q	Dispersion parameter. Subscripts z and c refer to dispersions produced by zinc sulfide and cryolite respectively, Chapter II, Appendix A.
Q	Quenching rate of an excited state, Chapter VI.
$Q_{n,n'}$	Deactivation rate of species in state n′ to state n.
$Q_{\perp,\parallel}$	Q defined in terms of the perpendicular and parallel polarized components, Appendix A.
$Q_{i,j}$	Refers to OH Q branch emission for OH transitions of upper level i to lower level j.
r	Radial distance of the aperture slit from the objective axis intersect in the aperture plane.

LIST OF SYMBOLS (Continued)

Symbol	Definition
r_{min}	The minimum r value of an aperture of finite r; $r_{min} = \delta r/2$ at $\phi = 0°$.
r_{max}	The maximum radius a slit is to achieve for $\Delta\lambda_{max}$.
$R_{\sigma_i}(E)$	A parameterization factor of several cross section ratios, where i refers to the upper vibrational state of $N_2 B^2 \Sigma_u^+$ indicated by N_2^{+*}, used for $O^+(^2P)$ production by electron impact.
S_1	Distance between the filter and the capture lens in the spectrophotometer.
S_2	Separation between the capture lens and the detector in the spectrophotometer.
SF_A	Rocket channel sensitivity factors where A refers to wavelength of channel.
t	Spacer thickness.
Te	Electron temperature (°K).
T_∞	Exospheric temperature (°K).
T_i^j	Transmission of a particular atomic or molecular state (i) through a filter whose wavelength is noted in superscript j, Chapters VII and VIII.
v_n	Initial electron velocity of species n, Chapter VI.
V_A	Signal measured from a particular photometer channel or wavelength where A denotes wavelength of channel or wavelength position, Chapter VII and VIII.
X	Number of layers of reflective 1/4 wave layers in a given stack of an all-dielectric filter.
$X^2 \Sigma_g^+$	Lower state of N_2^+1NEG band transition.
ZnS	Zinc sulfide.

LIST OF SYMBOLS (Continued)

Symbol	Difinition
α	Slope of wavelength versus tilt angle squared (tilt angle in degrees), Chapters I-V.
α	Power law coefficient for electron energy distributions (Chapter VI).
Å	Angstrom, 10^{-8} cm.
β	Slope of ϕ versus $\Delta\lambda$.
γ_i	$O^+(^2P)$ collisional deactivation rate. Subscript i refers to particular reactions referenced in Chapter VI or the species doing the quenching.
δ	Phase shift, Appendix A.
δ^A	Phase change produced by a reflective stack adjacent to an immersed media (Air), Appendix A.
δ^G	Phase change produced by a reflective stack on glass substrate.
δr	Radial breadth of aperture slit.
δr_{max}	δr at $r = r_{max}$.
$\delta\lambda$	Increment of wavelength, Å.
$\delta\lambda_o$	Generalized bandpass function when function is constant.
$\delta\lambda_A$	Bandpass broadening resultant from all aperture effects.
$\delta\lambda_B$	Bandpass broadening due to the finite breadth of the aperture spiral.
$\delta\lambda_C$	Bandpass broadening due to the curvature of the aperture spiral.
$\delta\lambda_I$	Bandpass broadening due to all instrumental effects.
$\delta\lambda_F$	Bandpass broadening resultant from all filter effects.

LIST OF SYMBOLS (Continued)

Symbol	Definition
$\delta\lambda_p$	Bandpass broadening due to polarizing in a filter.
$\delta\lambda_\psi$	Bandpass broadening due to the cone angle allowed through the filter.
$\delta\lambda_{\|\|}$	Bandpass broadening observed in a filter with collimated light.
$\delta\phi$	Angle of annular slit of an aperture whose apex is the objective axis.
$\delta\phi_0$	Same as $\delta\phi$ except this subscript form refers to the angle being constant at all r.
$\Delta\lambda$	Wavelength displacement of maximum transmission through a filter, $\lambda - \lambda_0$, (Å).
$\Delta\lambda_{max}$	Maximum wavelength shift required of a given filter.
$\Delta\lambda_\perp$	Wavelength shift of the perpendicularly polarized component.
$\Delta\lambda_{\|\|}$	Wavelength shift of the parallel polarized component.
ϵ	Phase shift angle.
$\eta(\ )_i$	Volume rate of change with initial (upper) state or particular emission wavelength indicated in parenthesis. See footnote 10 for meaning of subscript.
μ	Index of refraction.
θ	Angle of incidence to a filter.
θ_{min}	Minimum angle of tilt possible for a given aperture configuration.
θ_{max}	Maximum angle of tilt required for a given r_{max}.
λ	Wavelength (Angstroms). A four digit number following λ refers to a particular wavelength.
λ_0	Wavelength of maximum transmission through a filter at normal incidence.

LIST OF SYMBOLS (Continued)

Symbol	Definition
μ_C	Index of refraction for cryolite.
μ_H	The higher index dielectric in an alternating stack.
μ_K	Index of spacer.
μ_L	The lower index dielectric in an alternating stack.
μ_r	Ratio of the high index to the low index of refraction of the dielectrics used in creating a bandpass stack.
μ_Z	Index of refraction for zinc sulfide.
μ^*	Effective index of refraction of a filter.
$\mu^\perp$	Index of refraction for perpendicularly polarized component.
$\mu^{\parallel}$	Index of refraction for parallel polarized component.
ν	Wavenumber of a consituent emission.
$\sigma_j(E)$	Cross section for producing an atomic or molecular state, j, by electron impact. [Energy dependence of j implied by (E).] Subscripts include generalized states ($j=x'$), $O^+(^2P)$, ($J=0^+(^2P)$), all O^+($j=0^+$), effective $N_2B^3\pi$ leading to N_2 1PG ($j=1PG$), effective $N_2^+B^2\Sigma_u^+$ leading to N_2^+1NEG ($j=N_2^{+*}$), and all N_2^+ ($j=N_2^+$).
τ_λ	Einsteinian lifetime for a particular emission.
τ	Transmittance, I(t)/I(i), Appendix A.
Υ_λ	Transmittance maximum, Appendix A.
Υ_{max}	Angle of refraction a lightwave makes with a given filter layer, Appendix A.
ϕ	Angle an aperture spiral is rotated with reference (i.e., $\theta = 0°$) corresponding to $r = r_{min}$, Chapters II-V.
ϕ_{max}	Same as ϕ except the max refers to the angle rotated prior to repeating the cycle, Chapters II-V.

LIST OF SYMBOLS (Concluded)

Symbol	Definition
χ	Phase shift for a filter stack.
ψ	Cone half angle for a filter system.
ψ_0	ψ at $\theta = 0°$. Statistical weight of species n, Chapter VI, Appendix C.
ω	Solid angle of cone of intercept by a field stop and filter area arrangement.
$\Omega(n,n')$	Collisonal strength parameter for states n,n′, Chapter VI.
F	Finesse for a two parallel plate system.
$1\Sigma_g^+$	N_2 Ground state.

CHAPTER I
INTRODUCTION

The research described in this report involves two separate, but related, studies. The first study is that of a unique spatial scanning photometer system. The high throughput qualities found in flat plate interference systems and the near-constant transmittance and bandpass characteristics found traditionally in grating spectrometer systems are convolved properties of this unique system. The second study involves the investigation of the geophysical role of $O^+(^2P\text{-}^2D)$ emissions in electron aurora. The photometer system described in the first study is one of the tools used to investigate oxygen ion metastable emission.

The introductory chapter continues with a brief description of some spatial scanning schemes reported by other investigators, previous work done on the $O^+(^2P\text{-}^2D)$ in aurora (measurements and theories) and a brief description of the contents of the other chapters text.

1.1 PREVIOUS INVESTIGATIONS IN SPATIAL SCANNING OF ALL-DIELECTRIC FILTERS

The interference elements of this study are limited to solid spaced, all-dielectric filters. The spatial scanning discussion in the text, and history, will be confined to the field stop configuration in the aperture plane and· the shaping and positioning of that field stop in allowing imaged fringes, or portions of, to pass beyond the aperture plane.

The pin-hole, or circular field stop, is the most commonly used field stop in Fabry-Perot type systems. For solid spaced systems, the circular field stop passes the annular shaped fringe for a normal orientation of the interference element. Eather and Reasoner (1969) discuss extensively the photometer characteristics offered by tilting the interference element and translating the fringe pattern across the field stop. The tilting photometer offers the advantage of changing the peak bandpass wavelength of the photometer system and thus allowing a measurement of the background radiation underlying the emission of interest. In tilting the interference element, a bandpass distortion, or "broadening", occurs which must be compensated for in the interpretation of data. The field of view and pointing direction of the system remains fixed in the tilting photometer scheme.

A second type of spatial filtering has been accomplished by generating annular shaped field stops whose radial distances and annular breadths vary to accomplish a given resolution. Such a system is described in Shepherd et. al. (1965). Each annulus offers a different look angle through the interference element giving a bandpass shift at a constant resolution. Such a system requires a pointing lens to orient the look angle to the same sky position. A large number of annular stops are required such that appropriate peak transmittance stops can be achieved for a particular interference element.

1.2 EARLY MEASUREMENTS OF OII AURORAL EMISSION

Identification of the $O^+(^2P\text{-}^2D)$ emission in aurora was first reported by Omholt (1957). Omholt reported on several spectra obtained with a grating spectrograph from observations made at Yerkes Observatory in 1956. On two of the spectra a broad feature at λ7325Å was noted and believed to be the O^+ doublet. He noted that the doublet appeared most prominent in the 'upper' part of the aurora. He speculated that since the feature was not notable in the lower parts or in all spectra that the emission was probably quenched.

Dufay (1959) reported several measurements of a feature at λ7327Å, which he identified as the O^+ doublet. These measurements were made in 1957. For a particular aurora of September 30, an estimate of some relative intensities was given. Much like Ohmolt's measurements, these were primarily of an identifying nature and not of sufficient resolution to completely resolve the doublet.

A measurement was reported by Wallace (1960) from Yerkes Observatory for a December, 1958 aurora. This measurement was used to substantiate the presence of the emission to support the identification of the $O^+(^2P\text{-}^4S)$, 3727Å doublet in a spectrograph he was analyzing of the February 10/11, 1957 great 'Red Aurora'. In the December event reported (although no related emission spectra were reported) the $O^+(^2P\text{-}^2D)$ doublet was resolved and relative line strengths of the doublet were compared and verified with the Seaton and Osterbrock (1957) theoretical values.

Vallance Jones (1960) did obtain spectrograms of the 'Red Aurora' of February 10/11, 1957 at Saskatoon. The Jones' spectra was measured with a high dispersion instrument with a spectral slit of ~ 5.4Å. Jones identified relative intensities of many other atomic and molecular emissions including the N_2 $1PG_{5,3}$ at 7384.2Å. Intensities of interest to this study were the $O^+(^2P\text{-}^2D)$ wavelength positions at 7319.4Å, and 7330Å, and N_2 $1PG_{5,3}$ at 7384.2Å with relative intensities of 17.0, 11.8, and 2.7, respectively. According to Jones (1971), no further auroral measurements of the doublet have been reported. This particular aurora has been extensively studied. I_{6300}/I_{5577} ratios were reported between 3 and 10 by Shuisakaya (1967) in the 60-70° geomagnetic latitude range. Jones (1971) summarized various auroral spectral classes, and this type of aurora is estimated to have a typical lower border height of 250 km. The Jones' (1960) data will be examined more extensively in Chapter VIII.

Recently, Walker (1975) reported a measurement made on an Atmospheric Explorer Satellite from which pertinent $O^+(^2P)$ continuity parameters were deduced. These results will be discussed in Chapters VII and VIII.

1.3 EARLY THEORIES OF $O^+(^2P\text{-}^2D)$ AURORAL EMISSION

The atomic transition parameters for O^+ are given by Seaton and Osterbrock (1957). Electron impact ionization cross sections for O^+ from ionization threshold to several hundred electron volts were theoretically determined by Seaton (1959). The total ionization cross section was verified by Fite and Brackmann (1959). According to Seaton, the probabilities of ionizing to a ^2P, ^2D, or ^4S state are .2, .4, and .4, respectively. More recently, Kazaks et. al. (1972) calculated a breakdown of 3:5:4, respectively, for the ^2P, ^2D, and ^4S states. These values for ionization probability are for $E > 300$ ev, or the energy regions where the Born approximation describes the ionization cross section. For perspective, examination of the total ionization cross sections reviewed by Kieffer and Dunn (1966) suggests the total ionization cross section ratio of O to N_2 is $\sim .5$ for $E > 300$ ev.

Chamberlain (1961) has postulated that quenching of $O^+(^2P)$ must be large in light of the auroral measurements discussed above. Dalgarno and McElroy (1965), in treating dayglow analysis, estimated daytime intensities with and without a large deactivation rate (10^{-10} cm^3 sec^{-1}). They found resultant intensities consistent with their earlier estimates which required a large deactivation rate. Walker and Rees (1968) studied ionospheric electron densities and temperatures in aurora. In their analysis, the N_2 deactivation rate of $O^+(^2P)$ was assumed to be 10^{-10} cm^3 sec^{-1}. The high quenching rate is usually referenced to Dalgarno and McElroy (1965) (i.e., Jones, 1971; and Gerard, 1970). Dalgarno and McElroy, however, did not give an argument for the high deactivation rate in their dayglow study. Since they first used the high rate, however, reference will be made to their work for the rate.

Gerard (1970) made a study of the metastable oxygen ion and related optical emissions based on the Seaton (1959) cross sections and the Dalgarno and McElroy (1965) quenching rate of 10^{-10} cm^3 sec^{-1} Gerard related the volume emission rates of the oxygen metastable $O^+(^2P\text{-}^2D)$ and $O^+(^2D\text{-}^4S)$ to $N_2^+1NEG_{0,0}$ for a theoretical particle flux distribution of an IBC II type aurora. Gerard made comparisons of his computed results to spectra observed by Omholt (1957) and Wallace (1960) to verify his computed volume emission rates. Gerard's interpretation of the spectra used for comparison verified his analysis.

1.4 A BRIEF SUMMARY OF THIS WORK

A study of $O^+(^2P\text{-}^2D)$ emission was undertaken by this author to further clarify $O^+(^2P)$ metastable chemistry in aurora. The study involved the investigation of both ground based and rocket measurements of $O^+(^2P\text{-}^2D)$ emissions in aurora.

The ground based measurements were made with a unique photometer system which has application to investigations of other atmospheric glows. The first half of this report (Chapters II through V) describes this system.

Chapter II is aimed at giving the reader a fundamental understanding of the theoretical aspects of the spatial scanning photometer. Transmittance and bandpass characteristics are derived and described for the instrument in terms of transmission half-widths rather than analytic descriptions of the entire transmission function. The individual broadening functions and the convoluted instrument function are discussed. The achievement of a nearly constant instrument function for all slit positions is probably the most significant advantage of this scheme over other spatial scanning schemes.

The all-dielectric filter properties were investigated in the laboratory, independent of the photometer, to get an understanding of their properties as they apply to the instrument. The particular emphasis in the filter study was on the angular characteristics. These findings are the subject of Chapter III. Characteristics were found to be widely variable from filter to filter. Theoretical aspects of these elements are discussed in Appendix A.

A single spiral photometer was fabricated and studied in the laboratory to test the theoretical hypothesis of Chapter II. This study is reported in Chapter IV. Several objective configurations and filters were employed in the system and all are discussed in this chapter. A Fortran IV program is listed in Appendix B which generates the spatial slit functions described herein.

Finally, a ground based spectrophotometer was built with the instrument characteristics oriented to the measurement of $O^+(^2P\text{-}^2D)$ in aurora. A multi-spiral scheme was employed in the ground based system. The main advantage over the single spiral device is an increased throughput for a given resolution. This ground based system is described briefly in Chapter V. A thorough understanding of Chapters II and IV is necessary for the reader to fully understand what is presented in this chapter.

The last half of this report describes a study of the auroral $O^+(^2P\text{-}^2D)$ emission. The emission is weak and is surrounded by emissions of the N_2 1PG band system. Ground based measurements are further plagued with OH emissions emanating at wavelengths close to the emission wavelengths of $O^+(^2P\text{-}^2D)$.

The theory of $O^+(^2P\text{-}^2D)$ is presented in Chapter IV. The continuity equation for the $O^+(^2P)$ state is derived, with flux divergence considered negligible. The probability of $O^+(^2P)$ was related to the probability of N_2^+1NEG band emissions for convenience in analyzing the measurements of the subsequent chapters. Appendices C and D provide detailed $O^+(^2P)$ transition probabilities and production by electron impact information respectively.

In Chapter VIII, ground based observations of $O^+(^2P\text{-}^2D)$ and $N_2^+1NEG_{1,0}$ emissions are presented and analyzed. Theories of $O^+(^2P)$ for aurora are presented in terms of ratios of predicted I_{7319} and I_{4278}. Appendix E is dedicated to the details of reducing the ground based measurements. Appendix F describes the volume emission assumptions used for the $N_2^+1NEG_{1,0}$ emissions as based on previous investigations.

Chapter VIII reports the detailed analysis of a rocket measurement of the $O^+(^2P\text{-}^2D)$ and $N_2^+1NEG_{0,0}$ emissions. The efficiency of producing $O^+(^2P)$ by electron impact and quenching extremes were deduced from the data. The resultant values for these parameters are radically different from previous investigator's findings. Because of this, the data reduction and error analysis are belabored in Appendix G to lend credibility to the findings. The N_2 1PG band system used in this analysis is listed in

Appendix H in the Fortran IV language. Several 'New Models' are discussed in the Chapter which better describe these measurements than the models of previous investigators.

Chapter IX summarizes the primary conclusions arrived at in this study. The unique characteristics of the sector spectrophotometer system as well as auroral $O^+(^2P-^2D)$ investigations are discussed.

At the beginning of this study, two goals were visioned. The first was to explore a spatial scanning scheme for Fabry-Perot type interference generators. The desired characteristics of the scanning scheme included exploring the extent of wavelength range available in a single interference filter. Also desirable in the spatial scanning were a constant (wavelength independent) throughput, constant bandpass, and near continuous wavelength selectability or tuning of the instrument. In essence, an instrument having the scanning flexibility of a grating spectrometer but having the light gathering power of a Fabry-Perot aperture was desired. The second goal was to apply that instrument to measuring low light level emission, in aurora, that was of geophysical interest but difficult to examine with conventional techniques. The goal was to measure from the ground the $O^+(^2P-^2D)$ emission intensity at $\lambda 7319$Å to discern the radiative loss rate of the doublet. The continuity of production and loss of $O^+(^2P)$ in aurora was expected to be enlightened by such a measurement. A rocket measurement of the emission in aurora was added later in the study. The combined measurements afforded a unique opportunity to postulate some new concepts of $O^+(^2P)$ continuity in aurora.

CHAPTER II
SECTOR SPECTROPHOTOMETER INSTRUMENT THEORY

2.1 INTRODUCTION

The intent is to design a spectrophotometer with a high throughput and spectral resolution for faint light sources in the near infrared and visible wavelength region. The system ideally should have a constant resolution and throughput over the scanning range of the instrument. Ideally, the system would be a continuously scanning device which would permit spectral analysis and selectable exposure interrupts for time integrations at wavelengths of interest. Such a photometer is favorable for studying atomic and molecular emissions of chemical reactions originating from the earth's upper atmosphere.

A photometer was developed by Eather and Reasoner (1969) which employs a tilting principle to scan in wavelength. In their system, the aperture plane lies at the focal distance of the objective lens, which is fixed behind an interference filter. By tilting the filter, the fringe pattern passes over the aperture and the detector is exposed to a changing wavelength. In their photometer, Eather and Reasoner employed a dielectric interference filter to generate a fringe pattern. Filter characteristics were studied in the tilting filter photometer and filter properties suited for particular optical characteristics were investigated.

The interference fringe pattern generated by plane reflective surfaces of the Fabry-Perot type is characterized by a spatially narrowing fringe with increased radial distance from the objective axis in the focal plane (Born and Wolf, 1970). The dielectric interference filter generates an interference pattern but contains a solid spacer versus the gaseous type normally used with Fabry-Perot plates. The filters are also equipped with blocking elements to suppress the transmission of any wavelengths outside a specified band, that is, all orders are suppressed except one. Given a monochromatic source, a single fringe will be generated with a dielectric filter and the characteristics of this fringe can be described very similarly to the gas spaced Fabry-Perot. The spatial breadth of the fringe will depend on the radial distance from the objective axis intersect in the focal plane of the objective. A monochromatic source of a shorter wavelength would generate its fringe at a larger radial distance than a longer wavelength, due to the fixed spacer index and spacing.

By tilting the filter, the fringe pattern moves in the focal plane and a fringe generated by some monochromatic source can be made to pass over a slit in the focal plane of the objective. Eather and Reasoner (1969) employed this principle in their tilting-filter photometer. In their instrument a spatially fixed, circular aperture was used. Since the aperture was fixed, as the fringe pattern passed over the field stop, a greater breadth for short wavelength fringes was allowed to pass through the aperture, resulting in an instrument broadening, varying with tilt angle, and consequently, wavelength. To design a mechanical scanning instrument with a constant resolution, one must account for the spatially narrowing fringes generated at radially larger distances (i.e., at shorter wavelengths) from the objective axis intersect in the aperture plane. These effects have been compensated for in the sector spectrophotometer explored in this report.

2.2 INSTRUMENT THEORY (THE IDEAL INSTRUMENT)

2.2.1 APERTURE THEORY, WAVELENGTH AND THROUGHPUT

The relationship between the angle of tilt of a filter and the normal axis to a filter is reviewed in Appendix A. Equation A-10 of Appendix A can be put in abbreviated terms, i.e.,

$$\frac{\Delta\lambda}{\lambda_0} = \frac{1}{\mu^{*2}} \frac{\theta^2}{2} \qquad (1)$$

where

$$\frac{1}{\mu^{*2}} = \frac{P}{1 - Q} \quad \text{(P and Q are defined in Appendix A)}$$

μ^* – referred to as the effective index

θ – tilt angle (in radians) .

The slope of the wavelength shift versus θ^2 (θ in degrees) will be defined as α, where

$$\alpha = \frac{\lambda_0 \pi^2}{2\mu^{*2}(180)^2} \quad . \qquad (2)$$

It therefore follows that:

$$\Delta\lambda = \alpha\theta^2 \quad (\theta \text{ in degrees}) \qquad (3)$$

or

$$\Delta\lambda = a\theta^2 \quad (\theta \text{ in radians}) \qquad (4)$$

where

$$a = \frac{\lambda_0}{2\mu^{*2}} \quad . \tag{5}$$

A schematic of a filter, objective configuration employed by most photometers, is shown in Figure 1. This particular configuration will image an infinitive source at the aperture plane where the field of view is described by the aperture area and the objective aperture plane separation. The following definitions apply:

A_1 – area of interference filter

A_2 – area of the aperture (field stop)

f – focal length of the objective lens

r_1 – radius of interference filter

r – radial distance of the aperture slit from the objective axis intersect with the aperture plane

θ – previously defined .

The throughput of such a configuration is given by Born and Wolf (1970) as:

$$L = A\omega \tag{6}$$

where L is throughput, A is area of cone of intercept, and ω is the solid angle of cone of intercept. For a displaced aperture, as indicated in Figure 1, the throughput becomes

$$L = \frac{A_1 A_2}{f^2} \cos^4 \theta \quad . \tag{7}$$

In equation (7), note that for a given input aperture size (A_1) and focal length (f), A_2 or the aperture area must increase for L to remain constant. The most commonly used fixed wavelength photometers employ a circular pinhole for A_2 and fix $\theta = 0°$.

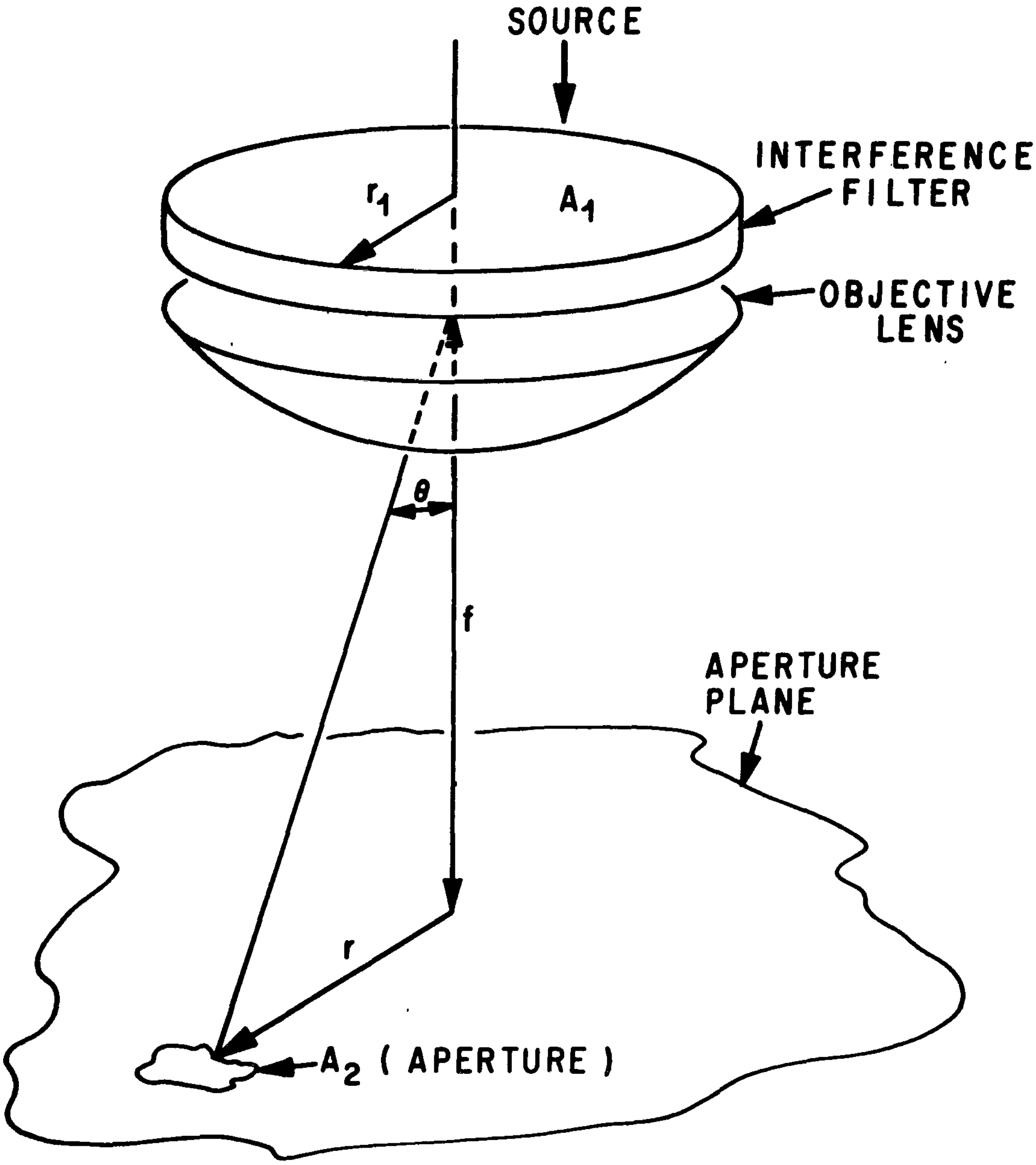

Figure 1. Optical schematic and symbol definitions of a source imaged on an aperture plane through an interference.

Examination of an arc-aperture or annulus sector, as depicted in Figure 2, will aid in evolving the principle of a unique system having considerable advantages over fixed field stops. In Figure 2 is shown a sector of a circular shaped slit with δr breadth at r distance from the objective axis intersect with the aperture plane subtending an angle $\delta\phi_0$. The area of such a sector is given by:

$$A_2 = r\delta r\delta\phi_0 \quad . \tag{8}$$

If one could move such a slit from $r = r_{min}$ to some r maximum, but decrease δr as the slit moves to account for the changing breadth of projected fringes, a constant throughput with scan could be approached. That is, since

$$r = f \tan\theta \tag{9}$$

where, f - objective lens focal length, Equation (7) can be rewritten as

$$L = \pi r_1{}^2 \frac{\delta r \delta\theta_0}{f} \tag{10}$$

where

$$\cos\theta = \frac{f}{(r^2 + f^2)^{1/2}} \quad \text{and} \quad \sin\theta = \frac{r}{(r^2 + f^2)^{1/2}} \quad . \tag{11}$$

A spatial scheme to move the slit in the $\delta\phi_0$ sector from r_{min} to r_{max} may be envisioned as follows. One can approximate the arc aperture with a "spiral" on a disk spiralling from $r = r_{min}$ to r_{max}. Visualize a second disk with a "pie" sector cut from it, overlaying the spiral disk. Now, by rotating the spiral disk overlayed by the spatially fixed disk, a spiral chord which moves from $r = r_{min}$[1] to $r = r_{max}$ is exposed in the sector "pie".

In order to scan in wavelength in uniform time, the relationship

$$r = f \tan\theta = f \tan\left(\sqrt{\frac{\lambda - \lambda_0}{a}}\right) \tag{12}$$

---

[1] $r_{min} \neq 0$ since δr must be finite demanding in turn that r be finite.

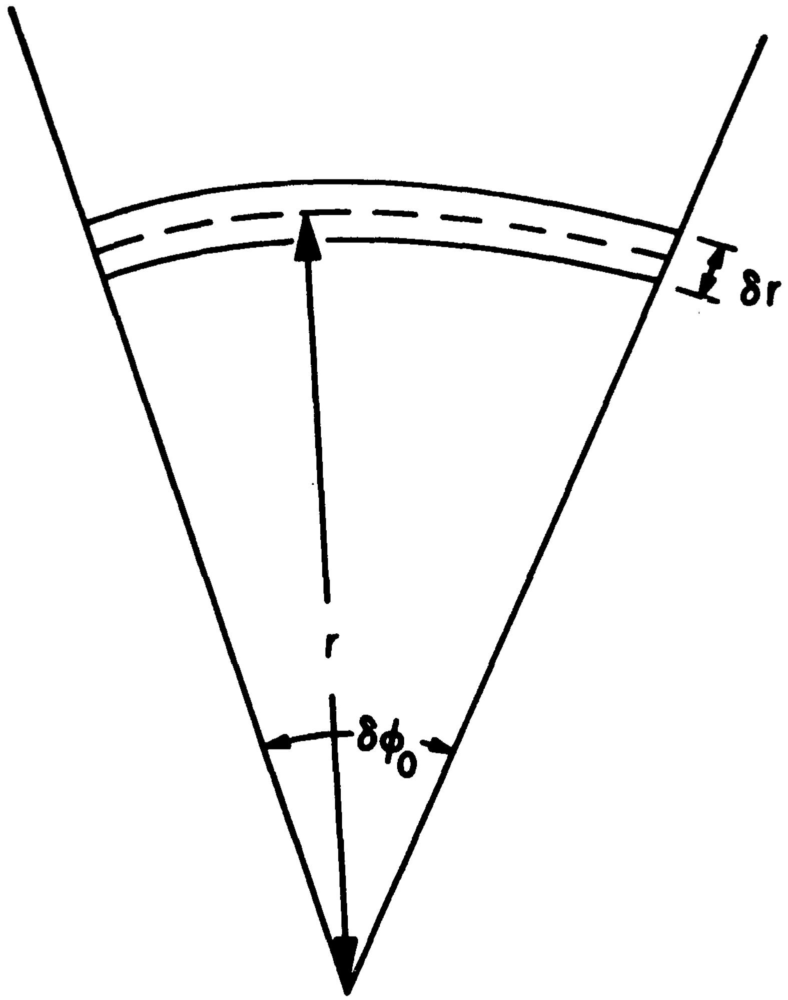

Figure 2. An aperture schematic for a radially shaped slit of δr breadth as viewed normal to the aperture plane through a sector with angle $\delta\phi_0$.

must be examined. Consider turning the disk at a uniform rate from $\phi = 0°$ to ϕ_{max} requiring

$$\phi = \beta(\lambda - \lambda_0) \tag{13}$$

or

$$\frac{\delta\phi}{\delta t} = \frac{\beta\delta\lambda}{\delta t} = \text{constant} \tag{14}$$

where

$$\beta = \frac{\phi_{max}}{\Delta\lambda_{max}} = \text{constant} \quad . \tag{15}$$

It follows then that

$$r = f \tan\left(\sqrt{\frac{\phi}{\beta a}}\right) \quad . \tag{16}$$

But,

$$\phi_{max} = 2\,\pi n \tag{17}$$

where n = number of turns in the spiral from $r = r_{min}$ to r_{max} or the number of rotations per scan.[2]

Thus, for a constant wavelength scan, it can be written that

$$r = f \tan\left(\sqrt{\frac{\Delta\lambda_{max}\,\phi}{2\,\pi n a}}\right) \quad . \tag{18}$$

---

[2] It is possible to have n greater than one if some mechanism is employed to mask the unwanted spiral chords in the sector exposing only a single chord to the detector for a given spiral position.

Another way of expressing Equation (18) may be derived by manipulating Equation (4) to read

$$\theta = \sqrt{\frac{\Delta\lambda}{a}} \quad , \tag{19}$$

or

$$\theta_{max} = \sqrt{\frac{\Delta\lambda_{max}}{a}} \tag{20}$$

resulting in

$$r = f \tan\left(\theta_{max} \sqrt{\frac{\phi}{2\pi n}}\right) \quad . \tag{21}$$

Expressions (18) and (21) both describe the criterion for r with respect to ϕ for a constant wavelength scan rate in a fixed rotation rate spiral system. Note in Equation (21) that for $\phi = \phi_{max}$,

$$r_{max} = f \tan \theta_{max} \quad . \tag{22}$$

2.2.2 APERTURE THEORY, BROADENING CHARACTERISTICS

Since a $\delta\phi_0$ arc is exposed in the sector, there exists an integral number of $\delta\phi$ increments in that arc sector, i.e.,

$$\delta\phi = \beta\delta\lambda \quad \text{[A derivative of Equation (13)]} \quad . \tag{23}$$

For the $\delta\phi_0$ of the sector then,

$$\delta\phi_0 = \beta\delta\lambda_C \tag{24}$$

where $\delta\lambda_C$ is the broadening introduced by approximating the circular fringe pattern by a spiral chord. In a sense, the instrument broadening dependence on tilt mentioned earlier has been minimized, but a curvature broadening as described above has been introduced. Equation (24) can be rewritten to read:

$$\frac{\delta\lambda_C}{\delta\phi_0} = \frac{1}{\beta} = \frac{\Delta\lambda_{max}}{2\,\pi n} \tag{25}$$

or

$$\frac{\delta\lambda_C}{\Delta\lambda_{max}} = \frac{\delta\phi_0}{2\,\pi n} \quad . \tag{26}$$[3]

This is a square function broadening with the curvature finesse now written as

$$N_C = \frac{2\,\pi n}{\delta\phi} \quad . \tag{27}$$

The broadening introduced by a finite aperture (breadth broadening-$\delta\lambda_B$) may be computed by first approximating Equation (1) as

$$\lambda - \lambda_0 = \Delta\lambda = a \sin^2 \theta \quad . \tag{28}$$

The breadth broadening, written in terms of θ follows from Equation (28) as

$$\delta\lambda_B = 2a \sin\theta \cos\theta \, \delta\theta \quad . \tag{29}$$

In order to express Equation (29) in terms of r, Equation (9) is differentiated to read:

$$\delta\theta = \frac{\cos^2\theta}{f} \, \delta r \tag{30}$$

---

[3] $\Delta\lambda_{max}/\delta\lambda_C$ is analagous to finesse, when speaking of a Fabry-Perot system (Born and Wolf, 1970). In this instrument, finesse (N) will be defined as $\Delta\lambda_{max}/\delta\lambda$ or in this case, the curvature finesse is $N_C = \Delta\lambda_{max}/\delta\lambda_C$.

which may be substituted into Equation (29), along with the definitions of sin θ and cos θ, to yield:

$$\delta\lambda_B = \frac{2\ arf^2\ \delta r}{(r^2 + f^2)^2} \quad . \tag{31}$$

Using a finesse definition analogous to the curvature broadening, the breadth finesse can be written as:

$$N_B = \frac{\Delta\lambda_{max}}{\delta\lambda_B} = \frac{\Delta\lambda_{max}\,(r^2 + f^2)^2}{2\ arf^2\ \delta r} \quad . \tag{32}$$

2.2.3 TOTAL INSTRUMENT FUNCTION

The ideal instrument is defined as one which satisfies a constant aperture broadening function, a constant instrumental throughput, and a constant wavelength change for a fixed spiral rotation rate, i.e.,

$$\delta\lambda_A = (\delta\lambda_C^2 + \delta\lambda_B^2)^{1/2} = \text{constant} \quad , \tag{33}$$

$$L = \frac{A_1}{f^2}\, r\delta r\delta\phi_0\, \frac{f^4}{(r^2 + f^2)^2} = \text{constant} \quad , \tag{34}$$

or

$$\frac{r\delta r\delta\phi_0}{(r^2 + f^2)^2} = \text{constant} = \frac{A\omega}{f^2 A_1} \simeq \frac{\omega_0}{f^2} \quad , \tag{34a}$$

where $\omega_0 = \omega$ at $\theta = 0°$, and

$$r = f \tan\theta_{max} \frac{\omega_0}{2\ \pi n} \quad , \tag{35}$$

where $\delta\phi/\delta t$ = constant.

From the previous relationships of $\delta\lambda_C$ and $\delta\lambda_B$, Equation (33) can be rewritten as

$$\delta\lambda_A = \left\{ \left[\frac{2\, a f^2\ r\, r}{(r^2 + f^2)^2}\right]^2 + [\beta\delta\phi_0]^2 \right\}^{1/2} . \tag{36}$$

However, from Equation (34a)

$$r\delta r = \frac{\omega_0 (r^2 + f^2)^2}{f^2\, \delta\phi_0} , \tag{37}$$

permitting a rewrite of Equation (36), i.e.,

$$\delta\lambda_A = \left[\left(\frac{2\, a\omega_0}{\delta\phi_0}\right)^2 + (\beta\delta\phi)^2 \right]^{1/2} . \tag{38}$$

It is shown, therefore, that with a constant throughput requirement, the breadth broadening is inversely proportional to $\delta\phi_0$. Thus, for constant (i.e., a "pie" shaped section, $\delta\phi_0$) the aperture function is constant [Equation (38)].

The aperture is then constructed by selecting an instrument finesse,

$$N_I = \frac{\Delta\lambda_{max}}{\delta\lambda_I} . \tag{39}$$

The aperture finesse becomes

$$\frac{1}{N_A^2} = \frac{1}{N_I^2} - \frac{\Delta\lambda_{max}^2}{\delta\lambda_{||}^2} - \frac{\Delta\lambda_{max}^2}{\delta\lambda_{\psi}^2} \qquad (40)^4$$

---

[4] $\delta\lambda_{||}$ and $\delta\lambda_{\psi}$ are filter characteristics contributing to the instrument function and are discussed in Appendix A.

By setting the two aperture finesses equal, the aperture finesse becomes:

$$N_B = N_C = \sqrt{2 N_A} \quad . \tag{41}$$

The sector angle can then be computed from Equation (27) depending on n selected and the spiral may be computed from Equations (31) and (35).

Another way of expressing Equation (37) is given by:

$$\delta r = \delta r_{max} \left(\frac{r^2 + f^2}{r_{max}^2 + f^2} \right) \frac{r_{max}}{r} \quad , \tag{42}$$

where

$$\delta r = \frac{(r_{max}^2 + f^2)^2 \; \delta\lambda\beta}{2 \; a r_{max} \; f^2} \quad . \tag{43}$$

Expression (43) serves as a convenient form for computing the spiral breadth as well as does Equation (31). The radial function r is computed as a function of ϕ [Equation (35)] to satisfy the constant wavelength scan rate criteria.

Broadening for the total instrument (instrument function) is due to the convolution of each broadening component in the instrument. The instrument function for a filter-aperture is made up by the convolution of these functions, i.e.,[5]

$$\delta\lambda_I = (\delta\lambda_F^2 + \delta\lambda_A^2)^{1/2} \quad , \tag{44}$$

where

$\delta\lambda_I$ – instrument function,

$\delta\lambda_F$ – filter broadening, and

$\delta\lambda_A$ – aperture broadening .

---

[5] An approximation. The aperture function is a square function broadening. The approximation involved in this convolution implies the filter broadening is a well behaved function, i.e., square, triangular, or Gaussian.

A $\delta\lambda_A$ relationship that is constant for a constant throughput has been derived. Note, however, that for $A\omega$ to be constant with θ, the cos θ dependence of A must be compensated by the inverse in ω. ω is related to the cone-half angle (ψ) by

$$\omega = \psi^2 \quad . \tag{45}$$

Note from Equation (A-13) that

$$\delta\lambda_\psi = G(\psi^2) \text{ or } G(\omega) \quad , \tag{46}$$

or, rewriting Equation (44), using Equation (A-13), it follows that

$$\delta\lambda_I = (\delta\lambda_{\|}^2 + \delta\lambda_\psi^2 + \delta\lambda_B^2 + \delta\lambda_C^2)^{1/2} \quad . \qquad (47)^{6}$$

The instrument apertures will then allow

$$\delta\lambda_\psi = \left(\frac{P}{1 - Q}\right) \frac{\lambda_0 \psi_0^2}{\cos\theta} \quad , \tag{48}$$

where ψ_0 - cone 1/2 angle at $\theta = 0°$. In terms of r and f, Equation (48) becomes

$$\delta\lambda_4 = \left(\frac{P}{1 - Q}\right) \frac{\lambda_0 (r^2 + f^2)^{1/2} \;\; \psi_0^2}{f} \quad . \tag{49}$$

For $\delta\lambda_I$ to be truly constant, then $\delta\lambda_\psi$ must be kept small relative to $\delta\lambda_{\|}$ and $\delta\lambda_A$. Therefore, once the aperture finesses and parameters have been computed, one should compute the solid angle of the instrument (ψ) and check $\delta\lambda_\psi$ (49) for cone angle effect on the total instrument function. Note that f controls r for a given A_2 and may be altered without affecting the aperture finesse.

---

6. Note that broadening due to polarizing has been ignored.

2.3 INSTRUMENT THEORY (MODIFIED)

The apertures, built for the spectrophotometers used in this study, employed a slight modification to the theory.

It was stated after Equation (44) that for a truly constant throughput, the cos θ change in A (A_1 cos θ) results in an inverse cos θ effect in (i.e., $\omega/\cos\theta$). If ω changes, the cone half angle or field of view of the instrument is allowed to change. This is not a desirable trait for an instrument to be used in the aurora.

Equation (8) was modified such that

$$L = A\omega = A_1\omega \quad , \tag{50}$$

which results in

$$\omega = \frac{A_2}{f^2}\cos^3\theta = \text{constant} \quad , \tag{51}$$

or, in terms of r and f,

$$\omega = \frac{rf\delta r\delta\phi_0}{(r^2 + f^2)^{3/2}} = \omega_0 \quad . \tag{52}$$

By substituting ω_0 [Equation (52)] into Equation (38), Equation (36) would become

$$\delta\lambda_A = \left\{\left[\frac{2\,arf\delta r}{(r^2 + f^2)^{3/2}}\right]^2 + [\beta\delta\phi_0]^2\right\}^{1/2} \tag{53}$$

and Equation (31) would become

$$\delta\lambda_B = \frac{2\,arf\,r}{(r^2 + f^2)^{3/2}} \quad . \tag{54}$$

In other words, by allowing L to change with cos θ, a constant ω and field of view are achieved. The sacrifice is for a $\delta\lambda_B$ varying as cos θ [Note Equation (54) differs from (31) by a cos θ factor]. A constant field of view also removes the cos θ effect from the cone half angle broadening function [Equation (48)].

CHAPTER III
FILTER CHARACTERISTICS – LABORATORY ANALYSIS

The purpose of this study was to analyze, in the laboratory, a number of available filters and examine their characteristics for potential instrument use. The filter broadening and transmission characteristics as a function of tilt angle were of primary interest. The transmission peaks of filters used were limited to the 5000-7500Å wavelength range. Both cryolite and zinc sulfide spacers are used in this region. Below ~ 4500Å, only cryolite is used due to dispersion in zinc sulfide (Lissberger, 1959).

The cone angle, temperature, dispersion, and spacer index effects have been studied by numerous authors (as referenced in Appendix A). The effective index and its use has also been explored by Lissberger and Wilcox (1959), Pidgeon and Smith (1964), Eather and Reasoner (1969), and others.

A monochromator arrangement, as depicted in Figure 3, was used to examine these filter characteristics. A collimated beam from the monochromator was passed through the filter and then a capture lens (not shown) imaged the beam on a detector. The filter was removed and the source intensity was determined and stored in a computer. The filter was then replaced and the source was again scanned for transmission versus wavelength computations.

The effective θ^2 slope versus $\Delta\lambda$ is shown in Figure 4 for a high index (λ_0 = 6296Å) filter. Note that up to $\theta = 30°$, the slope is relatively constant as has been verified by others. The transmission bandpass ($\delta\lambda_{\parallel}$) is shown in Figure 5. It was noted that at 36°, the transmission slope showed two peaks with a very distorted shape as if the beam had polarized. Note a gradual increase in bandpass with tilt angle. This particular filter was not examined as to whether the gradual broadening was due to polarizing or some other effect.

Another filter (low index) was examined and the more rapid wavelength shift versus θ^2 is shown in Figure 6. Broadening with tilt is more extreme than the high index filter discussed previously, as displayed in Figure 7.

It was noted in the filter section that the low-index filters should theoretically polarize at lower angles for a given order filter. The order of these filters is unknown but the index trend is apparent. What is not explainable is that the broadening is apparent at very low angles of tilt, and follows a near θ^2 effect rather than the very abrupt polarizing effect derived in the filter theory (Appendix A) with respect to the polarizing broadening.

This effect is furthermore born out in the λ_0 = 6308Å (low index) filter shown in Figure 8. In this case, the transmission profile was examined at 0° and 10° tilt, with and without a polarizer. Even at 0° tilt to the beam, this transmission curve shows an obvious

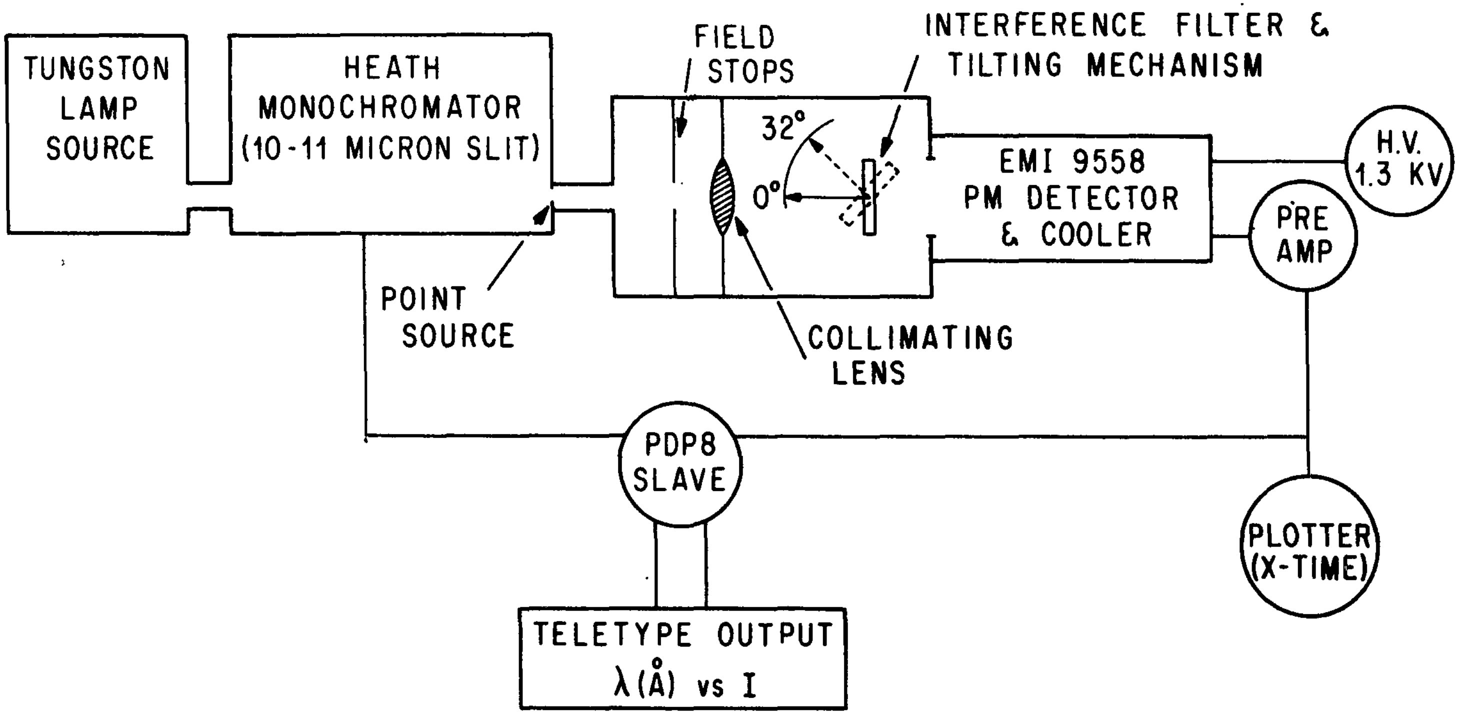

Figure 3. Schematic of the laboratory arrangement used for filter transmission studies.

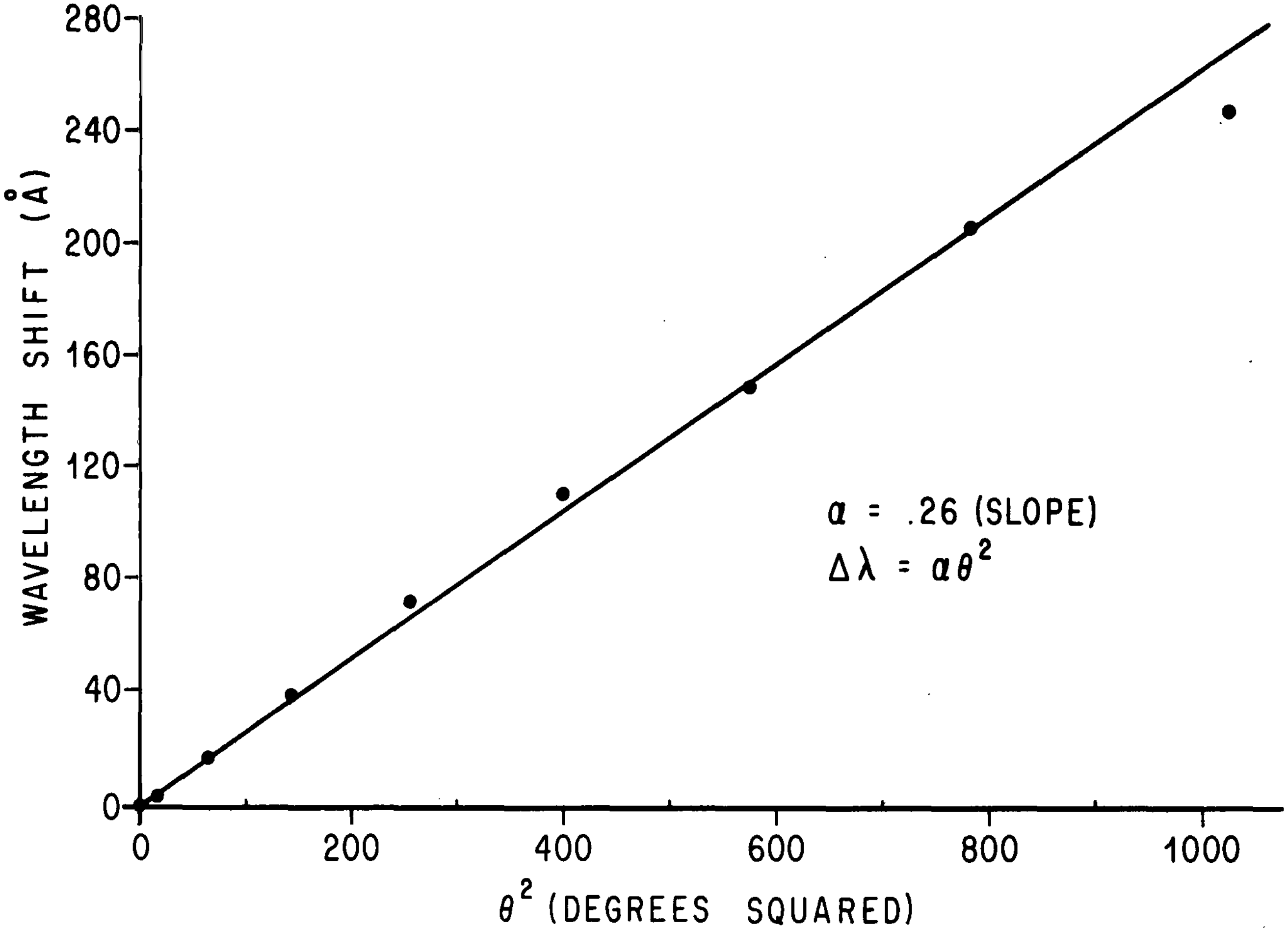

Figure 4. Wavelength versus θ^2 as deduced from the laboratory arrangement shown in Figure 3 for a λ_0 = 6300Å filter.

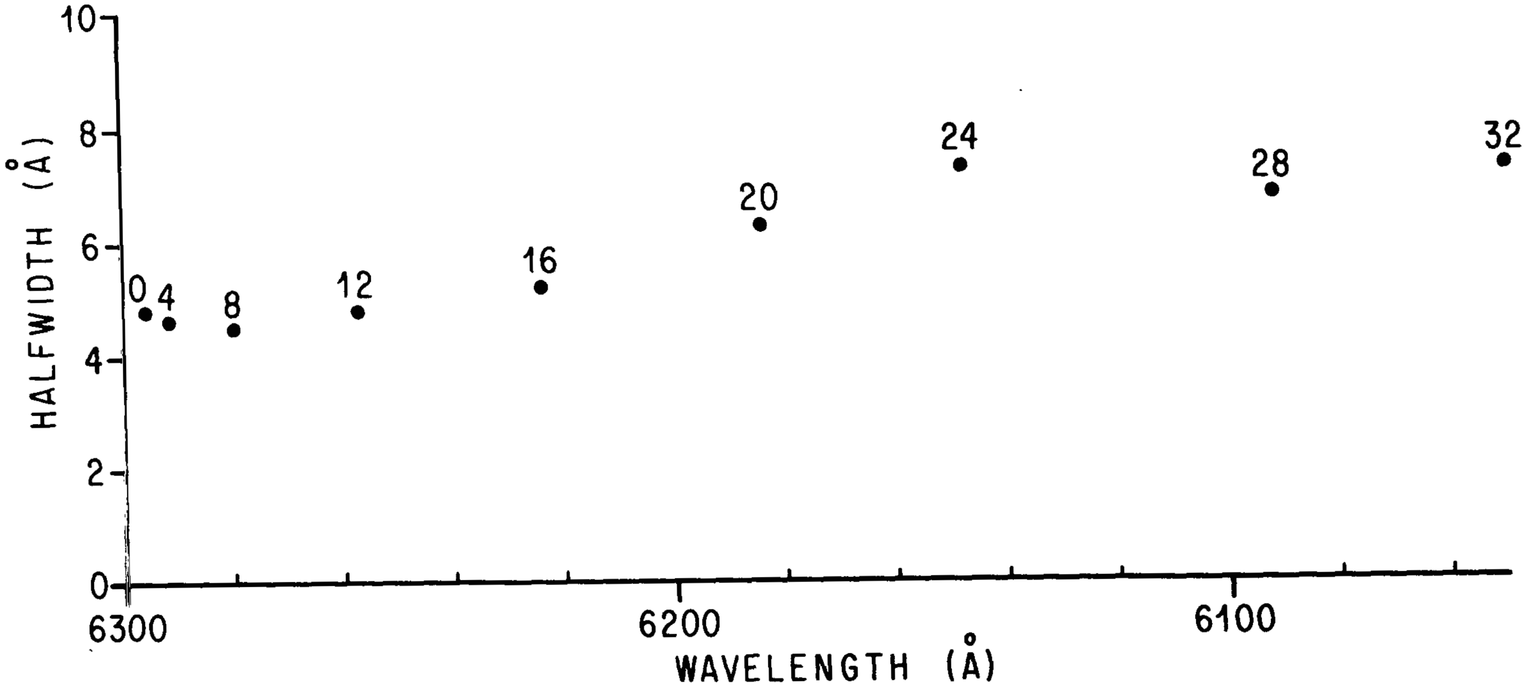

Figure 5. Halfwidth (full width at half maximum transmission) versus wavelength measured at incremental tilt angles for the λ_0 = 6300Å filter shown in Figure 4.

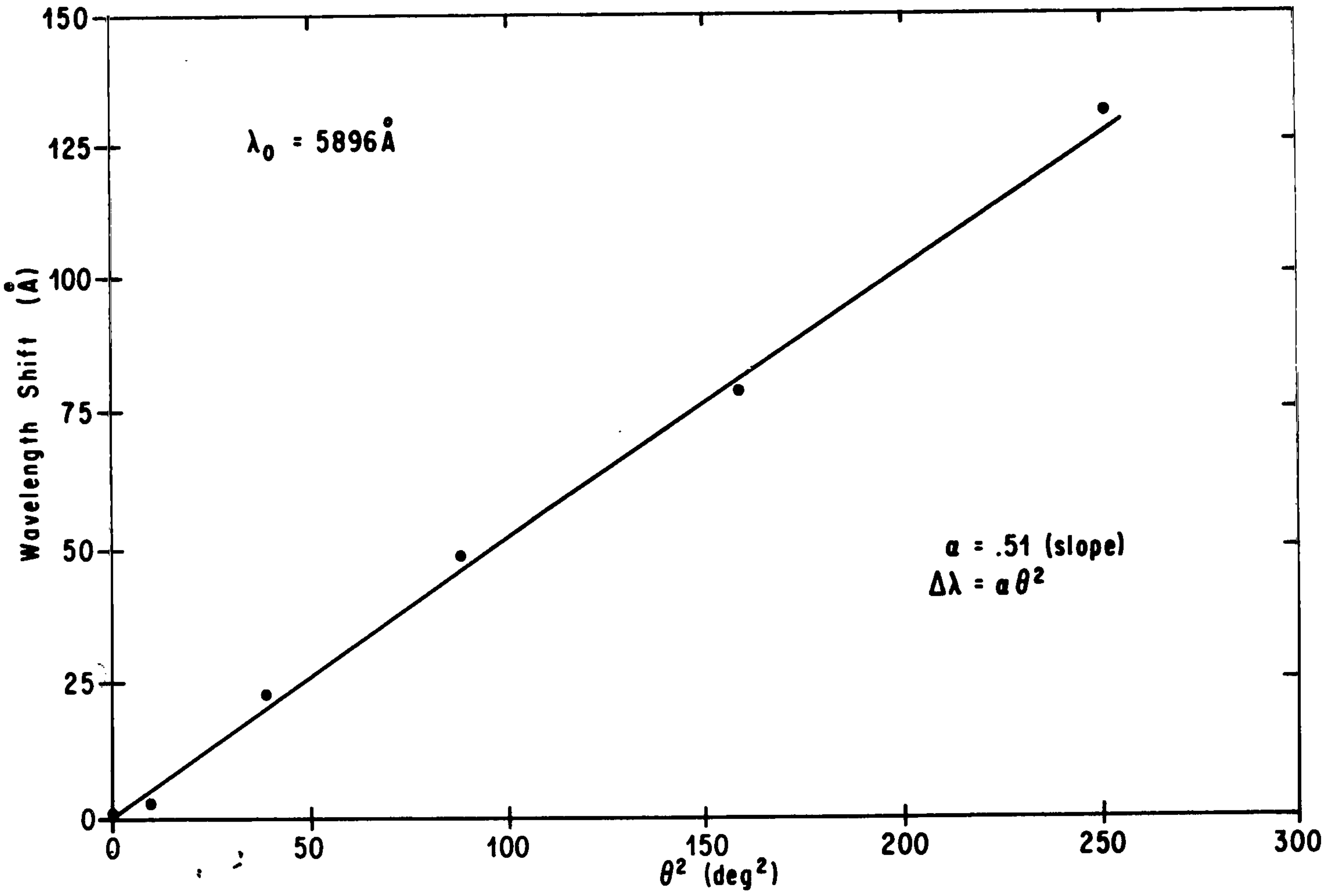

Figure 6. Wavelength shift versus θ^2 for a high index filter (λ_0 = 5896Å).

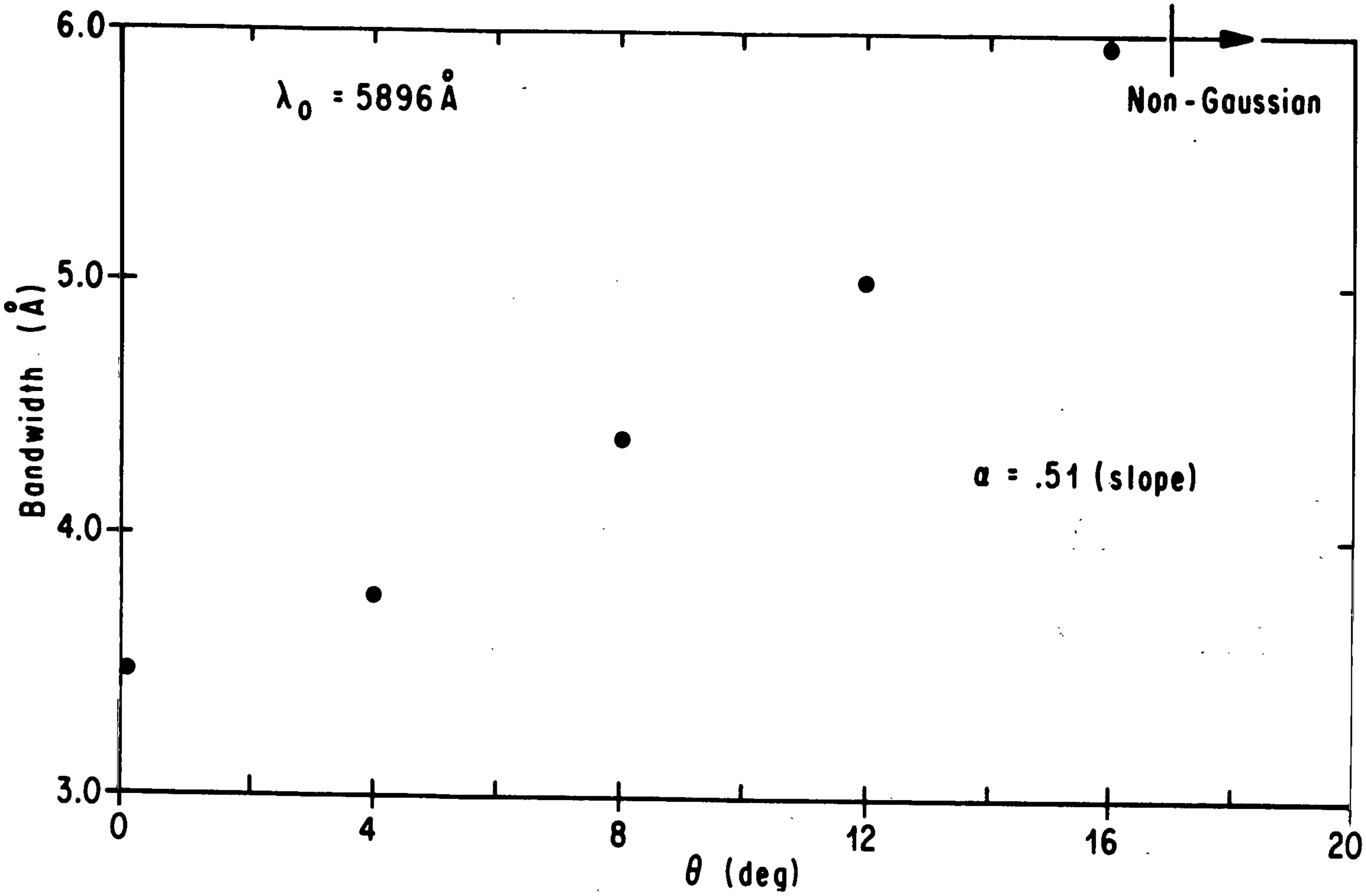

Figure 7. Halfwidth versus θ measured at incremental tilt angles for the λ_0 = 5896Å filter shown in Figure 6.

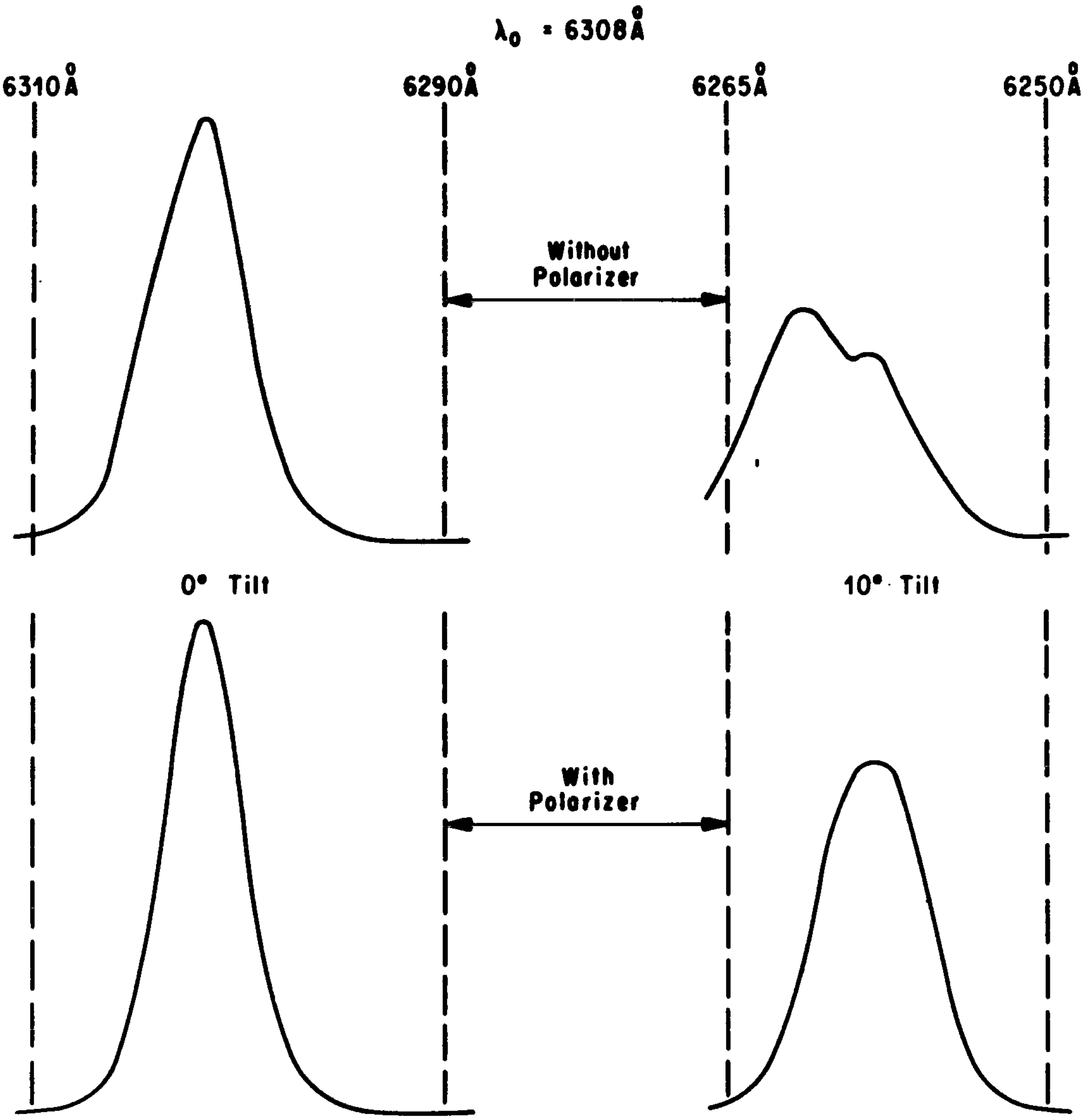

Figure 8. Transmission shape of a low index filter (λ_0 = 6308Å) with extreme polarizing characteristics. It is noted that even at 0° tilt, a distortion in the transmission profile exists which is removed with a polarizer.

distortion of the transmission profile, due to a polarized splitting. At 10°, the polarizing effect is very notable. One also notes that the polarizer did not account for all of the broadening. It can only be speculated that this non-polarized broadening, as observed with a collimated beam, might be due to roughness of film deposition, resulting in a changing reflectivity of a given film with angle, This is only speculation but users of the very narrow band filters should be aware that the effect exists.

In summary then, there are two effects not well defined. The polarized effect ($\delta\lambda_P$) does not adhere to the simplified theory examined in Appendix A. The trend that the high index filters (Z_nS spacer) polarize at much higher tilt angles than the low index (cryolite) is verified, although as noted in the last case, the degree and angular dependence are not well defined by the theory presented in Appendix A. The non-polarized broadening as a function of tilt is not explained. The investigation shows approximately 2 to 3 Angstroms gradual broadening prior to a tilt, corresponding to transmission distortion of a non-Gaussian nature. The rate of this change seems to follow a θ^2 relationship.

CHAPTER IV
A SINGLE SPIRAL SECTOR SPECTROPHOTOMETER

The previous two chapters have outlined the theoretical aspects of a spatial scanning photometer, and theoretical and laboratory investigations of some all-dielectric filters have been discussed. The next step, then, was to build a fairly simple instrument, primarily for laboratory investigation of the spatial scanning technique. This chapter describes the concept, fabrication, and testing of the first sector spectrophotometer.

4.1 BASIC CONCEPTS AND DETECTOR

It was decided to specify the initial spectrophotometer as having a single spiral ($n=1$) and individual finesses of 20 (i.e., $N_B=N_C=20$). Equation (27), of Chapter II, now sets $\delta\phi_0$ at 18°.[7]

The radial limit of r (r_{max}) taxes the requirement for the optics in the capture-detection portion of the instrument. The r_{max} can be increased with increased photomultiplier detection surface, with nearness of the detector to the aperture, and with decreasing angle (θ) of acceptance through the aperture, which depends on f and r. In this case, an EMI 9558 photomultiplier tube was used, offering a circular detection diameter of 44 mm. The tube was cooled to -20°C to reduce the dark count requiring a minimum physical separation distance of 9 cm between the photomultiplier tube face and the capture lens because of the cooler constraints. The determining factor remaining in ascertaining r_{max} was the capture lens, the lens diameter, and the angular dispersion of photons through the aperture to be focused on the phototube detector. A further restriction on r_{max}, of course, was that it must not exceed the small angle approximation in θ_{max} as required in the theory section.

4.2 CAPTURE AND OBJECTIVE OPTICS

The capture lens imaged the objective lens on the photomultiplier (since the source is diffuse). Figure 9 depicts a sketch of the lenses and detector where S_2 is fixed at 9 cm as previously mentioned.

It was decided to restrict the objective lenses to reasonably thin lenses and to shelf items. Objective lenses of 166 mm, 106 mm, 88 mm, and 57 mm were selected, and all objective combinations were used with the same aperture, capture lens, and detector combination. With S_2 (Figure 9) fixed, a capture lens focal length of near 45 mm was approximated as being an optimum focal length for the objective selected by inspection

---

[7] An aperture configuration is specified by the number of degrees a spiral rotates in going from $\phi = 0$ to $\phi = \phi_{max}$, where $\phi_{max} \approx 2\pi n$. For $n = 1$, ϕ_{max} is 2π and we term this as the 2π or single spiral spectrophotometer. An $n = 3$ system will be discussed later which will be classified as a multi-spiral spectrophotometer.

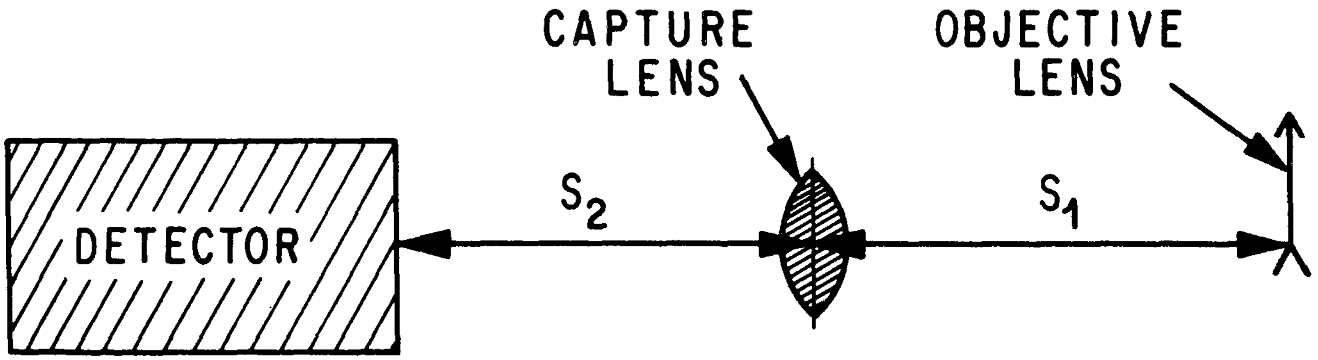

Figure 9. Schematic of the capture optics used in the sector system.

of the lens maker's formula (Jenkins and White, 1957). This is only a crude approximation, since the thin lens approximation is not totally justified. On a bench, a number of capture lenses were tried with the objectives chosen. A non-focused image on the detector resulted in a wander of the image on the tube face as the slit was moved in the aperture plane. A lens with a focal length of 52 mm was chosen for the capture lens and an r_{max} of 25 mm (~ 1 inch) was selected as a result of the bench study. The capture lens was a plano-convex lens with the flat side positioned up against the aperture to minimize angular loss with various positions of r of the slit. The r_{max} limit was such that all positions of r from r_{min} to r_{max} would permit capture on a mock tube face at the detector position in the bench study. Noticeable wander of the image across the tube face did occur for the 57 mm objective, but the remaining objectives yielded no detectable wander of the image. The θ_{max}'s for the selected r_{max}'s ranged from 8° for the 166 mm objective to 23° for the 57 mm objective. The optics chosen are summarized in Figure 10.

Note in Figure 10 that the capture optics are offset from the objective axis. The scan involves moving the aperture radially away from the objective axis, which necessarily centers the capture lens over the sector. This is best put into perspective by examining Figure 11, which shows the capture lens and optics as viewed from the detector. Since the object (the objective lens) is at an angle to the capture lens axis, the detector must be offset from the capture lens to capture the image.

An additional point on the "semi-focused" image on the detector should be made. The intent is to count the total number of photons passing through the aperture. They can be counted as long as they hit the detector surface of the tube, which ideally would be equally efficient over all areas of its surface. Most photomultipliers decrease in efficiency to the outer extremes of the tube face. For a wandering image, efficiency variations in the photomultiplier must necessarily be accounted for.

4.3 INTERFERENCE FILTER

The filter used in the spectrophotometer was a λ_0 = 6300Å dielectric, which had drifted towards the blue to 6296Å (peak transmission at θ = 0°). It was felt that the filter could still function for nightglow spectroscopy in looking at the (9,3) hydroxyl band at λ6356Å.

The filter was first studied, independent of the spectrophotometer system, to determine its characteristics. The 6300Å filter described in the previous chapter was used for this purpose. This filter was a high index (Spacer - Z_nS) all-dielectric with $\alpha \approx .26$.

The above filter and its role in the photometer system are discussed in this chapter. Before proceeding, examination of the effect of the index of refraction of the spacer in the system may be enlightening to other potential users of the technique.

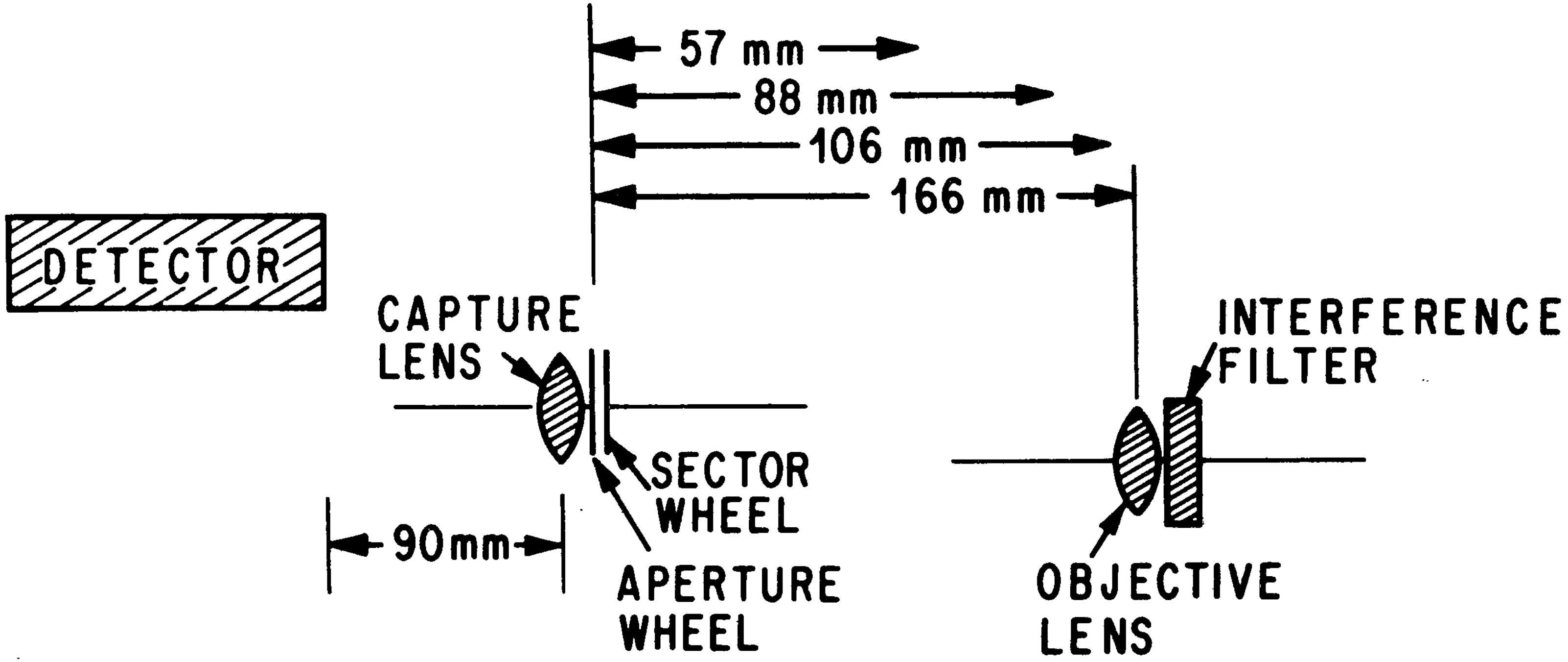

Figure 10. Schematic of the single spiral sector spectrophotometer optical arrangement. The objective focal lengths used in the spectrometer are indicated at the top of the figure.

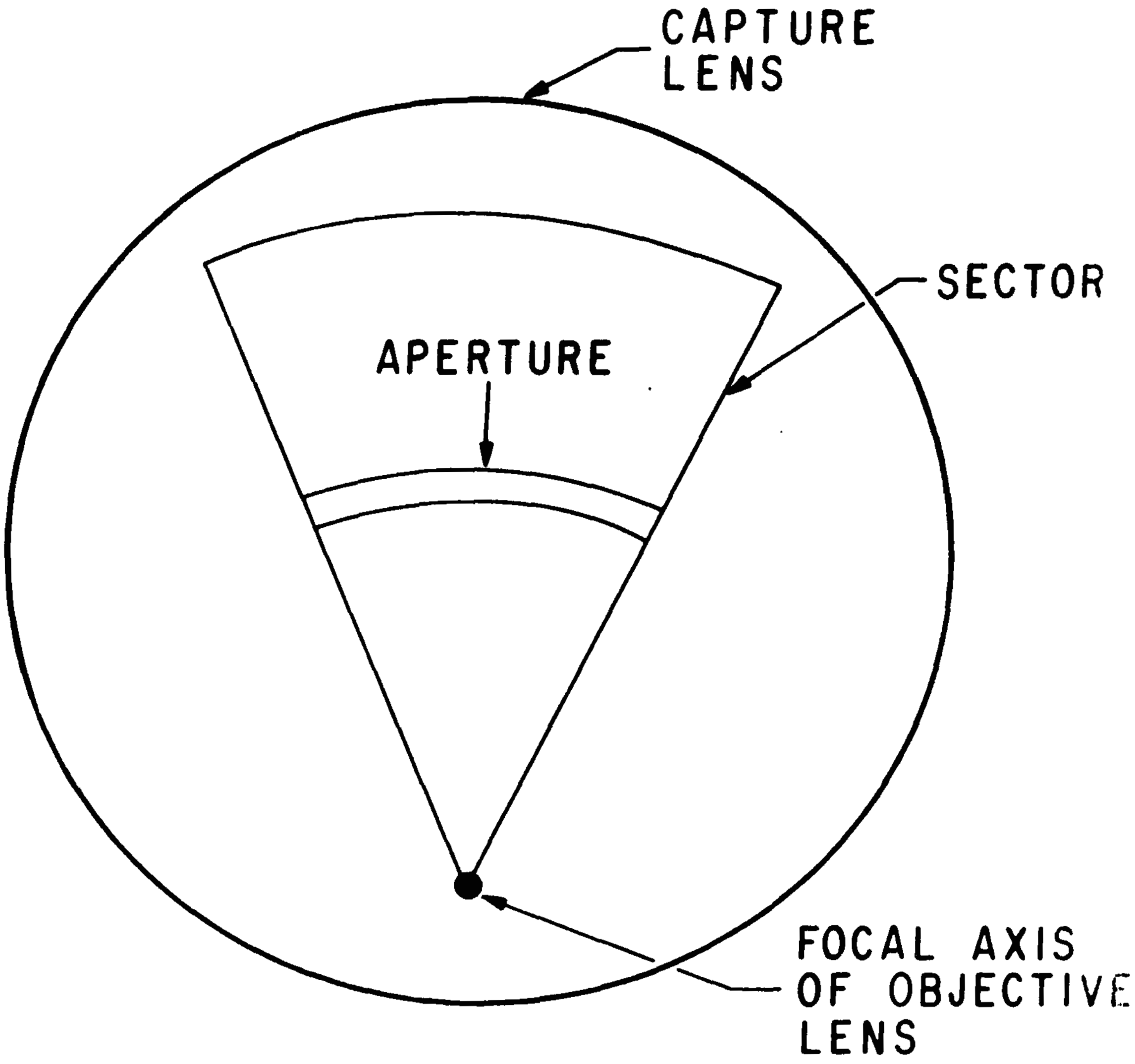

Figure 11. Schematic of the sector and aperture slit arrangement as viewed normal to the aperture plane from the back of the instrument through the capture lens.

Should a low index (cryolite) spacer be employed with the same $\delta\lambda_{||}$ as above, an effective index of 1.34 would yield an α of .5 (a factor of two larger slope). For a given objective, the scan range would have been doubled. However, as noted in Equation (31), $\delta\lambda_B = G(\alpha)$ requiring a larger f for a given $\delta\lambda_B$. For faint source work, a slower scan rate would be necessary to match the count rates detected for the spectral range of the high index filters, since now the throughput would be less. In addition, the angle at which a filter polarizes, as noted earlier, occurs at lower tilt angles for the low index filters.

4.4 APERTURE AND SECTOR

The sector, or fringe mask, is best fixed very close to the spiral disk to accommodate the planar concept derived in the theory. The aperture must be rotated behind the sector in the spectrometer arrangement (Figure 12).

The sector was made by overlapping two semicircles. The two semicircles comprising the sector disk and the aperture disk were generated by computer plots, etched on rubylithe masters, photographically reduced, and chemically milled on 3 mil-304-rolled stainless. The sector and spiral disks were then mounted into a block so that the sector was fixed and the sprial could be rotated with a d.c. motor.

It should be noted in Figure 12 that the aperture spiral can be in a position which exposes to the detector, the two ends of the spiral. The portion of a rotation for which this exists is 18° or 1/20 of a rotation and will henceforth be termed as the transition period. This transition takes place when returning to the high wavelength portion of the scanning cycle to begin a new scan.

The final assembly is depicted in Figure 13. The optical portions were enclosed in a box and the detector cooler was butted into a press fit o-ring in the rear plate of the instrument.

4.5 CALIBRATION TESTS

4.5.1 LABORATORY CALIBRATIONS

The test set-up used in generating the intensity and transmission profiles is depicted in Figure 14. Note that in these tests, one is observing what the instrument, as a whole, is doing to the shape of near-delta function (~ 1Å) input provided by the monochromator. In simpler terms, the transmission profiles are a convolution of the integrated effect of the interference filter, aperture, and capture optics on the source.

Figure 15 depicts the transmission curves with the 166 mm, 106 mm, and 88 mm objective configurations.[8] The scatter in the transmissions is largely due to the inability

---

[8] The 57 mm configuration required a spacer in the instrument that prohibited the removal of the filter in the setup without disturbing the source. True transmission profiles could not be calculated as a result of this physical restriction.

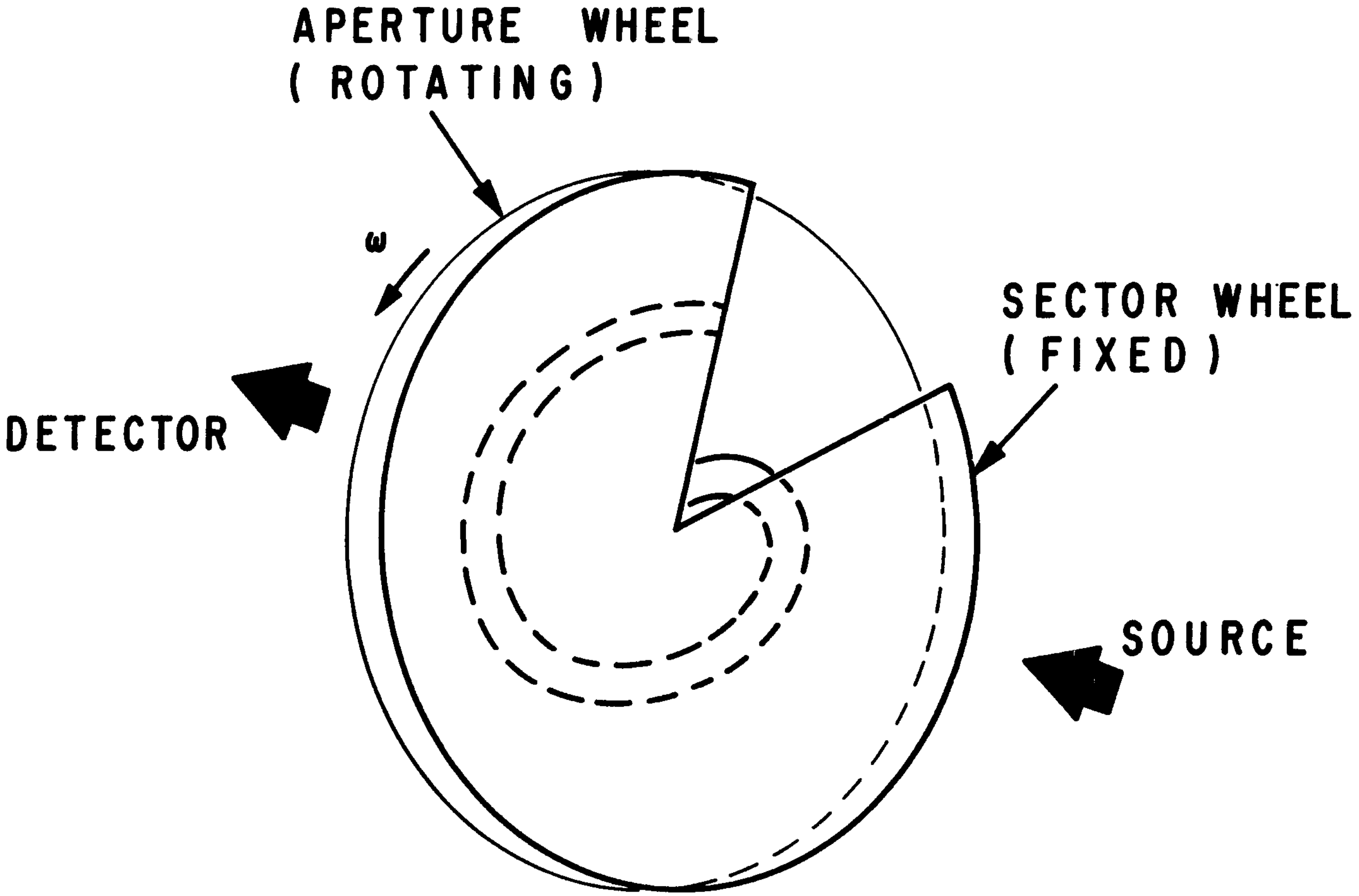

Figure 12. Sector and aperture wheel configuration for an n = 1 spiral.
The sector disk is fixed and the spiral rotated.

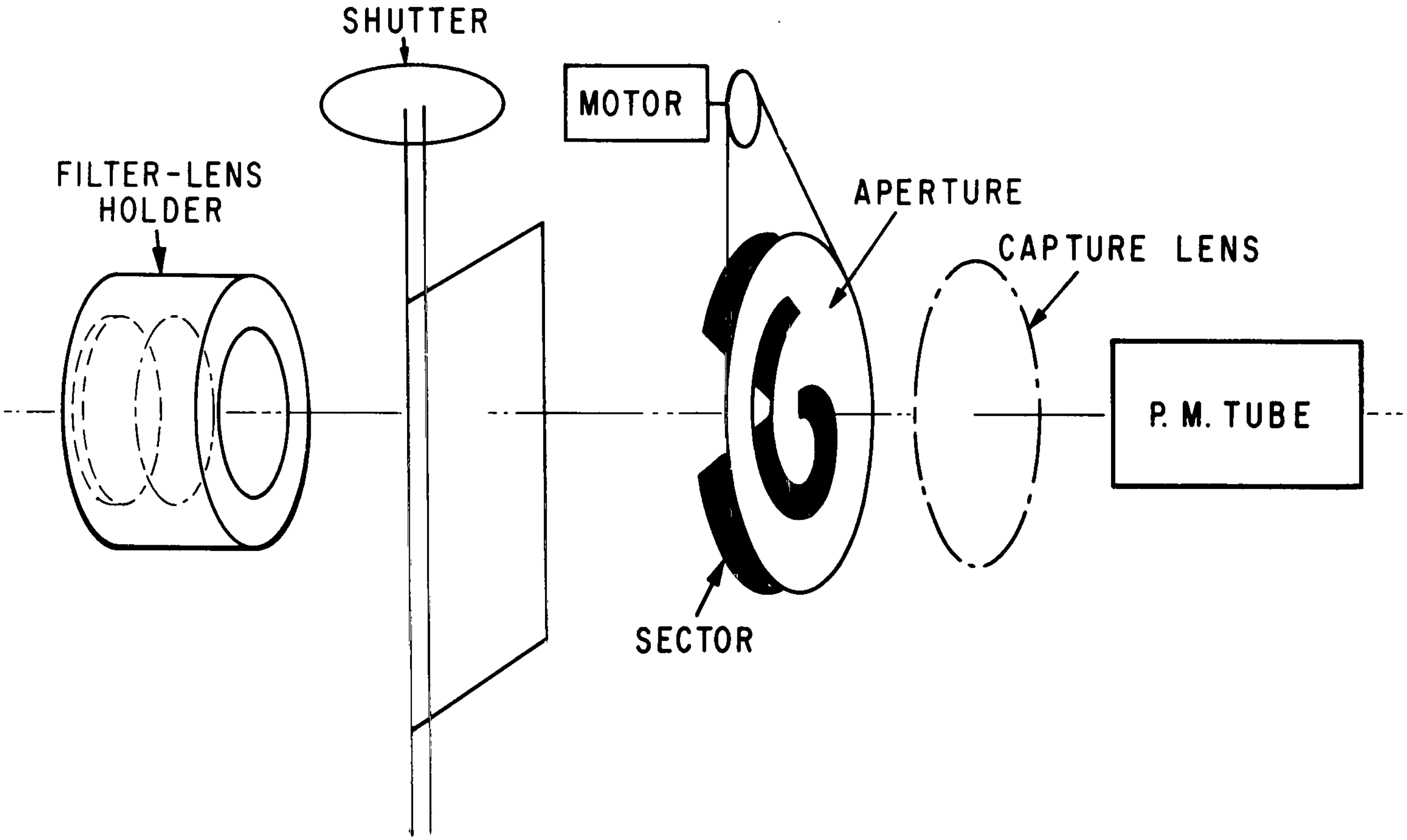

Figure 13. Sketch of the single spiral spectrophotometer. The aperture-sector wheels were mounted in a block to which the motor was attached. The capture lens was mounted in another block. All components were then fastened to a metal plate and boxed in a light tight environment.

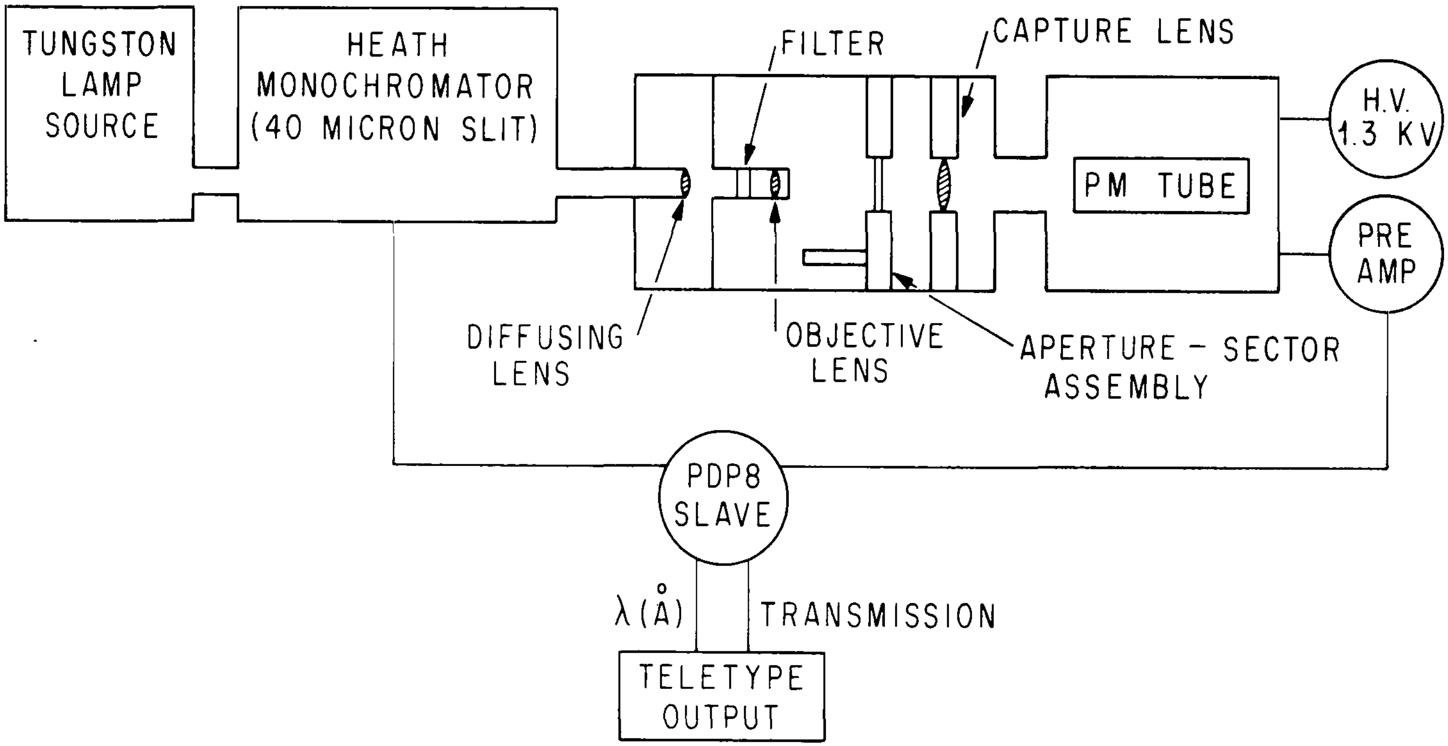

Figure 14. Schematic of the laboratory arrangement used for the study of the single spiral spectrophotometer.

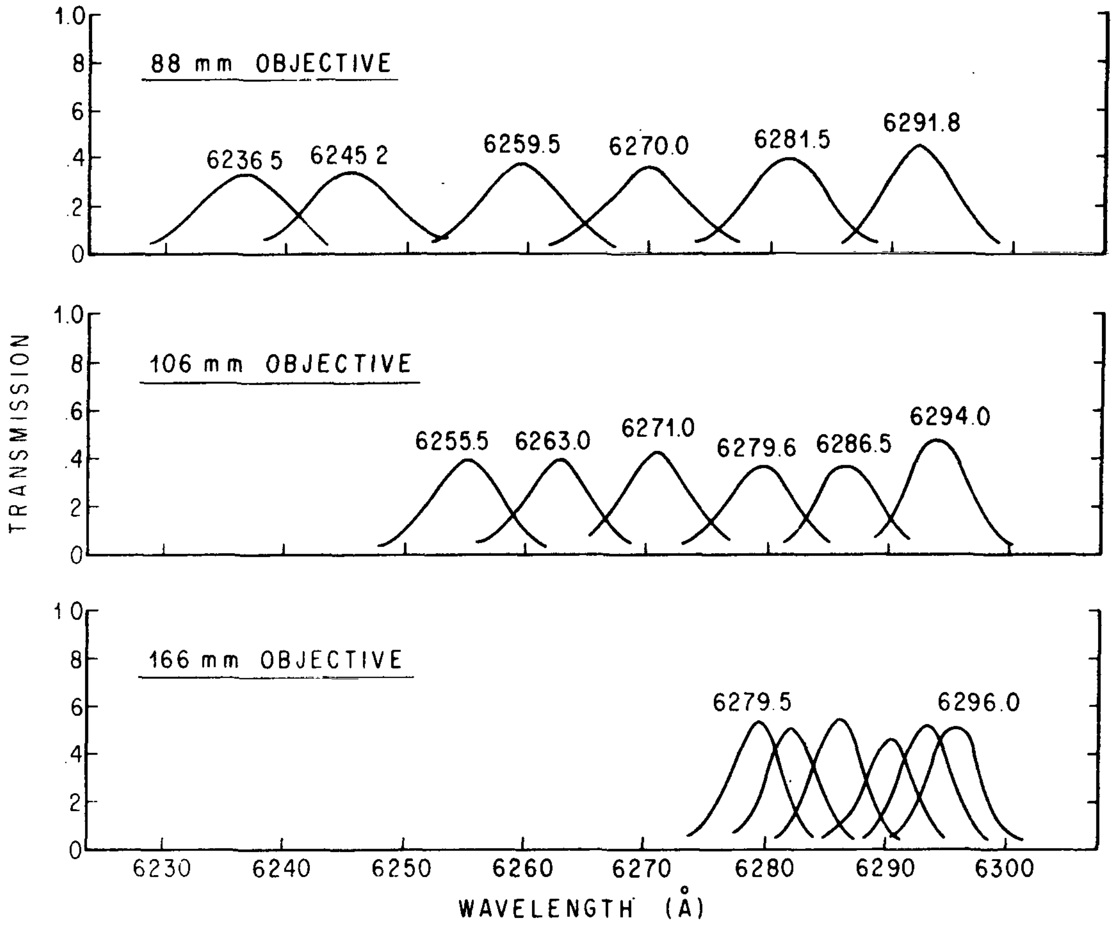

Figure 15. Transmission profiles versus wavelength for three objective configurations used in the single spiral system. The 57 mm objective configuration is not shown since true transmission profiles were not feasible due to physical limitations of the instrument.

to replace the source precisely, since it had to be moved between the filter-out and filter-in scans from which given transmission curves were generated.

The trend of the peak transmissions is to decrease with decreasing wavelength or higher θ. For example, in the extreme case, the 88 mm objective configuration showed a transmission change from .45 at the high wavelength end to .33 at the low wavelength end. This loss is partially attributed to the same loss observed in studying the filter alone. Whether the photons are entering the filter specularly or diffusely, the filter itself generates a forward lobe in the transmission. The reflective loss at the filter is greater for higher angles (or lower wavelengths).

The halfwidth of the transmission curves for the configurations are summarized in Figure 16. Note that some broadening occurred with increased angle for the 88 mm and 106 mm configurations, but a narrowing with wavelength exists with the 57 mm objective. The explanation, as to the broadening slopes for the various configurations, is attributed to the fact that there is a combined filter and aperture effect. As pointed out earlier, there exists a slight angular dependence of filter broadening possibly due to irregularities of the interference surfaces in the filter itself. For the longer focal length objectives, the instrument function is primarily due to the filter. Figure 5 of the previous chapter displays the angular broadening of this particular filter. In the 57 mm configuration, a dominating aperture effect is observed. In the ideal aperture [Equation (36)], the breadth broadening expands as $(r^2 + f^2)^2/r$ and in the modified slit used here [Equation (53)], the breadth expands as $(r^2 + f^2)^{3/2}/r$. The aperture then is not a perfectly unchanging resolver of the spectral line. The modified slit is narrower at a given r than the ideal slit to maintain a constant field of view discussed in Chapter II. The modified slit then should correspond to a narrowing bandpass as is observed in the 57 mm configuration. For a given objective configuration, that is for a given filter and objective distance, the spiral aperture could be modified by opening or closing the slit produced by the sector to yield a constant broadening by the instrument over the spectral range.

Degradation of transmission over the spectral range of each configuration was questionable with the monochromator arrangement, due to the specular nature of the source. A diffuse source was placed in front of each arrangement and scans of the continuum were made. (The source was a tungsten lamp behind multiple layers of opal glass). The transmission loss over the spectral range, as summarized in Table 1, was computed from this arrangement rather than from the monochromator.

A summary of the instrument under the various configurations is shown in Table 1. The counts/sec/rayleigh are for the peak transmission at the high wavelength position of each objective configuration. A Carbon 14 source, which had recently been calibrated by NBS, was used for this calibration.

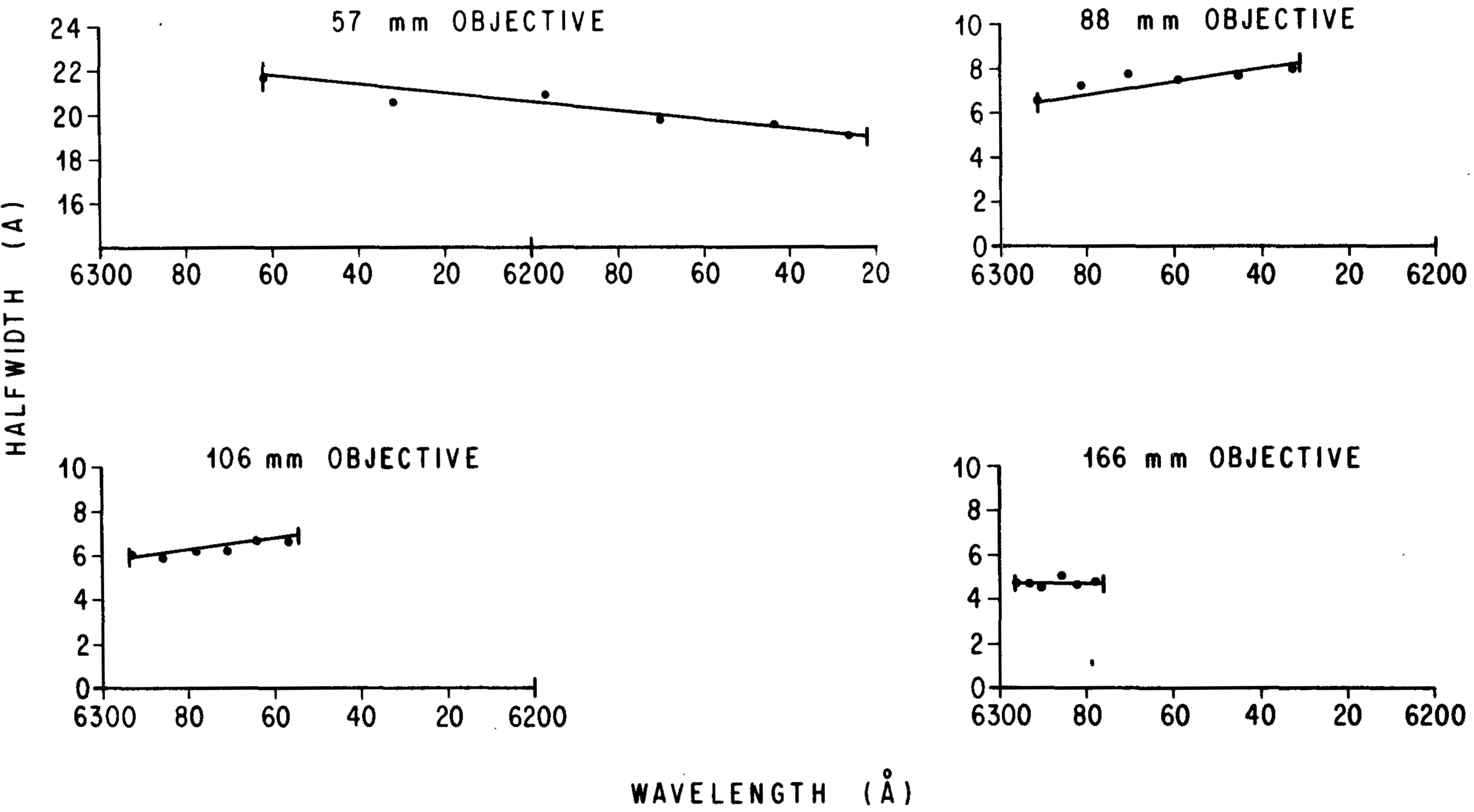

Figure 16. Summaries of halfwidth versus wavelength of the objective configurations with a 6300Å filter. The 57 mm halfwidth is deduced from intensity profiles as was done for the other three configurations.

TABLE 1. SUMMARY OF SPECTROMETER CHARACTERISTICS WITH 6300Å FILTER ($\alpha = .26$)

Objective Focal Length	Spectral Range	$\Delta\lambda_{1/2}$	θ_{max}	Transmission Loss Over SR (approx)	$A\omega$ (cm^2 Steradian)	$^{C/S}/_{Ray}$
166 mm	17.5Å	4.6Å	8.4°	6%	.0073	–
106 mm	43Å	6.3Å	13°	24%	.018	16.5
88 mm	62Å	7.5Å	15.6°	30%	.025	32.5
57 mm	140Å	20.0Å	23°	50%	.056	–

A second filter was examined for the purpose of a nightglow observation to be discussed next. The filter was a λ6305Å filter, whose characteristics are summarized in Table 2. The reason this filter was used was to capture the OI, λ6300Å line emission, as well as, the (9,3) hydroxyl band for comparison. The α was very near that of the λ_0 = 6300Å filter, A calibration plot of wavelength versus wheel position (in degrees) is plotted in Figure 17. The beginning of a scan is generated by a microswitch trigger on the scanning aperture wheel. Note the 18° of transition discussed earlier and the starting wavelength of 6300Å. The starting wavelength is less than the normal filter transmission maximum, since the minimum θ is $\theta_{\min}$ and not zero degrees.

4.5.2 A NIGHTGLOW OBSERVATION

Figure 18 depicts a section of nightglow data taken from Broadfoot and Kendall (1968). Note in the range scanned are the OI, λ6300Å emission and the $P_{1,2}$, $P_{2,2}$, Q_2, and Q_1 lines of the OH (9,3) band.

The data in Figure 19 were taken with the single spiral sector spectrophotometer on August 11, 1971, at Ann Arbor, Michigan. The intensity of the 6300Å line was measured to be 50 rayleighs and 15 rayleighs for the $P_{2,2}$ line of the OH (9,3) band system. The scan is coming up on the Q_2, Q_1 lines just prior to transition, but the peak is not reached prior to transition. This observation was made with the 106 mm configuration as summarized in Table 2. This particular scan was made with a seven minute scan rate at 11:00 p.m. E.S.T. on the date mentioned. The sky was very clear and the moon had not yet risen when the observation was made. It is noted that the $P_{1,2}$ line at λ6287.6Å was not evident on this night in the observation but is very prominent in the Broadfoot and Kendall data shown in Figure 28. It is not the purpose of this report to examine the OH in detail. Had a filter comprising a low index spacer of the same resolution been employed, the remainder of the band system, including the R1-R2 branch, could have been scanned.

TABLE 2. SUMMARY OF SPECTROMETER CHARACTERISTICS WITH 6305Å FILTER ($\alpha = .24$)

Objective Focal Length	Spectral Range	$\Delta\lambda_{1/2}$	θ_{max}	Transmission Loss Over SR	$A\omega$ (cm^2 Steradian)	C/S/Ray
106	40Å	6.25Å	13°	22%	.018	23.5

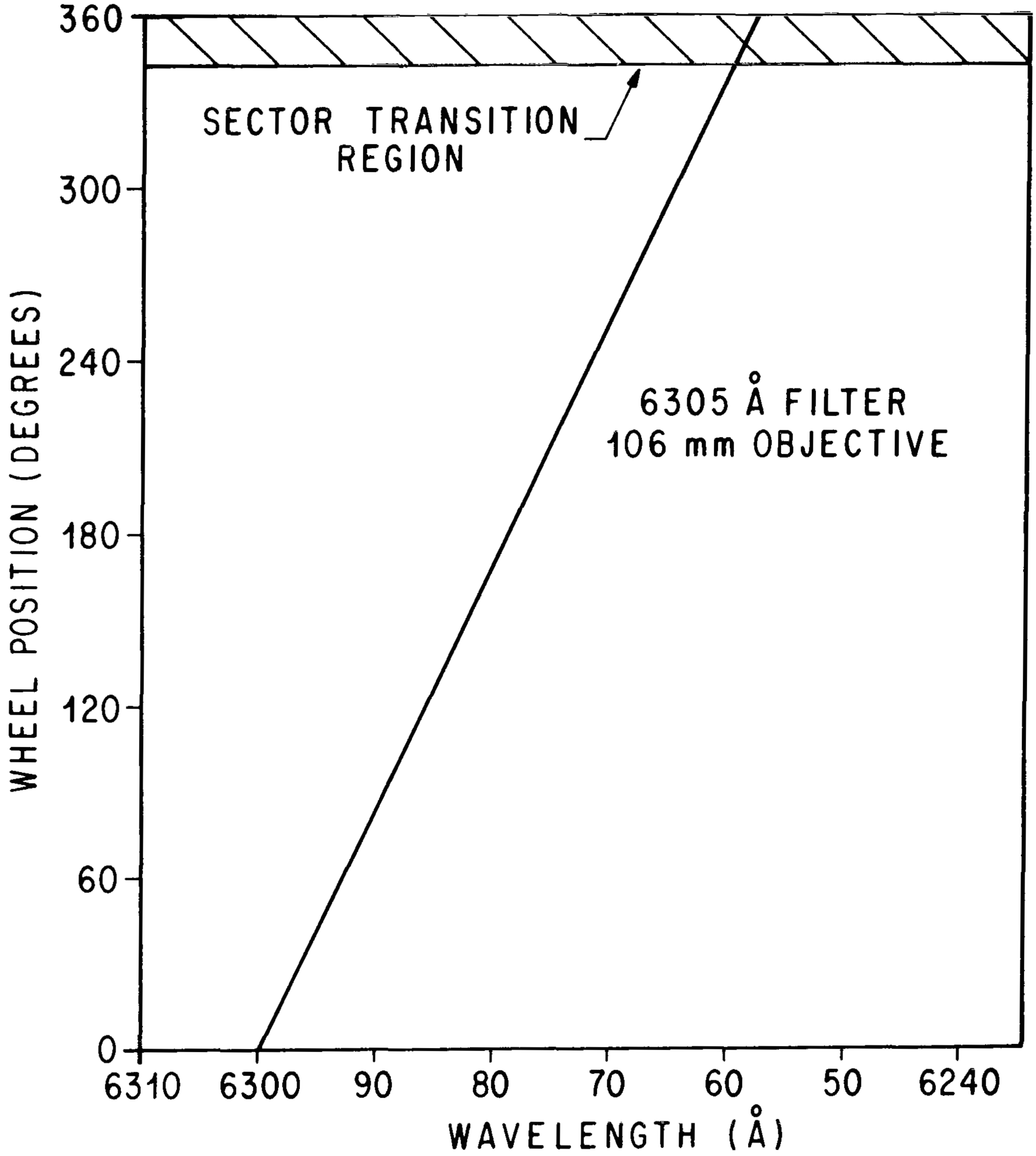

Figure 17. Peak wavelength versus angle of rotation of the aperture wheel for a 6300Å filter, as deduced in the laboratory.

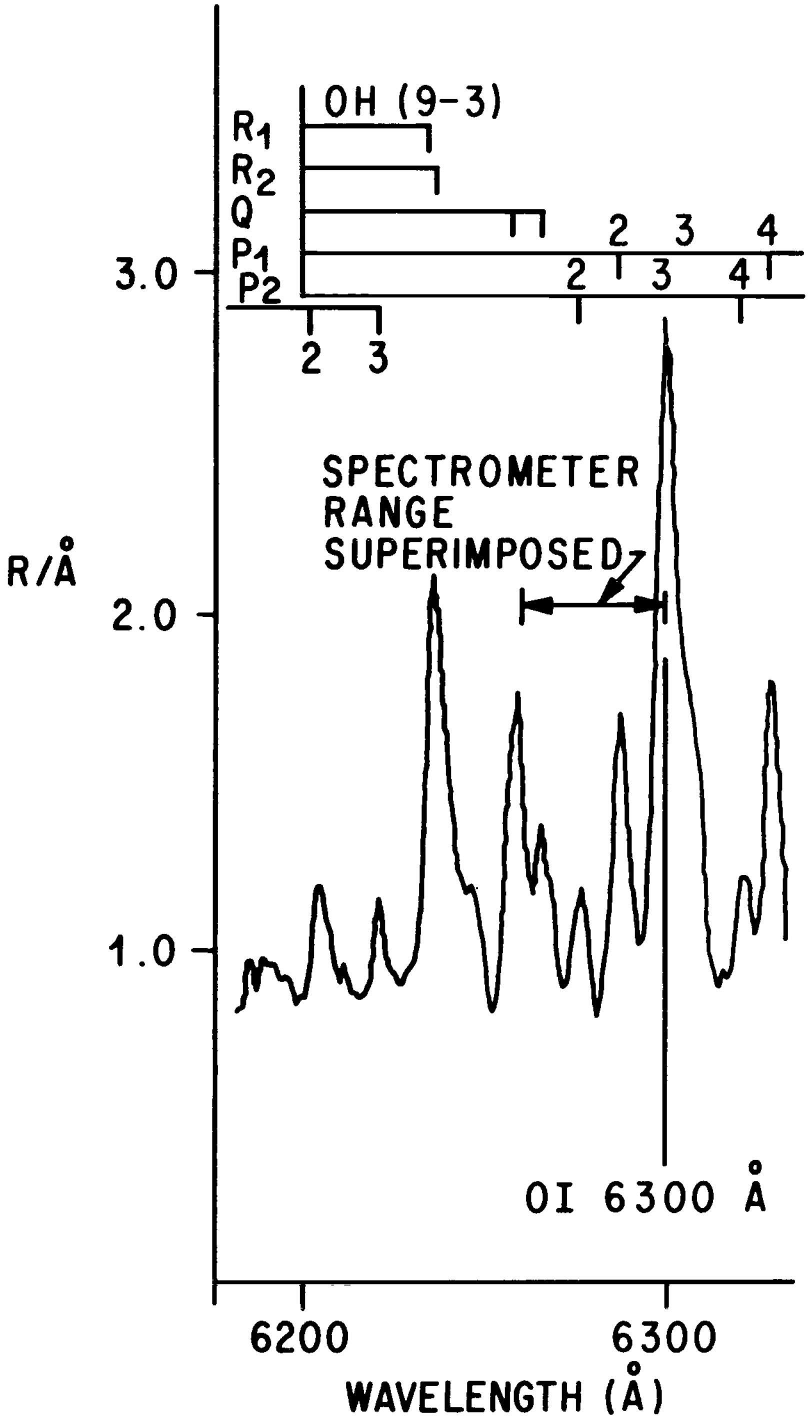

Figure 18. Nightglow data observed by Broadfoot and Kendall (1968) with the range of the single spiral spectrophotometer superimposed.

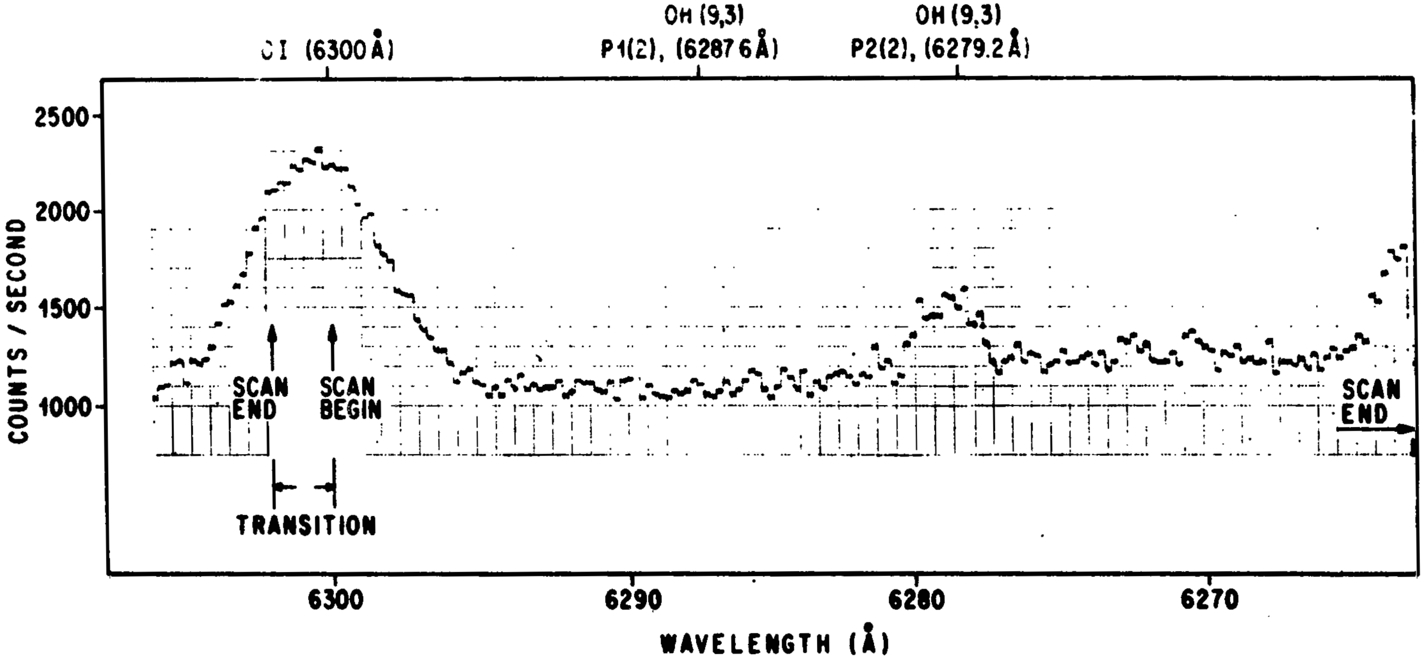

Figure 19. Data taken with the spectrophotometer system on August 11, 1971, at 11:00 EST at Ann Arbor, Michigan.

CHAPTER V
A MULTI-SPIRAL SECTOR SPECTROPHOTOMETER FOR MEASUREMENT OF AURORAL $O^+(^2P-^2D)$ EMISSIONS

5.1 INTRODUCTION

A ground based instrument was then designed and built to accomplish a particular measurement [$O^+(^2P-^2D)$, 7319Å] in the auroral zone. The theory of the emission will be discussed in the next chapter.

The object was to build a spectrometer with a high throughput and sensitivity with two inch optics to examine the $O^+(^2P-^2D)$ emission and to scan and, thus, separate the nearby OH and N_2 1PG background emissions from the signal.

5.2 OPTICS

A high index filter peaked at λ_0 = 7325Å with a $\delta\lambda_{||}$ = 5.1Å was acquired for the instrument.

The detector was an EMI 9658R tube, with a .30 mm diameter sensitive area. The tube was housed in a thermo-electric cooler to minimize dark count. Glass lenses were used in the system. The capture lens was selected after a bench study similar to that discussed for the single spiral instrument.

5.3 APERTURES AND SECTOR

For this machine, a 3n (6π) spiral was chosen to expand the throughput (i.e., $A\omega$ = 3x larger for a given curvature finesse). A second spiral disk (shutter spiral), rotating at 1/3 the rate of the aperture spiral, was necessary to mask off two of the three spiral sectors exposed to the detector at a given aperture spiral position. In summary, the aperture scanning configuration involves a fixed sector disk, a rotating n=3 spiral aperture disk, and a rotating n=1 spiral mask disk. Figure 20 depicts the aperture schematic. The value for r_{max} was set at 25 mm for detector capturability similar to the single spiral system. The masking spiral was generated by examining the boundary of the aperture at the sector extremes for a given angle and enlarging by a small increment to insure that no vignetting of the aperture mask would take place.

The two rotating wheels were individually rotated by stepping motors. A single pulse translator was used with a divide by three circuit going to the mask spiral. Microswitches were used on the apertures as a scan fiducial and for a mask alignment pulse. The wheel alignment was electronically checked and realigned after each scan by synchronizing pulses generated by the microswitches.

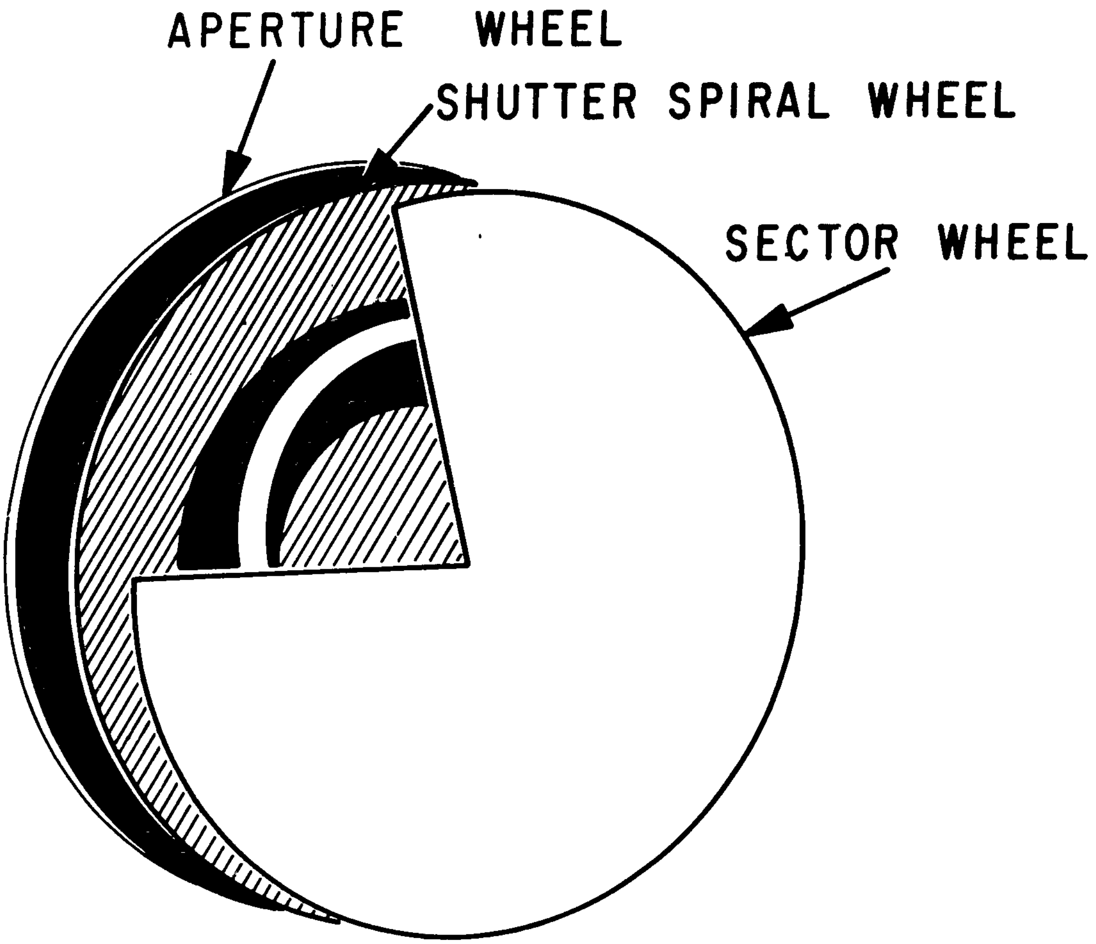

Figure 20. The sector-aperture configuration for an n=3 spiral as employed in the second instrument built for field use.

5.4 GENERAL DESCRIPTION

An instrument schematic is shown in Figure 21. The primary optical components are indicated.

A generalized electronics flow chart is shown in Figure 22. The dashed lines indicate the preferred data acquisition scheme, however, a magnetic tape recorder was not used in gathering the data reported in this report.

Six thousand motor steps resulted in one scan, making the scanner essentially continuous. The main advantage of stepping was position accuracy, digitizing convenience, and versatility such as computer control of a stepping sequence or exposure interrupts.

The instrument was mounted on a cassegrain telescope yoke mount and a synchronous motor control of zenith angle was used to point the instrument.

The scanning scheme involves accepting light at various angles through the filter. A large fresnel lens, with its focal point being the filter, was attached to the front of the instrument in order to keep the instrument from scanning across the sky in the process of looking at various angles through the filter.

5.5 CALIBRATIONS

A resolution summary is shown in Table 3. A range summary for other objectives is shown in Table 4. The transmission profiles as measured at various angles are shown in Figure 23. Laboratory calibrations were made by an arrangement similar to that described for the single spiral spectrophotometer described in Chapter IV.

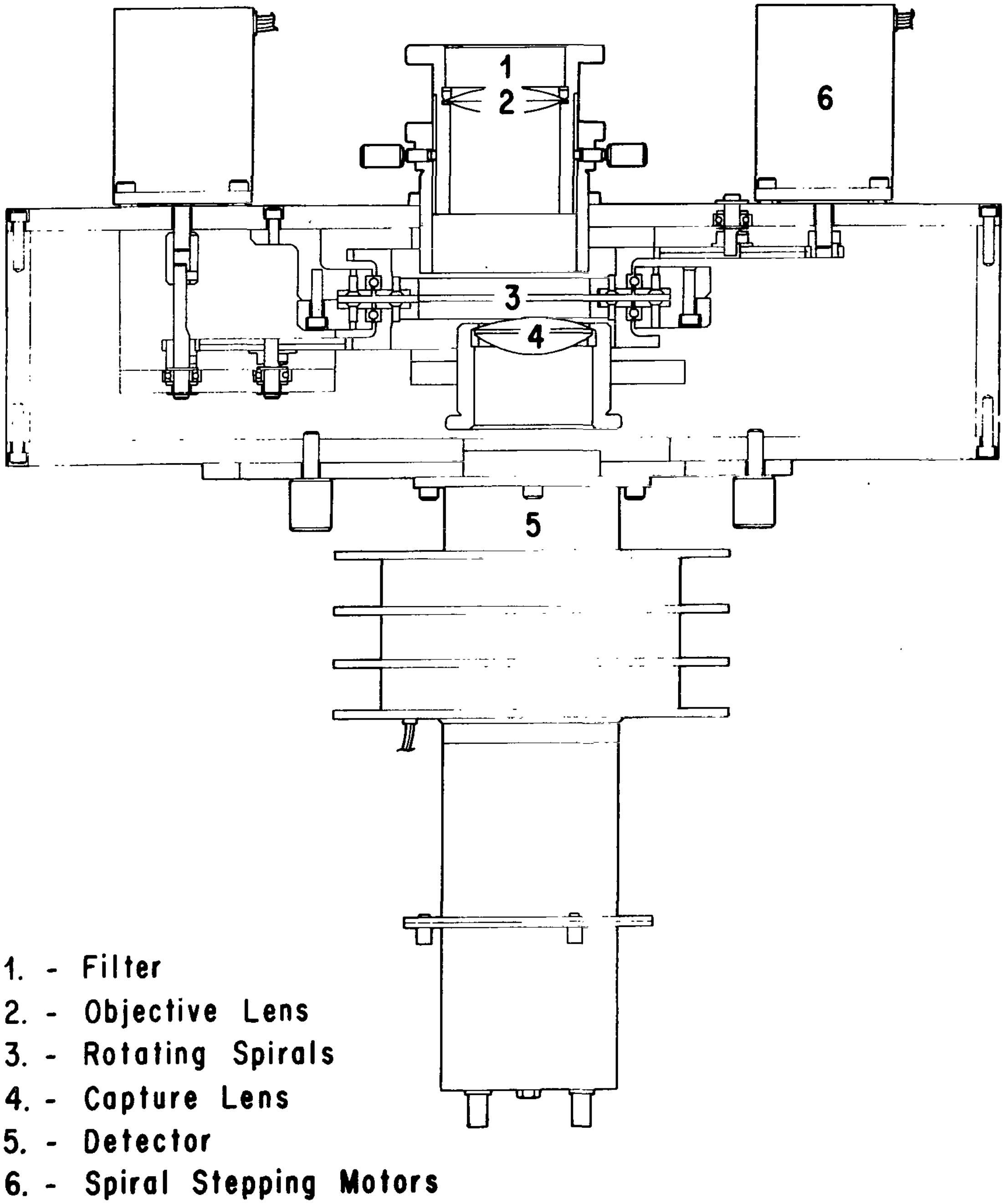

Figure 21. An assembly schematic of the optical, scanning, and detecting components used in the multi-spiral sector spectrophotometer system.

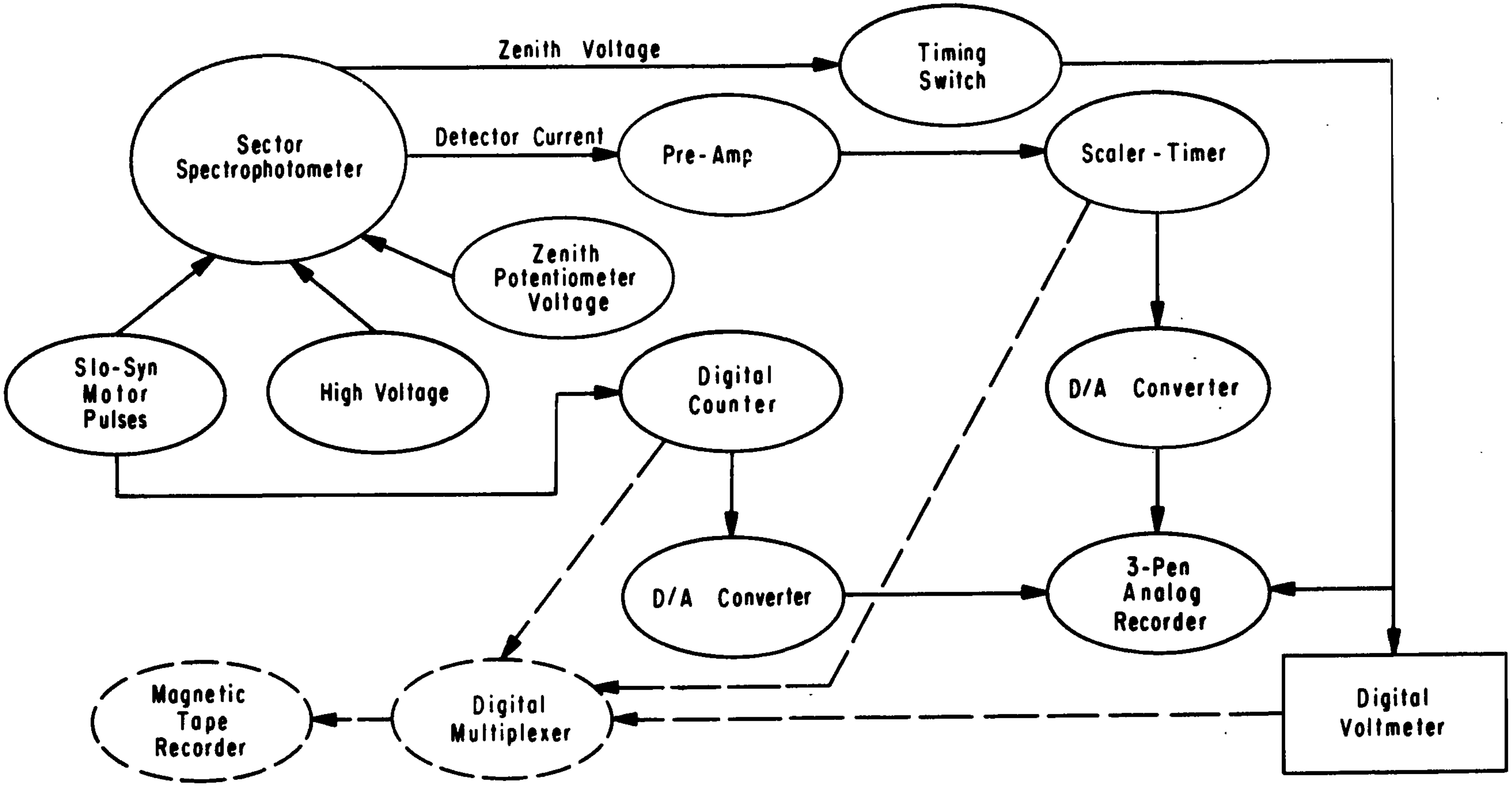

Figure 22. A general electronic flow diagram outlining the main components of the field system. The dashed lines indicate the capability in data acquisition, although a tape recorder was not available for use for data reported in this study.

TABLE 3. SUMMARY OF RESOLUTION CHARACTERISTICS OF THE MULTI-SPIRAL SPECTROPHOTOMETER (λ_0 = 7326Å)

Filter

$u^* \approx 1.9$

λ_0 = 7326Å

$\delta\lambda_{||}$ = 5.1Å

Instrument

f (objective focal length) = 127 mm

θ_{min} = 2 1/2°

θ_{max} = 10 1/4°

Wavelength (Å)	Instrument Temperature (°C)	
	22°C	8°C
λ_0 (Filter)	7328Å	7326.1Å
λ_{min}	7326.5Å	7324.7Å
λ_{max}	7301.3Å	7299.4Å

$\delta\lambda_{\psi}$ = 2.3Å

$\delta\lambda_C \approx \delta\lambda_B \approx$ 1.3Å

$\delta\lambda_I$ (Theoretical) = 6.2Å

$\delta\lambda_I$ (Measured) = 6.1Å

TABLE 4. SUMMARY OF RANGE CHARACTERISTICS OF THE MULTI-SPIRAL SPECTROPHOTOMETER

($\lambda_0 \sim 7326\text{Å}$, $u^* = 1.9$)

Objective Focal Length (mm)	θ_{min}	θ_{max}	$\Delta\lambda_{min}$ (Å)	$\Delta\lambda_{max}$ (Å)	Scan Range (Å) (approximate)
	θ^2_{min} (deg sq)	θ^2_{min} (deg sq)			
57	5°40′	22°0′	9.9	149.4	140
	32	484			
88	3°36′	16°0′	4.0	66.5	62
	13	256			
106	2°58′	13°20′	2.7	46.3	43
	9	177			
127	2°30′	11°12′	1.9	32.6	30
	6 1/4	125			
166	1°55′	8°35′	1.1	19.4	18
	3 2/3	73 1/2			

NOTE: If $\lambda_0 \sim 3660\text{Å}$, the last 3 columns are multiplied by 1/2. If $u^* \sim 1.3$ (low index filter), the last three columns are multiplied by 2.

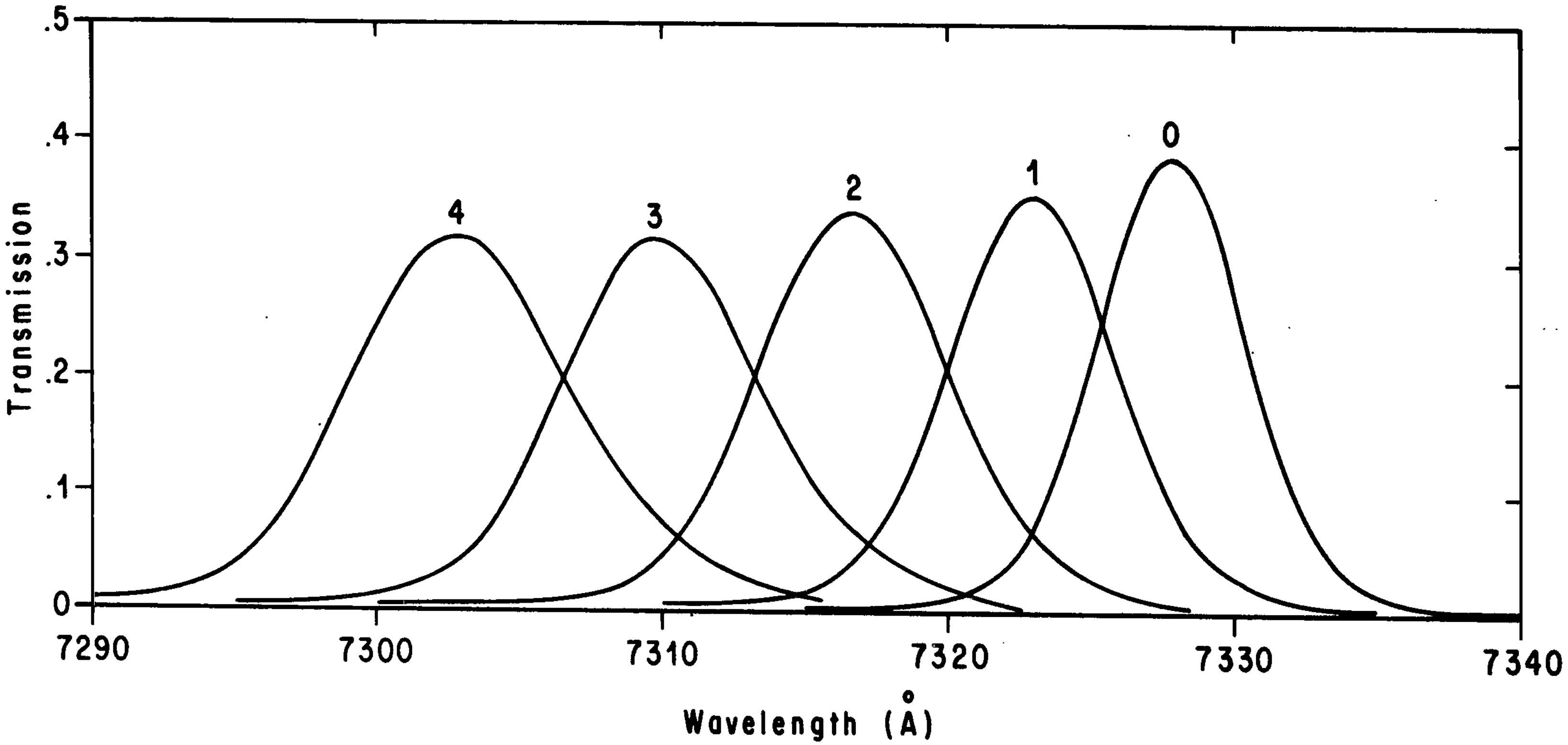

Figure 23. Transmission versus wavelength as measured for incremental aperture positions. The 0 profile refers to the upper wavelength position of the spirals (i.e., $\theta = \theta_{\min}$). Positions 1, 2, 3, and 4 refer to the number of motor steps from 0 (in thousands) the spiral was stepped for the indicated transmission curve. Beyond step 4000, the spiral was in transition and shuttered at 5000 steps and began a new scan at 6000 (or 0) steps.

CHAPTER VI
THEORY OF $O^+(^2P\text{-}^2D)$ EMISSION IN ELECTRON AURORA

6.1 INTRODUCTION

The study of auroral emissions from ground stations has been a fundamental and useful tool in analyzing many physical phenomena of the aurora. With increasing knowledge of ionization cross sections by electron impact, constituent distributions, and measurement capabilities, further refinements of the physical understanding of the aurora can be recognized from ground observations.

The distribution and morphological characteristics of auroral primary electrons have been reviewed and summarized by Rees (1969). Rees summarized the measured electron energy and pitch angle distributions. In general, the energy distributions are representable by a power law function with a wide range of function coefficients representing the various measurements. The power law distribution takes the form

$$G(E_0) \propto E_0^{-\alpha} \quad . \tag{55}$$

An exponential form is also used where the power law distribution fails and takes the form

$$G(E_0) \propto E_0 e^{-E_0/\alpha} \quad . \tag{56}$$

Rees (1963) theoretically analyzed electron streams and deduced ionization rate height profiles for various primary electron energy distributions. Berger et. al. (1970) performed a detailed study of the energy disposition of auroral electrons in the atmosphere. More recently, Banks et. al. (1974) have performed a detailed analysis of auroral ionization calculated from a measured incident electron distribution which included the secondary distribution and its energy degradation with height.

Height distributions of ionization rates can be deduced by examining emission rates arising from the fraction of ions generated in excited states. N_2^+1NEG emissions have been extensively examined for this purpose due to their prominence and simplified vibrational and rotational structure (Jones, 1971). Borst and Zipf (1970) have shown that the ratio $N_2^+1NEG_{0,0}$ electron excitation cross section to the total ionization cross section is .07 for electron energies ranging from ~ 30ev to 10Kev. Since collisional frequencies of the atmospheric constituents at auroral altitudes are much less than the emission lifetime of $N_2^+1NEG_{0,0}$,[9] the emission rate is indicative of the electron

---

[9] The collisional frequency at 90 km is ~10^4 sec^{-1}. The transition probability is $1. \cdot 10^7$ (Shemansky and Broadfoot, 1971) which corresponds to a lifetime of $9.1 \cdot 10^{-8}$ sec.

ionization rate for precipitating auroral electrons. The energy required for generating the $N_2^+(B^2\Sigma_u^+)$ from the $N_2(X^1\Sigma_g^+)$ is ~ 19ev. Banks et. al. (1974) suggest that 60 to 70% of the auroral ions generated are due to the primaries in the upper altitudes of precipitation, and the remaining 30% are due to $E < 500$ev electrons. The percentage of primaries responsible for ionization decreases at lower altitudes and the percentage due to secondaries increases.

Historically, the $OI(^1D-^3P)$ i.e., λ6300Å , emission has been used, along with N_2^+1NEG emission, as a photometric indication of auroral electron hardness or atmospheric range (Eather, 1969, Rees and Luckey, 1974). The oxygen emission is a high altitude phenomena relative to the nitrogen emission due to the differential constituent distribution of the atmosphere. Secondly, the $OI(^1D-^3P)$ emission is quenched at lower altitudes leading to a height dependence of the two emissions.

The weakness of the above technique is two fold. First of all, the $OI(^1D)$ has a 110 sec lifetime, is not bound to the magnetic field, and diffuses or plumes in discrete forms. The allowed N_2^+1NEG emission does not diffuse prior to emission. The flux divergence effect of $OI(^1D)$ then can be significant. Interpretation of magnetic zenith or distant arc photometry measurements should consider divergence when using $OI(^1D)$ as a hardness or range indicator of precipitating electrons. A second weakness lies in the possible source functions for the $O(^1D)$ state. The 1.96ev threshold is significantly different from the ~ 19ev threshold required for N_2^+1NEG emissions generated from ground state molecules. As the downward flux of electrons changes in altitude or the initial distribution varies from one aurora to another, preferential generation of one emission over the other is possible.

The $O^+(^2P-^2D)$ emission is studied here to better understand its geophysical characteristics in aurora and to explore its use as an electron hardness indicator in lieu of the $OI(^1D-^3P)$ emission discussed above. The $O^+(^2P-^2D)$ has several advantages over the $OI(^1D-^3P)$. The lifetime, or reciprical emission probability, is ~ 5 secs versus 110 secs for $OI(^1D)$. Consequently, it will not diffuse in discrete forms to the degree $OI(^1D)$ will. Secondly, it is an ion and the displacement will primarily be controlled by magnetic field. Another advantage is that the $O^+(^2P)$ has an excitation threshold ~ 18.5 ev from ground state OI. The excitation energy, consequently, is very near that required of N_2^+1NEG emissions. There should not be the problem, therefore, of the emission being generated from a different portion of the electron energy distribution as is the case for $OI(^1D)$. Furthermore, the $O^+(^2P)$ arises from neutral oxygen and is quenched as is $OI(^1D-^3P)$ emissions.

Among the disadvantages in the $O^+(^2P-^2D)$ emission is its relatively low intensity compared to $OI(^1D-^3P)$ and N_2^+1NEG emissions (Chamberlain, 1961). Further complication arises from the fact that it underlies a strong N_2 1PG band. When observing the emission from the ground, nearby mesospheric OH contaminants complicate the ability to resolve the $O^+(^2P-^2D)$ emission.

The theory of $O^+(^2P\text{-}^2D)$ emissions as related to N_2^+1NEG emissions is derived in the remaining portions of this chapter. The derivation of the volume emission rate relationship of these two emissions includes an investigation of what historical investigations have found for the quenching rates, probabilities of emission, and pertinent excitation cross sections. New measurements and new found values for some of these rates are discussed in the two subsequent chapters.

6.2 CONTINUITY OF $O^+(^2P)$ IN ELECTRON AURORA

Since diffusion rates are small relative to the spontaneous lifetime below 300 km, the continuity equation will be represented as a simple production and loss.

6.2.1 LOSS – RADIATIVE

The spontaneous cascade of $O^+(^2P)$ to lower O^+ states is given by

$$O^+(^2P) \xrightarrow{A_\lambda} O^+(^2D,^4S) + \frac{hc}{\lambda} \qquad (57)$$

where

A_λ – Spontaneous emission probability,

h – Planck's constant,

c – Speed of light in vacuum,

λ – Emitting wavelength .

The $O^+(^2P)$ has two substates $(O^+(^2P_{1/2})$ and $O^+(^2P_{3/2}))$ whose statistical weights are 2 and 4, respectively. The $O^+(^2D)$ also has two substates $(O^+(^2D_{3/2})$ and $O^+(^2D_{5/2}))$, whereas, $O^+(^4S)$ has one $(O^+(^4S^0_{3/2}))$. The subscripts on the term values above refer to the J value, or total angular momentum quantum number associated with the particular substate. As a result, there are six possible loss channels from the $O^+(^2P)$, three from the $^2P_{1/2}$ state, i.e.,

$$^2P_{1/2} \rightarrow {}^2D_{3/2} \quad , \quad {}^2D_{5/2} \quad , \quad \text{or} \quad {}^4S^0_{3/2} \qquad (58)$$

and three from ${}^2P_{3/2}$ state, i.e.,

$${}^2P_{3/2} \rightarrow {}^2D_{3/2} \ , \ {}^2D_{5/2} \ , \text{ or } {}^4S^0_{3/2} \quad . \tag{59}$$

All six probabilities are finite for both electronic quadrapole and magnetic dipole transitions. Seaton and Osterbrock (1957) have provided the atomic parameters for $O^+(^2P)$ in Table 1-C of Appendix C. A diagram describing the spontaneous loss from $O^+(^2P)$ is shown in Figure 1-C of Appendix C. The total radiative loss of $O^+(^2P)$ can be written as:

$$\eta(O^{+2}P)_R = \eta(7319Å) + \eta(7330Å) + \eta(2470Å) = .219\, n[O^{+2}P] \quad . (60)^{10,11}$$

In this study, particular volume emission losses were experimentally measured in aurora and these fractional losses of $O^+(^2P)$ are related to the total $O^+(^2P)$ population. The particular losses were determined in Appendix C. Specifically, the total $O^+(^2P\text{-}^2D)$ loss can be written as:

$$\eta(7319\text{-}30Å) = .171\, n[O^{+2}P] \tag{61}$$

(See Equation C-11), or

$$\eta(7319Å) = .098\, n[O^{+2}P] \quad . \tag{62}$$

(See Equation C-13).

---

[10] $\eta(\ )_i$ refers to the volume rate of change of the constituent state inside the parenthesis or the volume emission rate in the case of a wavelength. The subscript i refers to radiation loss rate (i=R), to quenching loss rate (i=Q), to a production rate only (i=P), or to a loss rate only (i=L). Absence of a subscript implies that all volume changes are considered.

[11] The wavelengths 7319Å, 7330Å, and 2470Å reflect closely spaced wavelength pairs since these pairs are not resolved spectroscopically in this study, i.e.,

$\eta(7319Å) = \eta(7318.6Å) + \eta(7319.4Å)$,
$\eta(7330Å) = \eta(7329.9Å) + \eta(7330.7Å)$, and
$\eta(2470Å) = \eta(2470.3Å) + \eta(2470.4Å)$.

Another combination employed in this study combines the two pairs combining all ${}^2P\text{-}{}^2D$ emissions, i.e., $\eta(7319\text{-}30Å) = \eta(7319Å) + \eta(7330Å)$.

6.2.2 LOSS RATES – QUENCHING

The following reactions were considered as quenching losses for the ion metastable:

$$O^+(^2P) + N_2 \xrightarrow{\gamma_{N_2}} O^+(^2D,^4S) + N_2 \qquad (63)^{12}$$

($\gamma_{N_2} \simeq 10^{-10}$, Dalgarno and McElroy, 1965.)

and

$$O^+(^2P) + e \xrightarrow{\gamma_e} O^+(^2D,^4S) + e \quad . \qquad (64)^{13,14}$$

($\gamma_e = 3 \cdot 10^{-8}$, Seaton and Osterbrock, 1957.)

---

[12] Walker et. al. (1975) recently deduced a preliminary value of $\gamma_{N_2} \sim 5 \cdot 10^{-10}$ from analysis of 7319Å measurements taken on Atmospheric Explorer C Satellite. Their data analysis was for dayglow passes of the satellite.

[13] Seaton and Osterbrock (1957) determined the deactivation coefficient for inelastic electron collisions in the form of the collisional strength parameter $\Omega_{(n,n')}$ (Hebb and Menzel, 1940, and Seaton, 1953). The deactivation rate takes the following form:

$$Q_{nn'} = \pi\Omega_{(nn')}/K_n^2\,\omega_n$$

where

$K_n = 2\,\pi m\, v_n/h$,
m = electron mass,
v_n = initial electron velocity,
ω_n = statistical weight of level n,
h = Planck's constant,
$\Omega_{(n,n')}$ = collisional strength parameter for states n, n′.

The ratio $\Omega_{(n,n')}/\omega_n$ ranges from .06 to ~ .15 for substate collision possibilities. A value of .148 for the ratio corresponds to the dominating $^2P_{1/2} - {}^2D_{3/2}$ transition. The $Q_{n,n'}$ expression for $O^+(^2P)$ reduces to: $Q_{n\,n'} = 1.3 \cdot 10^{-6}/\sqrt{T_e}$ when applying the collisional strength factor, etc., provided by Seaton and Osterbrock (1957). For a range of T_e from 300°K to ~ 3000°K, $Q_{nn'}$ takes the values of 2.2 to $5.5 \cdot 10^{-8}$ respectively.

[14] Henry et. al. (1969) deduce a value for γ_e of $\sim 2 \cdot 10^{-7}$ for $T_e \sim 300$°K.

Two loss mechanisms for O^+ include

$$O^+ + N_2 \xrightarrow{\gamma_{N_2}} NO^+ + N \quad , \qquad (65)$$

$$(\gamma_{N_2} = 2 \cdot 10^{-12} \text{ , Fite, 1969})$$

and

$$O^+ + O_2 \xrightarrow{\gamma_{O_2}} O_2^+ + O \qquad (66)$$

$$(\gamma_{O_2} = 2 \cdot 10^{-11} \text{ , Fite, 1969})$$

These rates have been determined in the laboratory or deduced in the atmosphere where $O^+(^4S)$ is the dominant ionic state. It has not been determined, to the author's knowledge, whether these rates (65 and 66) are accelerated or decelerated for the $O^+(^2P)$ state. Without a reason to speculate them to be different, it will be assumed they cannot be less for $O^+(^2P)$.

Recently, Walker et. al. (1975) also suggested a possible alternative to large N_2 quenching (See footnote (12)), i.e.,

$$O^+(^2P) + O(^3P) \xrightarrow{\gamma_O} O^+(^4S,^2D) + O(^3P) \quad . \qquad (67)$$

$$(\gamma_O \simeq 2 \cdot 10^{-10} \text{ , Walker et. al., 1975})$$

It was suggested by Walker et. al. (1975) that if γ_O was as large as $2 \cdot 10^{-10}$, then $\gamma_{N_2} \simeq 5 \cdot 10^{-11}$ rather than $5 \cdot 10^{-10}$ as indicated in footnote 11. At any rate, the day glow analysis of Walker et. al. suggest that large quenching of $O^+(^2P)$ by either N_2 or O was required to account for the measured surface brightness profiles of $O^+(^2P\text{-}^2D)$ emission measured on Atmospheric Explorer Satellite.

The quenching loss for $O^+(^2P)$ can be written as

$$\eta(O^{+2}P)_Q = \sum_i \gamma_i \, n[i] \; n[O^{+2}P] \qquad (68)$$

where

γ_i – collisional deactivation rate of $O^+(^2P)$ by constituent i,

n[i] – volume density of constituent i .

The quenching possibilities were described above in expressions (63) through (68).

The total continuity loss, therefore, can be written by adding the radiative loss (60) to the collisional loss (68), i.e.,

$$\eta(O^{+2}P)_L = .219\, n[O^{+2}P] + \sum_i \gamma_i\, n[i]\, n[O^{+2}P] \quad . \tag{69}$$

6.2.3 PRODUCTION OF $O^+(^2P)$ BY ELECTRON IMPACT

The next consideration will be the production of $O^+(^2P)$ by electron impact, i.e.,

$$OI + e \rightarrow O^+(^2P) + e + e \quad . \tag{70}$$

The relationship for producing $O^+(^2P)$ by electron impact is derived as a function of the volume emission rate of $N_2^+ 1NEG_{0,0}$ in Appendix D, i.e.,

$$\eta(O^{+2}P)_P = R_{\sigma_0}(E) \cdot \eta(3914Å) \cdot \frac{n[OI]}{n[N_2]} \tag{71}$$

where

$$R_{\sigma_0}(E) = \frac{\sigma_{O^{+2}P}(E)}{\sigma_{O^+}(E)} \cdot \frac{\sigma_{O^+}(E)}{\sigma_{N_2^+}(E)} \cdot \frac{\sigma_{N_2^+}(E)}{\sigma_{N_2^{+*}}(E)} \quad . \tag{72}$$

The cross section factor ($R_{\sigma_0}(E)$) is discussed in Appendix D. The cross section ratios vary $< 30\%$ for $E > 50$ev and will be assumed constant for the interaction of auroral electrons in this study (See Figure 1-D). Seaton (1959) eatimated

$\sigma_{O^{+2}P}(E)/\sigma_{O^+}(E)$ to be .2 and Kazaks et. al. (1972) estimated a value of .25. The total O to N_2 ionization cross section $(\sigma_{O^+}(E)/\sigma_{N_2^+}(E))$ was estimated at .5 from the Kieffer and Dunn (1966) review of previous measurements (Appendix D, Figure 1-D). The ratio of the total N_2 ionization cross section $(\sigma_{N_2^+})$ to the cross section leading to $N_2^+B^2\Sigma_u^+$ in the zeroth vibrational level $(\sigma_{N_2^{+*}})$ was found to be ~ 14.1 by Borst and Zipf (1970). The $N_2^+B^2\Sigma_u^+$ state in the zeroth vibrational level emits the λ3914Å band system. Seaton's (1959) value for $\sigma_{O^{+2}P}(E)/\sigma_{O^+}(E)$ of .2 and the ratios discussed above for the remaining cross sections yield a value of 1.41 for $R_{\sigma_0}(E)$. These historical values are theoretically and experimentally verified with the exception of $\sigma_{O^{+2}P}(E)/\sigma_{O^+}(E)$ which has been determined theoretically.

Another frequently observed emission in aurora is that arising from the $N_2^+B^2\Sigma_u^+$ in the first vibrational level (the λ4278Å band system). The work of Shemansky and Broadfoot (1971) suggests the cross section for the zeroth vibrational state is ~ 3.3 times larger than for the first vibrational state of $N_2^+B^2\Sigma_u^+$. For the cross section factor corresponding to the λ4278Å emission $(R_{\sigma_1}(E))$, the above historical values give a value of 4.65 for $R_{\sigma_1}(E)$. The production term (Equation 71) would now read

$$\eta(O^{+2}P)_P = R_{\sigma_1}(E) \cdot \eta(4278\text{Å}) \cdot \frac{n[OI]}{n[N_2]} \quad . \tag{73}$$

6.2.4 CONTINUITY SUMMARY OF O+(2P)

The continuity equation can be written in terms of cross section ratios, emission rates, and quenching rates by setting the production of $O^+(^2P)$ (Equation 71) equal to the loss (Equation 69), i.e.,

$$R_{\sigma_0}(E) \cdot \eta 3914\text{Å}) \cdot \frac{n[OI]}{n[N_2]} = .219n[O^{+2}P] + \sum_i \gamma_i\, n[i] \cdot n[O^{+2}P] \quad . \tag{74}$$

The $O^+(^2P)$ population can be related to the emission rates resulting from the excited population. The population has been related to the total ^2P-^2D volume emissions (η(7319-30Å)) and to the $^2P_{1/2,3/2} \rightarrow {}^2D_{5/2}$ emissions (η(7319Å)) in Appendix C, i.e.,

$$\eta(7319\text{-}30\text{Å}) = .171\ n[O^{+2}P] \tag{75}$$

and

$$\eta(7319\text{Å}) = .098\,n[O^{+2}P] \quad . \tag{76}$$

Equations (74) and (75) can be combined to eliminate the term and solved for the volume emission rate ratio, i.e.,

$$\frac{\eta(7319\text{-}30\text{Å})}{\eta(3914\text{Å})} = R_{\sigma_0}(E) \cdot \frac{n[OI]}{n[N_2]} \left\{ \frac{.171}{.219 + \sum_i \gamma_i\, n[i]} \right\} \quad . \tag{77}$$

Similarly, Equations (74) and (76) can be combined to give

$$\frac{\eta(7319\text{Å})}{\eta(3914\text{Å})} = R_{\sigma_0}(E) \frac{n[OI]}{n[N_2]} \left\{ \frac{.098}{.219 + \sum_i \gamma_i\, n[i]} \right\} \quad . \tag{78}$$

If the production is written in terms of the 4278Å emission rate, expressions similar to (77) and (78) can be written considering the branching ratio discussion of Appendix D, i.e.,

$$\frac{\eta(7319\text{-}30\text{Å})}{\eta(4278\text{Å})} = R_{\sigma_1}(E) \cdot \frac{n[OI]}{n[N_2]} \left\{ \frac{.171}{.219 + \sum_i \gamma_i\, n[i]} \right\} \tag{79}$$

and

$$\frac{\eta(7319\text{Å})}{\eta(4278\text{Å})} = R_{\sigma_1}(E) \cdot \frac{n[OI]}{n[N_2]} \cdot \left\{ \frac{.098}{.219 + \sum_i \gamma_i\, n[i]} \right\} \quad . \tag{80}$$

To repeat, historically $R_{\sigma_0}(E) \simeq 1.41$, and $R_{\sigma_1}(E) \simeq 4.65$. Equation (80) will be used extensively in the following chapter in interpreting ground based surface brightness ratios of λ7319Å and λ4278Å emissions. In the following chapter, a rocket payload measurement of λ7319-30Å to λ3914Å intensity ratios will be interpreted with the aid of Equation (77) above.

CHAPTER VII
THEORETICAL INTERPRETATION AND MEASUREMENT OF $O^+(^2P\text{-}^2D)$, 7319Å and $N_2^+1NEG_{1,0}$, 4278Å EMISSION INTENSITIES IN AURORA FROM GROUND STATIONS

7.1 INTRODUCTION

A number of measurements were made at College, Alaska, of the intensity of the λ7319Å doublet (I_{7319}) along with the $N_2^+1NEG_{1,0}$ intensity (I_{4278}). Expression (80) of the last chapter relates the volume emission rates of these emissions. This expression will prove to be valuable in this chapter when interpreting the ground based data.

In the theoretical development of the previous chapter, it was assumed that the primary electrons were mainly responsible for the N_2^+ ionization rate and resultant N_2^+1NEG emissions. In interpreting the total volume emitting layer, in a ground based measurement where one is oriented to measure along the flux tubes, a significant contribution to the total intensity comes from the lower scale height of the atmospheric range of the precipitating particles. Significant energy degradation is beginning to take place in the primary electron energy distribution at these altitudes. One of the intentions here is to ascertain where the electrons are ranging into the atmosphere. Consequently, the description of this production function shape is pertinent to this interpretation. Berger et. al. (1970) and Banks et. al. (1974) have calculated theoretical profiles of N_2^+ production in aurora for monoenergetic, isotropic electron beams in the atmosphere. The particle range indicative of these investigations and spectroscopic studies by Rees and Luckey (1974) will be utilized in the interpretation of these ground based measurements.

Previous theories of $O^+(^2P)$ quenching and branching will be presented and compared to the ground based observations.

The refinement of the theory and applied methods describing the $O^+(^2P)$ and N_2^+1NEG emission relationship in the context of interpreting ground based measurements is discussed near the end of the chapter.

7.2 GROUND BASED OBSERVATIONS OF I_{7319} AND RELATED EMISSIONS

7.2.1 INTRODUCTION TO THE GROUND BASED MEASUREMENTS

The multi-spiral spectrophotometer (discussed in Chapter V) was set up and operational between February 2, 1973, and February 24, 1973, at the University of Alaska, Geophysical Institute (Ester Dome). The instrument was mounted on the roof of Ester Dome Observatory in a magnetic meridian orientation with a range of ±60° from the zenith.

The University of Michigan Airglow Observatory was located adjacent to Ester Dome. The Michigan facility was equipped with a four channel, tilting filter photometer which monitored the OI, 6300Å, and 5577Å, as well as H_β, 6563Å, and $N_2^+ 1NEG_{1,0}$, 4278Å emissions. The orientation of the Michigan photometer and the sector spectrophotometer (set up for 7319Å) were position aligned by imaging the moon through the instruments for calculated moon zenith positions. A time reference was frequently coordinated between the two systems. The cone half angle of the two systems was 2°.

7.2.2 OBSERVATIONAL PROCEDURE AND RAW DATA SAMPLES

The primary mode of operation was to keep both instruments oriented to the magnetic zenith. Arc scans would have been useful provided photometer triangulation scans for arc location were made simultaneously. When weather, moon conditions, and aurora cooperated for such an observation, equipment did not. This type of scan would be desirable for future measurements.

A strong band system ($N_2 1PG_{5,3}$) induces a varying background in the $O^+(^2P\text{-}^2D)$ wavelength region (Chamberlain, 1961). The ground based observations are also contaminated by OH(8,3) band emissions originating from the upper mesospheric region. Specifically, the $P_{1,2}$(7316.4Å) and $P_{2,2}$(7304.5Å) fell within the scanning range of the instrument.

A monochromator was placed inside the spectrophotometer dome and calibrations were run after each night's sky data was gathered. A calibration of February 8, 1973, is shown in Figure 24. Spectrophotometer scans of the monochromator source for 7319Å and the two OH positions are shown in the figure.

The hydroxyl was always present. Figure 25 shows a typical series of scans with aurora absent (i.e., determined by lack of I_{4278} emission for this same time period). Note in Figure 25 that the instrument did not totally separate or resolve the OH at 7316.4Å from the $O^+(^2P\text{-}^2D)$ at 7319Å. The data reduction scheme used to discern the $O^+(^2P\text{-}^2D)$ will follow in the data reduction section.

A typical 7319Å enhancement with an overhead auroral surge is shown in Figure 26. Scan one of this figure typifies a hydroxyl only type scan. In the succeeding scans, the peak was shifted to a higher wavelength than indicated in spectra one. This indicates the 7319Å was enhanced and not the OH. The scan rate in this case was ~ 1 per minute.

7.2.3 GROUND BASED REDUCED DATA SAMPLES

The deduction of the I_{7319} and $I_{7316.4}$ (OH) intensities from the instrument scan involved an algebraic deconvolution of the effective instrument transmission at the two wavelength positions of emission. This procedure was necessary since the instrument did not totally resolve the λ7319Å emission from the λ7316.4. The details involving the analytic technique for reducing the respective intensity values are given in Appendix E.

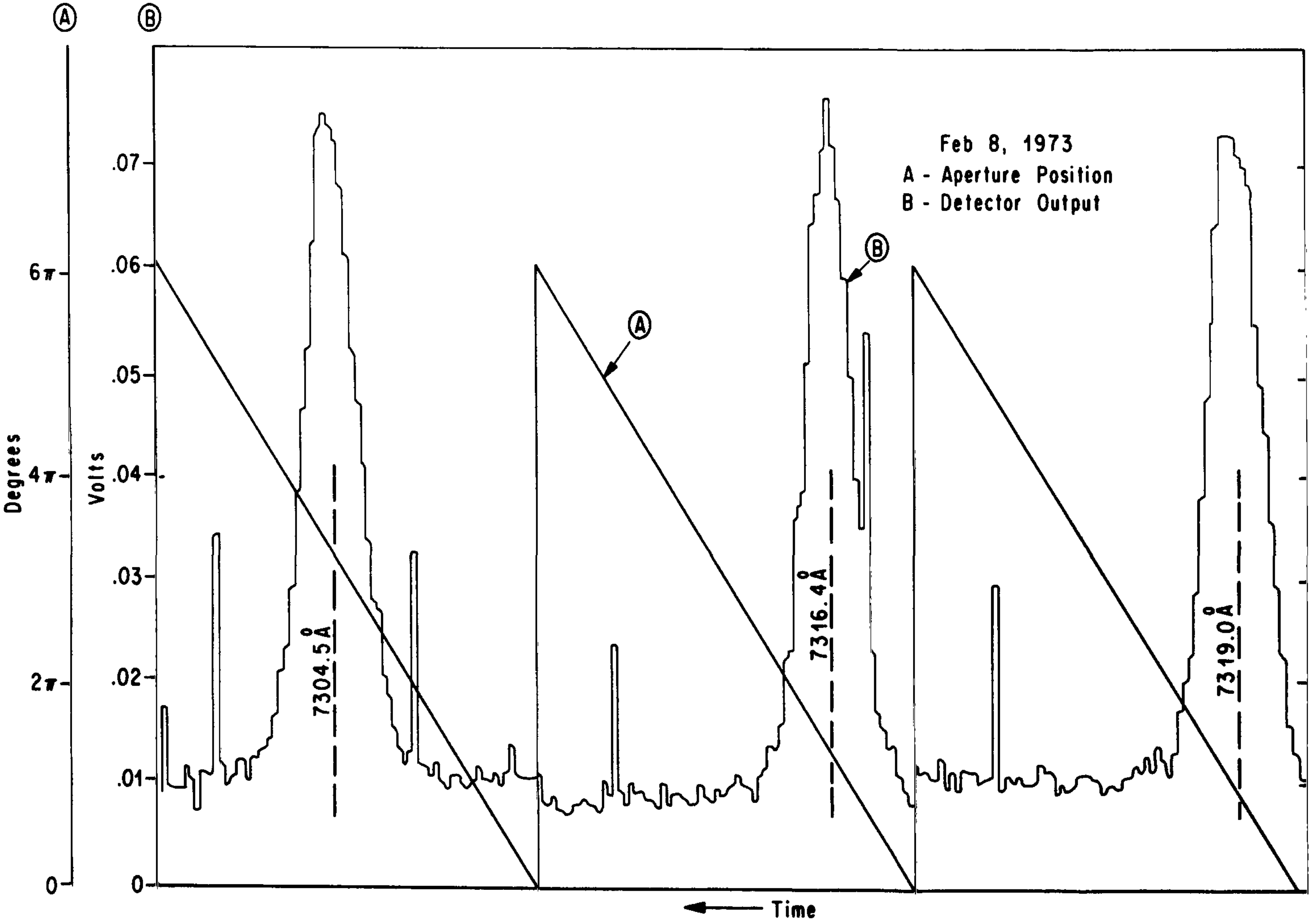

Figure 24. Spectrophotometer scans of a monochromator source tuned to wavelength positions 7319Å, 7316.4Å and 7304.5Å on Feb. 8, 1973, after the Feb. 7/8 sky data scans at Ester Dome, Alaska.

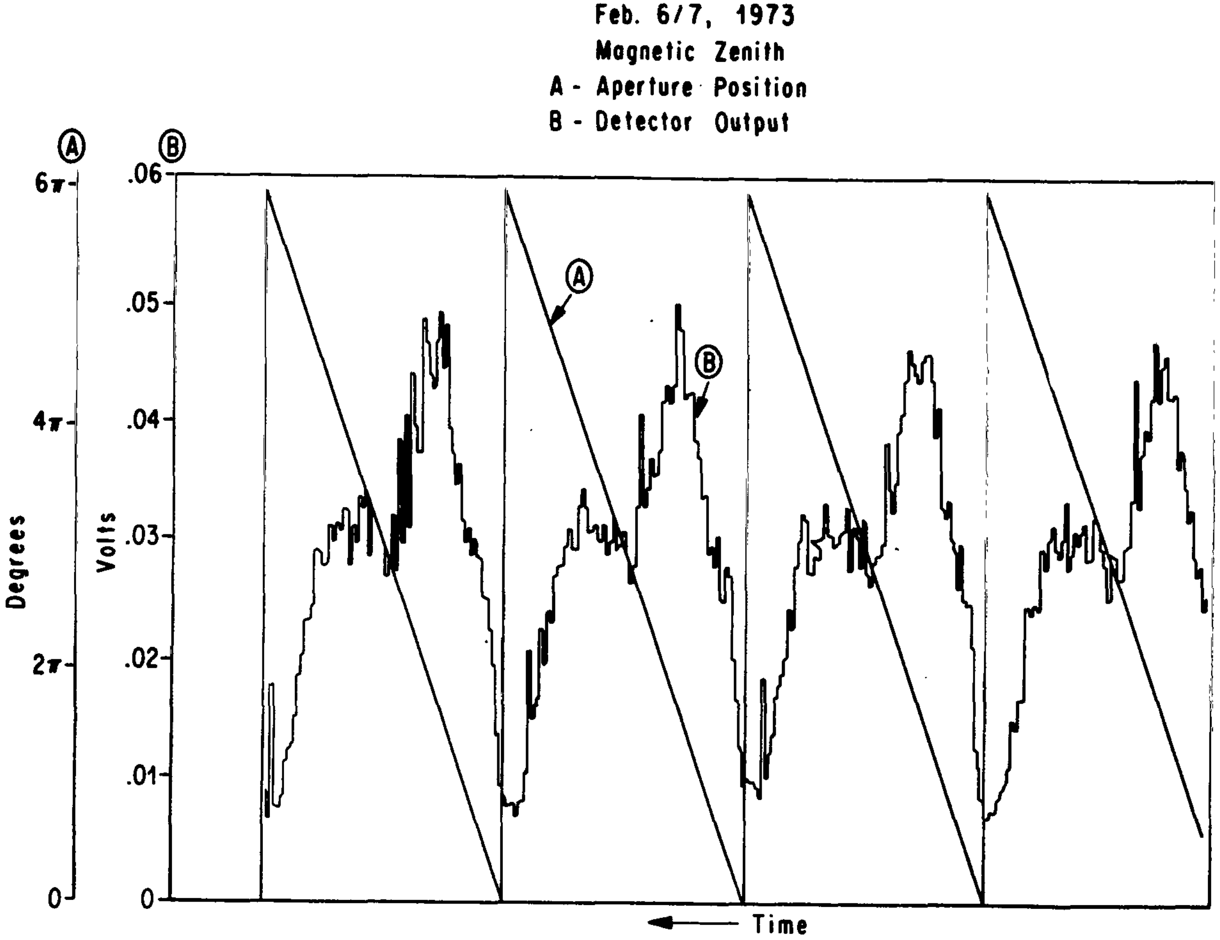

Figure 25. Spectrophotometer scans of the sky on Feb. 6/7 at Ester Dome, Alaska. No aurora was evident and these scans typify OH presence in the night sky. The main feature corresponds to OH $P_{1,2}$ at 7316.4Å.

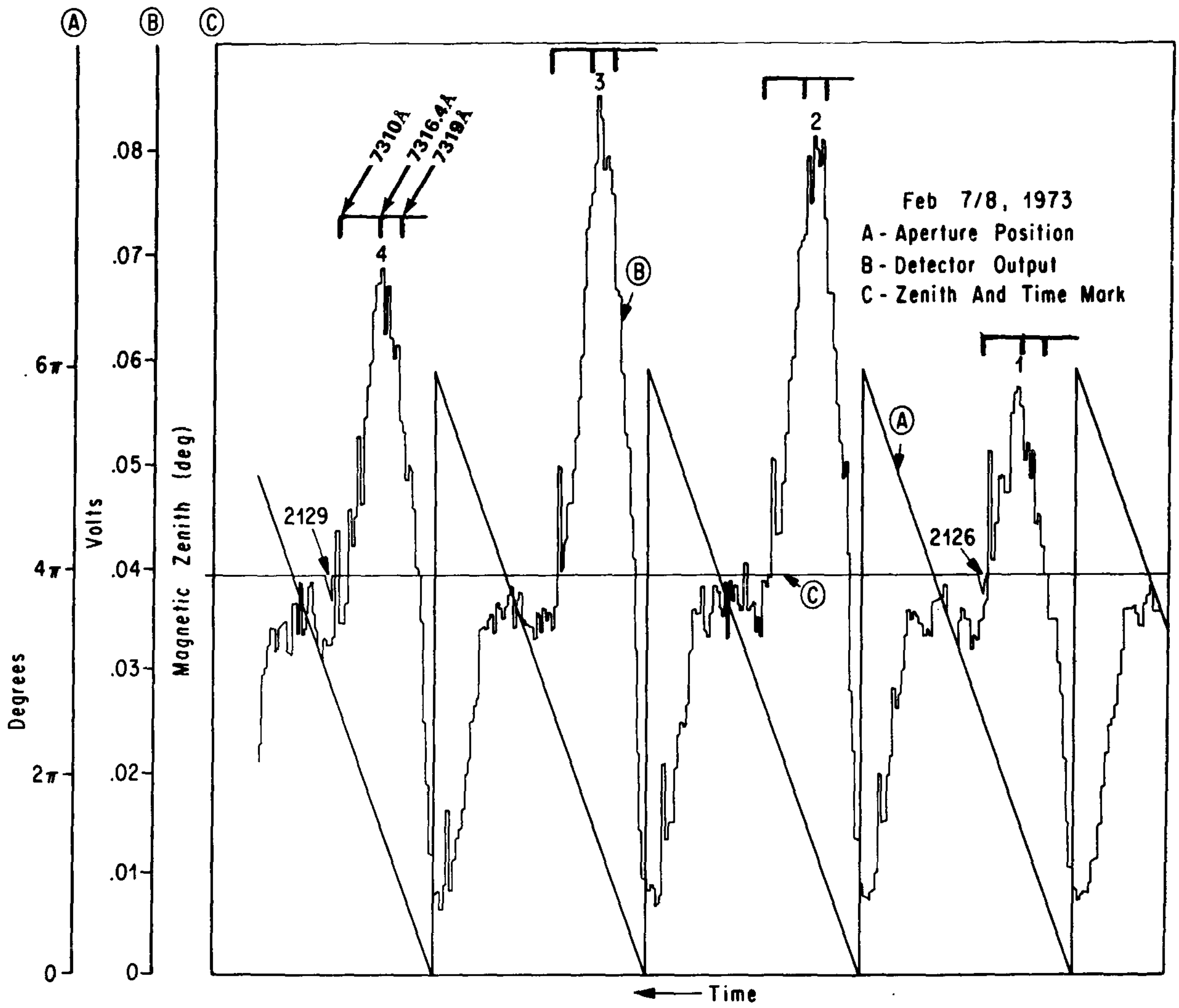

Figure 26. Spectrophotometer scans of the sky (magnetic zenith) on Feb. 7/8, 1973, at Ester Dome. This series of scans typify the passage of an auroral surge passing through the magnetic zenith with ~ 35 rayleighs 7319Å present in scans 2 and 3. The flag over each spectra indicates the 7310Å(BG), 7316.4Å, and 7319Å wavelength positions by vertical hashmarks. Note that the peak shifts towards 7319Å wavelength with increased signal amplitude.

Reduced intensities of 7316.4Å and 7319Å for a two hour period during an auroral breakup on February 22/23, 1973, are shown in Figures 27 and 28 respectively. The scatter in the OH $P_{1,2}$ data is ~ 8 rayleighs with a mean of ~ 14 rayleighs for the two hour period. The scatter increases during periods of enhanced aurora and resultant 7319Å bursts depicted in Figure 28.

Figure 29 shows a plot of the time history of the intensities of λ4278Å and λ6300Å for the same time period as the previous two figures. Figure 30 represents the ratio of the two emissions displayed in Figure 29.

A cursory examination of the 7319Å and 6300Å data shows the 6300Å emission enhanced over nightglow intensities between events but the 7319Å data is not. The 7319Å data is much more bursting in nature. There is, however, a high event correlation between the 6300Å, 7319Å, and 4278Å data. A closer look at Figure 30 suggests a ratio of I_{6300}/I_{4278} value of .5 prior to 2325 A.S.T. and after 0025 A.S.T. with a ratio of 1. for the hour in between. These values correspond to those of Eather and Mende (1971) for the oval region. There also appears to be a slight ratio decrease trend in the period just before midnight. At eight minutes after the hour, note that a major event occurred in all data.

Figure 31 further suggests the implication made earlier that I_{7319}/I_{6300} is very erratic. The 6300Å data has a large continuous background, as well as the 4278Å data, but 7319Å does not and it is further reflected in the variation of I_{7319}/I_{6300} in this plot.

Another case of 7319Å and 4278Å history plots is displayed for February 7/8, 1973 in Figure 32. Here also noted is a high event correlation and again a major event very near midnight with a large amplitude in 7319Å emission. Note the scales differ by an order of magnitude for the two emissions on the figure. A total of seventeen nights of data was taken with about half of them being fairly active. The February 7/8 and February 22/23, 1973, cases represent some of the more active periods.

7.3 INTERPRETATION OF GROUND BASED I_{7319}/I_{4278} DATA

The approach used to interpret the ground based measurements of I_{7319}/I_{4278} ratios takes advantage of what is already known about the I_{6300}/I_{4278} ratio.

Rees and Luckey (1974) have calculated the I_{6300}/I_{4278} ratios for particular monoenergetic, isotropic electron beams in the thermosphere. Berger et. al. (1970) and Banks et. al. (1974) have computed N_2^+ ionization profiles for similar monoenergetic isotropic electron beams. The altitudes of maximum ionization for given energies from Berger et. al. (1970) and Banks et. al. (1974) are point plotted in Figure 33 and a hand drawn fit is drawn through the points.

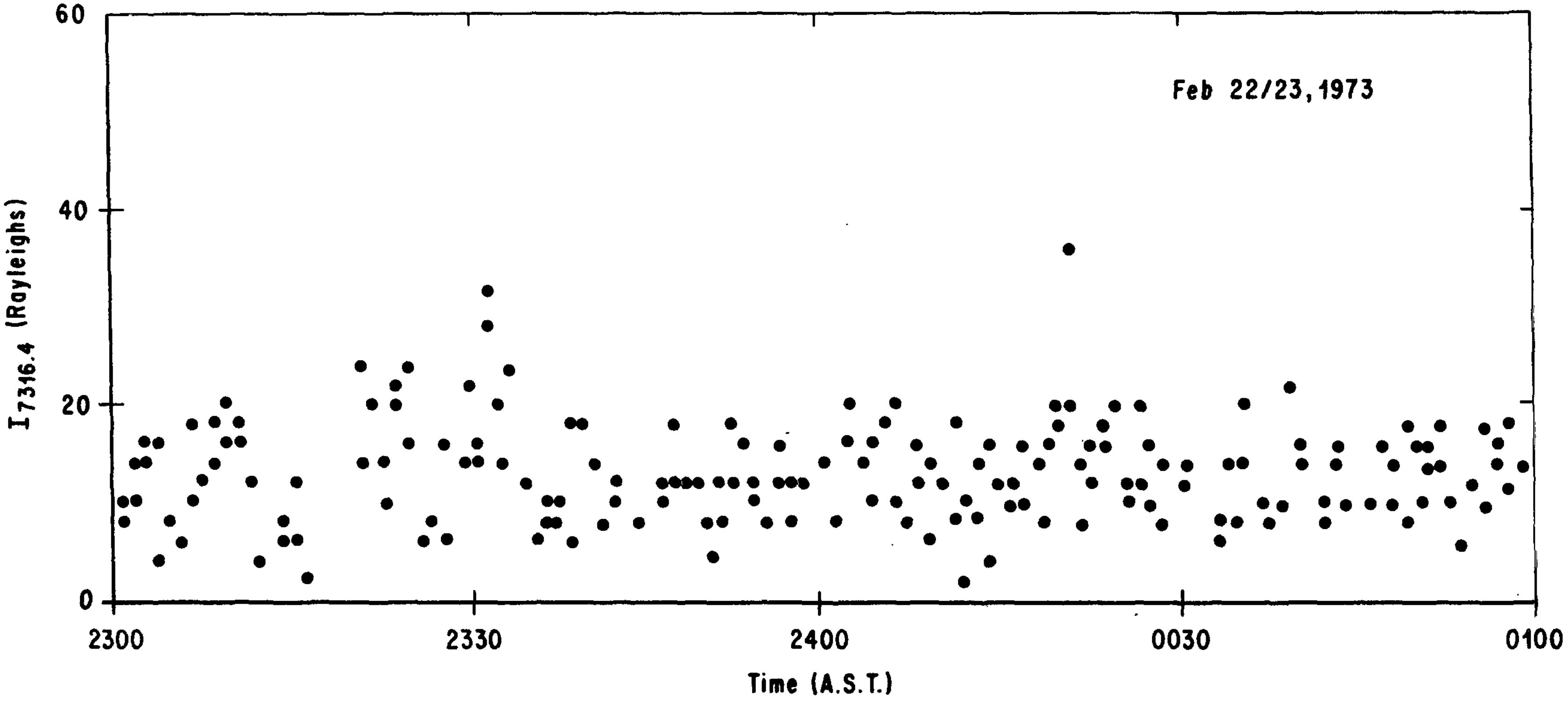

Figure 27. $I_{7316.4}$ versus time for a two hour period near midnight on Feb. 22/23, 1973. The point plot shows a scatter of ±8 rayleighs which is typical for a 30 sec scan rate used on this night.

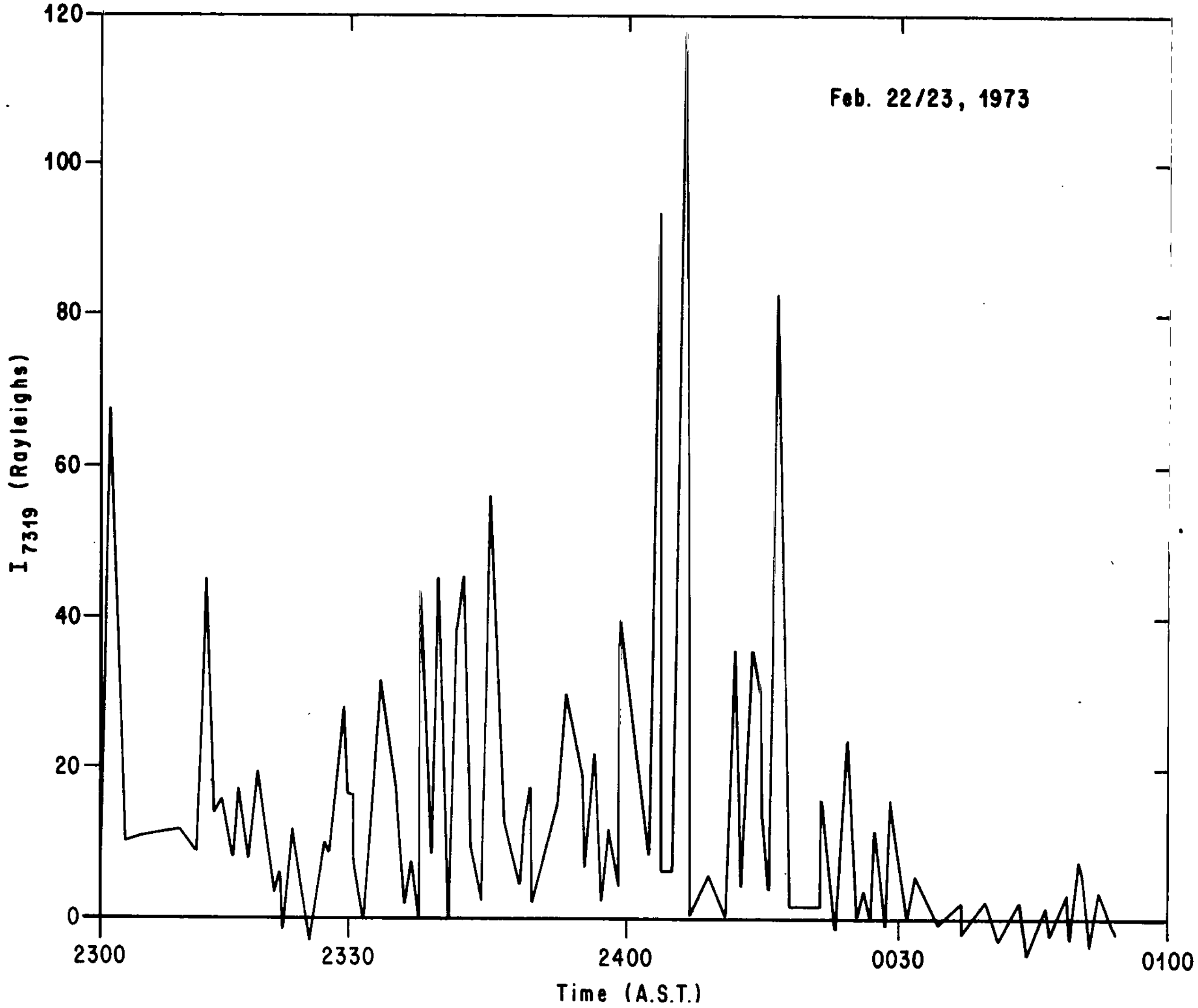

Figure 28. I_{7319} versus time for a two hour period near midnight on Feb. 22/23, 1973. The data points have been straight line segmented to bring out the bursting nature of the emission.

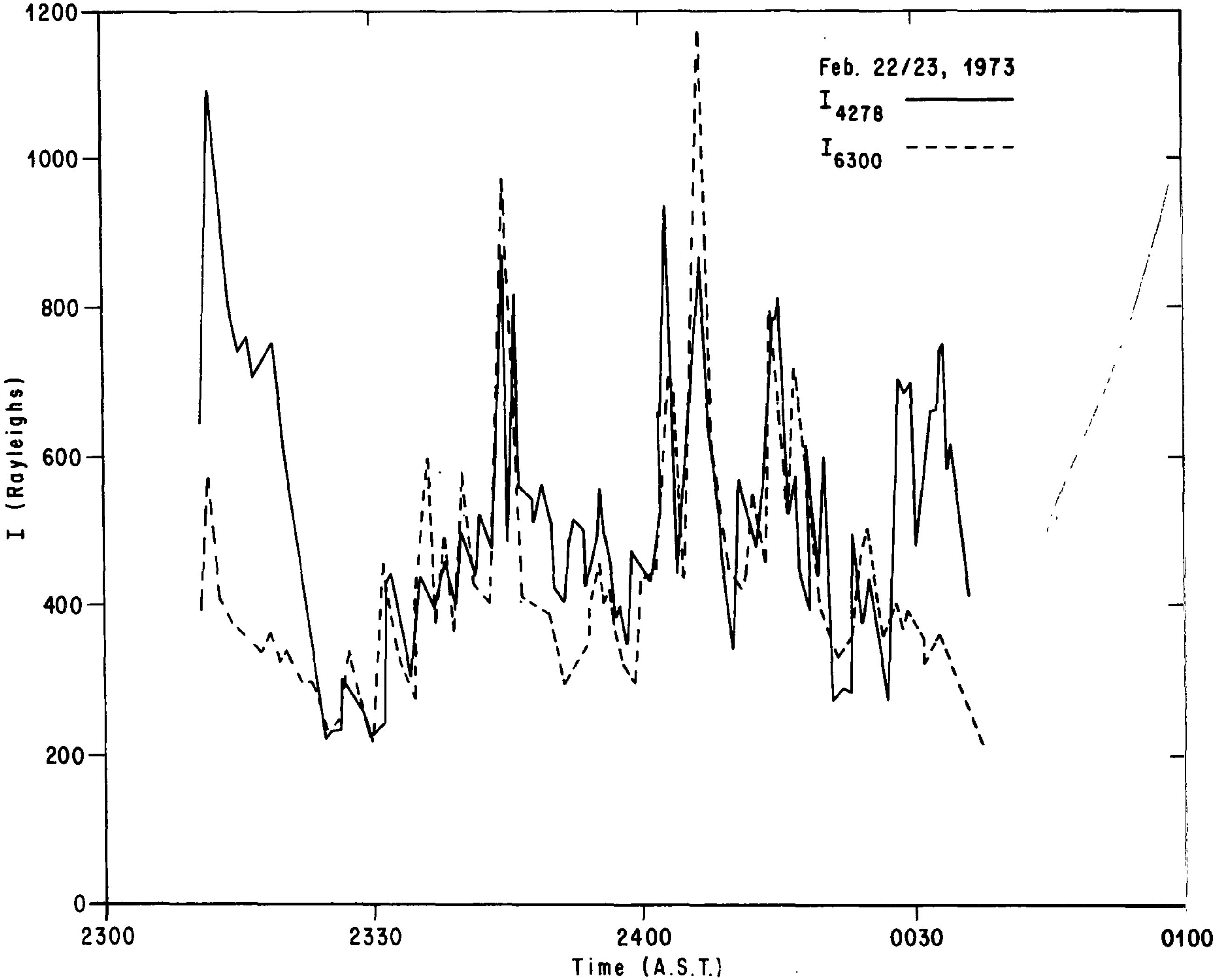

Figure 29. I_{4278} and I_{6300} versus time from the Michigan tilting photometer for same time period shown in Figures 45 and 46. The data rate for the tilting filter was ~ 1 measurement every 20 seconds.

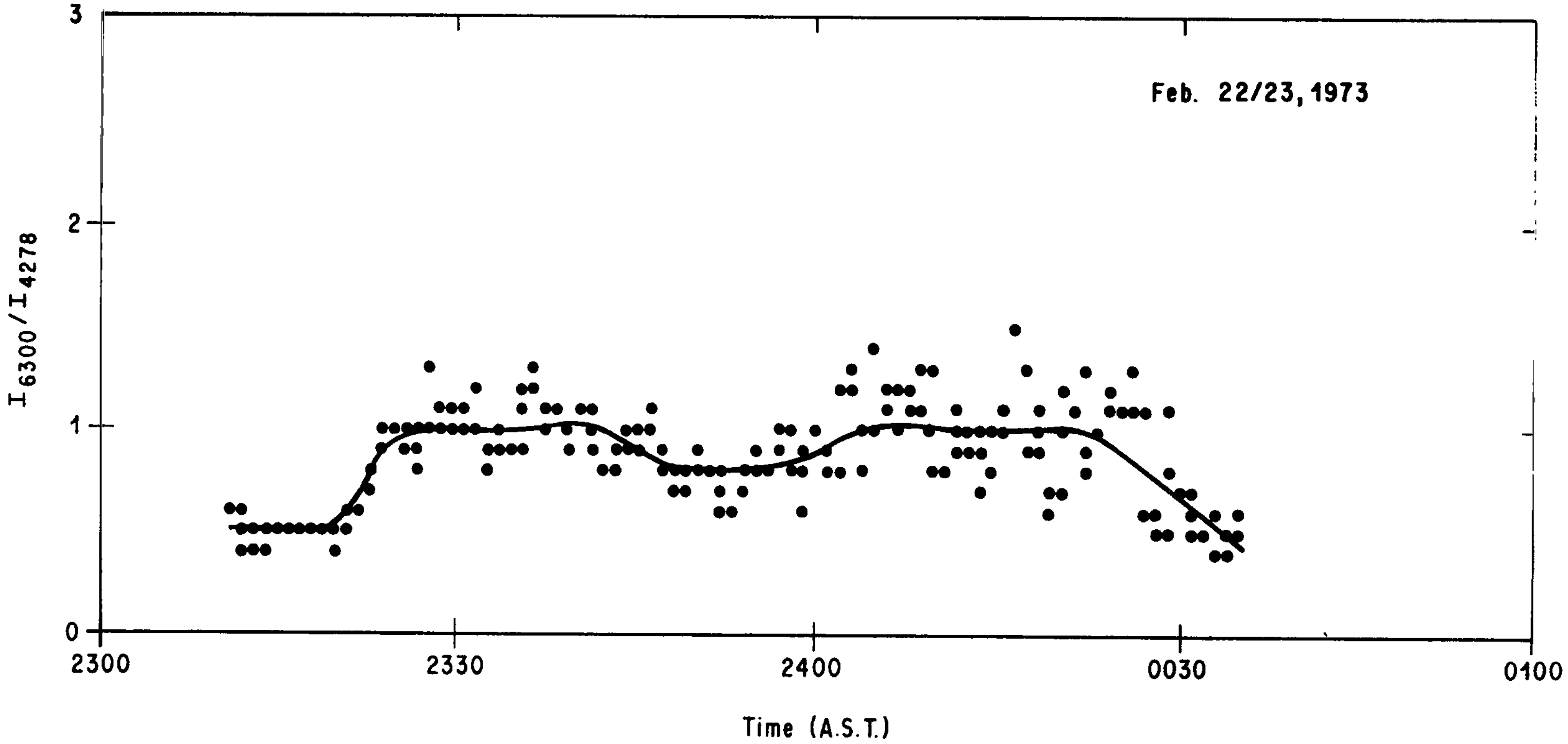

Figure 30. Ratio of I_{6300}/I_{4278} for Feb. 22/23, 1973. I_{6300} was time interpolated to correspond to the time of the I_{4278} measurement for ratio calculations.

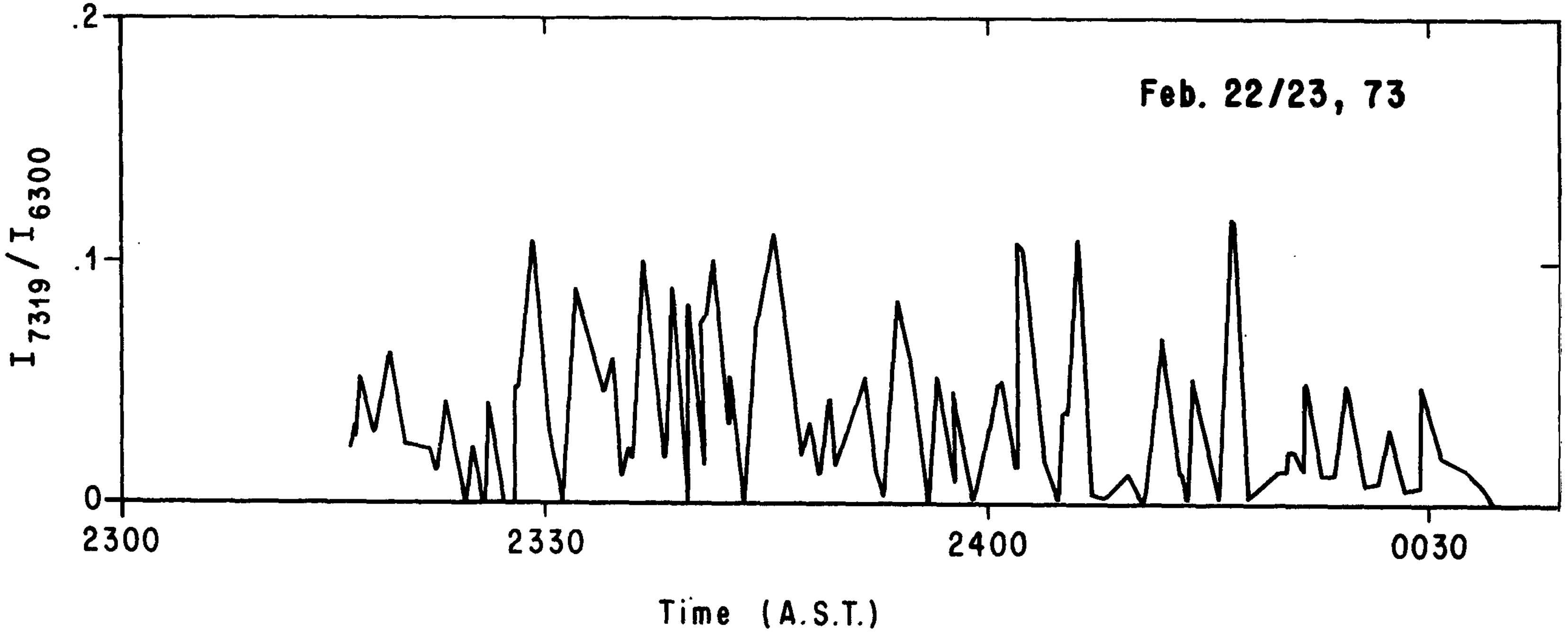

Figure 31. Ratio of I_{7319}/I_{6300} for Feb. 22/23, 1973. I_{6300} was time interpolated to correspond to the time of the I_{7319} measurement for ratio calculations.

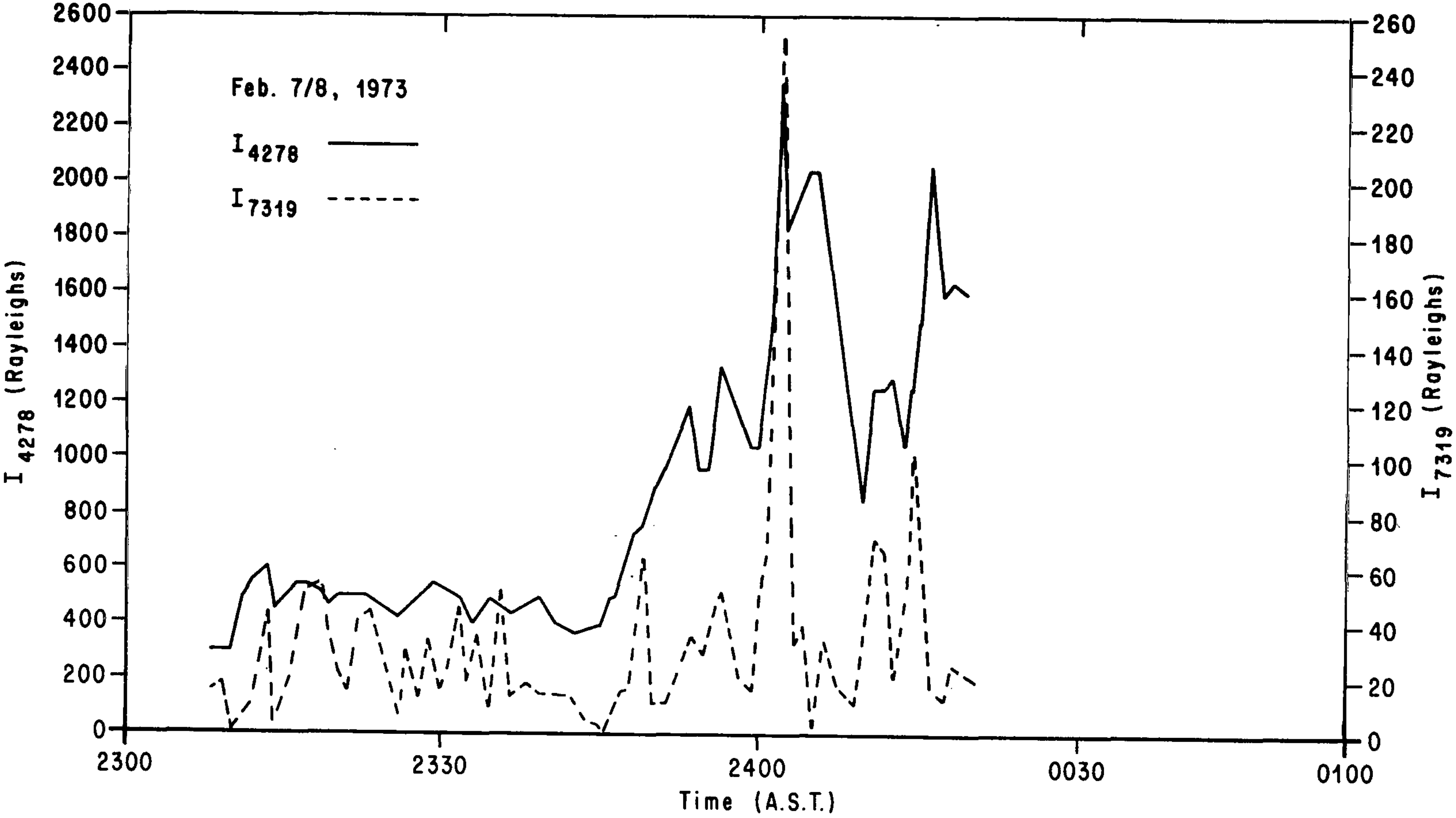

Figure 32. I_{4278} and I_{7319} versus time for a two hour period near midnight on Feb. 7/8, 1973. The orientation of the instruments was the magnetic zenith.

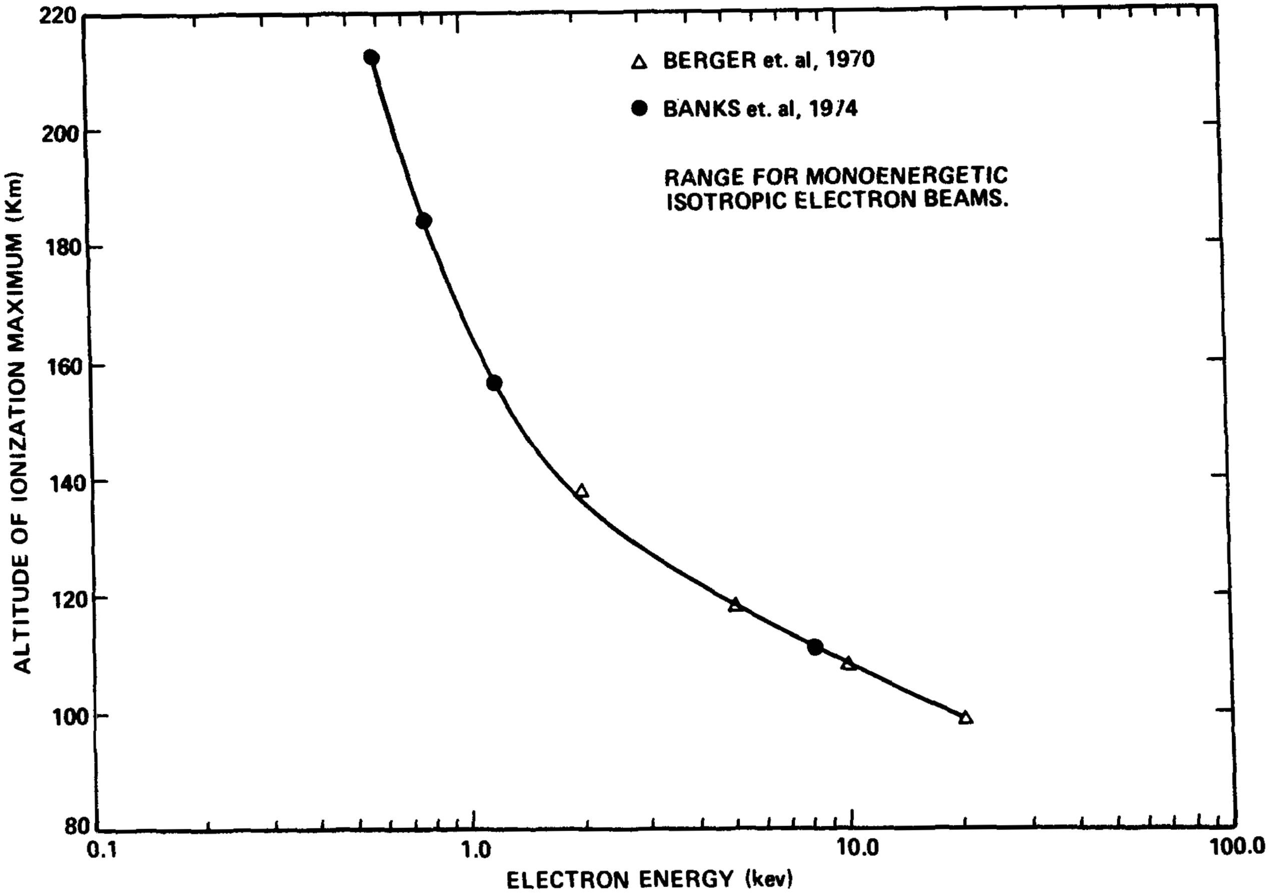

Figure 33. Altitude of ionization maximum versus initial electron energy for monoenergetic, isotropic electron beams. The points are provided by Berger et. al. (1970) and Banks et. al. (1974). The curve through the points is a hand fit to the points on the figure.

Rees and Luckey (1974) values of I_{6300}/I_{4278} are plotted in Figure 34 (Curve A) where the energy to altitude conversion was made using the range curve plotted in Figure 33 which was discussed above. The interpretation then is that a given intensity ratio of I_{6300}/I_{4278} as measured along the magnetic field should have an ionization maximum at the corresponding altitude for a monoenergetic, isotropic electron beam.

A plot of the I_{7319}/I_{4278} ratio can also be generated using the information discussed in the previous chapter. The intensity of the respective emissions can be expressed as the integrated volume emission rates, i.e.,

$$I_{7319} = \int_z^\infty \eta(7319\text{Å})\, dz \quad . \tag{81}$$

Equation (80) of the previous chapter can now be expressed in an integral form as

$$I_{7319} = R_{\sigma_1}(E) \int_z^\infty n[OI]\, \frac{\eta(4278\text{Å})}{n[N_2]} \left\{ \frac{.098}{.219 + \sum_i' \gamma_i\, n[i]} \right\} dz \tag{82}$$

The integral of Equation (82) can be further simplified with some reasonable assumptions. In the derivation of the N_2^+ production by electron impact in Appendix D, the production to density relationship was related to an energy integral (Equation 2-D). Further assuming that $\eta(N_2^+) \propto \eta(4278\text{Å})$ (Borst and Zipf, 1970), expression (2-D) can be written as

$$\frac{\eta(4278\text{Å})}{n[N_2]} = C \int_E F(E)\, \sigma_{N_2^+}(E)\, dE \tag{83}$$

where C is a proportionality constant.

In the interpretation of the I_{6300}/I_{4278} intensities Rees and Luckey (1974) used exponential functions (discussed in the introduction to Chapter VI) in the description of F(E) for auroral electrons. It was assumed that the Rees and Luckey (1974) assumption is very near the shapes described by Berger et. al. (1970) and banks et. al. (1974) which were used as a source for the altitude of maximum ionization indicated by the Rees and Luckey (1974) intensity ratios.

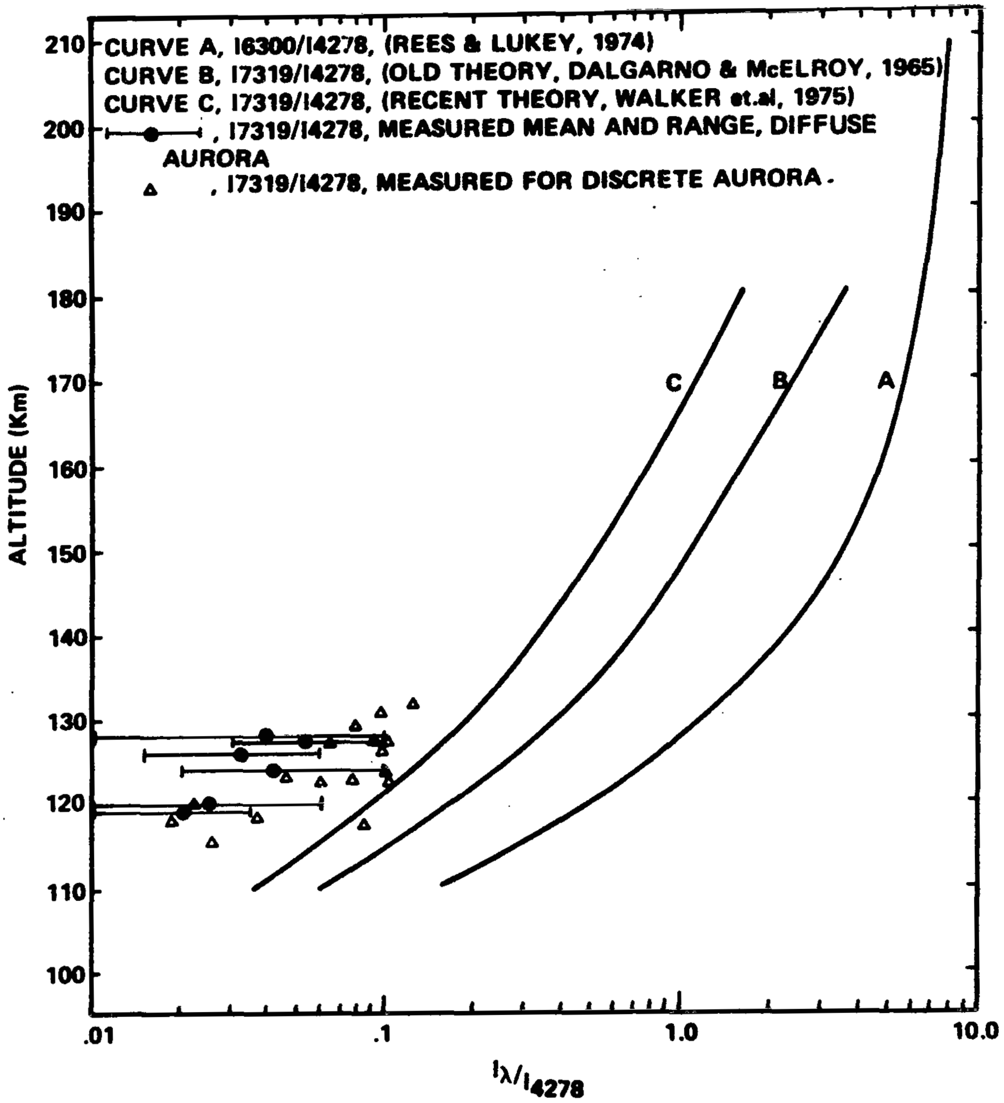

Figure 34. Altitude versus I_λ/I_{4278} where λ refers to 6300Å emission or 7319Å emission. A theory for I_{6300}/I_{4278} and two theories for I_{7319}/I_{4278} are plotted on the figure and discussed in the text. Ground based measurements of I_{7319}/I_{4278} are plotted for diffuse aurora and for "discrete events".

In Appendix F, a broad range of N_2^+ production shapes is plotted and compared. It was deduced that the N_2 proportional profile shape, as described in Appendix E, closely parallels the exponential shapes of the previous models, particularly for the very energetic beams ranging below 200 km. The N_2 proportional shape assumes that the volume production of the emissions arising from the N_2^+ excited states is constant to the range altitude of the electrons, and zero below. This assumption enables the ratio described in Equation (84) to be specified as constant over all altitudes in the electron precipitation regions, and furthermore, may be expressed in the integral form, i.e.,

$$\frac{\eta(4278Å)}{n[N_2]} = \frac{\int_z^\infty \eta(4278Å)\,dz}{\int_z^\infty n[N_2]\,dz} \quad . \tag{84}$$

For an exponential atmosphere, (84) becomes

$$\frac{\eta(4278Å)}{n[N_2]} = \left.\frac{I_{4278}}{n[N_2]\cdot H_{N_2}}\right|_Z \tag{85}$$

where H_{N_2} is the nitrogen scale height.

Equations (83) and (85) can now be combined to give the expression for the I_{7319}/I_{4278} ratio as

$$\frac{I_{7319}}{I_{4278}} = \frac{R_{\sigma_1}(E)}{n[N_2]\ H_{N_2}} \int_z^\infty n[OI] \left\{ \frac{.098}{.219 + \sum_i \gamma_i\, n[i]} \right\} dz \quad . \tag{86}$$

Two theoretical profiles of I_{7319}/I_{4278} (Curves B and C of Figure 34) were generated using Equation (86) above. They represent an 'Old Theory' (Curve B) and a 'Recent Theory' (Curve C).

The 'Old Theory' assumed values of $\gamma_{N_2} = 1 \cdot 10^{-10}$ (Dalgarno and McElroy, 1965), $\gamma_e = 3 \cdot 10^{-8}$ (Seaton and Osterbrock, 1957), and a $\sigma_{O^{+2}P}(E)/\sigma_{O^+}(E)$ of .2 after Seaton (1959) (i.e., $R_{\sigma_1}(E) = 4.65$). The neutral composition and temperature model of Jacchia (1971) for $T_\infty = 1000°K$ was used for this curve and all theoretical curves which follow in this study. A value of $10^6\,cm^{-3}$ was assumed for n[e].

The 'Recent Theory' (Curve C of Figure 34) was generated identical to that above except for revised quenching coefficients. Walker et. al. (1974) values of $\gamma_O = 2 \cdot 10^{-10}$, and $\gamma_{N_2} = 5 \cdot 10^{-11}$, replace the N_2 quenching of the 'Old Model' and the $\gamma_e = 2 \cdot 10^{-7}$ value of Henry et. al. (1969) replaces the 'Old Theory' above.

The curves plotted in Figure 34 will assist in assessing measured ratios of I_{6300}/I_{4278} and I_{7319}/I_{4278}. Rees and Luckey (1974) have carefully worked out the ratios of the classical auroral lines included in Curve A of Figure 34. It was assumed that Curve A was correct and, for a measurement of I_{6300}/I_{4278}, the altitude of maximum ionization was inferred from the height relationship of Figure 33. As discussed earlier, the ground based measurements included I_{6300}/I_{4278} measurements as well as I_{7319}/I_{4278}. The measured I_{7319}/I_{4278} was then plotted on Figure 34 at the altitude which corresponded to that indicated by the I_{6300}/I_{4278} ratio discussed above. This was accomplished for two types of aurora discussed below.

Time histories of I_{7319}/I_{4278} ratios for all data points are plotted in Figures 35 and 36 for the two nights' data sample previously discussed. These data points include the 'Diffuse Aurora' as well as discrete events. A hand fit mean (solid curve) and extremes (dashed curve) on each of the two figures indicate the ratio tendencies for the indicated time periods. Figure 30 shows the time changes in the observed I_{6300}/I_{4278} ratio for the night of February 22/23, 1973. In Figure 30, it is noted that the I_{6300}/I_{4278} ratio remains nearly constant for approximately 15 minute time periods. I_{6300}/I_{4278} ratios were selected from Figure 30 at ~ 15 minute intervals and the mean and range of the I_{7319}/I_{4278} were determined from Figure 35 for the same local time. The mean I_{7319}/I_{4278} and the range are indicated in Figure 34 by a point and range bar respectively, as described in the previous paragraph. The same was done for the February 7/8 which has also been plotted on Figure 34.

Discrete events are also plotted on Figure 34 (triangles). In these cases, the diffuse aurora component was removed from both the I_{6300} and I_{4278} measurements and the ratios were taken at their maximum value as that maximum occurred in the field of view of the instrument. The I_{7319} showed little or no background as shown in Figure 28.

The altitude coverage of the ground based measurements was not large, as indicated in Figure 34. The I_{6300}/I_{4278} ratio ranged from ~ .5 to ~ 1.0 on both nights indicating that most of the aurora was ranging to the 120 to 130 km region. It is apparent that the theoretical prodictions of the I_{7319}/I_{4278} ratio are larger than the measurements. The predicted ratio of Curve C (Walker et. al., 1975, quenching reference) suggests a value of .13 for I_{7319}/I_{4278}, whereas the measurements suggest a ratio of .06, a factor of 2 difference. The 'Old Theory' (Curve B) predicts ratios much larger than those measured at these altitudes, on the order of a factor of 5 difference.

The picture is expanded in the next chapter by adding ratios measured at higher altitudes. Further theory and measurement inconsistencies will be discussed following the addition of this other data.

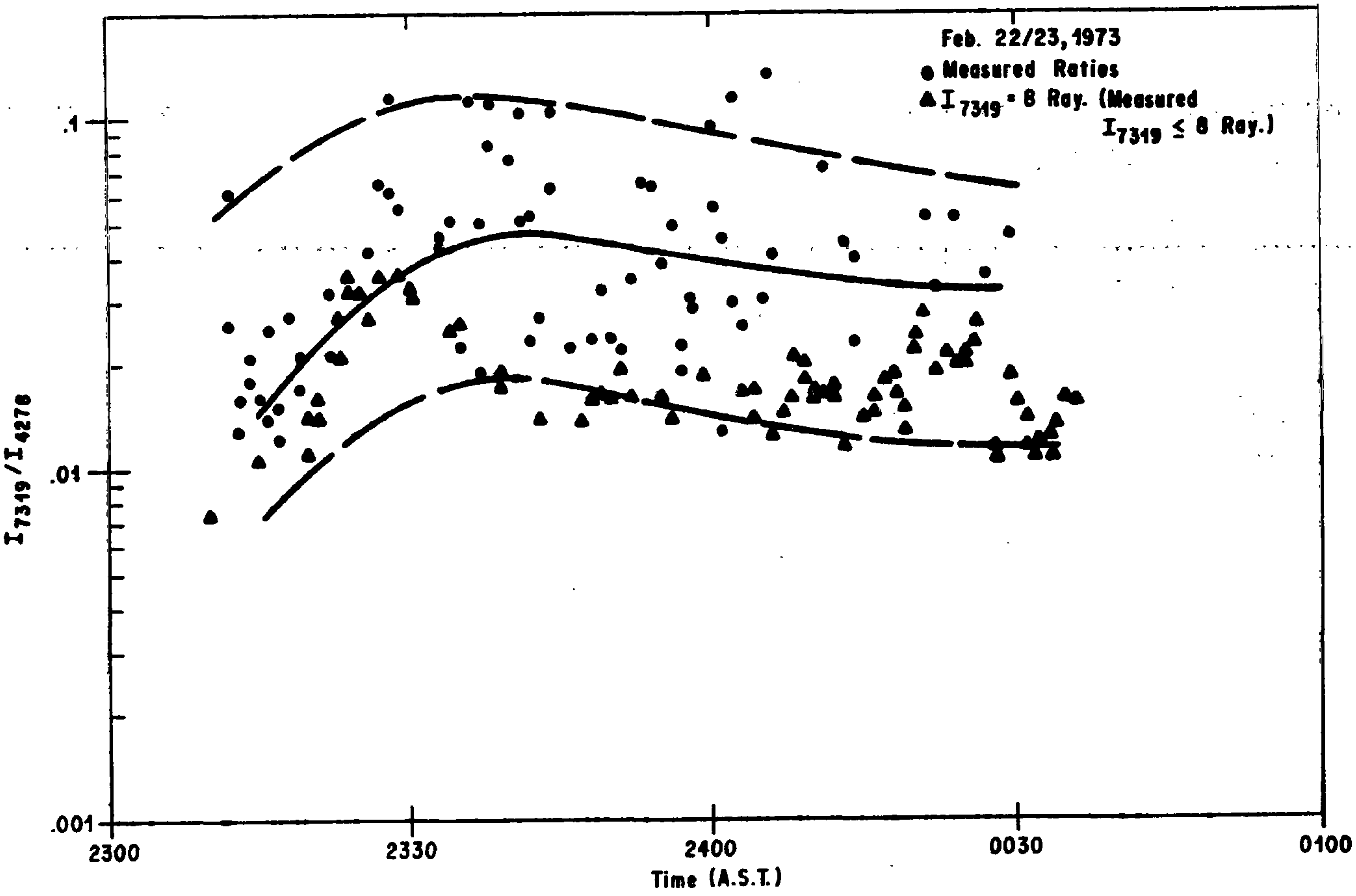

Figure 35. Ratio of I_{7319}/I_{4278} for Feb. 22/23, 1973. I_{4278} was time interpolated to the time of I_{7319} for ratio calculations. The solid curve represents a hand fit mean of the data and the dashed, the extremes.

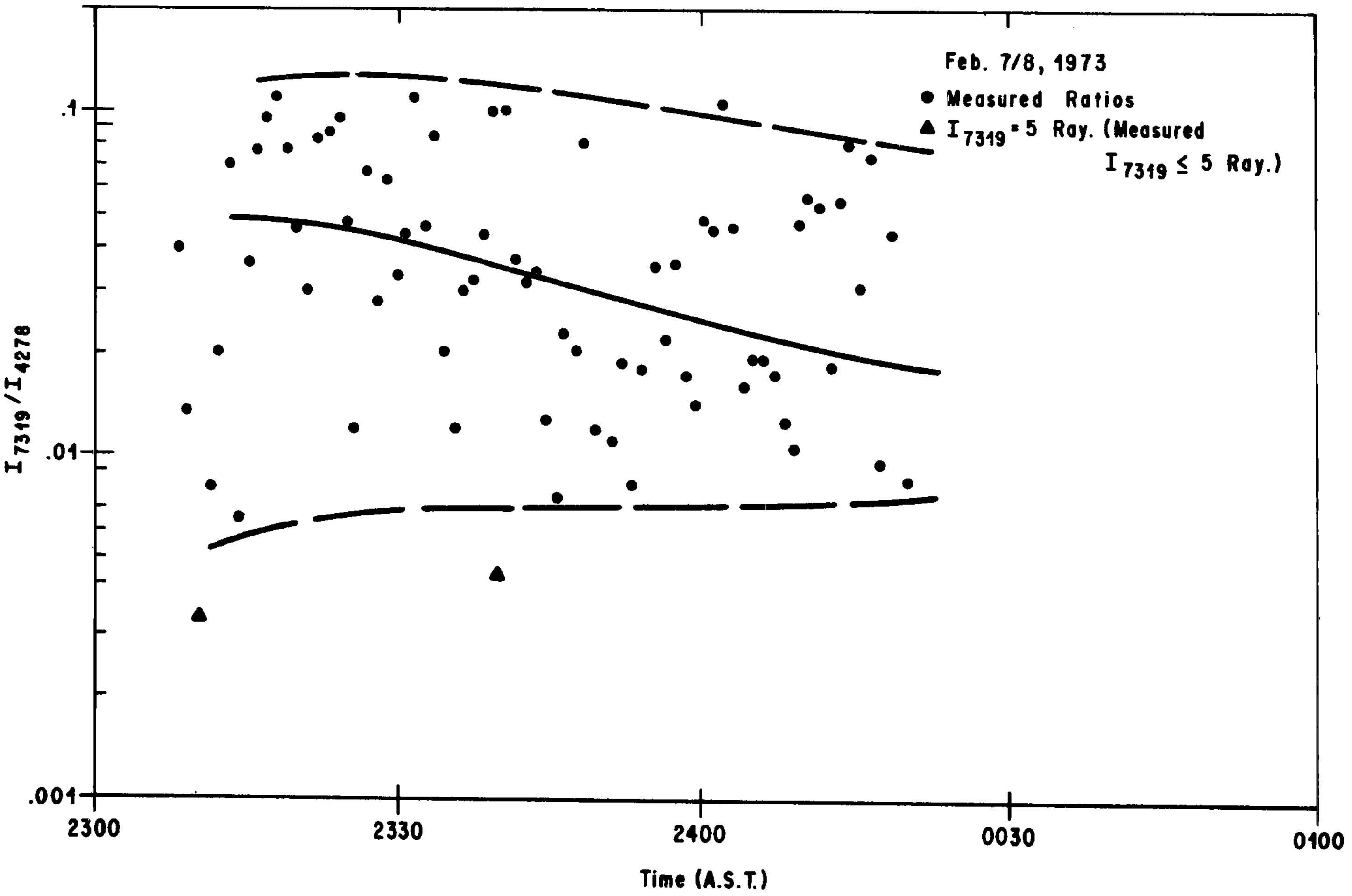

Figure 36. Same as Figure 35, except for Feb. 7/8, 1973.

CHAPTER VIII
N_2 1PG$_{5,3}$, N_2^+1NEG$_{0,0}$, AND $O^+(^2P\text{-}^2D)$ INTENSITY PROFILES IN AN AURORA AND DEDUCED $O^+(^2P)$ ELECTRON IMPACT PRODUCTION EFFICIENCY AND QUENCHING RATE

8.1 INTRODUCTION

Described in this chapter are the data, data analysis and geophysical interpretation of $O^+(^2P\text{-}^2D)$, N_2^+1NEG$_{0,0}$, and N_2 1PG$_{5,3}$ emission measurements made on a rocket payload in an active aurora.

In the introduction to Chapter VI, some discussion was given on the difficulty in measuring the $O^+(^2P\text{-}^2D)$ emission. The 7319Å, 7330Å emissions of the metastable ion are surrounded by N_2 1PG emissions. Chamberlain (1961) has published auroral ground based spectra of this wavelength region. The N_2 1PG$_{5,3}$ and N_2 1PG$_{6,4}$ bands are both overlapping the $O^+(^2P\text{-}^2D)$ emission. The ground based spectra also shows nearby OH emissions which originate in the mesosphere. The OH contaminants do not need to be considered on a rocket payload located above the OH emission altitudes.

The next section of this chapter presents the rocket photometer data in its measured form and also includes the electron density profile as deduced from a Langmuir probe on the payload. The three photometer channels shown were bandpass peaked at 3914Å, 7326Å, and 7354Å. The data analysis section (Appendix G) describes how the rocket photometer outputs of the previous section were used to deduce the amount of respective N_2^+1NEG$_{0,0}$, N_2 1PG$_{5,3}$, and $O^+(^2P\text{-}^2D)$ emissions present in the field of view of the rocket photometers.The technique used in deducing the amount of $O^+(^2P\text{-}^2D)$ and N_2 1PG$_{5,3}$ was somewhat complex. The amount of N_2 1PG passed by the 7326Å and 7354Å channels required an N_2 1PG band model to synthesize the band shape. The N_2 1PG$_{5,3}$ and $O^+(^2P\text{-}^2D)$ emission intensities were then deconvolved from the 7326Å and 7354Å channel currents.

One of the outcomes of the analysis was the intensity ratio of the N_2 1PG$_{5,3}$ and N_2^+1NEG$_{0,0}$ band systems. This ratio is discussed next before proceeding into the main outcome of the measurement, the $O^+(^2P\text{-}^2D)/N_2^+$1NEG$_{0,0}$ intensity ratio.

The appropriate emission branching ratios were applied to the $O^+(^2P\text{-}^2D)$ and N_2^+1NEG$_{0,0}$ measured emissions to convert to the I_{7319}/I_{4278} 'measurement'. This was done so that the data of the last chapter might be compared and plotted with this data. The rocket payload and ground based I_{7319}/I_{4278} data were found in good agreement and the 'Old Theory' and 'Recent Theory' discussed in the last chapter did not describe the measurement.

Two approaches were taken to modify the theory such that appropriate quenching and cross section ratios would in turn describe the measurements. One approach was to reduce the quenching previous investigators had applied to $O^+(^2P)$, as well as, the rate at which $O^+(^2P)$ was produced by electron impact. The second approach was to accept large quenching and postulate an additional low altitude source of $O^+(^2P)$. The chapter concludes with some limits on the manipulated parameters.

8.2 NASA 4.329 AURORAL MEASUREMENTS

On March 39, 1972, NASA 4.329 was launched into an active aurora from Fort Churchill, Canada (58.7°N, 93.8°W). The University of Michigan Airglow Payload was equipped with a turret photometer, particle detector, and Langmuir probe from which the following analysis was made (Sharp and Hays, 1972, and Sharp and Hays, 1974).

The particle detector scanned from .5ev to ~ 500ev electrons. Particles were first detected at 120 km. This altitude was used to discern that the payload was in the aurora above 120 km and prior (or below) this altitude, the emissions observed from the photometers were that of the aurora above the payload.

The photometer channels (3914Å, 7326Å, and 7354Å) were broadband ($\Delta\lambda_1/_2 \simeq$ 20Å to 30Å) and the channel voltage profiles are plotted in Figures 37, 38, and 39 for the three channels of interest in this study. The circles and dots shown on Figures 38 and 39 represent measurements using a wide angle and narrow angle field of view. The curve on the two figures represents a hand fit of the data. This was done to interpolate values at 2 km increments over the range of data as required for the data analysis. The sensitivities were determined with a C_{14} low brightness source calibrated by the National Bureau of Standards (Appendix G). The detector dark current has been subtracted from these profiles prior to making these plots.

Finally, the electron density, as deduced from the Langmuir probe, is plotted versus altitude in Figure 40. This data is required for the theoretical application of electron quenching in analyzing the continuity equation of $O^+(^2P)$.

8.3 REDUCED AURORAL EMISSION FROM NASA 4.329

The data reduction procedure involved the laborious task of deconvolving the $O^+(^2P-^2D)$ emission signal and the contribution from the neighboring N_2 1PG band emissions from the two photometer channels peaked at 7326Å and 7354Å. This procedure is described in Appendix G and the final results are plotted in Figure 41. The curve for the $O^+(^2P-^2D)$ emission represents a hand fit curve through the data points.

The rocket payload passed through an enchanced region beginning at ~ 140 km altitude. It is uncertain as to whether a new discrete event formed while the payload was ascending or whether the payload moved through an existing event.

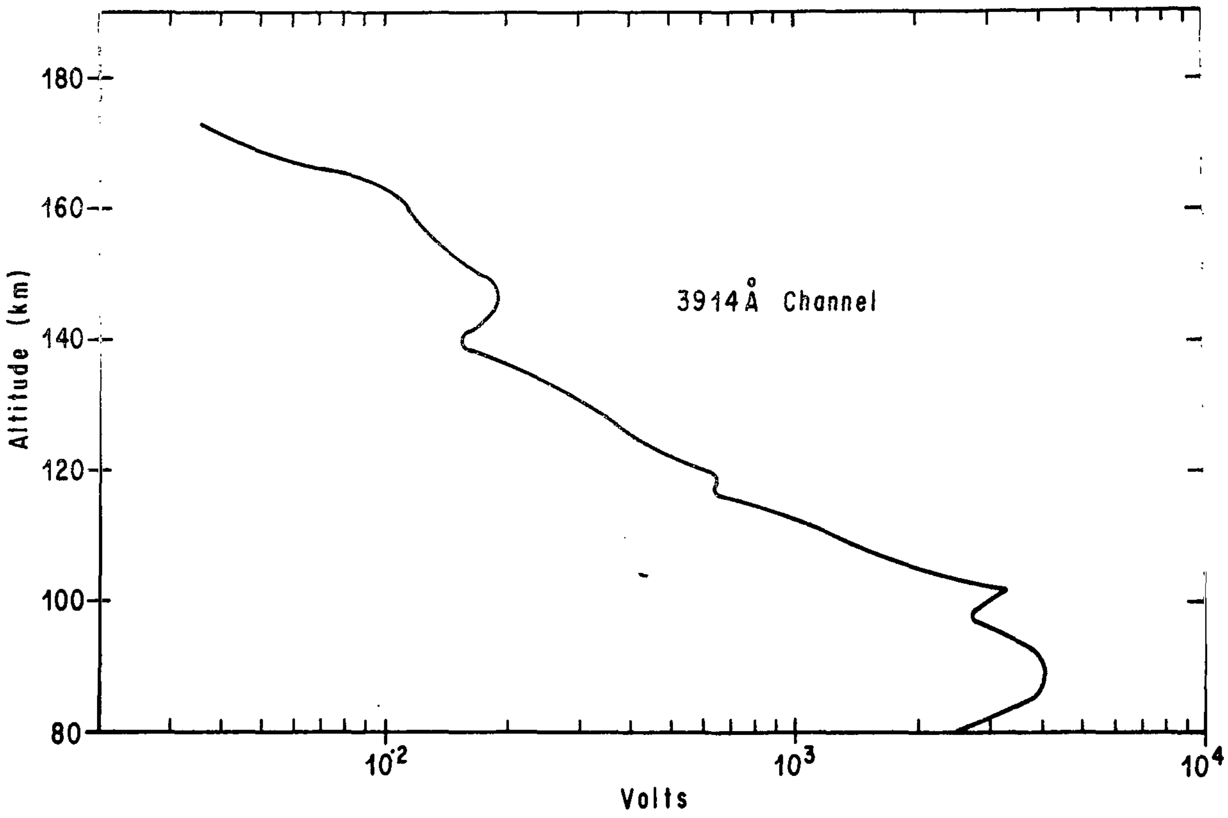

Figure 37. Altitude versus channel voltage for the 3914Å channel for NASA 4.329.

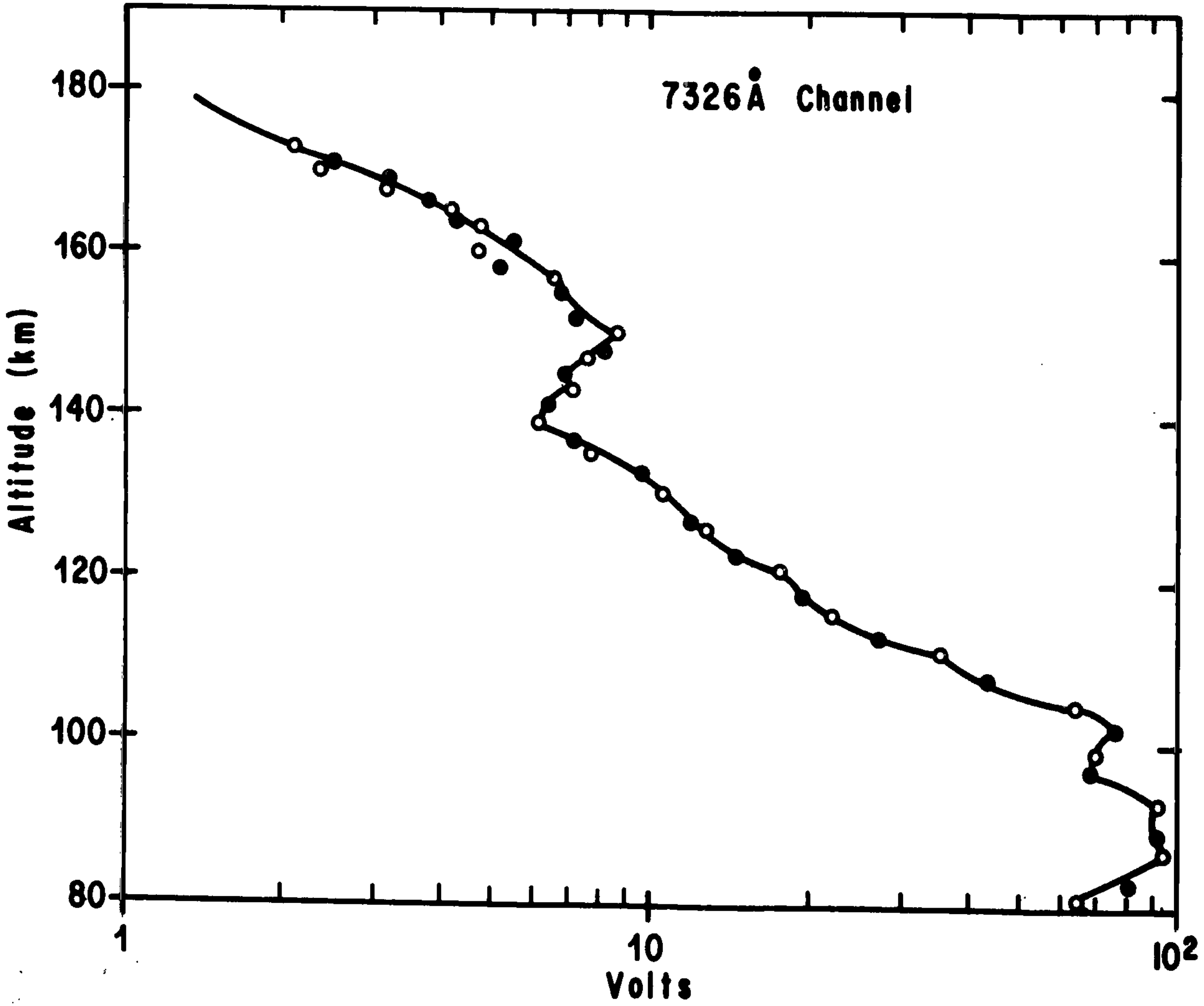

Figure 38. Altitude versus channel voltage for the 7326Å channel for NASA 4.329. The circles and dots represent measurements using a wide angle and narrow angle field of view, respectively.

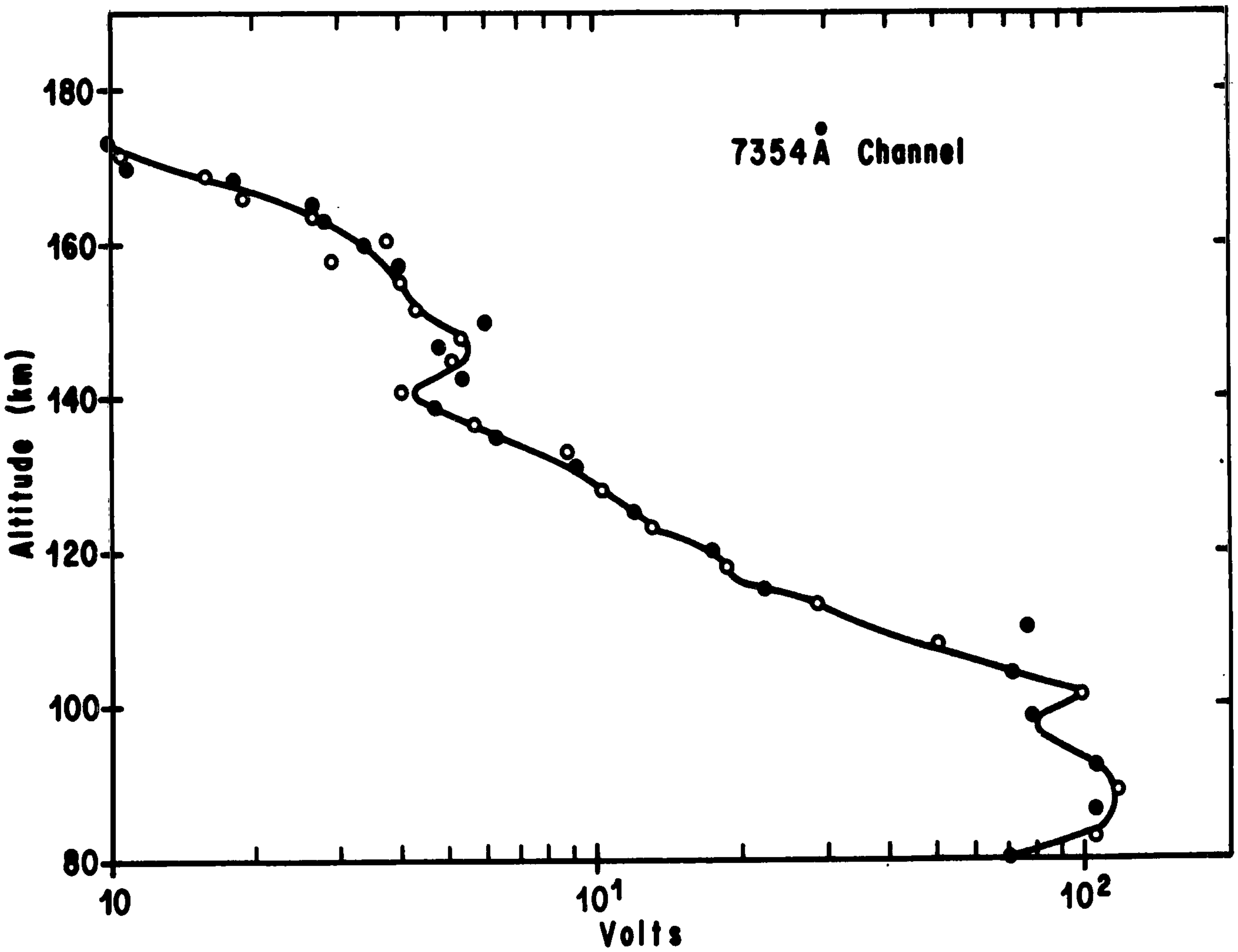

Figure 39. Altitude versus channel voltage for the 7354Å channel for NASA 4.329. See Figure 38.

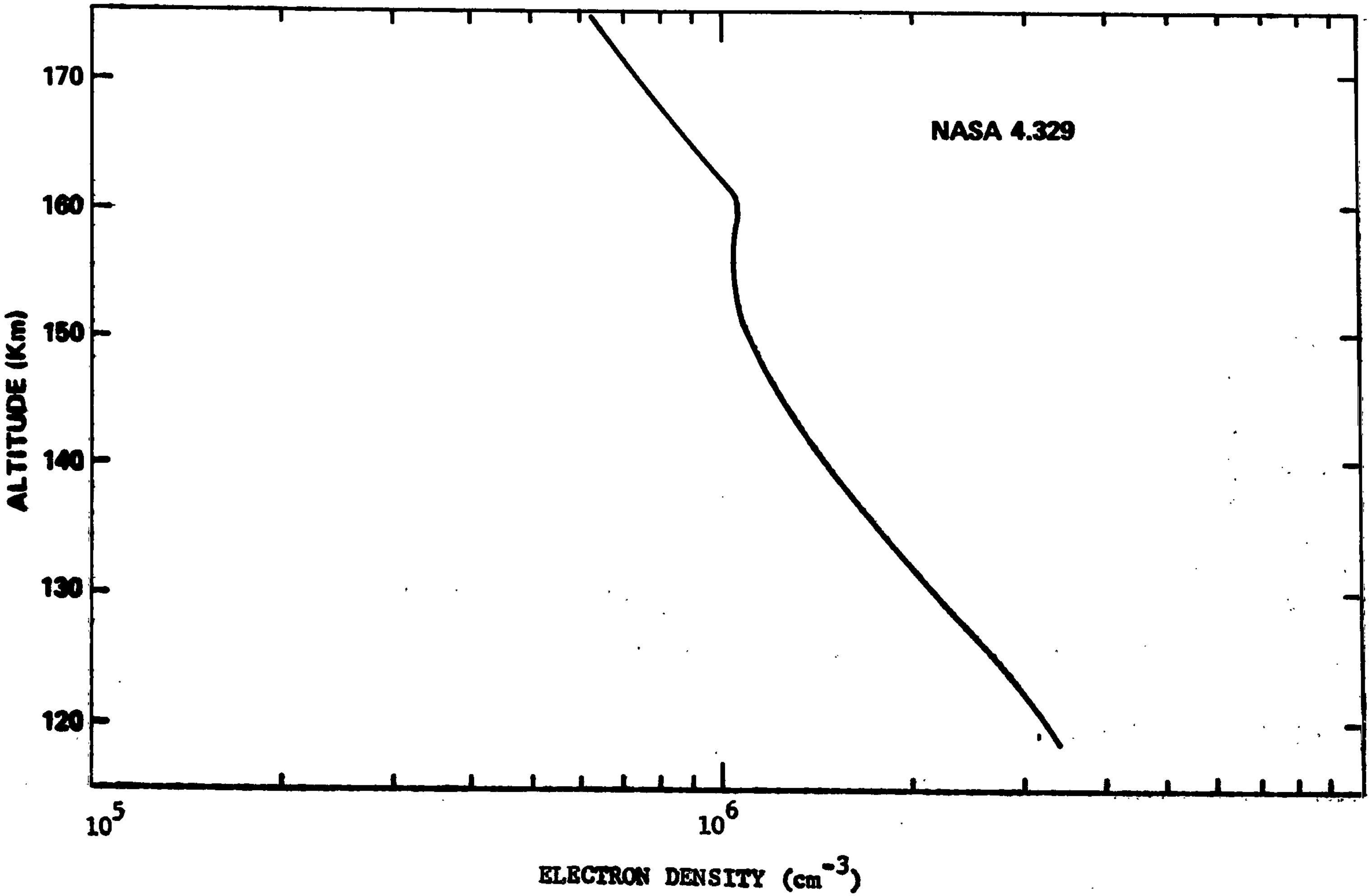

Figure 40. Electron density versus altitude deduced from a Langmuir probe on NASA 4.329.

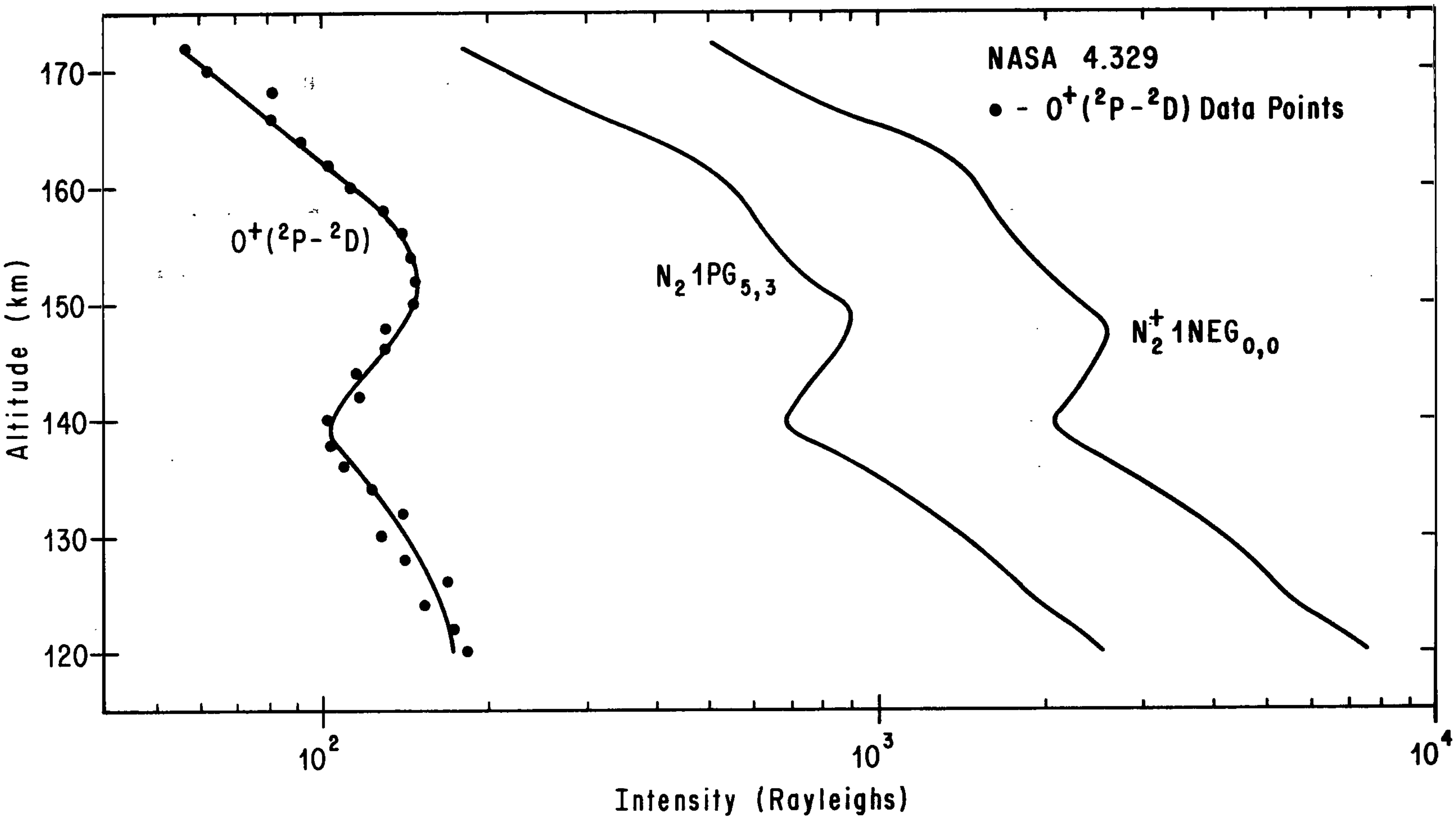

Figure 41. Altitude versus intensity of $O^+(^2P\text{-}^2D)$, $N_2\,1PG_{5,3}$, and $N_2^+1NEG_{0,0}$ as measured on NASA 4.329.

8.4 A DISCUSSION OF THE I1PG AND I1NEG INTENSITY RATIOS FROM NASA 4.329

Before going into the analysis of $O^+(^2P)$ continuity theory and deduction of the quenching and production efficiency coefficients, a brief discussion of the nitrogen emissions will follow.

Plotted in Figure 42 is the intensity ratio observed on NASA 4.329 which is shown to change very little over the altitude range of measurement. The measured data (point plots) were hand fit with a straight line (dashed curve) which is drawn at a ratio of .34. The data deviated very little from this and the scatter seen is most probably measurement noise rather than actual ratio changes.

A measurement summary of this ratio was discussed by Shemansky et. al. (1972) with respect to energy distributions of auroral electrons. The author speculates that the reason previous investigators have observed this ratio to change with altitude in aurora is due to misinterpretation of N_2 1PG photometer data. The temperature dependence of the band shape and the manner in which band shape alters effective filter transmission must be considered for proper interpretation of this photometer measurement.

Examination of electron impact ionization cross sections leading to the N_2^+1NEG emissions (as reviewed by Kieffer and Dunn, 1966, and Green et. al., 1973) show threshold energies of ~ 19ev with maximum ionization efficiency at energies ~ 100ev. The threshold for creating the $B^3\pi_g$ state of N_2 is ~ 7ev and the excitation cross section peaks at ~ 20ev (Green et. al., 1973).

Opal et. al. (1971) have studied the energy distribution and angular dependence of secondary electrons generated by the impact of 100-200ev electrons for a number of gases including N_2. They found that the average energy of the secondaries for the impact energy range used was ~ 13ev and the distribution was fairly insensitive to the energy of the impact electrons (primaries).

The number of secondaries is of course directly related to the number of electron impact ionizations on the ambient amtospheric constituents. The number of $N_2^+1NEG_{0,0}$ photons is directly proportional to the N_2 ionization rate and the number of secondaries produced. Since the energy distribution of the secondaries doesn't vary with the energy of the primaries and presuming the secondaries are the source of $N_2B^3\pi_g$ state, the N_2 1PG emission intensity should be directly proportional to $N_2^+1NEG_{0,0}$ as observed here.

8.5 COMPARISON OF NASA 4.329 DATA WITH PREVIOUS THEORY

The intensity measurements versus altitude provide another data source to add to the picture begun in the last chapter with the ground based measurements. In Figure 34 of the previous chapter there were plots of two theoretical I_{7319}/I_{4278} versus altitude

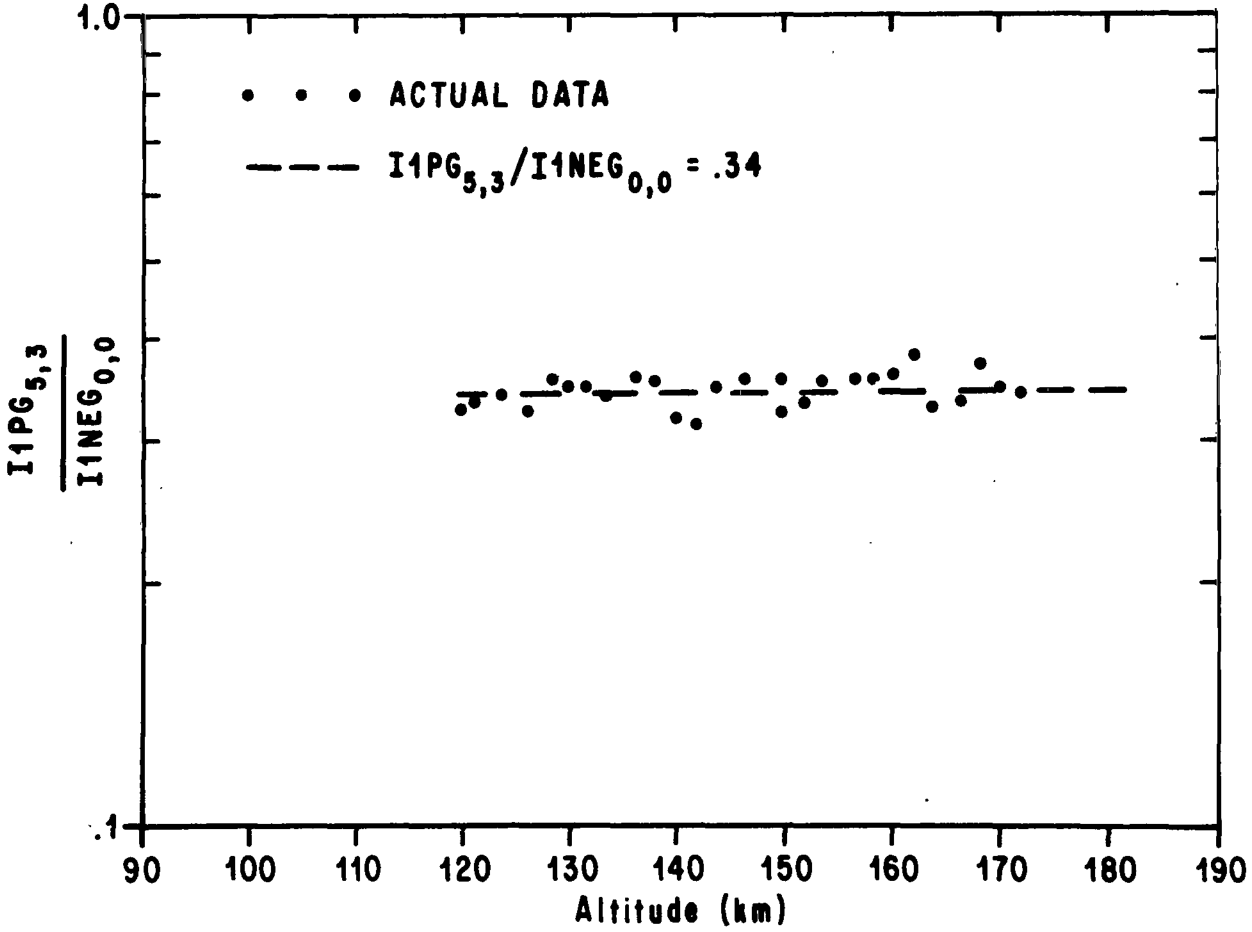

Figure 42. Ratio of $I1PG_{5,3}/I1NEG_{0,0}$ versus altitude for NASA 4.329.

and ground based data. NASA 4.329 measured $I_{7319\text{-}30}$ and I_{3914} values as a function of altitude. The appropriate branching ratios (discussed in the last chapter and Appendix C) were applied to NASA 4.329 data to interpret the I_{7319}/I_{4278} 'measured' ratio. The x's in Figure 43 represent this new addition of measured values. This rocket payload measurement agrees quite well with the ground based measurements but deviates significantly from the theoretical curves. Furthermore, the error analysis discussed in Appendix G suggests the error in the measurement is least at the higher altitudes where the theoretical ratio predictions are in large disagreement with the measurement.

8.6 THEORETICAL EXPLANATIONS OF THE AURORAL $I_{7319}/_{4278}$ MEASUREMENTS

The basic formulation for generating the theoretical ratio curves of Figure 43 was Equation (86) as developed in the previous chapter i.e.,

$$\frac{I_{7319}}{I_{4278}} = \frac{R_{\sigma_1}(E)}{n[N_2]\,H_{N_2}} \int_z^{\infty} n[OI] \left\{ \frac{.098}{.219 + \sum_i \gamma_i\, n[i]} \right\} dz \tag{86}$$

where the values for parameters previously discussed were taken from historical findings and a model atmosphere. To review, Curves B and C of Figure 43 were generated using values of $3{\cdot}10^{-8}$ for γ_e and $1{\cdot}10^{-10}$ for γ_{N_2} for Curve B and $2{\cdot}10^{-7}$ for γ_e, $2{\cdot}10^{-10}$ for γ_O and $5{\cdot}10^{-11}$ for γ_{N_2} for Curve C.

Fundamentally, there are two basic disagreements between 'old' and 'recent' theories and measurements depicted in Figure 43. The theoretical shapes of the ratios with altitude suggest a larger change or larger slope over the altitude range than the data. Examination of (86) suggests that the ratio changes as a result of two possibilities. If all γ_i were zero, the integral would reduce to $n[OI]_z \cdot H_0$, thus setting a lower limit on the altitude dependence of the ratio to approximately the $N[OI]/n[N_2]$ ratio. Finite values for γ_i tend to increase the ratio change with altitude.

Secondly the magnitude of the ratio predicted by theory is much larger than measured, particularly at the upper altitudes where the measurement is least in error (Table 2-G). Assuming that the error in the emission probabilities and model atmosphere parameter errors are small, the $R_{\sigma_1}(E)$ parameter (cross section ratios) requires examination. Of the product ratios involved in this factor (Chapter 6), only one, $\sigma_{O^{+2}P}(E)/\sigma_{O^+}(E)$ is not both theoretically and experimentally verified. A departure from the Seaton (1959) ratio of .2 for this branching ratio will be necessary to theoretically predict the lower ratios of I_{7319}/I_{4278} observed in these measurements.

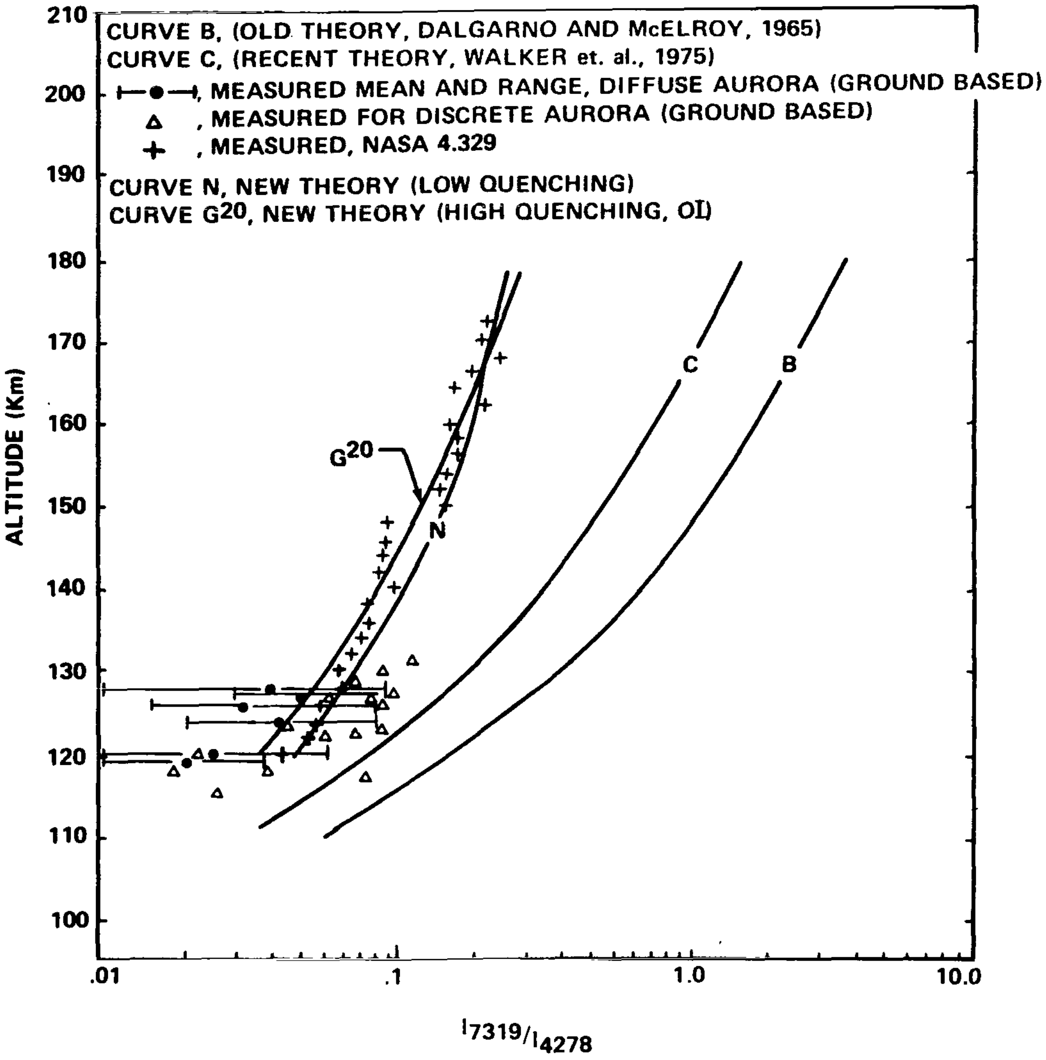

Figure 43. Altitude versus I_{7319}/I_{4378}. The plot includes two previous theories (discussed with Figure 34) two new theory curves and the ground based and rocket measurements of I_{7319}/I_{4278}. The particulars of the figure are discussed in the text.

A pictorial evolution of several theoretical possibilities will begin with the NASA 4.329 measured ratio of Figure 43 replotted in Figure 44. The solid line through the data (D) is a hand drawn fit of the data and the error flags represent the non-systematic error of I_{7319} described below. The error bar reflects the assumption that all the uncertainty in the ratio lies in the uncertainty in the I_{7319} measurement. The non-systematic errors were a result of the root summed square of the statistical error and the error component in the first four columns of Table 2-G, which exceeded those systematic errors at the top of the profile. The filter drift error, for instance, was not treated as a non-systematic error. It was assumed that if the filter peak drifted between calibration and the measurement time, the filter stayed shifted for the measurement period and was considered systematic to the entire profile. The calibration error, however, varied from ±36% at 120 km to ±24% at 160 km. If the measurement was a single measurement and not a deconvolution, these errors would be constant, or also systematic with altitude. The component of 12% at 120 km for the calibration table then was also treated as a total shape error component or non-systematic error.

It should be noted at this point, also, that all the theoretical synthesis from this point on involved a synthesis of the measured profile of I_{7319}/I_{4278} from NASA 4.329. In the theoretical treatment, the measured electron density (Figure 40) was used rather than the $1 \cdot 10^{+6}$ cm^{-3} assumed in the last chapter as it applied to Equation 86.

8.6.1 THEORY 1, THEORY OF 'LOW QUENCHING'

The first approach was to ignore early theories as to the quenching rate of $O^+(^2P)$, as well as the $\sigma_{O^{+2}P}(E)/\sigma_{O^+}(E)$ branching ratio. Instead, these parameters were iterated until a combination was found which would put theory and measurement in agreement. It was felt by the author that lower limits on quenching should exist for 'well established' or well understood processes. It was assumed that γ_e could not be less than $3 \cdot 10^{-8}$ and that γ_{N_2} could not be less than $2 \cdot 10^{-12}$. The minimum was postulated since the additional internal energy associated with $O^+(^2P)$ would not decelerate the rate of dissociative recombinate over the established $O^+(^4S)$ rate of $2 \cdot 10^{-12}$ (Chapter VI).

The first step involves taking the theoretical curve B of Figure 43 and reducing the $\sigma_{O^{+2}P}(E)/\sigma_{O^+}(E)$ branching ratio until it was normalized to the data curve at 170 km. This is shown as curve E on Figure 44 and is not within the confines of the error of the measurement. The branching ratio was reduced from the .2 value of Seaton to .018 for this normalization.

The next step was to normalize the curve to the extreme ratio upper limit at the upper altitude (170 km) and to decrease the N_2 quenching until the lower part of the curve was in the error limit of the data. This profile was generated by an N_2 quenching rate of $1 \cdot 10^{-11}$ and a branching ratio of .010 (γ_e was assumed at $3 \cdot 10^{-8}$). This is plotted as curve F in Figure 44. By using a value for γ_{N_2} of $2 \cdot 10^{-12}$, γ_e of $3 \cdot 10^{-8}$, and a branching ratio of .008, the theoretical profile becomes almost identical to that of Curve D, the hand fit data curve.

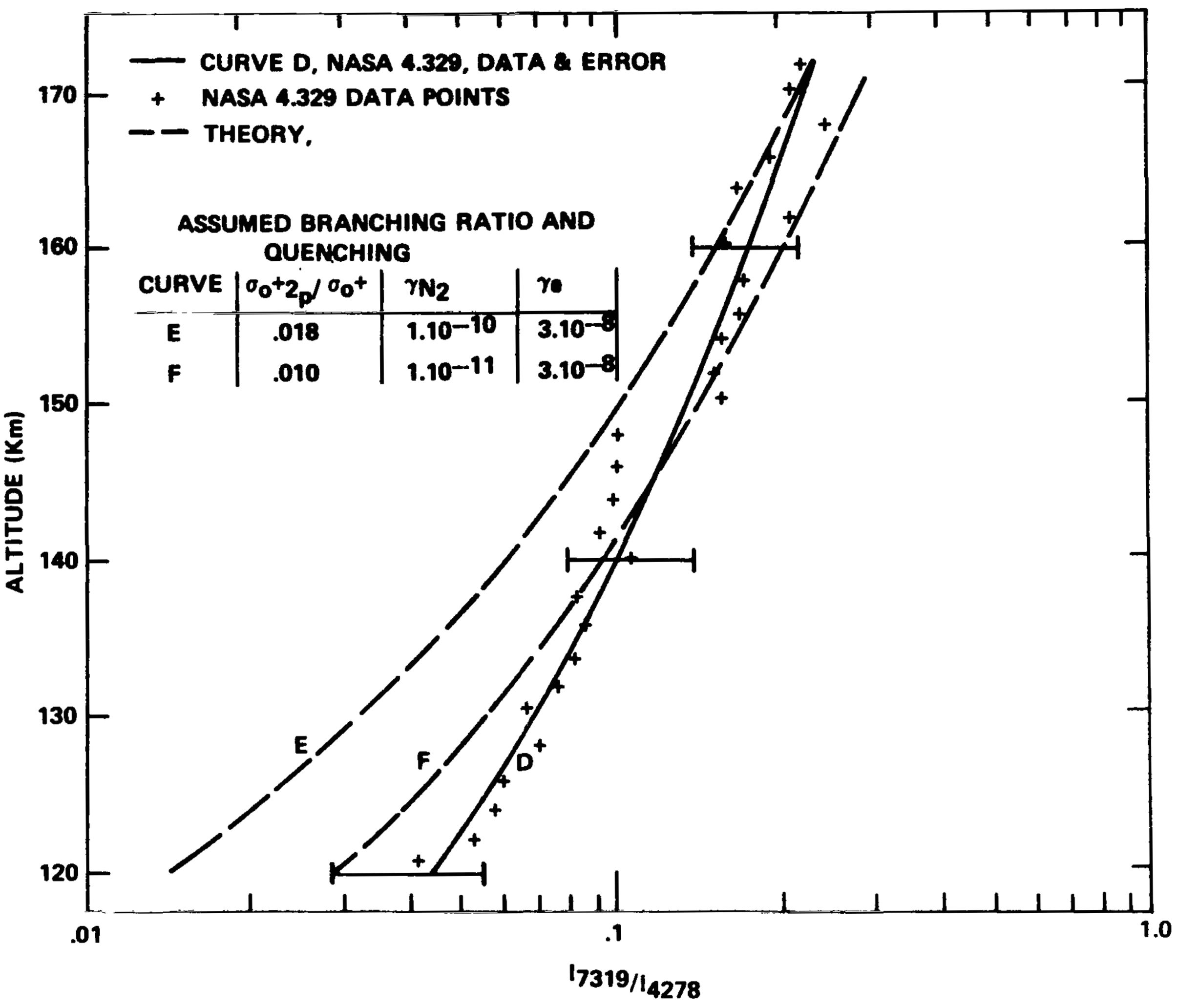

Figure 44. Altitude versus I_{7319}/I_{4278}. The data from NASA 4.329 and two theoretical curves are plotted showing the effects of altering $\sigma_{O^{+2}P}(E)/\sigma_{O^+}(E)$ and γ_{N_2} of early theories.

In summarizing, the above analysis suggests that the error limits on the data curve confine or define the following:

$\sigma_{O^{+2}P}(E)/\sigma_{O^+}(E) = .008$	Most probable
$> .005, < .10$	Extremes
$\gamma_e = 3 \cdot 10^{-8}$	Assumed
$\gamma_{N_2} = 2 \cdot 10^{-12}$	Most probable
$< 1 \cdot 10^{-11}$	Extreme

The most probable values above were applied to Equation (86) to generate Curve N of Figure 43, which represents one possible combination of parameters in the theory that describes the data.

The above combination is one possibility, but a recent analysis of data reported by Walker et. al. (1975) strongly suggests that large quenching is required of $O^+(^2P)$ to explain intensity measurements of 7319Å emission on Atmospheric Explorer Satellite in dayglow. Examination of curve E on Figure 44 which represents large quenching by N_2 does not fall in the error bars of the measurement. The only remaining possibility is that Equation (86) is not complete and that there possibly exists another production mechanism for $O^+(^2P)$ that has not been considered.

8.6.2 THEORY 2, LARGE QUENCHING AND $N^+(^1S)$ PRODUCTION OF $O^+(^2P)$

Many other possible production schemes were considered, such as direct dissociation of the O_2 by electron impact, but only one appears to be potentially large enough at low altitude to overcome large collisional deactivation. Torr (1975) suggested that

$$N^+(^1S) + O(^3P) \rightarrow N + O^+(^2P) \qquad (87)$$

could possibly occur at a near kinetic rate. It was assumed here that for every $N^+(^1S)$ produced, an $O^+(^2P)$ was also produced.

At what rate might $N^+(^1S)$ be produced in aurora? Jones and Rees (1973) give a rate of N^+ production as related to the N_2^+ volume production rate as:

$$\eta(N^+)_P = \frac{\sigma_{N^+}(E)}{\sigma_{N_2^+}(E)}\,\eta(N_2^+) \qquad (88)$$

where $\sigma_{N^+}(E)/\sigma_{N_2^+}(E)$ was estimated at .25. Next, the volume production rate of N_2^+ is related to the λ3914Å volume emission rate by

$$\eta(N_2^+)_P = \frac{\sigma_{N_2^+}(E)}{\sigma_{N_2^{+*}}(E)}\,\eta(3914\text{Å}) \tag{89}$$

(See chapter VI). To the author's knowledge, the branching ratio for producing $N^+(^1S)$ to N^+ is unknown (i.e., $\sigma_{N^{+1}S}(E)/\sigma_{N_2^+}(E)$). The $\sigma_{N_2^+}(E)/\sigma_{N_2^{+*}}(E)$ was discussed in Chapter VI. To further simplify, Equations (88), (89) and the $N^+(^1S)$ to N^+ branching ratios may be combined to give:

$$\frac{\eta(N^{+1}S)_P}{\eta(3914\text{Å})} = \frac{\sigma_{N^{+1}S}(E)}{\sigma_{N^+}(E)} \cdot \frac{\sigma_{N^+}(E)}{\sigma_{N_2^+}(E)} \cdot \frac{\sigma_{N_2^+}(E)}{\sigma_{N_2^{+*}}(E)} \quad . \tag{90}$$

It was further assumed above that $N^+(^1S)$ immediately reacted to produce an $O^+(^2P)$. The new production source of $O^+(^2P)$ may be written, using historical values for the known branching ratios, as

$$\eta(O^{+2}P)_P = C_{\sigma_0}(E) \cdot \eta(3914\text{Å}) \tag{91}$$

or as

$$\eta(O^{+2}P)_P = C_{\sigma_1}(E) \cdot \eta(4278\text{Å}) \tag{92}$$

where $C_\sigma(E)$ is the cross section ratio product of Equation (90), where the subscript refers to the upper vibrational level of $N_2^+B^2\Sigma_+^u$.

Next is a cursory comparison of the combined production terms (i.e., the charge exchange process described above and the electron impact source treated earlier). The total production term may be obtained by summing the above source (Equation 92) with the electron impact source (Equation 73) to read

$$\eta(O^{+2}P)_P = R_{\sigma_0}(E)\,\frac{n[OI]}{n[N_2]}\,\eta(4278\text{Å}) + C_{\sigma_1}(E)\,\eta(4278) \quad . \tag{93}$$

In the model atmosphere used in this study, the $n[OI]/n[N_2]$ ratio is ~ 1 at 160 km. For the historical value of 4.65 for $R_{\sigma_1}(E)$ a branching ratio of .4 for $\sigma_{N^{+1}S}(E)/\sigma_{N^+}(E)$ would make the two production sources equal. The other cross section ratios making up $C_{\sigma_1}(E)$ have been previously discussed. Since $n[OI]/n[N_2]$ increases with altitude, the charge exchange mechanism becomes even more dominant at lower altitudes.

Another way of writing (93) involves isolating the volume emission rate, i.e.,

$$\eta(O^{+2}P)_P = \left(R_{\sigma_1}(E)\,\frac{n[OI]}{n[N_2]} + C_{\sigma_1}(E)\right)\eta(4278\text{Å}) \tag{94}$$

where

$$C_{\sigma_1}(E) \simeq 11.5\,\frac{\sigma_{N^{+1}S}(E)}{\sigma_{N^+}(E)} \quad . \tag{95}$$

The continuity equation of $O^+(^2P)$ in Chapter VI can now be rewritten using Equation (94) above for the production equation, i.e.,

$$\left(R_{\sigma_1}(E)\,\frac{n[OI]}{n[N_2]} + C_{\sigma_1}(E)\right)\eta(4278\text{Å}) = .219\,n[O^{+2}P] + \sum_i \gamma_i\,n[i]\,n[O^{+2}P] \quad . \tag{96}$$

This reduces to a volume emission ratio of the form

$$\frac{\eta(7319\text{Å})}{\eta(4278\text{Å})} = \left\{R_{\sigma_1}(E)\,\frac{n[OI]}{n[N_2]} + C_{\sigma_1}(E)\right\}\left\{\frac{.098}{.219 + \sum_i \gamma_i\,n[i]}\right\} \tag{97}$$

or in the integral form as:

$$\frac{I_{7319}}{I_{4278}} = \frac{R_{\sigma_1}(E)}{n[N_2]\,H_{N_2}} \int_z^\infty n[OI]\left\{\frac{.098}{.219 + \sum_i \gamma_i\,n[i]}\right\} dz + \frac{C_{\sigma_1}(E)}{n[N_2]\,H_{N_2}} \int_z^\infty n[N_2]\left\{\frac{.098}{.219 + \sum_i \gamma_i\,n[i]}\right\} dz \quad . \tag{98}$$

Expressions (97) and (98) follow the identical derivations (80) and (86) did in Chapters VI and VII.

Next, the quenching rates of Walker et. al. (1975) were assumed correct. First, it was assumed that $\gamma_O = 2{\cdot}10^{-10}$ and $\gamma_{N_2} = 5{\cdot}10^{-11}$. It was also assumed that $\gamma_e = 2{\cdot}10^{-7}$ (Henry et. al., 1969). The uncertainties in the two branching ratios, i.e., $\sigma_{O^{+2}P}(E)/\sigma_{O^+}(E)$ in $R_{\sigma_1}(E)$ and $\sigma_{N^{+1}S}(E)/\sigma_{N^+}(E)$ in $C_{\sigma_1}(E)$ remain as variables.

Plotted in Figure 45 is the hand drawn data curve and error bars as described for Figure 44. Also plotted are three theoretical curves using the quenching rates of Walker et. al. (1975) and Henry et. al. (1969) where the $N^+(^1S)$ branching ratio was assumed as .05, .10, and .20 for G^5, G^{10}, and G^{20} respectively. For each assumed $N^+(^1S)$ branching ratio, an $O^+(^2P)$ branching ratio was computed such that the theoretical curve was normalized to the data at 170 km. The required $O^+(^2P)$ branching ratio for each curve is indicated on the curve table in the figure. It is noted that if curve G^5 were shifted to the right error limit at 160 km, the lower portion would fall at the left error limit at the 120 km altitude. A branching ratio of .05 for $\sigma_{N^{+1}S}(E)/\sigma_{N^+}(E)$ is therefore a minimum acceptable rate for this quenching combination according to these limits. It should be added that a branching ratio of .24 for $N^+(^1S)$ requires that the $\sigma_{O^{+2}P}(E)/\sigma_{O^+}(E)$ branching ratio is zero for 170 km synthesis of the measured I_{7319}/I_{4278} ratio. Thus, an upper limit of $\sigma_{N^{+1}S}(E)/\sigma_{N^+}(E)$ of .24 is established for this quenching combination. Curve G^{20}, which closely parallels the data, has been plotted in Figure 43 for overall measurement comparison.

Walker et. al. (1975) also suggested that a value for γ_{N_2} of $5{\cdot}10^{-10}$ and zero OI quenching would describe their data. A similar analysis was accomplished for the above quenching combination as was done for the previous combination. The results are plotted in Figure 46. Analogous to the previous discussion, only Curve H^{20} can be shifted to fall in the error limits of the data, establishing a lower limit of $\sigma_{N^{+1}S}(E)/\sigma_{N^+}(E)$ at .20 for this quenching combination. A value of .23 for $\sigma_{N^{+1}S}(E)/\sigma_{N^+}(E)$ required $\sigma_{O^{+2}P}(E)/\sigma_{O^+}(E)$ to be zero at 170 km synthesis of the I_{7319}/I_{4278} ratio. The upper limit for $\sigma_{N^{+1}S}(E)/\sigma_{N^+}(E)$ is therefore .23.

8.7 DISCUSSION OF THEORETICAL COMBINATIONS

In the previous sections, discussion has surrounded three possible quenching combinations, all of which fall within the error limit of the measurements. In each case there are limits on two branching ratios which have not been previously verified by experimental measurement. The extremes and most probable values for these branching ratios are tabulated in Table 5.

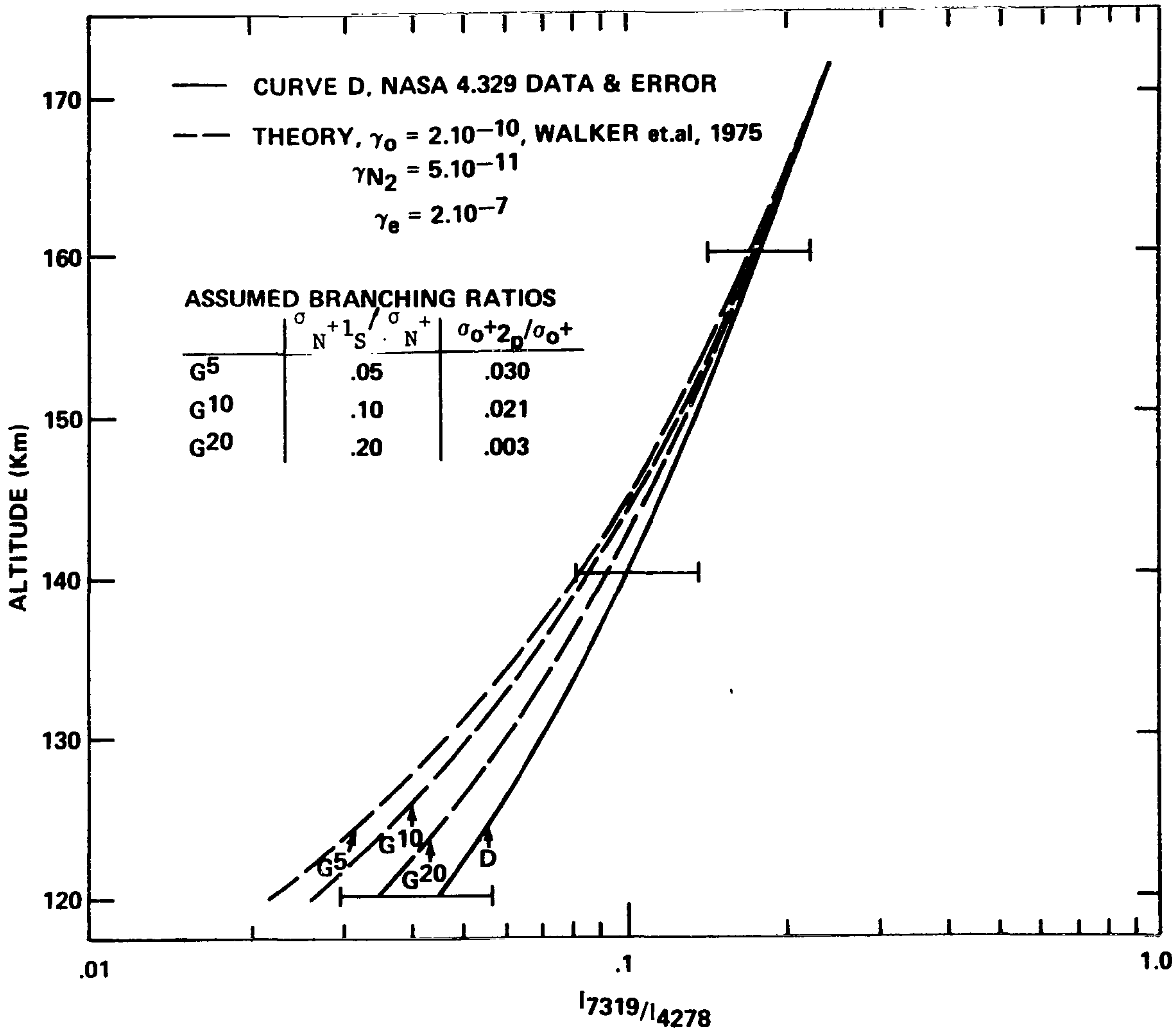

Figure 45. Altitude versus I_{7319}/I_{4278}. Same as Figure 44 except the theoretical curves show the effect of $N^+(^1S)$ production efficiency for the "Large Quenching, OI" model.

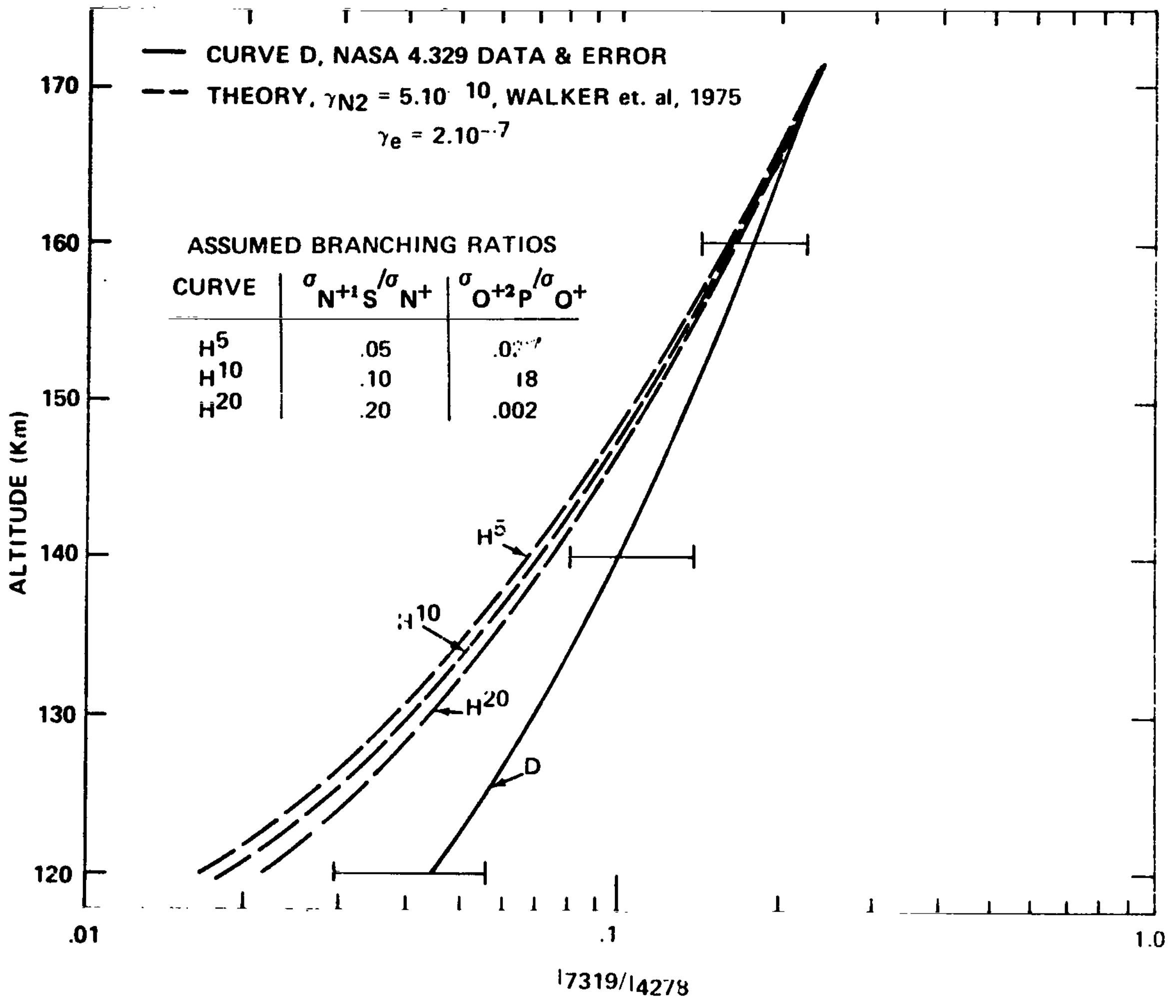

Figure 46. Same as Figure 45 except the theoretical curves show the effect of $N^+(^1S)$ production efficiency for the "Large Quenching, N_2" model.

TABLE 5. SUMMARY OF THEORETICAL COMBINATIONS DESCRIBING $O^+(^2P)$ CONTINUITY IN AURORA

Theory	$\frac{\sigma_{N^{+1}S}(E)}{\sigma_{N^+}(E)}$	Max Most Probable Min	$\frac{\sigma_{O^{+2}P}(E)}{\sigma_{O^+}(E)}$	Max Most Probable Min
Low Quenching $\gamma_{N_2} = 2 \cdot 10^{-12}$ $\gamma_e = 3 \cdot 10^{-8}$ (assumed)	.04		.010	
	0		.008	
	0		.005	
High Quenching, OI $\gamma_O = 2 \cdot 10^{-10}$ $\gamma_{N_2} = 5 \cdot 10^{-11}$ $\gamma_e = 2 \cdot 10^{-7}$ Walker et. al. (1975) and Henry et. al. (1969)	.24		.030	
	.24		0	
	.05		0	
High Quenching, N_2 $\gamma_{N_2} = 5 \cdot 10^{-10}$ $\gamma_e = 2 \cdot 10^{-7}$ Walker et. al. (1975) and Henry et. al. (1969)	.23		.003	
	.23		0	
	.20		0	

The low quenching case essentially did describe the data with a single production source by electron impact (See Curve N on Figure 43). A very low branching ratio for $N^+(^1S)$ produced an additional source of $O^+(^2P)$ at low altitude beyond the error limit. The limits of $\sigma_{O^{+2}P}(E)/\sigma_{O^+}(E)$ given in Table 5 produce theoretical I_{7319}/I_{4278} ratios at the error extremes of the data.

In the 'high quenching, OI' case, a range of .05 to .24 was deemed acceptable according to the earlier discussion surrounding Figure 45. It was noted that even the .20 branching ratio curve (G^{20} of Figure 45) did not totally fit the data curve. If the charge exchange production mechanism completely dominated over electron impact, the theoretical curve would bend closer to the measured curve at the lower altitudes.

The 'high quenching, N_2' theory required a large efficiency in $\sigma_{N^{+1}S}(E)/\sigma_{N^+}(E)$ to even skirt the error bars as discussed in relation to Figure 46. Even with all production due to the $N^+(^1S)$ mechanism, the criteria of falling in the measurement error is not met. The author feels this mechanism is least likely.

In summarizing the investigation then, some conclusions can be drawn. First, in all theories, the upper limit acceptable for the branching ratio $\sigma_{O^{+2}P}(E)/\sigma_{O^+}(E)$ is .030. This is significantly lower than the values proposed by Seaton (1959) and Kazaks et. al. (1972) of .2 and .25 respectively. It has further been postulated that this ratio could be zero if large quenching does exist. Secondly, an upper limit of .24 has been established for $\sigma_{N^{+1}S}(E)/\sigma_{N^+}(E)$ considering all three theories, with a lower limit of zero. Once the quenching rates have been truly established, the bounds on the branching ratios can be narrowed.

A puzzle remains. Why should the efficiency for producing $O^+(^2P)$ by electron impact be at least a factor of 7 lower than the .2 value deduced by Seaton (1959)? This is especially puzzling since Walker et. al. (1975) were successful in describing the dayglow satellite measurement with a branching ratio comparable to Seaton's. Lassetre (1969) suggests that differences in cross sections do exist for photon interaction versus electron impact in several molecular systems. It is difficult to understand why the difference here described is so large.

8.8 A RE-EXAMINATION OF EARLY MEASUREMENTS

The previous section contined discussion of several theoretical possibilities which describe the I_{7319}/I_{4278} ratio measurements. It has been shown in this discussion that high quenching of $O^+(^2P)$ as proposed by the Walker et. al. (1975) measurement can describe $O^+(^2P)$ continuity balance in aurora, provided the electron production efficiency for producing $O^+(^2P)$ is reduced from the .20 value of Seaton (1959), and an additional low altitude source mechanism, such as $N^+(^1S)$ charge exchange, is introduced. Yet unexplained is why Gerard (1971) concluded that the low altitude source was not present and that reduced electron impact was not necessary to explain early auroral observations. Many of the historical observations of these emissions have been accomplished from ground observatories. Historically, spectrometers from these ground stations viewed distant arcs and discerned altitudes of maximum emission of the respective emissions. To re-examine these ground based measurements it would be useful to plot a volume emission rate profile of the λ7319Å and λ4278Å emissions for a typical aurora as predicted by these theories. Since these early measurements viewed the aurora nearly perpendicular to the magnetic field rather than the magnetic zenith, it was assumed that the ratio measurements reflect volume emission ratios.

Plotted in Figure 47 are two curves which approximate the relative volume emission – altitude relationship of the two emitting species, $O^+(^2P)$ and $N_2^+B^2\Sigma_u^+$. The η(4278Å) profile was assumed as being the N_2-proportional type discussed in Appendix F. That is, the η(4278Å) emission was defined proportional to above 120 km, and zero below. Equation (80) of Chapter VI was used to generate the η(7319Å) profile with the most probable values of the 'Low Quenching' theory of Table 5 as input parameters. The 'High Quenching, OI' theory with most probable values of Table 5 predicts a nearly identical profile for η(7319Å). The important point to be stressed is the volume emission peak for η(7319Å) lies very low (~ 135 km in this case). A volume emission peak of ~ 220 km is predicted by Gerard (1971) using the Seaton (1959) value of .2 for $\sigma_{O^{+2}P}(E)/\sigma_{O^+}(E)$ and large N_2 quenching with no additional $O^+(^2P)$ source other than electron impact on OI.

Plotted in Figure 48 are volume emission ratios – altitude relationships for the 'Old Theory' ($\gamma_{N_2} = 1.10^{-10}$, $\gamma_e = 3.10^{-8}$) verified by Gerard (1971) and a new theory. The new theory plotted is the low quenching model although, as discussed earlier, the 'High Quenching, OI' (Most probable, Table 5) theory now predicts a near identical profile. The curves were generated using the reciprocal of Equation (78) with the input parameters reflected by the previously discussed quenching and $\sigma_{O^{+2}P}(E)/\sigma_{O^+}(E)$ efficiencies.

To culminate this study, reference is made to the early measurements and speculation as to why the high efficiency and quenching rate were verified by Gerard (1971) and others, especially in light of the Wallace (1960) data.

Jones (1971) mentioned that the OII Auroral lines were at least three times the intensity of the N_2 1PG$_{5,3}$ band for the Jones' (1960) spectra of the February 10/11, 1958, aurora. A relative intensity of 2.8 at λ7384Å was reported for the spectra measured with an instrument containing a 5.2Å instrument function.

A 5.2Å triangular slit function peaked at λ7384Å was passed through the N_2 1PG band model, previously described, with a rotational temperature of 700°K. This resulted in a determination of the percentage of the band intensity measured at the quoted

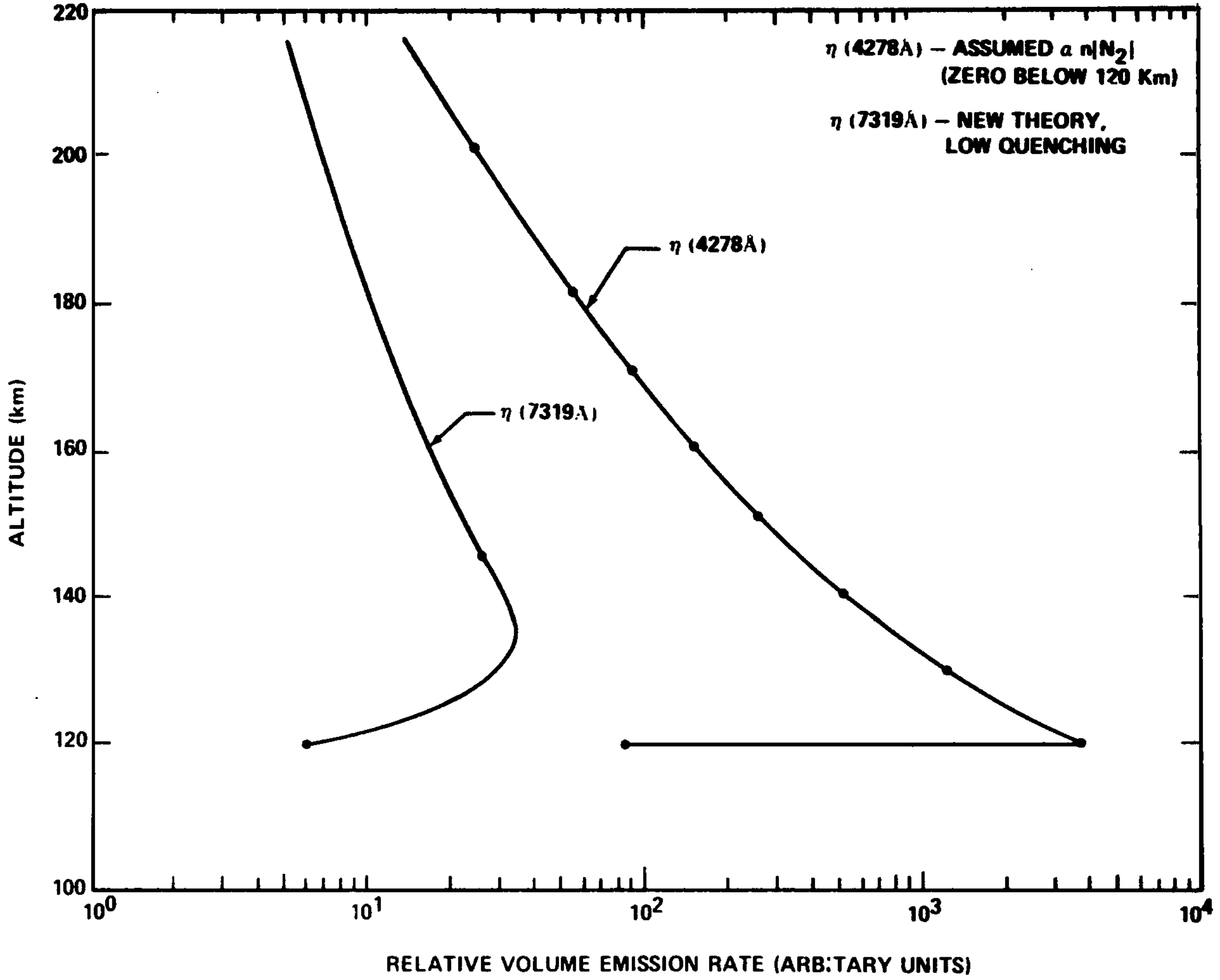

Figure 47. Altitude versus relative volume emission rates of η(7319Å) and η(4278Å) assumed as a typical aurora. The η(4278) is proportional to n[N_2] to 120 km and zero below. η(7319Å) was produced by a new model (Low Quenching, Table 5).

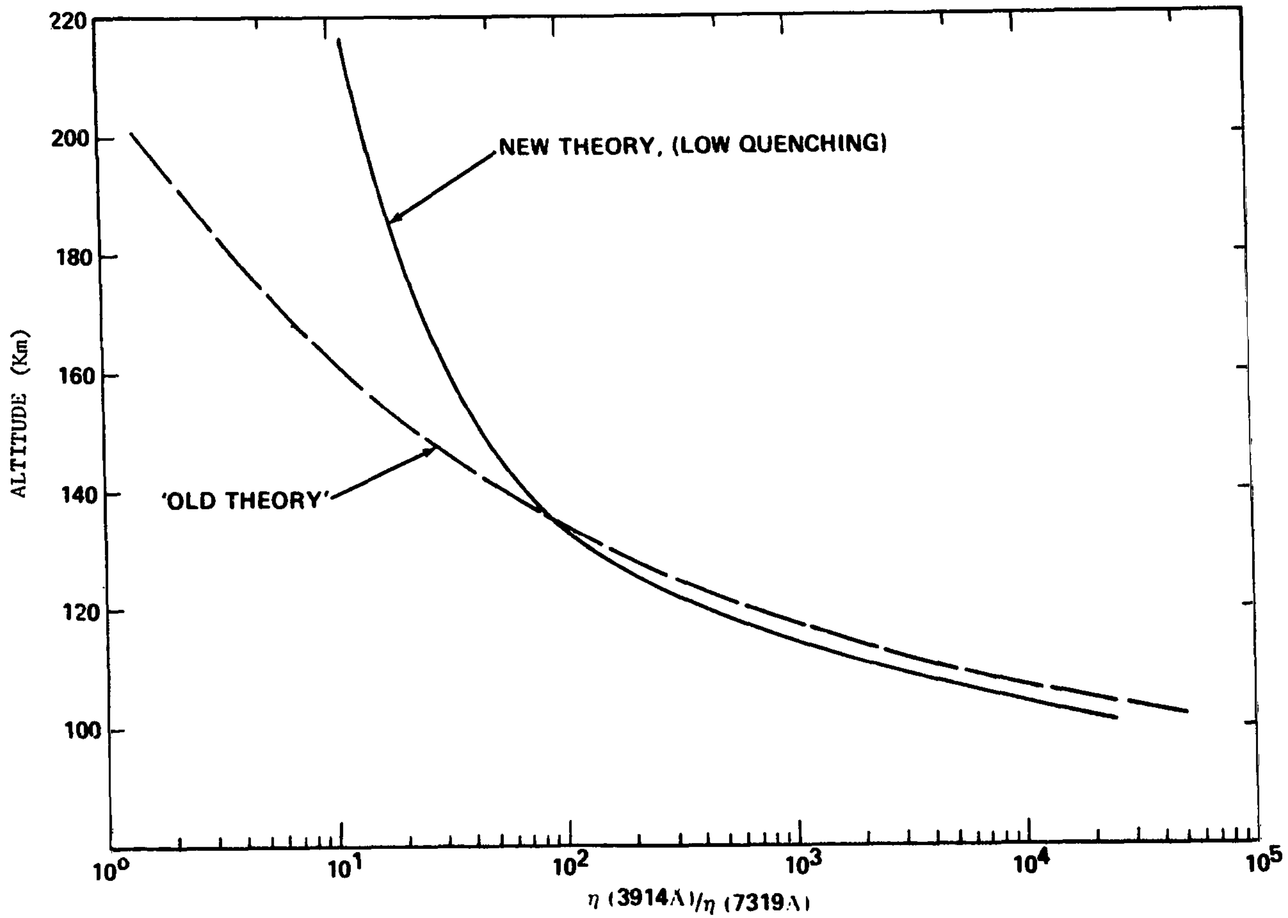

Figure 48. Altitude versus $\eta(3914Å)/\eta(7319Å)$ for the "Old Theory" ($\sigma_{O^{+2}P}(E)/\sigma_{O^+}(E) = .2$ and $\gamma_{N_2} = 10^{-10}$) and a new model (Low Quenching, Table 5). This figure is meant to aid in interpreting early ground based spectroscopic measurements.

wavelength and amounts to ~ 5% of the total N_2 $1PG_{5,3}$ band intensity. This would infer that the relative intensity of N_2 $1PG_{5,3}$ was 56 resulting in an $\eta(7319)/\eta(7387)$ of .3. Jones (1971) suggested the doublet was three times the intensity of N_2 $1PG_{5,3}$ for the same data but the above analysis disputes this. It was pointed out in the rocket data analysis earlier that $I1NEG_{1,0}/I1PG_{5,3}$ was ~ 1 at all altitudes, which would infer that $\eta(1NEG_{1,0})/\eta(1PG_{5,3})$ should also be one. This would mean that the interpretation of the Wallace (1960) data would correspond to a $\eta(7319)/\eta(4278)$ of .3, or $\eta(3914)/\eta(7319)$ of ~ 11. From examination of Figure 48, the 'Old Theory' would suggest a corresponding altitude of ~ 150 km. For the 'New Theory' of the same figure, the altitude indicated would be near 220 km. As pointed out earlier, Jones (1971) classified this type of aurora as having a lower border of ~ 250 km.

The main argument given by Gerard (1971) for observational verification of his volume emission rate theory of OII Auroral emissions was Omholt's ratio of .1 for $\eta(7319\text{-}30)/\eta(5577)$ as measured in the upper portions of a spectrograph taken in 1957. As reviewed by Jones (1971), the green line to N_2^+ $1NEG_{0,0}$ ratios are believed to be in the neighborhood of two. This inference leads to $\eta(3914)/\eta(7319\text{-}30)$ of 5 or $\eta(3914)/\eta(7319)$ ~ 8.3. Again, examination of Figure 48 suggests ~ 170 km for the 'Old Theory', and the 'New Theory' would correspond to ~ 235 km. It is difficult to speculate how high Omholt's 'upper' portions of aurora were. Spectra exposed to aurora for long time periods is subject to exposure to many different types of auroral displays. The fact that the lower parts of the Omholt spectra showed ratios and intensities similar to several other spectra, where the doublet was not noted, could imply that these types of aurora took place, as well as higher altitude "red" type events during the exposure period of the particular plate.

CHAPTER IX
SUMMARY AND RECOMMENDATIONS FOR FUTURE WORK

The previous eight chapters were dedicated to the description of research performed in two disciplines. Background and early investigations were summarized for both the spatial scanning photometer and auroral $O^+(^2P-^2D)$ emissions in the first chapter.

9.1 SUMMARY OF THE SECTOR SPECTROPHOTOMETER DEVELOPMENT

Chapters II through V discussed the evolution of a unique spatial scanning photometer system.

The second chapter gave the reader an understanding of the theoretical principles of the spatial scanning scheme. This was accomplished with a simplified half-width treatment rather than with analytic transmission functions. This chapter concluded that theoretically, at any rate, a rotating spiral slit could be designed into a photometer system so that the instrument would have many desirable characteristics over other photometers. It was deduced that a scanning aperture could be built which had a near constant throughput and bandpass for all slit positions. It was also recognized that the wavelength scan rate could be made proportional to the rotation rate of the spiral slit and that a continuous wavelength region was accessible for a continuous spiral. In essence, the evolution of an instrument having scanning characteristics of grating type spectrometers with the throughput advantages of flat plate interference elements was possible.

A study of the interference elements both theoretically (Appendix A) and in the laboratory (Chapter II) was required. The purpose of this study was to determine to what angle filters could be pushed from normal (i.e., what wavelengths), to determine filter cone angle effects, and to explore general filter characteristics. The two effects limiting filters in this application were the polarizing effect (more prevalent in low index filters) and a slight low angle broadening of undetermined origin. In Chapter II, the cone angle effect of the filters did impact the characteristics of slit design in striving to achieve a constant instrumental throughput and broadening. All filters were found to differ. The limitations of these elements as they apply to the sector spectrophotometer were covered in this chapter and the noted Appendix.

A single spiral photometer was built and tested in the laboratory to validate the theory described earlier. The development and laboratory analysis were discussed in Chapter IV. It worked!

A more complex device which allowed for more light gathering power at a given resolution was described in Chapter V. This system was designed for ground based measurements of auroral $O^+(^2P-^2D)$ emission. This instrument system included a multi-spiral aperture. Multi-spiral slits can provide two to three times the instrumental throughput over single spiral devices for a given bandpass resolution.

Two disadvantages of the system include the large detector for image capture, which results in more detector noise than would be in, e.g., a tilting photometer system with a fixed field stop. The second disadvantage is that in spatially shifting the aperture and changing the look angle through the filter, the source is also spatially scanned (i.e., a wavelength scan describes an arc in the sky). A large lens imaged at the interference element corrects for this, but does cause some throughput loss.

9.2 SUMMARY OF THE $O^+(^2P$-$^2D)$ IN ELECTRON AURORA

The theory of $O^+(^2P$-$^2D)$ as related to N_2^+1NEG emissions was the subject of Chapter IV. The analysis of ground based data and a rocket payload pertinent to $O^+(^2P$-$^2D)$ analysis were the subjects of Chapters VII and VIII respectively.

In Chapter VI, pertinent cross sections and their ratios were analyzed. An expression of the ratio of the volume emission rates of $O^+(^2P)$ to N_2^+1NEG emissions expected in an electron bombarded atmosphere was developed. The ratio was found to be functionally dependent on collisional deactivation rates and populations of N_2 and e in addition to the cross section ratios and transition probabilities. The source and values of the ratio dependent parameters were discussed from a historical standpoint.

Ground based measurements of I_{7319}/I_{4278} ratio in the magnetic zenith were presented and compared with previous theories. It was found that the measurements produced lower ratios for aurora than early theories predicted.

Rocket payload data from an aurora were analyzed and added to the data base of I_{7319}/I_{4278} in Chapter VII. The rocket analysis measurements were found to be in good agreement with the ground based measurements of the previous chapter and previous theories did not describe the measurement. New theories were presented that did describe the data which included a 'low, quenching' model and two 'large quenching' models. The 'large quenching' models required a large, low altitude source for $O^+(^2P)$. Charge exchange of $O(^3P)$ with $N^+(^1S)$ was a suggested source for the 'large quenching' models. The 'large quenching' models were required to coincide with the Walker et. al. (1975) dayglow results and it was found that the 'large quenching, OI' model represented the auroral data better than the 'large quenching, N_2' model. In all the new theories, a large reduction in the direct electron production efficiency of $O^+(^2P)$ (i.e., $\sigma_{O^{+2}P}(E)/\sigma_{O^+}(E)$) from the Seaton (1959) value of .2 was required.

9.3 AREAS FOR FUTURE RESEARCH

It would be of interest to make the auroral rocket measurement to a higher altitude and verify the findings of NASA 4.329. I believe that an N_2 1PG band emission would suffice for the nitrogen component to the ratios of interest. A narrower bandpass filter (something ~ 7-10Å, peaked at λ7319Å) would reduce the background and give a better signal to noise ratio. Actually, a tilting filter might be ideal to give adjacent background information for an improved measurement in light of the $O^+(^2P$-$^2D)$ faintness. (The sector spectrophotometer could also perform the measurement, but the tilting filter would suffice since no OH would be present.)

Other measurements from the ground would be ideal, especially in the 'soft' auroral zone poleward of the oval. Eather and Mende (1971) have done morphology of 6300Å and 4278Å in this region. Examination of their data and Figure 44 suggests intensities of 10 rayleighs of I_{7319} should be present according to the results found in this analysis.

It would furthermore be interesting to look for the emission in SAR arcs. Even though the emission is less than it might be in one of the molecular band systems, the line nature of the emission might make it more attractive from an analysis standpoint.

Further clarification of the production efficiency of the metastables over the ground state by electron impact may be feasible in the laboratory. Ideally, these cross sections should be known out to ~ 10kev or even larger. Simultaneous measurements of the $O^+(^2D-^4S)$ and $O^+(^2P-^2D)$ doublets would be of interest for clarity as to the branching or metastable partitioning probability per ionization.

The instrumentation studied was designed for a particular purpose and each wavelength region has its own peculiarities. Primarily, however, I believe that the greatest improvement required lies in the filter. The availability of narrow band filters, with good off axis transmission characteristics (minimum polarization etc.), is the main component of the system studied. The value of optimizing the spatial technique is dependent on the quality of this first element of the system. The high throughput advantage, however, vastly improves signal to noise characteristics offered by conventional grating spectrometers, which is a trait of the Fabry-Perot type interference generators. Where short wavelength scans are satisfactory and a high throughput is required, this system should be examined.

The author ranks the 'large quenching, OI' model as being the favored theory of the three presented. The Walker (1975) data strongly supports large quenching of $O^+(^2P)$ for dayglow continuity and certainly the auroral atmosphere differs little from the daytime atmosphere in terms of populations of quenching species. With large quenching, there must be a low altitude source of $O^+(^2P)$ in aurora in addition to direct electron bombardment on OI. The $N^+(^1S)$ mechanism is a very plausible one. The 'high quenching, N_2' model is less favored due to the fact that the N_2 scale height leads to a marginally acceptable synthesis of the NASA 4.329 measurement. It is possible that temperature effects in the quenching rate (by N_2 or OI) may be large. In addition to the random thermal rate of collisions, electric fields can produce large relative non-neutral motions, particularly at the higher altitudes. The higher altitudes could have an accelerated deactivation rate over the low altitudes. This effect would tend to nullify the arguments made on the OI versus N_2 scale height effect on the altitude shape of the emission rates. These effects are not known in these measurements.

APPENDIX A

FILTER THEORY

Narrow bandpass filter ($\delta\lambda_{||} < 10\text{Å}$) technology is continuously being refined. A review of fundamental filter theory will be explored in this appendix to aid in understanding its utilization in the instrument design. The reader should realize that building filters is an art left to thin film specialists who put theory into practice. I will attempt to give some insight into theory, such that, these effects might be understood and compensated or anticipated by a user of the instrument investigated. The art of communicating to the manufacturer the filter requirements for a particular task requires some knowledge of filter theory and how and what particular optical properties are inherent in the dielectric filter. In addition to cone angle and dispersion effects that most users are aware of, off axis transmissions introduce polarizing properties that must be considered.

It is the purpose of this appendix to summarize some filter theory so that some insight into optimizing specifications or trading off lesser undesirables of a filter for others, might aid the reader. The work of Lissberger and Wilcox (1959), Lissberger (1959), and Pidgeon and Smith (1964) offer two approaches to the theory. The approach of Pidgeon and Smith (1964) offers a rigorous matrix layer inversion scheme and transmission equations that give a laboratory specialist a tool in theoretically programming and building a filter. The earlier work of Lissberger and Wilcox (1959) and Lissberger (1959) follows a less rigorous approach, but one which yields nearly the same results. I will follow the Lissberger and Wilcox approach.

The transmission of a light beam through two parallel reflective surfaces (such as a Fabry-Perot) is given by the well known Airy formula (Born and Wolf, 1970)

$$I(t) = \frac{I_{(i)}}{1 + F \sin^2 \delta/2} \quad , \tag{A-1}$$

where I (t), I (i) = transmitted and initial beam intensity

$$F = \frac{4R}{(1 - R)^2} \tag{A-2}$$

where R is reflectivity of the surfaces

$$\delta = 2\pi m = 2\pi \cdot \frac{2\mu t}{\lambda} \qquad \text{(A-3)}$$

μ – spacer index of refraction

t – spacer thickness

λ – wavelength .

The half-width (full-width at half height) of a monochromatic beam can be expressed in terms of the above expression at half-width

$$\delta = 2m\pi \pm \frac{\epsilon}{2} \quad , \qquad \text{(A-4)}$$

where (A-1) becomes

$$\frac{1}{2} = \frac{1}{1 + F \sin^2 \epsilon/4} \quad , \qquad \text{(A-5)}$$

or, for ϵ small

$$\epsilon = \frac{4}{\sqrt{F}} \quad . \qquad \text{(A-6)}$$

The separation of neighboring orders (finesse) can therefore be written as

$$\mathcal{F} = \frac{\pi\sqrt{F}}{2} \quad . \qquad \text{(A-7)}$$

All dielectric filters are made with multiple layers of quarterwave layers of alternating high and low index for the reflective stack, and a multiple half-wave layer for the spacer. Theories have been derived for filter stacks similar to the simple two-layer Fabry-Perot reviewed above. Lissberger (1959), Lissberger and Wilcox (1959), and Pidgeon and Smith (1964) have made theoretical and experimental studies of the all-dielectric filter. A sketch of the theory involved and, in particular, examination of the major filter characteristics as they apply to the sector spectrophotometer will follow.

Figure 1-A depicts a schematic of a simple all-dielectric filter borrowed from Lissberger and Wilcox (1959). The dielectrics used in stacks are usually cryolite (μ_C = 1.34) and zinc sulfide (μ_z = 2.34) which in turn are built on a glass substrate. Lissberger (1959) and Lissberger and Wilcox (1959) developed a general theory for the simple type filter shown in terms of the Fresnel coefficients of the boundaries and optical thicknesses of the layers. Pidgeon and Smith (1964) did a similar study with similar results. The subsequent review will follow the Lissberger (1959) and Lissberger and Wilcox (1959) and for brevity, this work will be abbreivated as LW and the Pidgeon and Smith (1964) as PS.

The multilayer stacks (Figure 1-A), separated by a spacer layer of thickness t, can be represented by equivalent "single" layers separated by the same spacing. The equivalence relationship is shown in the right half of Figure 1-A where the equivalent Fresnel amplitude ($R^{A,G}$) of the air and glass stacks are related to initial amplitudes ($R^{OA,OG}$) and phase change within a particular stack ($\delta^{A,G}$). For details of the derivation, reference can be made to LW papers. The following are the results of the LW work in abbreviated form.

The Airy formula takes the form:

$$\tau_\lambda = \frac{\tau_{max}}{1 + F \sin^2 \chi/2} \tag{A-8}$$

where

$$\chi = \delta + \delta^G + \delta^A \tag{A-9}$$

δ – previously defined

δ^A, δ^G – phase change in the glass and air stacks, respectively

τ_{max} – peak transmission.

By making a small angle assumption ($\cos \theta = 1 - \theta^2/2$), excluding polarizing effects, and accounting for dispersion, the angular dependence of τ_{max} versus λ becomes

$$\frac{\Delta\lambda}{\lambda_0} = \left\{\frac{P}{2(1-Q)}\right\} \theta^2 \tag{A-10}$$

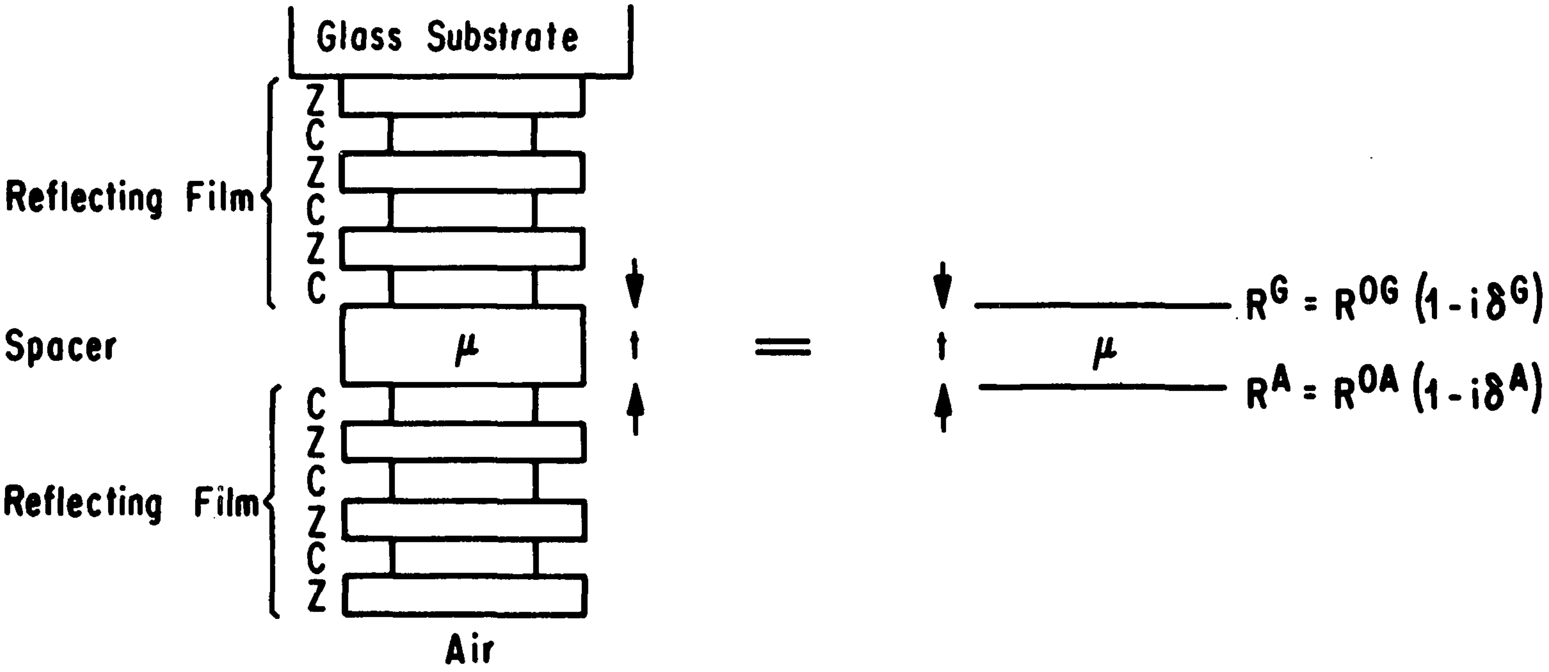

Figure 1-A. Schematic of a dielectric filter as referenced in Lissberger and Wilcox (1959).

where

$$\Delta\lambda = \lambda - \lambda_0$$

λ_0 – wavelength of τ_{max} for $\theta = 0$ (where θ is external incident angle of light to filter)

where for a high index (Z_n5) spacer

$$P_z = \frac{1}{\mu_z^2}\left\{\frac{n + \dfrac{\mu_z^2 + \mu_c^2 - \mu_c\mu_z}{\mu_c(\mu_z - \mu_c)}}{n + \dfrac{\mu_c}{\mu_z - \mu_c}}\right\} \tag{A-11}$$

and

$$Q_z = \frac{1}{n + \dfrac{\mu_c}{\mu_c - \mu_z}}\left\{\left(n + \frac{\mu_c^2}{\mu_z^2 - \mu_c^2}\right)\frac{\lambda_0}{\mu_z}\,\frac{\delta\mu_z}{\delta\lambda} + \frac{\mu_c\mu_z}{\mu_z^2 - \mu_c^2}\,\frac{\lambda_0}{\mu_c}\,\frac{\delta\mu_c}{\delta\lambda}\right\} \tag{A-12}$$

or for a low index (C) spacer

$$P_c = \frac{1}{\mu_c^2}\left\{\frac{n + (\mu_c^2/\mu_z(\mu_z - \mu_c))}{n + (\mu_c/(\mu_z - \mu_c))}\right\} \tag{A-13}$$

$$Q_z = \frac{1}{n\left(\dfrac{\mu_c}{\mu_z} - \mu_c\right)}\left\{\frac{\mu_c\mu_z}{\mu_z^2 - \mu_c^2}\,\frac{\lambda_0}{\mu_z}\,\frac{\delta\mu_z}{\delta\lambda} + \left(n + \frac{\mu_c^2}{\mu_z^2 - \mu_c^2}\right)\frac{\lambda_0}{\mu_c}\,\frac{\delta\mu_c}{\delta\lambda}\right\} . \tag{A-14}$$

The half-width (for parallel – normally incident light) for a first order filter, as derived by PS, may be written as

$$\delta\lambda_{||} = \frac{2\lambda_0}{\pi F_k} \qquad \text{(A-15)}$$

where

$$F_k = \frac{\mu_k \mu_r^{2x+1}}{1(\mu_r - 1)} \qquad \text{(A-16)}$$

$\mu_r = \mu_H/\mu_2$

μ_H – High Index

μ_L – Low Index

x – Number of layers of reflective 1/4 wave layers

μ_K – Index of spacer .

The above relationship suggests that the narrow bandpass is achieved by many layers (high X) and to a certain extent, with high index spacers.

The cone angle has a broadening effect on the transmission characteristics of a filter. According to LW, the bandpass relationship is as follows:

$$\delta\lambda_F = (\delta\lambda_{||}^2 + \delta\lambda_\psi^2)^{1/2} \qquad \text{(A-18)}$$

where

$$\delta\lambda_\psi = \left(\frac{P}{1-Q}\right)\frac{\lambda_0 \psi^2}{2} \qquad \text{(A-19)}$$

P, Q, λ_0 – previously defined

ψ – cone 1/2 angle (in radians) .

At visible wavelengths, a 3° cone 1/2 angle corresponds to ~ 2Å broadening. Therefore, for narrow bandpass applications ($\delta\lambda_{||} < 10$Å at visible wavelengths) care should be taken not to design an instument such that the cone angle effect alters the bandpass significantly. On the other hand, one normally wants as large a cone angle as possible where light gathering power is important, such as in nightglow.

Dispersion has been discussed by LW. For Z_nS type filters, the dispersion is small and normally not of concern for $\lambda < 4500$Å. For blue wavelengths, it becomes more significant. The effect is to make the tilting slope (P/1-Q) smaller than it would be if dispersion were absent. Dispersion of Z_nS is discussed in detail in Hall and Ferguson (1955). Dispersion due to cryolite is negligible in the visible wavelength region (LW).

The effect of most concern, and observed in many filters by this author, was the polarizing effect with tilt. The effect was complex and was simply treated such that some indication of the filter characteristics primarily responsible for the phenomena might be identified. The simplified approach was only meant to give tendencies and not to be taken as explicitly defining the phenomena. As will be observed in the text of the laboratory analysis, some filters showed very large polarizing characteristics at very small angles (~ 2° tilt), much smaller angles than this theory would predict. Others polarized at larger angles than would be predicted. The following theory does suggest that the high index filters tend to polarize at larger tilt angles than the low index filters, and this general tendency was observed in the laboratory analysis discussed in the text.

The approach was to redefine Equation (A-10) in terms of $\Delta\lambda_{||}$ and $\Delta\lambda_{\perp}$ where $P_{\perp}$, $Q_{\perp}$, $P_{||}$, and $Q_{||}$ (Equations (A-11, 14)) were redefined in terms of $\mu^{\perp} = \mu \cos \phi$ and $\mu^{||} = \mu/\cos \phi$ where ϕ is the angle of refraction in a given layer. This was related to the external angle of incidence by Snell's law of refraction. The separation of the two components can then be represented by

$$\delta\lambda_P = \Delta\lambda_{\perp} - \Delta\lambda_{||} \quad . \tag{A-20}$$

Figure 2-A shows a plot of some theoretical separations ($\delta\lambda_P$) based on this simplified approach. To minimize the polarizing tilting effect, a higher spacer order is indicated, as well as, a higher index spacer. The spacer index is the most marked effect but recall that the wavelength shift for a given tilt is almost twice as great for a low index filter.

The transmission of one component versus another with tilt has not been treated here. However, the total bandpass integral did not change for several filters tilted to $\theta >$ 30°. This study should be carried further with a more refined theory, to account for the observed separations. A thorough knowledge of the particular filter stack and of the individual components with tilt for many different spacer indexes, orders, and stack

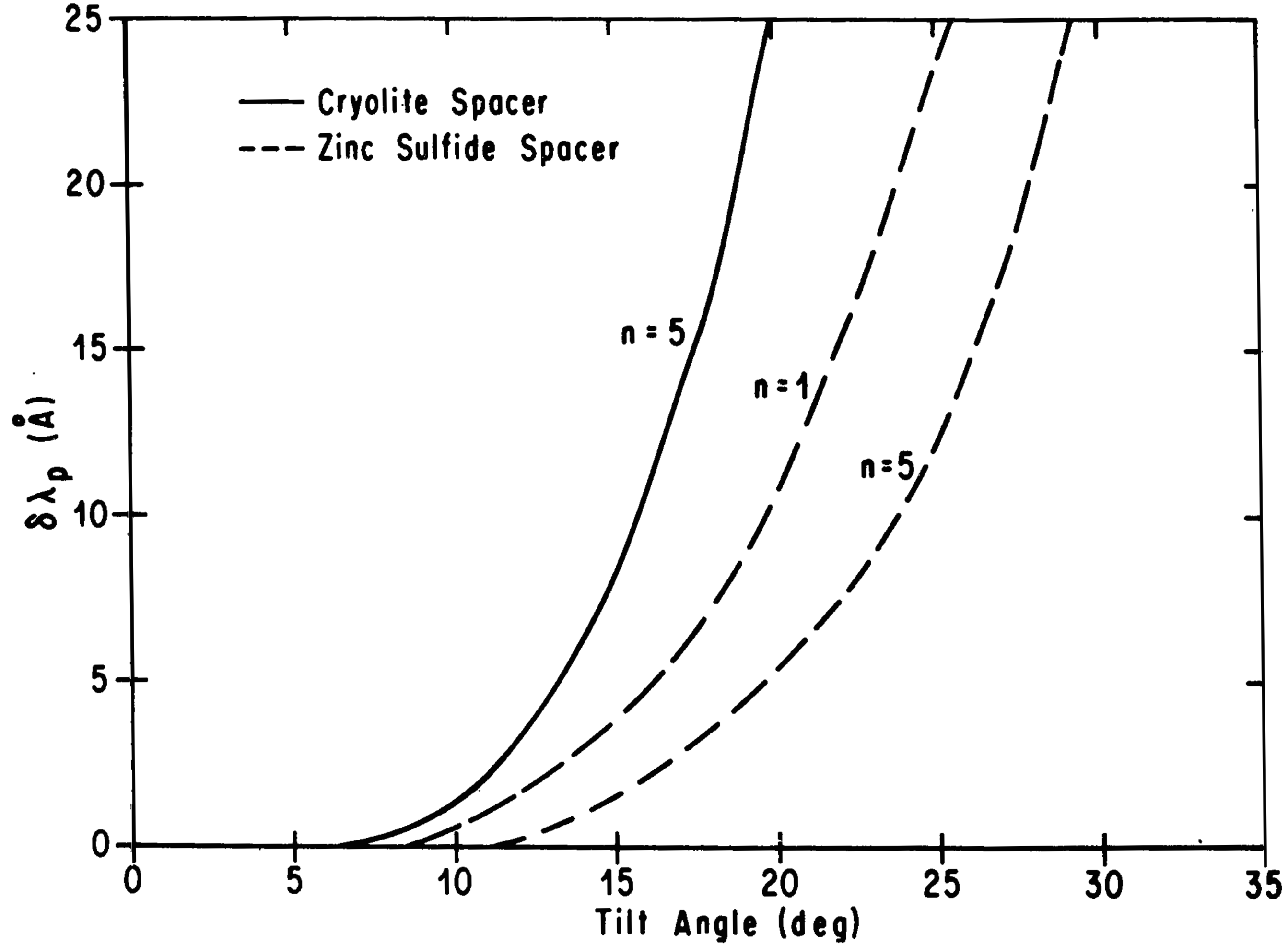

Figure 2-A. Theoretically generated polarizing broadening ($\delta\lambda_P$) versus tilt angle where n refers to the order of the spacer.

layers would be necessary to understand this effect. The study in Baumeister (1961), if extended to include the spacer stack, would be an ideal tool for analyzing particular requirements of this sort. The use of polarizers (although a loss of 60% in throughput results) is recommended in instrument design, where large tilt angles or large wavelength scans are desired.

For other sources of interest, the author suggests referring to Baumeister and Jenkins (1957), Eather and Reasoner (1969), MacLeod (1969), and Thelen (1966). Temperature effects are discussed by Baker and Yen (1967).

APPENDIX B

FORTRAN IV PROGRAM USED IN GENERATING THE DATA ARRAY FOR THE APERTURE SPIRAL AND A MASKING SPIRAL

INPUT:

XNA = Breadth finesse

XNC = Curvature finesse

F = Focal length of objective (cm)

RM = R Maximum (cm)

DPHI = Angular increments desired in array (degrees)

AMAX = $\lambda - \lambda_0$, at R maximum (angstroms)

OUTPUT:

PHII = Angle of aperture point from r = 0 reference (degrees)

RDRP, RDRM = Radial distance bounding aperture at given angle (cm)

PHSM1, RSMM = Angle and radius of inner masking spiral boundary (degrees, cm)

PHSP1, RSPP = Angle and radius of outer masking spiral boundary (degrees, cm)

```
C     UNITS IN CM
      READ(5,1)XNA,XNC,F,RM,N,DPHI,AMAX
    1 FORMAT(1XF3.0,1XF4.1,1XF5.2,1XF5.2,1XI2,1XF5.0,1XF6.2)
      RAD=57.29578
      XIN=.39370
      CM=2.54000
      RM=RM*CM
      TM=ATAN(RM/F)
      TM1=TM*RAD
      DRM=F*TM*((1.0/COS(TM))**2)/XNC
      PI=3.14159
      A=RM*RM*PI
      DPHI=DPHI/RAD
      PHI=4.0/RAD
      PHM=2.0*PI*N
      DELPHI=PHM/XNC
      PHMM=PHM+90./RAD
      OMEG=DELPHI*TM*TM/XNA
      A01=A*OMEG
      ALPH=AMAX/(TM*TM)
      NN=1
   10 R=F*TAN(TM*(PHI/PHM)**.5)
      DR=DRM*(((R*R+F*F)**1.5)/((RM*RM+F*F)**1.5))*(RM/R)
      RDRP=R+DR/2.0
      RDRM=R-DR/2.0
      T=ATAN(R/F)
      A02=PI*RM*RM*DR*DELPHI*COS(T)*COS(T)*SIN(T)/F
      ANA=T*COS(T)*COS(T)*DR/(F*TM*TM)
      ANA=1.0/ANA
C THE FOLLOWING PERTAINS TO THE SHUTTER
      PHS=PHI/3.0
      PHSME=PHI-DELPHI/2.0
      PHSPE=PHI+DELPHI/2.0
      IF(PHSME)63,63,64
   63 PHSME=0.0
```

```
      RSM=0.0
      RSMM=0.0
      RNE=0.0
      GO TO 95
   64 B=F*TAN(TM*(PHSME/PHM)**.5)
      RSM=F*TAN(TM*(PHSME/PHM)**.5)+(DRM/2.0)*(((B*B+F*F)**1.5)/((RM*RM+
     1F*F)**1.5))*(RM/B)
      RSMM=RSM+.1000
      C=F*TAN(TM*((PHSME+2.0*PI+DELPHI)/PHM)**.5)
      RNE=C-(DRM/2.0)*(((C*C+F*F)**1.5)/((RM*RM+F*F)**1.5))*(RM/C)
   95 CONTINUE
      D=F*TAN(TM*(PHSPE/PHM)**.5)
      RSP=F*TAN(TM*(PHSPE/PHM)**.5)-(DRM/2.0)*(((D*D+F*F)**1.5)/((RM*RM+
     1F*F)**1.5))*(RM/D)
      RSPP=RSP-.1000
      PHSM=PHS-DELPHI/2.0
      PHSP=PHS+DELPHI/2.0
      CHEC=PHSPE-2.0*PI-DELPHI
      IF(CHEC)98,98,99
   98 RNLT=0.0
      GO TO 100
   99 E=F*TAN(TM*((PHSPE-2.0*PI-DELPHI)/PHM)**.5)
      RNLT=E+(DRM/2.0)*(((E*E+F*F)**1.5)/((RM*RM+F*F)**1.5))*(RM/E)
  100 CONTINUE
      PHS1=PHS*RAD
      PHSM1=PHSM*RAD
      PHSP1=PHSP*RAD
      PHII=PHI*RAD
      IF(PHII.LE.360.)GO TO 27
      PHII=PHII-(NN-1)*360.
   27 CONTINUE
      PIP=PHI/NN
      PI2=PI*2.0
      WRITE(6,25)PHII,RDRP,RDRM,PHSM1,RSMM,PHSP1,RSPP
```

```
25 FORMAT(F6.2,F7.5,F7.5,F6.2,F7.5,F6.2,F7.5)
   IF(PI2.GE.PIP)GO TO 29
   NN=NN+1
29 CONTINUE
   IF(PHI-PHMM)11,11,12
11 PHI=PHI+DPHI
   GO TO 10
12 WRITE(6,17)TM1,DRM,AO1,ALPH
17 FORMAT(/10XF5.2,2XF6.5,2XE10.3,2XE10.3)
   WRITE(6,1)XNA,XNC,F,RM,N,DPHI,AMAX
   END
   END
END OF FILE
```

APPENDIX C

SPONTANEOUS EMISSIONS FROM $O^+(^2P)$

The $O^+(^2P)$ "nebulium lines" (Herzberg, 1944) have been studied and reported by astronomers due to their noted dominance in spectra made of cosmic nebulae. Studies of the $O^+(^2P)$ and the forbidden emissions originating from the state provided astronomers with a radiative signature of the environment in which such emissions were originating.

Seaton and Osterbrock (1957) calculated the effective transition probabilities, emission wavelengths, and line strength factors for spontaneous emission from the $O^+(^2P)$ and $O^+(^2D)$ states. Figure C-1 portrays the fortrat diagram for those magnetic dipole and electronic quadrapole transitions originating from the $O^+(^2P)$ state. The three equivalent electrons of the outer shell can be in a ^4S, ^2D or ^2P term configuration with total angular momentum quantum numbers of 3/2 for the S term, 3/2 and 5/2 for the D term and 1/2 and 3/2 for the P term. The spin coupling results in two ^2P states ($^2P_{1/2}$ and $^2P_{3/2}$), where the relative populations of the two states are given by their statistical weights. Spontaneous cascade from the ^2P states can occur through either a magnetic dipole or electronic quadrapole transition to the ^2D levels or the ^4S level.

Table 1-C depicts the atomic transition parameters for spontaneous emission from the $^2P_{1/2}$ and $^2P_{3/2}$ states of OII. Note the transition probabilities represent the total transition probability including both the electronic quadrapole and magnetic dipole transitions.

The total radiative loss rate of $O^+(^2P)$ is given by the sum of the loss occurring from the $^2P_{1/2}$ state and the $^2P_{3/2}$ state, i.e.,

$$\eta(O^+(^2P))_R = \eta(O^{+2}P_{1/2})_R + \eta(O^{+2}P_{3/2})_R \quad . \tag{C-1}$$

The loss rate of the $^2P_{1/2}$ state becomes

$$\eta(O^{+2}P_{1/2})_R = n[O^{+2}P_{1/2}] \cdot A_{^2P_{1/2}} \tag{C-2}$$

and for the $^2P_{3/2}$ state

$$\eta(O^{+2}P_{3/2})_R = n[O^{+2}P_{3/2}] \cdot A_{^2P_{3/2}} \quad . \tag{C-3}$$

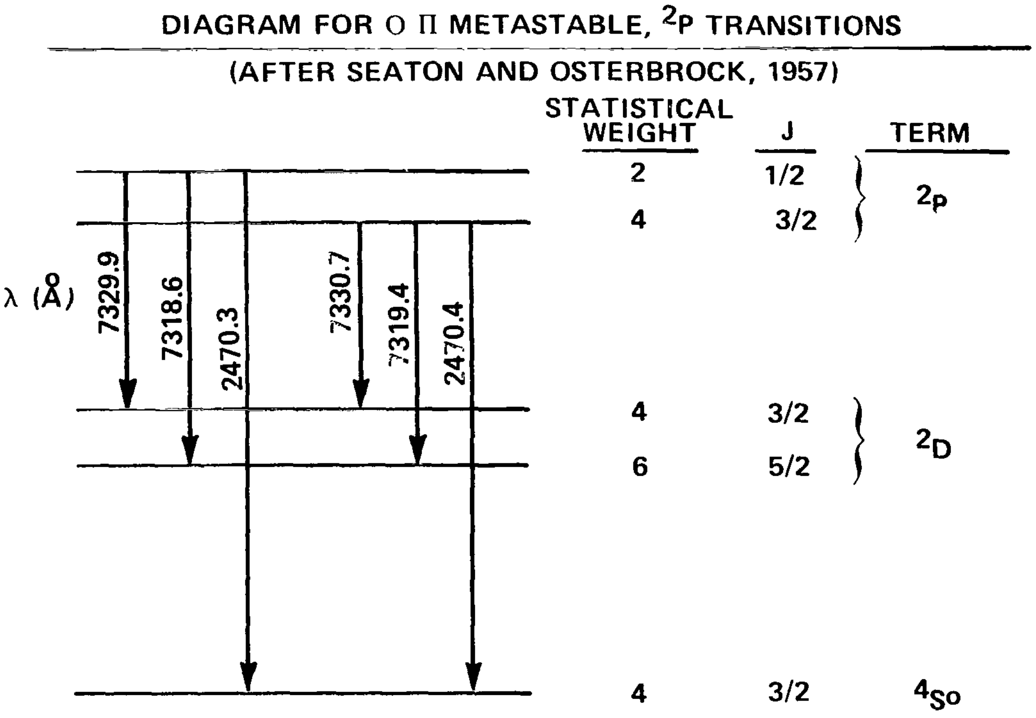

Figure 1-C. Diagram for OII Metastable, ^2P transitions (after Seaton and Osterbrock, 1957).

TABLE 1-C. ATOMIC PARAMETERS FOR $O^+(^2P)$ TRANSITIONS (SEATON AND OSTERBROCK, 1957)

Transition n → n′	Wavelength (Å)	A_λ* (sec^{-1})	ω**
$^2P_{1/2}$ $^2D_{3/2}$	7329.9	.100	2
$^2P_{1/2}$ $^2D_{5/2}$	7318.6	.061	2
$^2P_{1/2}$ $^4S_{3/2}$	2470.3	.024	2
$^2P_{3/2}$ $^2D_{3/2}$	7330.7	.061	4
$^2P_{3/2}$ $^2D_{5/2}$	7319.4	.115	4
$^2P_{3/2}$ $^4S_{3/2}$	2470.4	.060	4

*Includes summed electric quadrapole and magnetic dipole transition probabilities.

**Statistical weight, 2J + 1, of the upper state (n).

The statistical weights of the respective levels relate the populations of the substates to the total $O^+(^2P)$ population, i.e.,

$$n[O^{+2}P_{1/2}] = \frac{2}{6} \cdot n[O^{+2}P] \quad . \tag{C-4}$$

and

$$n[O^{+2}P_{3/2}] = \frac{4}{6} \cdot n[O^{+2}P] \quad . \tag{C-5}$$

Substituting (C-4) and (C-5) into (C-2) and (C-3) respectively, and substituting the respective transition probabilities from Table 1-C, the respective ^2P loss rates become

$$\eta(O^{+2}P_{1/2})_R = .062\, n[O^{+2}P] \tag{C-6}$$

and

$$\eta(O^{+2}P_{3/2})_R = .157\, n[O^{+2}P] \quad . \tag{C-7}$$

Further substitution of equations (C-6) and (C-7) into (C-1) gives the total radiative loss rate of $O^+(^2P)$ as

$$\eta(O^{+2}P)_R = .219\, n[O^{+2}P] \quad . \tag{C-8}$$

Considering the rocket payload measurements discussed in the text, it is desirable to represent the population of $O^+(^2P)$ in terms of the fraction of the $O^+(^2P)$ radiating to the $O^+(^2D)$ state. This total emission rate was measured on NASA 4.329 as discussed in the text. Equation (C-8) can be written as

$$\eta(7319\text{-}30\text{Å}) + \eta(2470\text{Å}) = .219\, n[O^{+2}P] \tag{C-9}$$

where η(7319-30Å) represents the radiative loss rate of ^2P to ^2D states and η(2470Å) the radiative loss rate of ^2P to ^4S. By substituting the emission probability and statistical weights for η(2470Å),

$$\eta(7319\text{-}30\text{Å}) = .219\, n[O^{+2}P] - \frac{2}{6} \cdot .024\, n[O^{+2}P] - \frac{4}{6} \cdot .060\, n[O^{+2}P] \quad ,\text{(C-10)}$$

or

$$\eta(7319\text{-}30\text{Å}) = .171\, n[O^{+2}P] \quad . \qquad \text{(C-11)}$$

The ground based measurements are directed at only the 7319Å doublet. By expanding (C-11) into the respective components, and representing the 7330Å emission by the statistical weight and transition probability, (C-11) becomes

$$\eta(7319\text{Å}) = .171\, n[O^{+2}P] - \frac{2}{6} \cdot .100\, n[O^{+2}P] - \frac{4}{6} \cdot .061\, n[O^{+2}P] \qquad \text{(C-12)}$$

or

$$\eta(7319\text{Å}) = .098\, n[O^{+2}P] \quad . \qquad \text{(C-13)}$$

APPENDIX D

PRODUCTION OF $O^+(^2P)$ BY ELECTRON IMPACT AND ITS RELATIONSHIP TO EXCITED N_2^+ EMISSIONS

The volume production rate for an impact source such as energetic electrons is determined by the product equation

$$\eta(x')_P = \int_E F(E)\, \sigma_{x'}(E)\, n[x]\, dE \quad , \tag{D-1}$$

where F(E) – energy dependent flux of streaming particles through the background gas, x; $\sigma_{x'}(E)$ – energy dependent cross section for producing an x′ state from an impact on species x; n[x] – volume density of species x; and $\eta(x')_P$ – production rate of species x′. The flux distribution (energetic and pitch angle distribution) of precipitating auroral electrons is difficult to measure but has recently been accomplished by several investigators for the low ev to tens of Kev range. The intent here was to relate the production rate to spectroscopic signatures since electron distribution measurements are not always available, particularly when making ground based measurements. It has been previously noted and referenced that the ionization rate of N_2 is related to the N_2^+1NEG emission. The approach taken was to relate the ionization rate of OI to the ionization rate of N_2, which in turn is related to the N_2^+1NEG emission rate.

Equation (D-1) can be written for N_2^+ and O^+ to read as,

$$\eta(N_2^+)_P = \int_E F(E)\, \sigma_{N_2^+}(E)\, n[N_2]\, dE \tag{D-2}$$

and

$$\eta(O^+)_P = \int_E F(E)\, \sigma_{O^+}(E)\, n[OI]\, dE \quad . \tag{D-3}$$

Borst and Zipf (1970) have found in laboratory analysis that for E > 30ev electrons, 7% of all N_2^+ generated emit the $N_2^+1NEG_{0,0}$ radiation. The 7% probability is nearly independent of energy and permits the production rate of N_2^+ to be written as:

$$\eta(N_2^+)_P = \frac{\sigma_{N_2^+}(E)}{\sigma_{N_2^{+*}}(E)}\,\eta(N_2^+ 1NEG_{0,0}) \qquad \text{(D-4)}$$

where $\sigma_{N^{+*}}(E)$ is the cross section for producing $N_2^+ B^2\Sigma_u^+$ state in the zeroth vibrational level. The identity now exists between Equations (D-2) and (D-4) that

$$\int_E F(E)\,\sigma_{N_2^+}(E)\,n[N_2]\,dE = \frac{\sigma_{N_2^+}(E)}{\sigma_{N_2^{+*}}(E)}\,\eta(3914\text{Å}) \quad . \qquad \text{(D-5)}$$

Equation (D-3) can be rewritten to look very similar to Equation (D-5) by removing the non-energy dependent n[OI] to the left side of the equation and multiplying by $n[N_2]$, i.e.,

$$\eta(O^+)_P \frac{n[N_2]}{n[OI]} = \int_E F(E)\,\sigma_{O^+}(E)\,n[N_2]\,dE \quad . \qquad \text{(D-6)}$$

The only difference between the integral portions of Equations (D-5) and (D-6) lies in the cross section.

The energy dependence of the total ionization cross sections of N_2 and O are summarized by Kieffer and Dunn (1966). More recently, Kazaks et. al. (1972) have added theoretical deductions for the oxygen cross section. The energy dependence of the cross sections of the two constituents are very similar. The major discrepancy in the cross sections of concern lie in OI from 20 to ~ 300ev. Broksenberg (1961) and Kazaks et. al. (1972) deduce a cross section of 30% higher at 100ev than Fite and Brackman (1959) and Rothe et. al. (1962). For $E > 300$ev, little disagreement exists in the OI cross section. The assumption was made after careful examination of these cross sections (Figure 1-D) that

$$\frac{\sigma_{O^+}(E)}{\sigma_{N^+}(E)} = \text{Constant} \qquad \text{(D-7)}$$

where the constant was deduced as being .5 by this author. In other words, it was assumed that at all energies, the OI ionization cross section was one half that of the N_2 cross section. Note in Figure 1-D that for $E < 50$ev, the ratio approaches one. It is the author's deduction that the .5 ratio gives a good representation of the overall cross section difference for the bulk of the auroral primary electron energy range.

Equations (D-6) and (D-7) can now be combined to give:

$$\frac{\sigma_{N_2^+}(E)}{\sigma_{O^+}(E)} \eta(O^+)_P \frac{n[N_2]}{n[OI]} = \int_E F(E)\, \sigma_{N_2^+}(E)\, n[N_2]\, dE \quad . \qquad \text{(D-8)}$$

An identity can now be written by eliminating the integral of equation (D-8) and (D-5), resulting in a relationship between the production rate of O^+ ions to the $N_2^+ 1NEG_{0,0}$ volume emission rate, i.e.,

$$\eta(O^+)_P = \frac{\sigma_{O^+}(E)}{\sigma_{N_2^+}(E)} \cdot \frac{\sigma_{N_2^+}(E)}{\sigma_{N_2^{+*}}(E)} \cdot \eta(3914Å) \cdot \frac{n[OI]}{n[N_2]} \quad . \qquad \text{(D-9)}$$

The next step is to determine the rate of $O^+(^2P)$ production specifically. The $O^+(^2P)$ production is related to the O^+ production rate by the relationship

$$\eta(O^{+2}P)_P = \frac{\sigma_{O^{+2}P}(E)}{\sigma_{O^+}(E)} \eta(O^+)_P \quad . \qquad \text{(D-10)}$$

By substituting Equation (D-9) into (D-10), the $O^+(^2P)$ production rate becomes

$$\eta(O^{+2}P) = \frac{\sigma_{O^{+2}P}(E)}{\sigma_{O^+}(E)} \cdot \frac{\sigma_{O^+}(E)}{\sigma_{N_2^+}(E)} \cdot \frac{\sigma_{N_2^+}(E)}{\sigma_{N_2^{+*}}(E)} \cdot \frac{\eta(3914Å)}{n[N_2]} \cdot n[OI] \quad . \qquad \text{(D-11)}$$

The first three cross section ratios could be reduced to simplify Equation (D-11), but previous investigations have presented values for these particular ratios. The first ratio, $\sigma_{O^{+2}P}(E)/\sigma_{O^+}(E)$ is indicated by Seaton (1959) to take on a value of .2 for all energies.

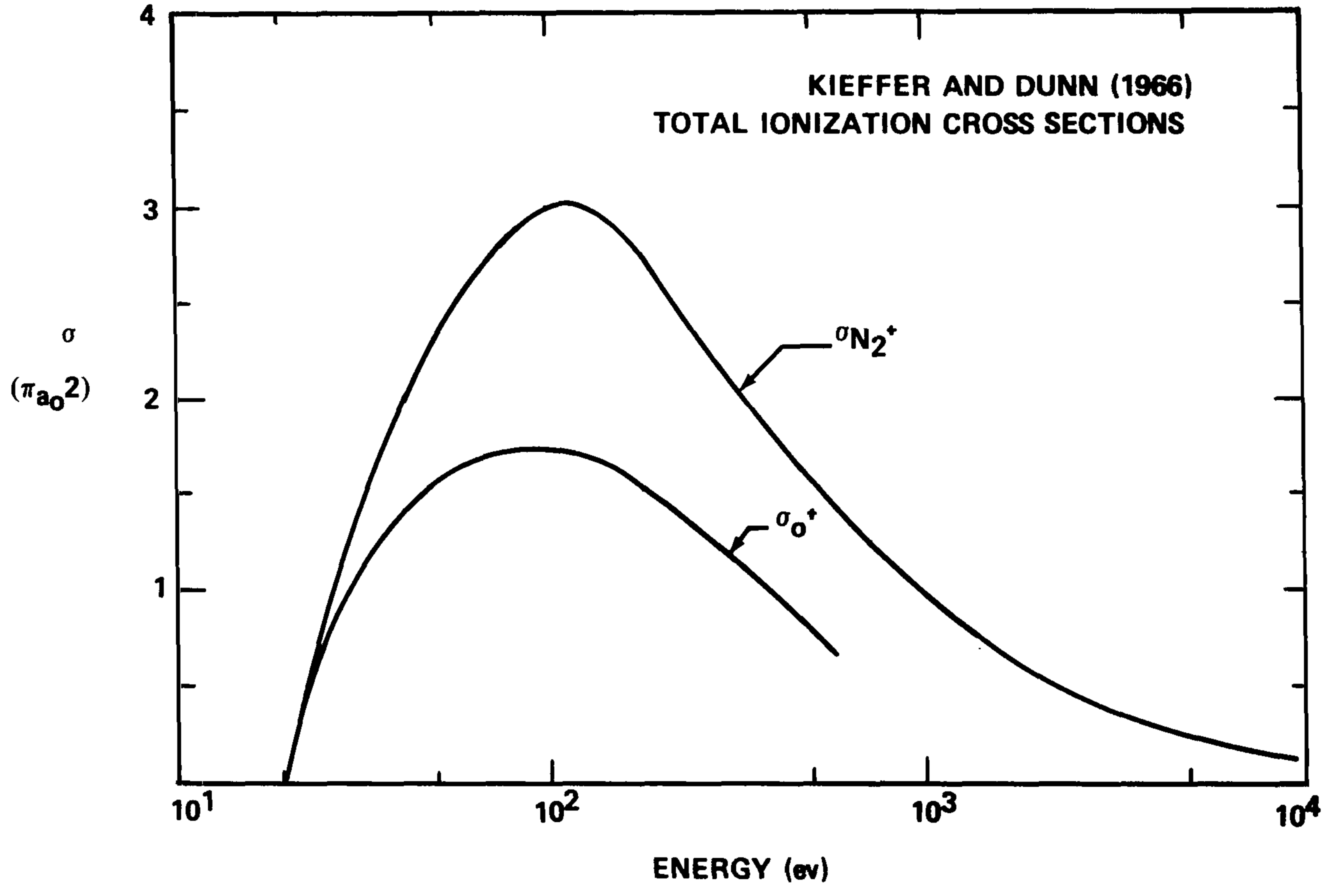

Figure 1-D. Cross section versus energy of ionization for N_2 and OI after Keiffer and Dunn, 1966.

Kazaks et. al. (1972) found a value of .25. The next two ratios of Equation (D-11) were discussed earlier. This author's examination of $\sigma_{O^+}(E)/\sigma_{N_2^+}(E)$ suggested a value of near .5 satisfied the bulk of the energy range. Finally, Borst and Zipf (1970) give a value of 14.1 for the third ratio of Equation (D-11) as discussed earlier. In the text of this report, these ratios will be referred to but for simplicity of the total continuity treatment, the ratios will be defined as:

$$R_{\sigma_0}(E) = \frac{\sigma_{O^{+2}P}(E)}{\sigma_{O^+}(E)} \cdot \frac{\sigma_{O^+}(E)}{\sigma_{N_2^+}(E)} \cdot \frac{\sigma_{N_2^+}(E)}{\sigma_{N_2^{+*}}(E)} \quad , \tag{D-12}$$

where the subscript on $R_\sigma(E)$ refers to the particular vibrational level of N_2^{+*}. This permits a rewrite of Equation (77) to read as:

$$\eta(O^{+2}P)_P = R_{\sigma_0}(E)\,\eta(3914Å)\,\frac{n[OI]}{n[N_2]} \quad . \tag{D-13}$$

By assuming the ratios are not dependent on energy and inserting the values discussed above, one finds that $R_{\sigma_0}(E) = 1.41$ if the historical values are retained.

It is also referred to in the text that the production of $O^+(^2P)$ is related to the emissions arising from the first vibrational state of $N_2^+B^2\Sigma_u^+$, which leads to the λ4278Å band emission. The work of Shemansky and Broadfoot (1971) suggest that $\sigma_{N_2^{+*}}(E)$ is a factor of 3.3 lower for the first vibrational level than for the zeroth level. For this particular $\sigma_{N_2^{+*}}(E)$, the ratios will be given by $R_{\sigma_1}(E)$ and (D-13) will become

$$\eta(O^{+2}P)_P = R_{\sigma_1}(E)\,\eta(4278Å)\,\frac{n[OI]}{n[N_2]} \quad . \tag{D-14}$$

Similarly, from historical values, $R_{\sigma_1}(E)$ takes a value of 4.65.

APPENDIX E

DATA REDUCTION OF λ7319Å GROUND BASED INTENSITIES

The intensity of 7319Å and OH $P_{1,2}$, (7316.4Å), were determined in the following manner. From Figure 24 it was deduced that when the spectrophotometer was peaked at 7319Å, the transmittance of 7316.4Å (T_{OH}) was 63% that of 7319Å. When the instrument was peaked at 7316.4Å, the transmittance of 7319Å ($T_{O^{+2}P}$) was 63% that of the OH (i.e., when the instrument is tuned such that T_{max} = 7316.4Å, then $T_{O^{+2}P} = .63\ T_{max}$ and when tuned to T_{max} = 7319Å, $T_{OH} = .63\ T_{max}$).

The calibration factor (CF) was 16.15 counts per second per rayleigh. CF was determined with a low brightness radioactive source recently calibrated by the National Bureau of Standards. The instrumental integrated transmission function was accounted for in this caluclation.

Instrument signal levels can be converted to intensity in the following manner. The equations for the two wavelength positions can be written. The equation for the 7316.4Å wavelength position can be written as:

$$\frac{V_{7316.4} - V_{BG}}{CF} = T_{O^{+2}P} I_{7319} + T_{max} I_{7316.4} \quad , \qquad \text{(E-1)}$$

and for the 7319Å wavelength position as:

$$\frac{V_{7319} - V_{BG}}{CF} = T_{OH} \cdot I_{7316.4} + T_{max} \cdot I_{7319} \qquad \text{(E-2)}$$

where $V_{\lambda^{1}S}$ are the measured photomultiplier signals for the 7319Å, 7316.4Å, and 7310Å (Background, BG) wavelength positions. The amount of background (V_{BG}) was determined at 7310Å, between two hydroxyl lines of concern. The two equations above can be solved for expressions of intensity, i.e.,

$$I_{7316.4} = \frac{\left(\dfrac{V_{7316.4} - V_{BG}}{CF \cdot T_{O^+}}\right) - \left(\dfrac{V_{7319} - V_{BG}}{CF \cdot T_{max}}\right)}{\left(\dfrac{T_{OH}}{T_{max}} - \dfrac{T_{max}}{T_{O^+}}\right)} \quad , \qquad \text{(E-3)}$$

and

$$I_{7319} = \frac{\left(\dfrac{V_{7319} - V_{BG}}{CF \cdot T_{OH}}\right) - \left(\dfrac{V_{2316.4} - V_{BG}}{CF \cdot T_{max}}\right)}{\left(\dfrac{T_{O^+}}{T_{max}} - \dfrac{T_{max}}{T_{OH}}\right)} \quad . \tag{E-4}$$

Recall from above that $T_{OH} = T_{O^+} = .63\ T_{max}$, where T_{max} is determined from Figure 23 of Chapter V.

The analog charts were reduced on a Gerber digitizer where the voltage amplitudes were punched on cards for 7319Å, 7316.4Å, and 7310Å wavelength positions of each spectral scan.

APPENDIX F

N_2^+ PRODUCTION FUNCTIONS FOR INTERPRETATION OF AURORAL EMISSION INTENSITIES

The ionization rate produced by incoming electron steams has been studied by Rees (1963), reviewed by Rees (1969), computed by Berger et. al. (1970), and recently examined by Banks et. al. (1974). Power law and exponential shapes have been compared to measured N_2^+1NEG volume emission rates in attempts to describe the production versus altitude, for various electron energy distributions.

The purpose of this study is not to analyze these electron energy distribution functions or flux rates. The purpose here is to give some indication of the altitude of maximum energy deposition and peak ionization rate. This is accomplished by viewing up the flux tubes along an auroral electron stream and measuring emission signatures of the perturbed atmosphere.

To typify or envelope the extremes of the production rates (for N_2 ions), three altitude distributions have been assumed in this study. The peak ionization rate for each was fixed and the distribution above and below that altitude was described by their respective functions. The three functions are described below.

Monoenergetic (M)

Rees (1963) studied the production rate of $N_2^+1NEG_{0,0}$ radiation as induced by isotropic streams (0°-80°) of monoenergetic electrons. The isotropic monoenergetic production rate then is that of Rees (1963), as inferred from his height versus normalized volume emission rate for the various energies that correspond to an altitude of peak ionization. Banks et. al. (1974) performed a study similar to Rees (1963) using refined electron scattering cross sections. Their results agreed with Rees (1963) for $E > 1$Kev primaries but lower energies peaked slightly higher in altitude. The Rees (1963) results are used here.

N_2 Proportional (P)

The N_2 proportional shape assumes that the emission rate is proportional to the N_2 number density above the peak of maximum ionization and drops to zero at the peak.

Chapman (C)

Chapman (1931) described a theory of electron production by photoionization, which has classically been termed Chapman's production function. This function and its many forms have been reviewed in many texts including Rishbeth and Garriot (1969), Chapter III. The form used here is for normal incidence to the atmosphere and is given by

$$P = P_0 \exp \left\{ 1 - h - e^{-h} \right\} \quad , \qquad \text{(F-1)}$$

where

$$h \text{ - reduced height } = \int \frac{dz}{H} \simeq \frac{z - z_0}{H}$$

and

z - altitude (km),

z_0 - altitude of maximum production,

H - scale height = kT/mg,

P_0 - maximum production rate at peak altitude .

Figures 1-F and 2-F show altitude profiles of the production rates versus altitude for the three functions described for peak production at 120 km and 200 km, respectively. The peaks are normalized to one and the intention is to convey the distribution of the rate above and below the peak for the respective functions.

When viewing an aurora from below with these types of production profiles, note that the peak of the Chapman profile corresponds approximately with the median point on the profile. For the monoenergetic and N_2 proportional types, the median is somewhat above the peak production point. At 200 km (Figure 2-F), the three profiles are shown to diverge to larger extremes in their drop off rates from the production peak altitude.

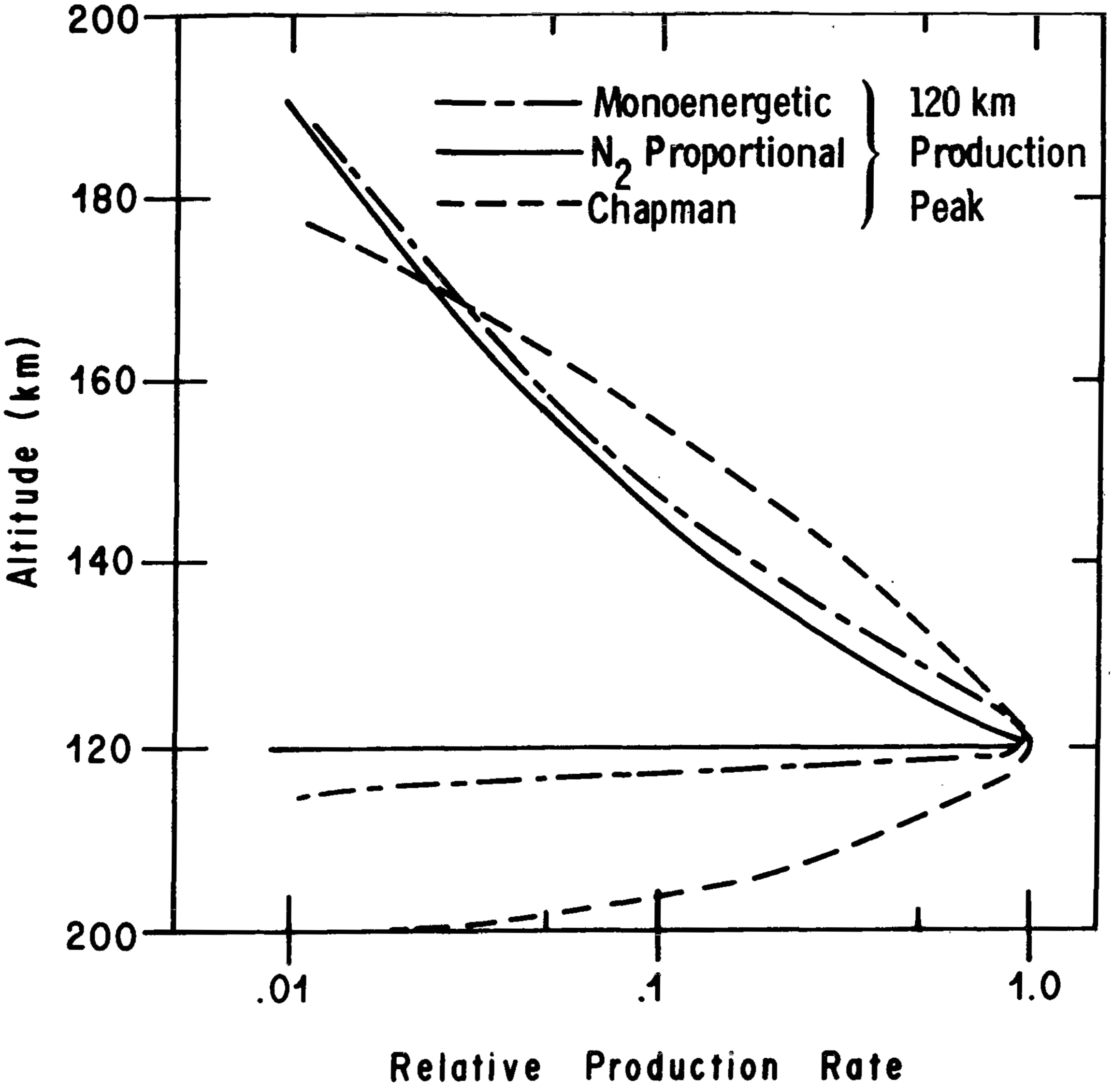

Figure 1-F. Altitude versus relative production rates with peak production at 120 km for a monoenergetic, N_2 proportional, and Chapman type production functions.

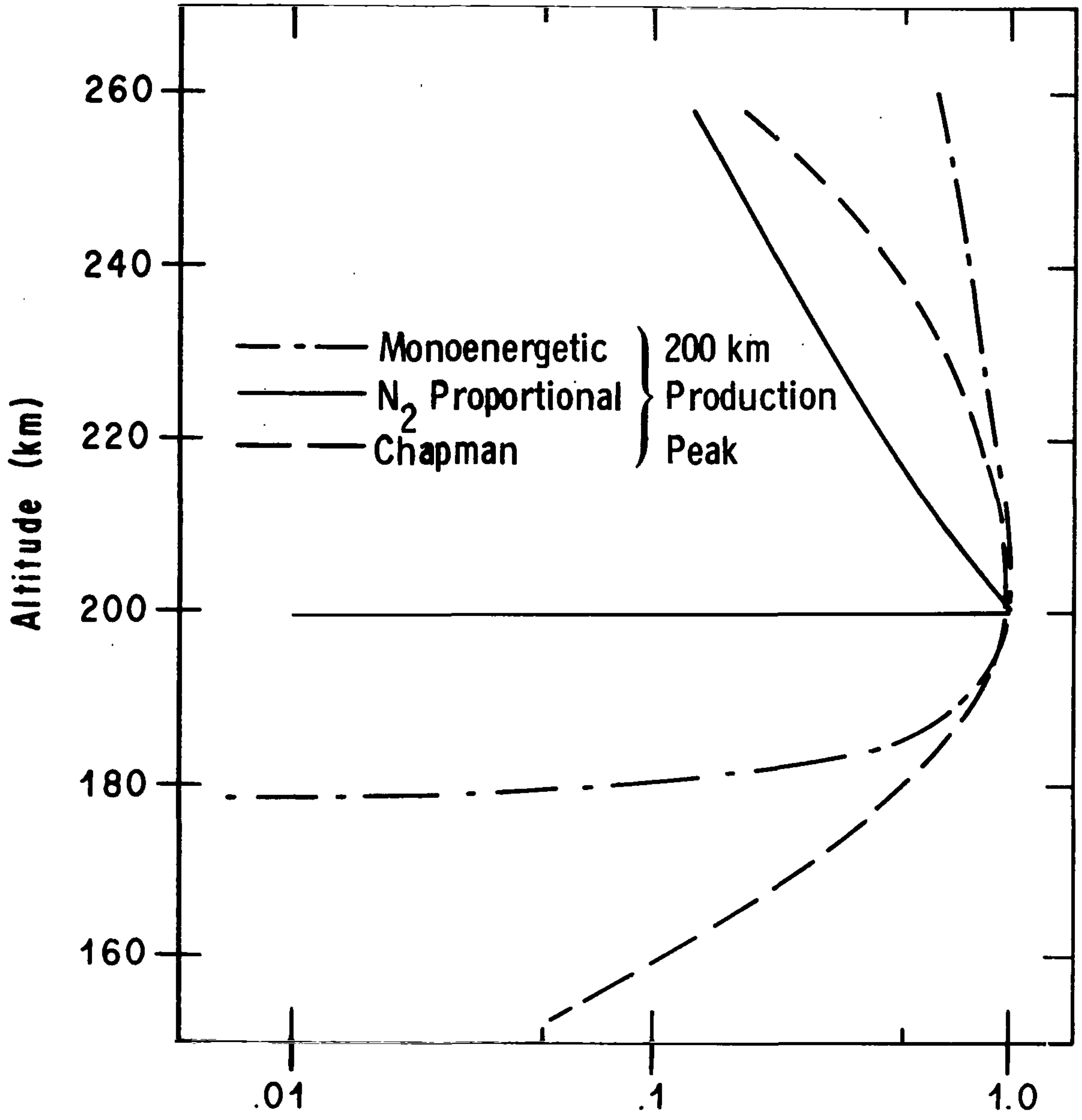

Figure 2-F. Same as Figure 1-F, except for peak production at 200 km.

APPENDIX G

DATA REDUCTION OF NASA 4.329 PHOTOMETER SIGNALS FOR INFERRED $O^+(^2P-^2D)$, $N_2^+1NEG_{0,0}$, AND $N_2 1PG_{5,3}$ EMISSION INTENSITIES

G.1 INTRODUCTION

The N_2^+1NEG system is a fairly narrow band system. The effective transmission of the 3914Å filter was determined to be 30%. This effective transmission was determined graphically using a 500°K laboratory spectra of the $N_2^+1NEG_{0,0}$ band. No attempt was made to compensate for a changing rotational distribution, which might result from changing thermospheric temperatures over the measurement range.

Figure 1-G depicts the reduced intensity of the $N_2^+1NEG_{0,0}$ emission (solid curve). Note on the figure that the altitude at which energetic electrons were encountered is at ~ 120 km as indicated by the particle detector. Below this altitude, the photometers are viewing aurora above which is either weakening during the payload ascent, or the payload is passing into a weaker form during flight. At 150 km, an enhancement is encountered which nearly doubles the emission intensity. The $\dot{n}[N_2] \cdot H_{N_2}$ or effective columnar density profile shape is shown in the dashed curve (no scale indicated). The purpose of this curve is to suggest that this particular observation departs significantly from an ideal, steady state situation.

G.2 $O^+(^2P-^2D)$ AND $N_2 1PG_{5,3}$ DATA ANALYSIS

The introduction to Chapter VIII discussed briefly the difficulty in discerning the $O^+(^2P-^2D)$ emission intensity which is surrounded by $N_2 1PG$ emission. This is particularly complex in broad band photometry where the spectra shape is not resolved. It was for this reason two channels (7326Å and 7354Å) were dedicated to the measurement. The data analysis requires a deconvolving of the emissions to discern their sky brightness.

G.3 EFFECTIVE CHANNEL TRANSMISSIONS OF $O^+(^2P-^2D)$

The filter transmission profiles are shown in Figures 2-G and 3-G for the 7326Å and 7354Å channels where the solid curves represent the measured transmission profiles. Examination of the $O^+(^2P-^2D)$ wavelength positions at 7319Å and 7330Å suggest a 78% transmission for both wavelengths through the 7326Å filter. The 7354Å filter allows 10% transmission of 7330Å and 3% of 7319Å emissions.

The effective transmission of $O^+(^2P-^2D)$ (i.e., T_{O^+}) was determined by weighting the transmission of the individual volume emitting probabilities. The effective transmission relationship for a given filter can be written as:

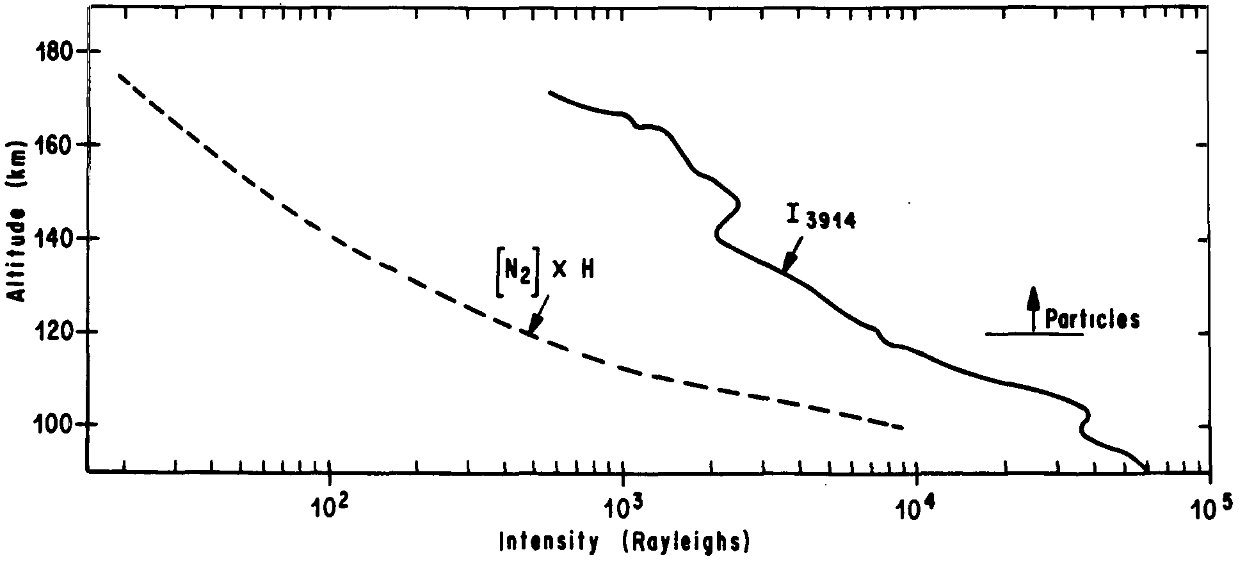

Figure 1-G. Altitude versus intensity of $N_2^+1NEG_{0,0}$ is indicated by the solid line. Particle altitude is noted at 120 km. Dashed line is columnar N_2 density (no scale indicated) for purpose of showing the changing aurora.

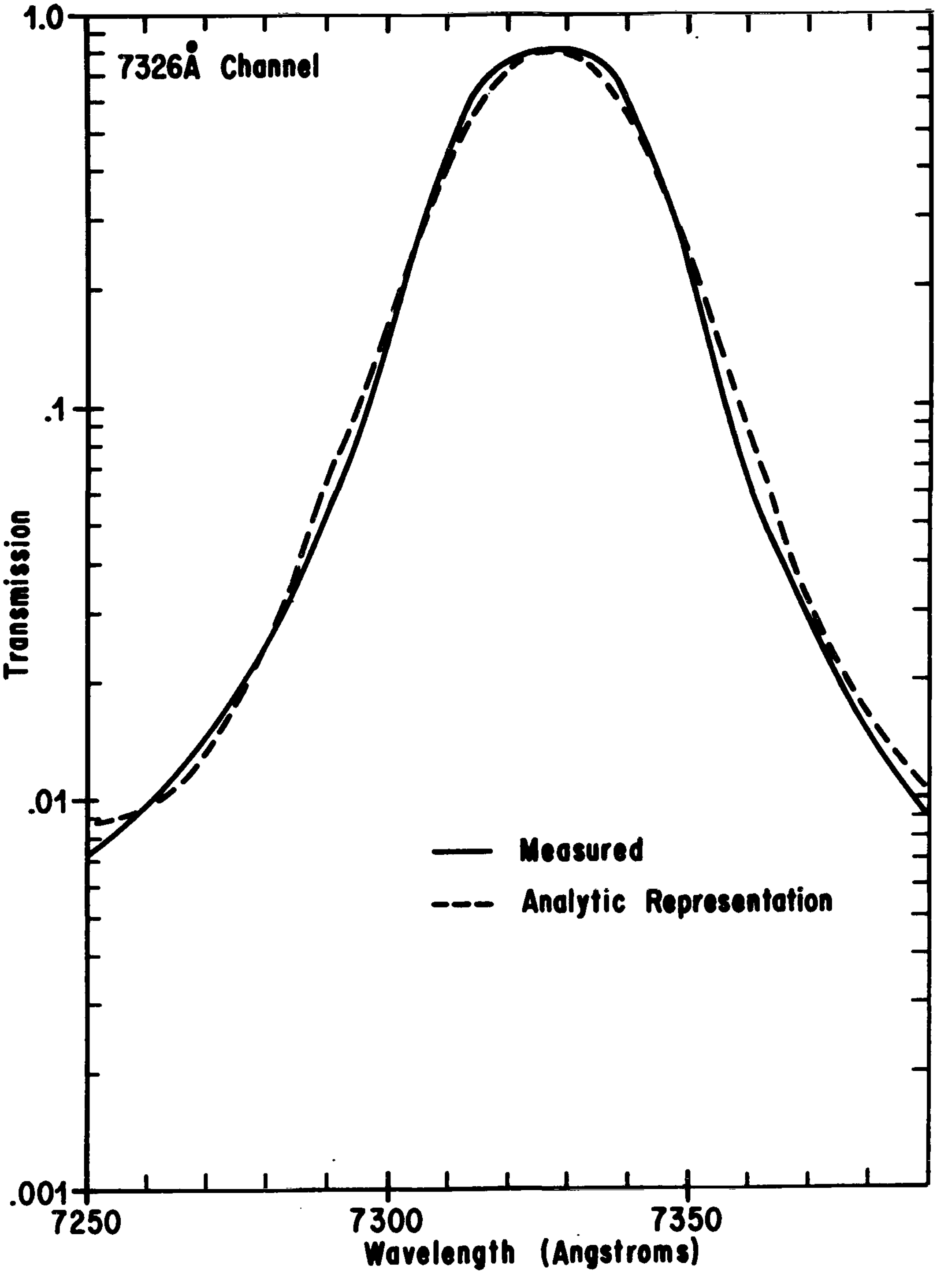

Figure 2-G. Transmission versus wavelength of the 7326Å channel for NASA 4.329.

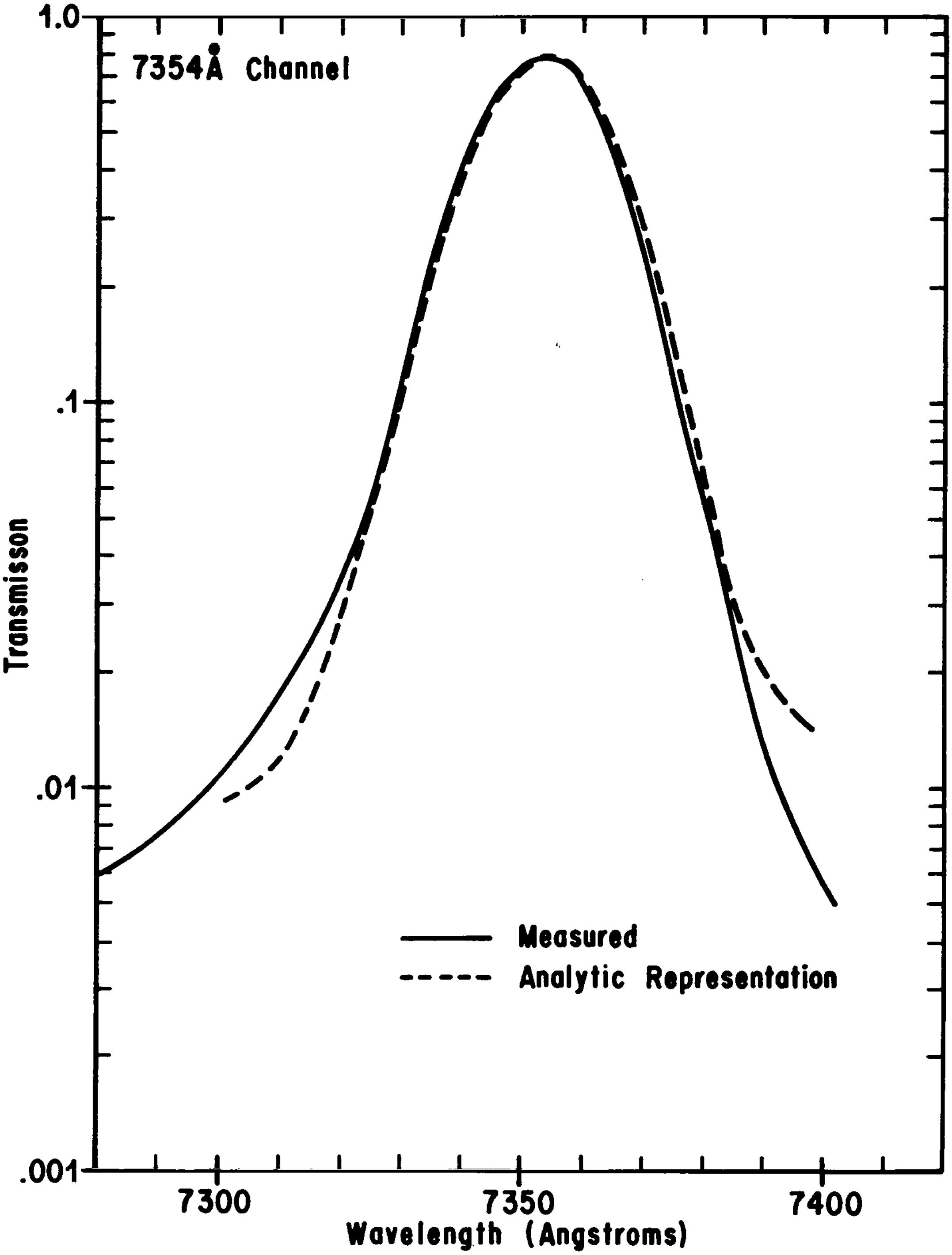

Figure 3-G. Transmission versus wavelength of the 7354Å channel for NASA 4.329.

$$T_{O^+} = \frac{A_{7319}}{A_{7319\text{-}30}} \cdot T_{7319} + \frac{A_{7330}}{A_{7319\text{-}30}} \cdot T_{7330} \quad , \qquad \text{(G-1)}$$

where A_λ has been previously defined (Appendix C) and T_λ represents the filter transmission at the line position of the particular emission. The effective transmission for the 7326Å channel ($T_{O^+}{}^{26}$) was .78 and for the 7354Å channel ($T_{O^+}{}^{54}$) was .068.

G.4 EFFECTIVE CHANNEL TRANSMISSIONS OF N_2 1PG

The effective N_2 1PG transmission for each channel was determined by modeling the N_2 1PG band system and finding the transmission of each rotational line of the band through a given filter. The N_2 1PG band model description, verification with laboratory spectra, and Fortran IV listing are in Appendix H. For each of the twenty-seven substates of the N_2 1PG band, twenty-nine rotational lines were computed and their effective transmission found. This process was performed for temperatures between 200°K and 1000°K, in 50°K increments to account for substate and rotational distribution changes effecting the band shape over the temperature range anticipated in the atmosphere.

Due to the number of transmission calculations involved, it was analytically expedient to fit the two filter transmission measurements and represent them analytically (the dashed curves of Figures 2-G and 3-G). The analytic representation permitted a transmission calculation for each line position versus a table look up and interpolated value from the measured profile.

To give perspective to the reader, the N_2 1PG$_{5,3}$ band is plotted in Figure 4-G for rotational distributions corresponding to 200°K and 700°K. The $O^+(^2P\text{-}^2D)$ wavelength positions and the peak bandpass locations of the photometer channels are also given.

The N_2 1PG$_{6,4}$ band (7274Å) also provides a background to the filters but to a lesser degree. Shemansky and Jones (1968) discuss relative band intensities and vibrational populations. Upon examining their discussion, the V=6 level was assumed to be populated 55% that of the V=5 level. This is further examined in the relative cross sections listed in Shemansky et. al. (1972). Considering the transition probabilities of N_2 1PG$_{5,3}$ and N_2 1PG$_{6,4}$ bands (Shemansky and Broadfoot, 1971), the intensity of the (6,4) was estimated at 16% that of the (5,3) band. The vibrational temperature range encountered in the atmosphere was not taken into account in this ratio, i.e., $I1PG_{6,4}/I1PG_{5,3} = .16 = \text{Constant}$.

Plotted in Figures 5-G and 6-G are the effective transmissions of the pertinent N_2 1PG bands for the 7326Å and 7354Å channels respectively. The temperature effect of the band on the effective transmission is most notable for the T < 600°K portion of the 7326Å channel. Although the N_2 1PG$_{6,4}$ transmission is ~ .3 the N_2 1PG$_{5,3}$ transmission for the 7326Å channel, the N_2 1PG$_{6,4}$ band strength is only ~ .16 that of the N_2 1PG$_{5,3}$.

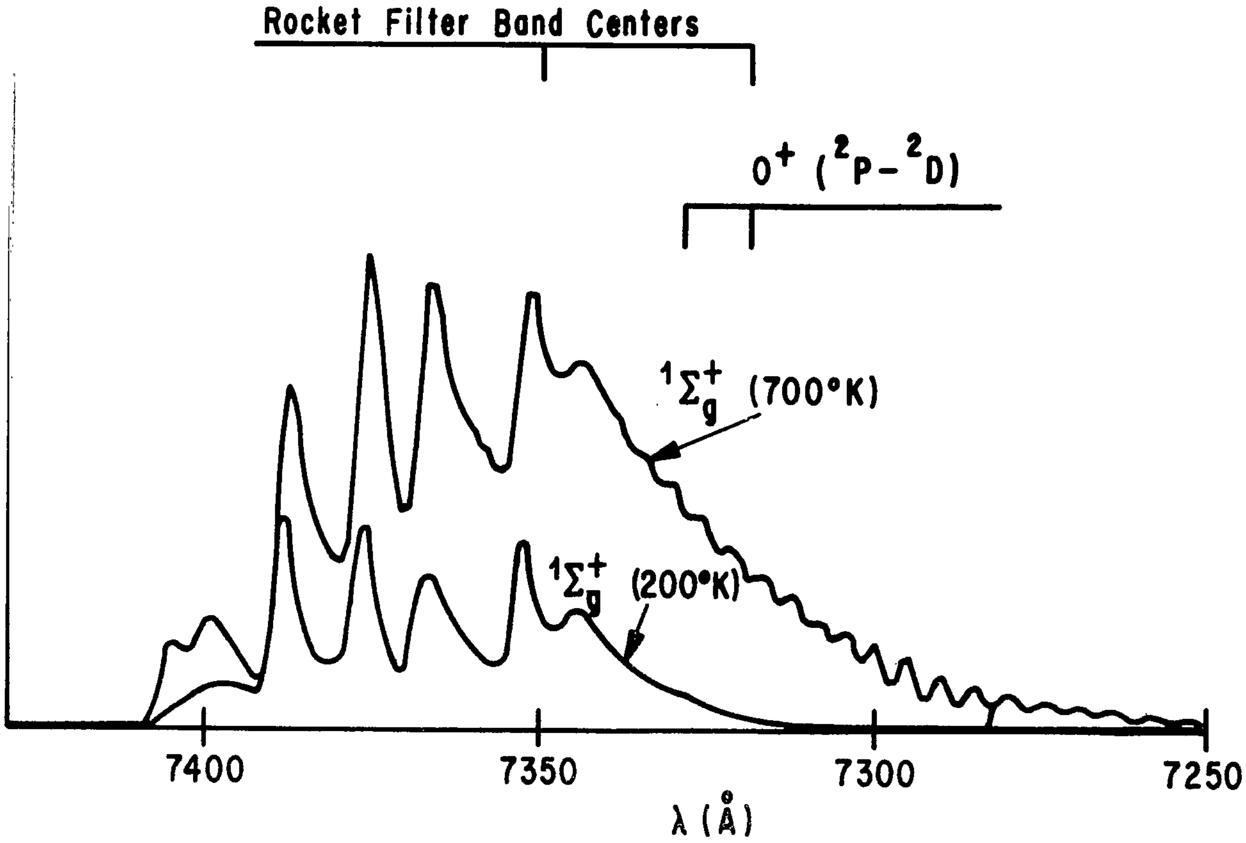

Figure 4-G. A 700°K and 200°K synthesis of N_2 1PG$_{5,3}$ with a 3Å triangular slit function. The rocket filter transmission peaks and the $O^+(^2P$-$^2D)$ emission line positions are noted in the figure.

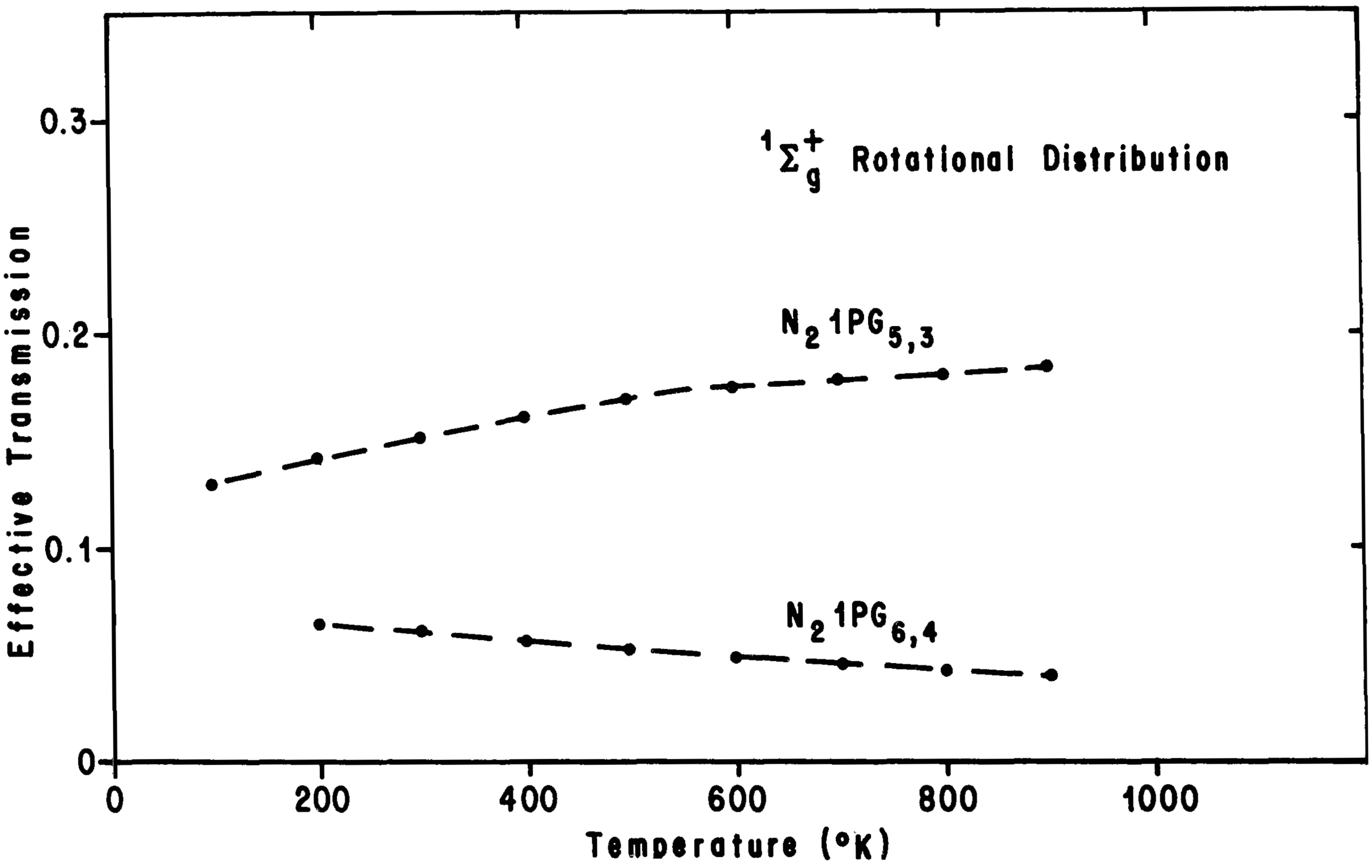

Figure 5-G. Effective transmission of N_2 1PG$_{5,3}$ versus temperature. The point plots are transmissions calculated for a temperature with the model using the analytic function plotted in Figure 2-G (7326Å channel). The dashed lines are linear legs used to represent the calculated values and values in between calculated points.

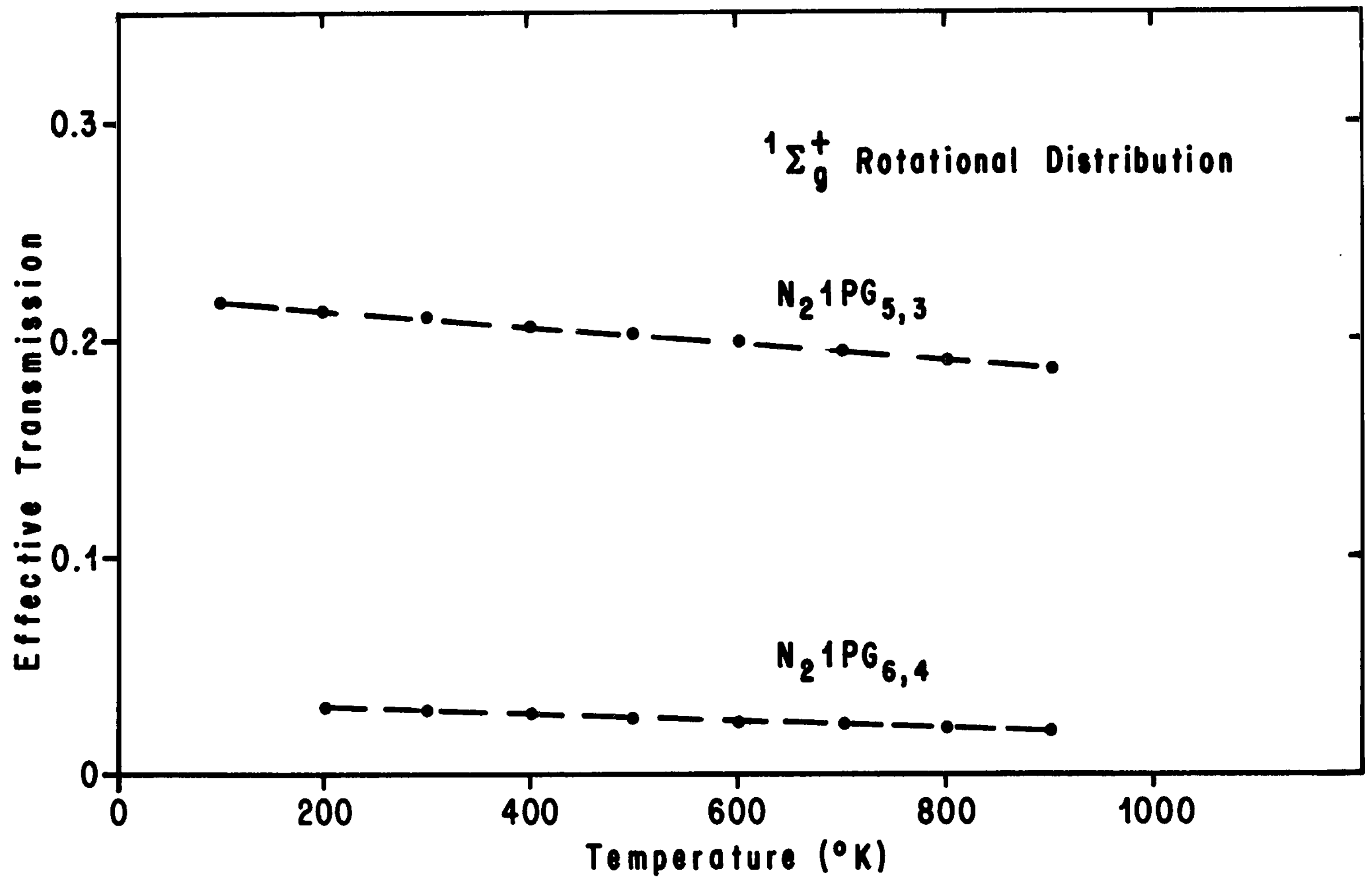

Figure 6-G. Same as in Figure 5-G, except for the analytic function plotted in Figure 3-G (7354Å channel).

G.5 REDUCTION OF $O^+(^2P\text{-}^2D)$ AND $N_2\,1PG_{5,3}$ INTENSITIES

This section will describe the deconvolution of the two emissions from the two (7326Å and 7354Å) channel signals.

The assumption was made that the only signal contribution to the two channels was due to the photon contribution resulting from the $O^+(^2P\text{-}^2D)$ and $N_2\,1PG$ emissions and the photomultiplier dark current. The dark current was measured on the payload and had been removed from the signal prior to plotting Figures 37 through 39 in Chapter VIII. The remaining signal may be equated to the sky brightness of the emissions (Intensity, i.e., $IO^+(^2P\text{-}^2D)$ for $O^+(^2P\text{-}^2D)$ emission and $I1PG$ for $N_2\,1PG$ band system in rayleighs), i.e.,

$$\frac{V}{SF} = I_{O^+(^2P\text{-}^2D)} \cdot T_{O^{+2}P} + I_{1PG} \cdot T_{1PG} \qquad \text{(G-2)}$$

where

V – the signal measured in a given channel (volts),

SF – sensitivity factor of the given channel, volts $\text{rayleigh}^{-1}\,\text{Å}^{-1}$ (Table 1-G),

$T_{O^{+2}P}, T_{1PG}$ – effective transmission of the system (subscript) for a given channel.

It was recognized in the previous subsection (G.4) that the first positive contribution was actually made by both the (5,3) and (6,4) bands. Equation (G-2) can then be rewritten as:

$$\frac{V}{SF} = I_{O^+(^2P\text{-}^2D)} \cdot T_{O^{+2}P} + I_{1PG_{5,3}} \cdot T_{1PG_{5,3}} + I_{1PG_{6,4}} \cdot T_{1PG_{6,4}} \qquad \text{(G-3)}$$

where the subscripts refer to the particular $N_2\,1PG$ band of a channel. It was further stipulated in the last section that the $I1PG_{6,4}$ band is weaker than the $I1PG_{5,3}$. Since a channel was not available to monitor its contribution to the other channels, it was assumed that

TABLE 1-G. CALIBRATION SENSITIVITIES FOR NASA 4.329 ROCKET PHOTOMETER

Channel	Sensitivity*
	(Volts per Rayliegh)
3914Å	.24
7326Å	.027
7354Å	.025

*Calibration error ±.003

$$I_{1PG_{6,4}} = .16\, I_{1PG_{5,3}} \quad . \tag{G-4}$$

Equation (G-3) now can be written as:

$$\frac{V}{SF} = I_{O^+(^2P\text{-}^2D)} \cdot T_{O^{+2}P} + I_{1PG_{5,3}} \left(T_{1PG_{5,3}} + .16\, T_{1PG_{6,4}}\right) \quad . \tag{G-5}$$

A cursory examination of the N_2 1PG effective transmissions of Figures 5-G and 6-G suggest $T_{1PG_{6,4}} \leqslant .3\, T_{1PG_{5,3}}$ or that the second term in the parenthesis of Equation (G-5) is 5% the first term.

Equation (G-5) can be written for each channel (7326Å and 7354Å). The respective channel signals (Figures 38 and 39), sensitivity factors (Table 1-G), effective $O^+(^2P\text{-}^2D)$ transmissions (Section G.3), and effective N_2 1PG transmissions (Section G.4 and Figures 5-G and 6-G) provide the necessary input for Equation (G-5) for both channels. The two channel equations (Equation G-5) can then be solved for the two emissions algebraically to yield:

$$I_{1PG_{5,3}} = \frac{\left(\dfrac{V^A}{SF^A \cdot T^A_{O^{+2}P}} - \dfrac{V_B}{SF^B \cdot T^B_{O^{+2}P}}\right)}{\left[\dfrac{\left(T^A_{1PG_{5,3}} + .16\, T^A_{1PG_{6,4}}\right)}{T^A_{O^{+2}P}} - \dfrac{\left(T^B_{1PG_{5,3}} + .16\, T_{1PG_{6,4}}\right)}{T^B_{O^{+2}P}}\right]} \tag{G-6}$$

and

$$I_{O^+(^2P\text{-}^2D)} = \frac{1}{T^A_{O^{+2}P}} \left[\frac{V^A}{SF^A} - I_{1PG_{5,3}} \left(T^B_{1PG_{5,3}} + .16\, T_{1PG_{6,4}} \right) \right] \qquad \text{(G-7)}$$

where superscripts A and B refer to the noted values of the 7326Å and 7354Å channels respectively.

The thermospheric temperature, as indicated by model atmospheres, changes by several hundred degrees over the altitude range of this measurement range. In Section G.4, the sensitivity of the effective transmission of the N_2 1PG band system to temperature in both photometer channels was discussed. In order to account for the temperature effect, it was assumed that the bulk of the N_2 1PG emission was originating from a half scale height above the payload for a given measurement altitude. It was further assumed that the effective temperature dictating the distribution of the N_2 1PG emission was that of the Jacchia (1971), $T_\infty = 1000°K$, model atmosphere. The nitrogen scale height was determined for a given measurement altitude, divided by two, and added to the measurement altitude to provide the reference temperature from the model atmosphere. The possible error induced in this method is discussed in the error analysis. All other inputs to Equations (G-5) and (G-6) were constant or were values at the measurement altitude.

The results of the data analysis of $N_2^+ 1NEG_{0,0}$ are plotted in Figure 41 of Chapter VII. The data is plotted only for the portion of the ascent in which the payload was in the aurora and not when it was being viewed from below. The solid curve drawn through the $O^+(^2P\text{-}^2D)$ data points is a hand drawn fit to the data.

G.6 ERROR ANALYSIS OF THE $O^+(^2P\text{-}^2D)$ PROFILE

A number of potential errors in the resultant $O^+(^2P\text{-}^2D)$ profile arise from the uncertainty in the quantity inputs of Equations (G-5) and (G-6) outlined in the previous section. The method used in treating these errors was to best estimate the potential deviation of the input parameter. The deviated value for that parameter was then input into Equations (G-6) and (G-7) with all other input quantities remaining fixed. A new $O^+(^2P\text{-}^2D)$ intensity profile was then computed, and the percent difference the resultant profile departed from the original $O^+(^2P\text{-}^2D)$ profile was computed.

One perturbation was made by increasing the model atmosphere temperature profile by 100°K, reflecting the rotational distribution or band shape effect of the N_2 1PG system. Additional perturbations were introduced by shifting the peak transmission of the photometer filters by 5Å, adding an additional 1% transmission to each photometer for N_2 1PG, and applying a ±12% uncertainty in the sensitivity factor. The percent deviations the perturbed profiles deviated from the original for each of these are listed in the first four columns of Table 2-G. Note that the model temperature assumption and the current leak error lead only to possible lower values of $O^+(^2P\text{-}^2D)$ emission than deduced. It was felt by the author that the exospheric temperature profile would not be less than the model assumption used in an auroral situation. Also note that the entire temperature profile was increased by 100°K for this error perturbation, rather than just the exospheric temperature. Ambient temperatures will tend to shift transmission peaks on filters. This reflects the second error perturbation. The third error, the current leak, accounts for the possibility that other emissions not treated here could be leaking through the filter wings and contributing to the signal. The sensitivity error results from the calibration source uncertainty (Table 1-G).

The statistical error or random error due to shot noise, counting statistics, transmitter noise, etc., is given in the last column of Table 2-G. As stated earlier, the data were reduced using the smoothed curve through the data points of Figures 37, 38, and 39. The data were also reduced using the actual measured values of Figures 37 through 39. The statistical error or scatter was determined as the deviation of the scattered input results to the measured $O^+(^2P\text{-}^2D)$ profile of Figure 41, where the curve in Figure 41 represents a hand fit smoothing of the results. The root sum square of all errors is displayed in the last column of Table 2-G.

TABLE 2-G. PERCENT ERRORS DEDUCED FOR $O^+(^2P-^2D)$ EMISSION DATA FROM NASA 4.329 ROCKET PHOTOMETER

Z(km)	Model Temperature (T, T + 100°K)	Filter Drift ±5Å	Current Leak $T_1PG = T_1PG + .01$	Calibration ±12%	Statistical Errors	$\sqrt{\Sigma(\text{Error})^2}$
120	-30%	±7%	-18%	±36%	±25%	+44%, -56%
140	-12%	±7%	-12%	±30%	±20%	+36%, -40%
160	-9%	±7%	-9%	±24%	±20%	+32%, - 34%

APPENDIX H

N_2 1PG$_{i,j}$ BAND MODEL

The N_2 1PG bands are very broad and contain twenty-seven branches of comparable intensity. The energy equations for the $B^3\pi_g$ state are given by Budo (1935, 1936) and for the $A^3\Sigma_u^+$ state by Schlapp (1927). The line strength factors as theoretically determined by Budo (1937) for Hund's case (a) and (b) coupling were used. The molecular constants used were those summarized by Shemansky and Jones (1968).

The model was verified by running a 3Å triangular slit function through the (1,0) band and comparing it against the data of Vallance Jones given by the Shemansky and Carleton (1969). The synthesis is shown in Figure 1-C where the $B^3\pi_g$ rotation equilibrium is depicted against a near 400°K spectra. Some slight mismatch is evident but considered insignificant for purposes of this analysis. N_2 1PG spectra in aurora has been discussed by Shemansky and Jones (1968). Their spectra suggests the N_2 1PG is in the ground state distribution ($^1\Sigma_g^+$). Transition probabilities for first positive, as measured by Shemansky and Broadfoot (1971), are too large to permit rotational relaxation to the $B^3\pi_g$ state prior to emission at collision frequencies corresponding to altitudes above 90 km. A Fortran IV program listing of the model follows Figure 1-H.

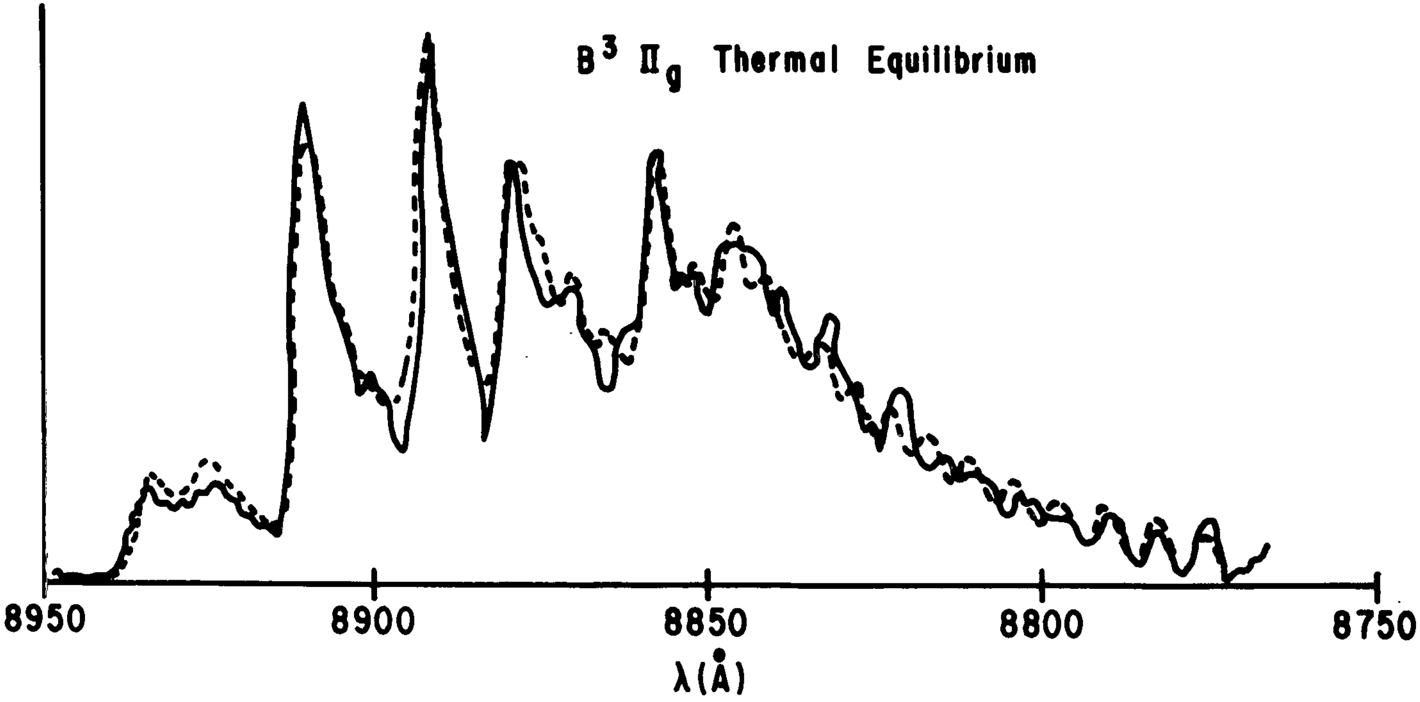

Figure 1-H. Dark line is 400°K spectra of Vallance Jone's as shown in Shemansky and Carleton (1969). The dashed line is a synthesis of N_2 $1PG_{1,0}$ as modeled utilizing a 3Å triangular slit function.

FORTRAN SOURCE LIST

```
      DIMENSION FG(30)
      DIMENSION AR11(30),AQ11(30),AP11(30),AR12(30),AQ12(30),AP12(30),AR
     113(30),AQ13(30),AP13(30),AR21(30),AQ21(30),AP21(30),AR22(30),AQ22(
     230),AP22(30),AR23(30),AQ23(30),AP23(30),AR31(30),AQ31(30),AP31(30)
     3,AR32(30),AQ32(30),AP32(30),AR33(30),AQ33(30),AP33(30)
      DIMENSION FU1(30),FU2(30),FU3(30),FL1(30),FL2(30),FL3(30),P11(30),
     1Q11(30),R11(30),P22(30),Q22(30),R22(30),P33(30),Q33(30),R33(30),P1
     22(30),Q12(30),R12(30),P13(30),Q13(30),R13(30),P21(30),Q21(30),R21(
     330),P31(30),Q31(30),R31(30),P32(30),Q32(30),R32(30),P23(30),Q23(30
     4),R23(30),XU1(30),XU2(30),XU3(30)
      DIMENSION XP11(30),XQ11(30),XR11(30),XP22(30),XQ22(30),XR22(30),XP
     133(30),XQ33(30),XR33(30),XP13(30),XQ13(30),XR13(30),XP12(30),XQ12(
     230),XR12(30),XP23(30),XQ23(30),XR23(30),XP31(30),XQ31(30),XR31(30)
     3,XP32(30),XQ32(30),XR32(30),XP21(30),XQ21(30),XR21(30)
      DIMENSION XP(3,3,30),XQ(3,3,30),XR(3,3,30),YP(3,3,30),YQ(3,3,30),Y
     1R(3,3,30),PP(3,3,30),QQ(3,3,30),RR(3,3,30)
      DIMENSION SP(3,3,30),SQ(3,3,30),SR(3,3,30)
C     CONSTANTS FOR THE UPPER AND LOWER STATES WERE GIVEN BY SHEMANSKY
C     CONSTANTS FOR THE UPPER AND LOWER STATES WERE GIVEN BY SHEMANSKY
C     AND JONES(1968,PLANET. SPACE SCI.,PP.1115)
      R=100.
      SL=2.99776E+10
      BK=1.36033E-16
      H=6.2234E-27
      E=H*SL/BK
      BEU=1.63748
      BEL=1.4545
      AU=.01794
      AL=.01796
      GAL=-.003
      GAM=-8.44E-05
      DEU=5.80E-06
      BETU=3.7E-08
    9 CONTINUE
C     READ UPPER AND LOWER VIBRATIONAL LEVELS AND TEMPERATURE
      READ(5,17)VU,VL,T
   17 FORMAT(F3.0,F3.0,1X,F5.0)
      WRITE(6,200)
  200 FORMAT(1H1)
      IT=T
      IF(IT.EQ.999)GO TO 99
C     COMPUTE WAVENUMBERS OF VIBRATION
      TEU=59621.51
      TEL=59205.96
      WU=1733.92
      WXU=14.399
      WYU=-.00401
      WZU=.000513
      WL=1460.62
      WXL=13.651
      WYL=.00625
      WZL=.00172
      WNU=TEU+WU*(VU+.5)-WXU*(VU+.5)**2.+WYU*(VU+.5)**3.-WZU*(VU+.5)**4.
      WNL=TEL+WL*(VL+.5)-WXL*(VL+.5)**2.+WYL*(VL+.5)**3.-WZL*(VL+.5)**4.
```

```
      DWN=WNU-WNL
      WNA=1./(DWN*1.0E-08)
      WRITE(6,7)VU,VL,T,WNA
    7 FORMAT(1X,4HBAND,F3.0,F3.0,10X,5HTEMP=,F5.0,10X,10HBAND HEAD=,F6.0
     1)
C     COMPUTE VIB DISTRIBUTION OF GROUND STATE
      TPI=6.2831
      E1=E/TPI
      WG=2359.61
      WXG=14.456
      WYG=.00751
      GGV=WG*(VU+.5)-WXG*(VU+.5)**2.+WYG*(VU+.5)**3.
      SG=0.0
      DO 2 I=1,10
      V=I
      X=V+.5
      GV=WG*X-WXG*(X**2.)+WYG*(X**3.)
      G=EXP(-GV*E1/T)
      SG=SG+G
    2 CONTINUE
      GN=1000.*EXP(-GGV*E1/T)/SG
      WRITE(6,75)GN
   75 FORMAT(9X,17H VIBRATION INTEN=,E10.3)
C     COMPUTE ROT ENERGIES IN GROUND STATE
C     A 1 IN COL. 20 WILL GIVE ROT DISTRIBUTION OF EXCITED STATE
      BVU=BEU-AU*(VU+.5)
      BVL=BEL-AL*(VL+.5)
      ALL=-1.335+.007*VL
      YU=25.68+.253*VU+.0028*(VU**2.)
      DVU=DEU+BETU*(VU+.5)
      BEG=2.010
      AEG=.0167
      DVG=(5.8-.001*(VU+.5))*1.0E-06
      BVG=BEG-AEG*(VU+.5)
      DO 19 J=1,30
      A=J-1
      FG(J)=BVG*A*(A+1.)-DVG*A*A*(A+1.)**2.
   19 CONTINUE
      WRITE(6,13)(FG(J),J=1,15)
   13 FORMAT(1X,15F7.0)
      WRITE(6,13)(FG(J),J=16,30)
C     COMPUTE ROT ENERGIES OF LOWER STATE OF TRANSITION
C     THE ROT LEVELS OF TRIP SIG STATE ARE GIVEN BY SCHLAPP(1937,PHYS.
C     REV.)
      DO 3 K=2,30
      D=K-2
      ALT=ABS(ALL)
      SR1=(((2.*D+3.)**2.)*(BVL**2.)+(ALT**2.)-(2.*ALL*BVL))**.5
      SR11=ABS(SR1)
      FL1(K)=BVL*D*(D+1.)+(2.*D+3.)*BVL-ALL-SR11+GAM*(D+1.)
    3 CONTINUE
      FL1(1)=0.0
      DO 4 K=1,30
      D=K-1
      FL1(K)=BVL*D*(D+1.)
```

```
    4 CONTINUE
      DO 5 K=1,30
      D=K
      ALT=ABS(ALL)
      PIP=ABS(2.*D-1.)
      SR2=((PIP**2.)*(BVL**2.)+(ALT**2.)-(2.*ALL*BVL))**.5
      SR22=ABS(SR2)
      FL3(K)=BVL*D*(D+1.)-(2.*D-1.)*BVL-ALL+SR22-GAM*D
    5 CONTINUE
      BB=BVL**2.+ALT**2.-2.*ALL*BVL
      RRR=ABS(BB)
      FL3(1)=BVL-ALL-(RRR**.5)-GAM
C     COMPUTE ROT ENERGIES OF UPPER STATE OF TRANSITION
C     THE ROT LEVELS OF TRIP PI STATE ARE GIVEN BY BUDO(1935,1936,Z.
C     PHYSIK)
      DO 11 J=1,30
      D=J-1
      Y1=YU*(YU-4.)+4./3.
      Y2=YU*(YU-1.)-4./9.
      YY=(Y2-2.*D*(D+1.))/(Y1+4.*D*(D+1.))
      YZ=(Y1+4.*D*(D+1.))
      YYZ=(ABS(YZ))**.5
      FU1(J)=BVU*(D*(D+1.)-YYZ-(2.*YY/3.))
   11 CONTINUE
      DO 10 J=1,30
      D=J-1
      Y1=4./3.
      Y2=-4./9.
      YY=(Y2-2.*D*(D+1.))/(Y1+4.*D*(D+1.))
      FU2(J)=BVU*(D*(D+1.)+(4.*YY/3.))
   10 CONTINUE
      DO 8 J=1,30
      D=J-1
      Y1=YU*(YU-4.)+4./3.
      Y2=YU*(YU-1.)-4./9.
      YY=(Y2-2.*D*(D+1.))/(Y1+4.*D*(D+1.))
      YZ=(Y1+4.*D*(D+1.))
      YYZ=(ABS(YZ))**.5
      FU3(J)=BVU*(D*(D+1.)+YYZ-(2.*YY/3.))
    8 CONTINUE
      DWN1=DWN
      DWN2=DWN
      DWN3=DWN
C     COMPUTE LINE STRENGTHS FOR 27 BRANCHES
C     LINE STRENGTH FACTORS ARE GIVEN BY BUDO(1937,Z.PHYSIK)
      DO 70 K=2,30
      D=K-1
      U1=(YU*(YU-4.)+4.*D**2.)**.5
      U3=(YU*(YU-4.)+4.*(D+1.)**2.)**.5
      C1=D*(D+1.)*YU*(YU-4.)+2.*(2.*D+1.)*(D-1.)*D*(D+1.)
      C2=YU*(YU-4.)+4.*D*(D+1.)
      C3=(D-1.)*(D+2.)*YU*(YU-4.)+2.*(2.*D+1.)*D*(D+1.)*(D+2.)
      ZIP=YU*(YU-4.)+4.*D*D
      ZIT=ABS(ZIP)
      CRU=(YU-2.)*((ZIT)**.5)-YU*(YU-4.)+4.*D
```

```
      C1=C1+CRU
      C3=C3+CRU
      BIL=D**2.
      AQ11(K)=(((BIL+D-1.)*U1+(YU-2.)+2.*D*(D*D-1.))**2.)/(D*C1)
      AQ22(K)=(8.*(2.*D+1.)*(D*D+D-1.)**2.)/(D*(D+1.)*C2)
      AQ33(K)=(((D*D+D-1.)*U3-(YU-2.)+2.*D*(D+1.)*(D+2.))**2.)/((D+1.)*C
     13)
      AQ12(K)=((2.*D+1.)*((D*D+D-1.)*(YU-2.)+U1)**2.)/(D*(D+1.)*C1)
      AQ13(K)=(((D*D+D-1.)*U1+(YU-2.)-2.*(D-1.)*(D+1.)**2.)**2.)/((D+1.)
     1*C1)
      AQ21(K)=(2.*(D*(YU-2.)-2.)**2.)/(D*C2)
      BI1=((D*D+D-1.)*(YU-2.)-U3)
      BI2=ABS(BI1)
      AQ32(K)=((2.*D+1.)*(BI2**2.))/(D*(D+1.)*C3)
      AQ23(K)=(2.*((D+1.)*YU-2.*D)**2.)/((D+1.)*C2)
      BJ1=(D*D+D-1.)*U3-(YU-2.)-2.*D*D*(D+2.)
      BJ2=ABS(BJ1)
      AQ31(K)=(BJ2**2.)/(D*C3)
   70 CONTINUE
      DO 71 J=2,30
      D=J
      U1=(YU*(YU-4.)+4.*D**2.)**.5
      U3=(YU*(YU-4.)+4.*(D+1.)**2.)**.5
      C1=D*(D+1.)*YU*(YU-4.)+2.*(2.*D+1.)*(D-1.)*D*(D+1.)
      C2=YU*(YU-4.)+4.*D*(D+1.)
      C3=(D-1.)*(D+2.)*YU*(YU-4.)+2.*(2.*D+1.)*D*(D+1.)*(D+2.)
      ZIP=YU*(YU-4.)+4.*D*D
      ZIT=ABS(ZIP)
      CRU=(YU-2.)*((ZIT)**.5)-YU*(YU-4.)+4.*D
      C1=C1+CRU
      C3=C3+CRU
      BIL=D**2.
      AR11(J)=((BIL-1.)*((D+1.)*U1-YU+2.*BIL)**2.)/(C1*(2.*D-1.))
      AR22(J)=(8.*(D-1.)*(D+1.)**3.)/(D*C2)
      AR33(J)=((D+1.)*((D*D-1.)*U3+(D-1.)*(YU-2.)+2.*D*D*(D+2.))**2.)/(D
     1*(2.*D-1.)*C3)
      AR12(J)=((D*D-1.)*((D+1.)*(YU-2.)-U1)**2.)/(D*C1)
      AR13(J)=(((D-1.)**2.)*(D+1.)*((D+1.)*U1-(YU-2.)-2.*D*(D+1.))**2.)/
     1(D*(2.*D-1.)*C1)
      AR21(J)=(2.*(D*D-1.)*YU*YU)/((2.*D-1.)*C2)
      AR32(J)=((D*D-1.)*(U3+(D+1.)*(YU-2.))**2.)/(D*C3)
      AR23(J)=(2.*(D+1.)*(D*(YU-4.)+2.)**2.)/(D*(2.*D-1.)*C2)
      AR31(J)=((D*D-1.)*((D+1.)*U3+(YU-2.)-2.*D*(D+2.))**2.)/((2.*D-1.)*
     1C3)
   71 CONTINUE
      DO 72 L=2,30
      D=L-2
      U1=(YU*(YU-4.)+4.*D**2.)**.5
      U3=(YU*(YU-4.)+4.*(D+1.)**2.)**.5
      C1=D*(D+1.)*YU*(YU-4.)+2.*(2.*D+1.)*(D-1.)*D*(D+1.)
      C2=YU*(YU-4.)+4.*D*(D+1.)
      C3=(D-1.)*(D+2.)*YU*(YU-4.)+2.*(2.*D+1.)*D*(D+1.)*(D+2.)
      ZIP=YU*(YU-4.)+4.*D*D
      ZIT=ABS(ZIP)
      CRU=(YU-2.)*((ZIT)**.5)-YU*(YU-4.)+4.*D
```

```
      C1=C1+CRU
      C3=C3+CRU
      AP11(L)=(D*(D*(D+2.)*U1+(D+2.)*(YU-2.)+2.*(D-1.)*(D+1.)*(D+1.))**2
     1.)/((D+1.)*(2.*D+3.)*C1)
      AP22(L)=(6.*D*D*D*(D+2.))/((D+1.)*C2)
      BK1=D*U3-(YU-2.)+2.*D*(D+2.)
      BK2=ABS(BK1)
      AP33(L)=(D*(D+2.)*(BK2**2.))/((2.*D+3.)*C3)
      AP12(L)=(D*(D+2.)*(D*(YU-2.)+U1)**2.)/((D+1.)*C1)
      AP13(L)=(D*(D+2.)*(D*U1+YU-2.*D*D)**2.)/((2.*D+3.)*C1)
      AP21(L)=(2.*D*((D+1.)*YU-2.*(2.*D+3.))**2.)/((D+1.)*(2.*D+3.)*C2)
      BL1=D*(YU-2.)-U3
      BL2=ABS(BL1)
      AP32(L)=(D*(D+2.)*(BL2**2.))/((D+1.)*C3)
      AP23(L)=(2.*D*(D+2.)*YU*YU)/((2.*D+3.)*C2)
      BM1=D*U3-(YU-2.)-2.*D*(D+1.)
      BM2=ABS(BM1)
      AP31(L)=(D*((D+2.)**2.)*(BM2**2.))/((D+1.)*(2.*D+3.)*C3)
   72 CONTINUE
C     COMPUTE WAVE NUMBERS FOR 27 BRANCHES FOR 29 ROT. SUBSTATES
      DO 21 L=2,29
      I=L+1
      N=L-1
      M=L+1
      K=L-1
      Q22(L)=DWN2+FU2(L)-FL2(L)
      XQ22(L)=R*AQ22(L)*EXP(-FG(L)*E/T)
      R33(L)=DWN3+FU3(M)-FL3(L)
      XR33(L)=R*AR33(L)*EXP(-FG(I)*E/T)
      Q21(L)=DWN2+FU2(L)-FL1(L)
      XQ21(L)=R*AQ21(L)*EXP(-FG(L)*E/T)
      R32(L)=DWN3+FU3(M)-FL2(L)
      XR32(L)=R*AR32(L)*EXP(-FG(I)*E/T)
      Q23(L)=DWN2+FU2(L)-FL3(L)
      XQ23(L)=R*AQ23(L)*EXP(-FG(L)*E/T)
      R31(L)=DWN3+FU3(M)-FL1(L)
      XR31(L)=R*AR31(L)*EXP(-FG(I)*E/T)
      Q11(L)=DWN1+FU1(L)-FL1(L)
      XQ11(L)=R*AQ11(L)*EXP(-FG(L)*E/T)
      R11(L)=DWN1+FU1(M)-FL1(L)
      XR11(L)=R*AR11(L)*EXP(-FG(I)*E/T)
      R22(L)=DWN2+FU2(M)-FL2(L)
      XR22(L)=R*AR22(L)*EXP(-FG(I)*E/T)
      Q12(L)=DWN1+FU1(L)-FL2(L)
      XQ12(L)=R*AQ12(L)*EXP(-FG(L)*E/T)
      R12(L)=DWN1+FU1(M)-FL2(L)
      XR12(L)=R*AR12(L)*EXP(-FG(I)*E/T)
      Q13(L)=DWN1+FU1(L)-FL3(L)
      XQ13(L)=R*AO13(L)*EXP(-FG(L)*E/T)
      R13(L)=DWN1+FU1(M)-FL3(L)
      XR13(L)=R*AR13(L)*EXP(-FG(I)*E/T)
      R21(L)=DWN2+FU2(M)-FL1(L)
      XR21(L)=R*AR21(L)*EXP(-FG(I)*E/T)
      R23(L)=DWN2+FU2(M)-FL3(L)
      XR23(L)=R*AR23(L)*EXP(-FG(I)*E/T)
```

```
   21 CONTINUE
      DO 22 L=3,29
      I=L+1
      N=L-1
      M=L+1
      K=L-1
      P22(L)=DWN2+FU2(K)-FL2(L)
      XP22(L)=R*AP22(L)*EXP(-FG(N)*E/T)
      Q33(L)=DWN3+FU3(L)-FL3(L)
      XQ33(L)=R*AQ33(L)*EXP(-FG(L)*E/T)
      P21(L)=DWN2+FU2(K)-FL1(L)
      XP21(L)=R*AP21(L)*EXP(-FG(N)*E/T)
      Q32(L)=DWN3+FU3(L)-FL2(L)
      XQ32(L)=R*AQ32(L)*EXP(-FG(L)*E/T)
      P23(L)=DWN2+FU2(K)-FL3(L)
      XP23(L)=R*AP23(L)*EXP(-FG(N)*E/T)
      Q31(L)=DWN3+FU3(L)-FL1(L)
      XQ31(L)=R*AQ31(L)*EXP(-FG(L)*E/T)
      P11(L)=DWN1+FU1(K)-FL1(L)
      XP11(L)=R*AP11(L)*EXP(-FG(N)*E/T)
      P12(L)=DWN1+FU1(K)-FL2(L)
      XP12(L)=R*AP12(L)*EXP(-FG(N)*E/T)
      P13(L)=DWN1+FU1(K)-FL3(L)
      XP13(L)=R*AP13(L)*EXP(-FG(N)*E/T)
   22 CONTINUE
      DO 23 L=4,29
      I=L+1
      N=L-1
      M=L+1
      K=L-1
      P33(L)=DWN3+FU3(K)-FL3(L)
      XP33(L)=R*AP33(L)*EXP(-FG(N)*E/T)
      P32(L)=DWN3+FU3(K)-FL2(L)
      XP32(L)=R*AP32(L)*EXP(-FG(N)*E/T)
      P31(L)=DWN3+FU3(K)-FL1(L)
      XP31(L)=R*AP31(L)*EXP(-FG(N)*E/T)
   23 CONTINUE
      CON=1.0E+08
C     CONVERT TO ANGSTROMS
      DO 30 K=1,29
      Q11(K)=CON/Q11(K)
      R11(K)=CON/R11(K)
      R22(K)=CON/R22(K)
      Q12(K)=CON/Q12(K)
      R12(K)=CON/R12(K)
      Q13(K)=CON/Q13(K)
      R13(K)=CON/R13(K)
      R21(K)=CON/R21(K)
      R23(K)=CON/R23(K)
   30 CONTINUE
      DO 26 K=2,29
      P11(K)=CON/P11(K)
      Q22(K)=CON/Q22(K)
      R33(K)=CON/R33(K)
      P12(K)=CON/P12(K)
```

```
      P13(K)=CON/P13(K)
      Q21(K)=CON/Q21(K)
      R32(K)=CON/R32(K)
      Q23(K)=CON/Q23(K)
      R31(K)=CON/R31(K)
   26 CONTINUE
      DO 27 K=3,29
      P22(K)=CON/P22(K)
      Q33(K)=CON/Q33(K)
      P21(K)=CON/P21(K)
      Q32(K)=CON/Q32(K)
      P23(K)=CON/P23(K)
      Q31(K)=CON/Q31(K)
   27 CONTINUE
      DO 28 K=4,29
      P33(K)=CON/P33(K)
      P32(K)=CON/P32(K)
      P31(K)=CON/P31(K)
   28 CONTINUE
      READ(5,159)SW,IROT,NEND,A
  159 FORMAT(2X,F6.1,12X,I1,2X,I3,2X,F6.0)
      IF(IROT.EQ.0) GO TO 310
      DO 311 J=2,30
      K=J-1
      L=J+1
      XP11(J)=R*AP11(J)*EXP(-FU1(K)*E/T)
      XQ11(J)=R*AQ11(J)*EXP(-FU1(J)*E/T)
      XR11(J)=R*AR11(J)*EXP(-FU1(L)*E/T)
      XP22(J)=R*AP22(J)*EXP(-FU2(K)*E/T)
      XQ22(J)=R*AQ22(J)*EXP(-FU2(J)*E/T)
      XR22(J)=R*AR22(J)*EXP(-FU2(L)*E/T)
      XP33(J)=R*AP33(J)*EXP(-FU3(K)*E/T)
      XQ33(J)=R*AQ33(J)*EXP(-FU3(J)*E/T)
      XR33(J)=R*AR33(J)*EXP(-FU3(L)*E/T)
      XP12(J)=R*AP12(J)*EXP(-FU1(K)*E/T)
      XQ12(J)=R*AQ12(J)*EXP(-FU1(J)*E/T)
      XR12(J)=R*AR12(J)*EXP(-FU1(L)*E/T)
      XP13(J)=R*AP13(J)*EXP(-FU1(K)*E/T)
      XQ13(J)=R*AQ13(J)*EXP(-FU1(J)*E/T)
      XR13(J)=R*AR13(J)*EXP(-FU1(L)*E/T)
      XP23(J)=R*AP23(J)*EXP(-FU2(K)*E/T)
      XQ23(J)=R*AQ23(J)*EXP(-FU2(J)*E/T)
      XR23(J)=R*AR23(J)*EXP(-FU2(L)*E/T)
      XP31(J)=R*AP31(J)*EXP(-FU3(K)*E/T)
      XQ31(J)=R*AQ31(J)*EXP(-FU3(J)*E/T)
      XR31(J)=R*AR31(J)*EXP(-FU3(L)*E/T)
      XP32(J)=R*AP32(J)*EXP(-FU3(K)*E/T)
      XQ32(J)=R*AQ32(J)*EXP(-FU3(J)*E/T)
      XR32(J)=R*AR32(J)*EXP(-FU3(L)*E/T)
      XP21(J)=R*AP21(J)*EXP(-FU2(K)*E/T)
      XQ21(J)=R*AQ21(J)*EXP(-FU2(J)*E/T)
      XR21(J)=R*AR21(J)*EXP(-FU2(L)*E/T)
  311 CONTINUE
  310 CONTINUE
C     LIST RESULTS
```

```
 575     31 FORMAT (3X,15F7.0)
 576     32 FORMAT(3X,15F7.0)
 577     52 FORMAT(10X,14F7.0)
 600     53 FORMAT(17X,13F7.0)
 601     54 FORMAT(23X,12F7.0)
 602     55 FORMAT(3X,14F7.0)
 603        WRITE(6,14)(J,J=1,15)
 610     14 FORMAT(3X,15I7)
 611        WRITE(6,15)(J,J=16,29)
 616     15 FORMAT(3X,14I7)
 617        WRITE(6,101)
 620    101 FORMAT(4H P11)
 621        WRITE(6,53)(P11(K),K=3,15)
 626        WRITE(6,53)(XP11(L),L=3,15)
 633        WRITE(6,55)(P11(K),K=16,29)
 640        WRITE(6,55)(XP11(L),L=16,29)
 645        WRITE(6,102)
 646    102 FORMAT(4H Q11)
 647        WRITE(6,52)(Q11(K),K=2,15)
 654        WRITE(6,52)(XQ11(L),L=2,15)
 661        WRITE(6,55)(Q11(K),K=16,29)
 666        WRITE(6,55)(XQ11(L),L=16,29)
 673        WRITE(6,103)
 674    103 FORMAT(4H R11)
 675        WRITE(6,52)(R11(K),K=2,15)
 702        WRITE(6,52)(XR11(L),L=2,15)
 707        WRITE(6,55)(R11(K),K=16,29)
 714        WRITE(6,55)(XR11(L),L=16,29)
 721        WRITE(6,104)
 722    104 FORMAT(4H P22)
 723        WRITE(6,53)(P22(K),K=3,15)
 730        WRITE(6,53)(XP22(L),L=3,15)
 735        WRITE(6,55)(P22(K),K=16,29)
 742        WRITE(6,55)(XP22(L),L=16,29)
 747        WRITE(6,105)
 750    105 FORMAT(4H Q22)
 751        WRITE(6,52)(Q22(K),K=2,15)
 756        WRITE(6,52)(XQ22(L),L=2,15)
 763        WRITE(6,55)(Q22(K),K=16,29)
 770        WRITE(6,55)(XQ22(L),L=16,29)
 775        WRITE(6,106)
 776    106 FORMAT(4H R22)
 777        WRITE(6,52)(R22(K),K=2,15)
1004        WRITE(6,52)(XR22(L),L=2,15)
1011        WRITE(6,55)(R22(K),K=16,29)
1016        WRITE(6,55)(XR22(L),L=16,29)
1023        WRITE(6,107)
1024    107 FORMAT(4H P33)
1025        WRITE(6,54)(P33(K),K=4,15)
1032        WRITE(6,54)(XP33(L),L=4,15)
1037        WRITE(6,55)(P33(K),K=16,29)
1044        WRITE(6,55)(XP33(L),L=16,29)
1051        WRITE(6,108)
1052    108 FORMAT(4H Q33)
1053        WRITE(6,53)(Q33(K),K=3,15)
```

```
1060          WRITE(6,53)(XQ33(L),L=3,15)
1065          WRITE(6,55)(Q33(K),K=16,29)
1072          WRITE(6,55)(XQ33(L),L=16,29)
1077          WRITE(6,109)
1100     109  FORMAT(4H R33)
1101          WRITE(6,52)(R33(K),K=2,15)
1106          WRITE(6,52)(XR33(L),L=2,15)
1113          WRITE(6,55)(R33(K),K=16,29)
1120          WRITE(6,55)(XR33(L),L=16,29)
1125          WRITE(6,200)
1126          WRITE(6,110)
1127     110  FORMAT(4H P12)
1130          WRITE(6,53)(P12(K),K=3,15)
1135          WRITE(6,53)(XP12(L),L=3,15)
1142          WRITE(6,55)(P12(K),K=16,29)
1147          WRITE(6,55)(XP12(L),L=16,29)
1154          WRITE(6,111)
1155     111  FORMAT(4H Q12)
1156          WRITE(6,52)(Q12(K),K=2,15)
1163          WRITE(6,52)(XQ12(L),L=2,15)
1170          WRITE(6,55)(Q12(K),K=16,29)
1175          WRITE(6,55)(XQ12(L),L=16,29)
1202          WRITE(6,112)
1203     112  FORMAT(4H R12)
1204          WRITE(6,52)(R12(K),K=2,15)
1211          WRITE(6,52)(XR12(L),L=2,15)
1216          WRITE(6,55)(R12(K),K=16,29)
1223          WRITE(6,55)(XR12(L),L=16,29)
1230          WRITE(6,113)
1231     113  FORMAT(4H P13)
1232          WRITE(6,53)(P13(K),K=3,15)
1237          WRITE(6,53)(XP13(L),L=3,15)
1244          WRITE(6,55)(P13(K),K=16,29)
1251          WRITE(6,55)(XP13(L),L=16,29)
1256          WRITE(6,114)
1257     114  FORMAT(4H Q13)
1260          WRITE(6,52)(Q13(K),K=2,15)
1265          WRITE(6,52)(XQ13(L),L=2,15)
1272          WRITE(6,55)(Q13(K),K=16,29)
1277          WRITE(6,55)(XQ13(L),L=16,29)
1304          WRITE(6,115)
1305     115  FORMAT(4H R13)
1306          WRITE(6,52)(R13(K),K=2,15)
1313          WRITE(6,52)(XR13(L),L=2,15)
1320          WRITE(6,55)(R13(K),K=16,29)
1325          WRITE(6,55)(XR13(L),L=16,29)
1332          WRITE(6,116)
1333     116  FORMAT(4H P21)
1334          WRITE(6,53)(P21(K),K=3,15)
1341          WRITE(6,53)(XP21(L),L=3,15)
1346          WRITE(6,55)(P21(K),K=16,29)
1353          WRITE(6,55)(XP21(L),L=16,29)
1360          WRITE(6,117)
1361     117  FORMAT(4H Q21)
1362          WRITE(6,52)(Q21(K),K=2,15)
```

```
1367          WRITE(6,52)(XQ21(L),L=2,15)
1374          WRITE(6,55)(Q21(K),K=16,29)
1401          WRITE(6,55)(XQ21(L),L=16,29)
1406          WRITE(6,118)
1407      118 FORMAT(4H R21)
1410          WRITE(6,52)(R21(K),K=2,15)
1415          WRITE(6,52)(XR21(L),L=2,15)
1422          WRITE(6,55)(R21(K),K=16,29)
1427          WRITE(6,55)(XR21(L),L=16,29)
1434          WRITE(6,200)
1435          WRITE(6,119)
1436      119 FORMAT(4H P32)
1437          WRITE(6,54)(P32(K),K=4,15)
1444          WRITE(6,54)(XP32(L),L=4,15)
1451          WRITE(6,55)(P32(K),K=16,29)
1456          WRITE(6,55)(XP32(L),L=16,29)
1463          WRITE(6,120)
1464      120 FORMAT(4H Q32)
1465          WRITE(6,53)(Q32(K),K=3,15)
1472          WRITE(6,53)(XQ32(L),L=3,15)
1477          WRITE(6,55)(Q32(K),K=16,29)
1504          WRITE(6,55)(XQ32(L),L=16,29)
1511          WRITE(6,121)
1512      121 FORMAT(4H R32)
1513          WRITE(6,52)(R32(K),K=2,15)
1520          WRITE(6,52)(XR32(L),L=2,15)
1525          WRITE(6,55)(R32(K),K=16,29)
1532          WRITE(6,55)(XR32(L),L=16,29)
1537          WRITE(6,122)
1540      122 FORMAT(4H P23)
1541          WRITE(6,53)(P23(K),K=3,15)
1546          WRITE(6,53)(XP23(L),L=3,15)
1553          WRITE(6,55)(P23(K),K=16,29)
1560          WRITE(6,55)(XP23(L),L=16,29)
1565          WRITE(6,123)
1566      123 FORMAT(4H Q23)
1567          WRITE(6,52)(Q23(K),K=2,15)
1574          WRITE(6,52)(XQ23(L),L=2,15)
1601          WRITE(6,55)(Q23(K),K=16,29)
1606          WRITE(6,55)(XQ23(L),L=16,29)
1613          WRITE(6,124)
1614      124 FORMAT(4H R23)
1615          WRITE(6,52)(R23(K),K=2,15)
1622          WRITE(6,52)(XR23(L),L=2,15)
1627          WRITE(6,55)(R23(K),K=16,29)
1634          WRITE(6,55)(XR23(L),L=16,29)
1641          WRITE(6,125)
1642      125 FORMAT(4H P31)
1643          WRITE(6,54)(P31(K),K=4,15)
1650          WRITE(6,54)(XP31(L),L=4,15)
1655          WRITE(6,55)(P31(K),K=16,29)
1662          WRITE(6,55)(XP31(L),L=16,29)
1667          WRITE(6,126)
1670      126 FORMAT(4H Q31)
1671          WRITE(6,53)(Q31(K),K=3,15)
```

```
1676          WRITE(6,53)(XQ31(L),L=3,15)
1703          WRITE(6,55)(Q31(K),K=16,29)
1710          WRITE(6,55)(XQ31(L),L=16,29)
1715          WRITE(6,127)
1716      127 FORMAT(4H R31)
1717          WRITE(6,52)(R31(K),K=2,15)
1724          WRITE(6,52)(XR31(L),L=2,15)
1731          WRITE(6,55)(R31(K),K=16,29)
1736          WRITE(6,55)(XR31(L),L=16,29)
1743          GO TO 9
1744       99 CONTINUE
1745          END
```

REFERENCES

Baker, M. L., and V. L. Yen, Effects of the Variation of Angle of Incidence and Temperature on Infrared Filter Characteristics, Appl. Opt., 6 (1967), 1343.

Banks, P. M., C. R. Chappell, and A. F. Nagy, A New Model of the Interaction of Auroral Electrons with the Atmosphere: Spectral Degradation, Backscatter, Optical Emission, and Ionization, J. Geophys. Res., 79 (1974), 1459.

Baumeister, P., The Transmission and Degree of Polarization of Quarter-Wave Stacks at Non-Normal Incidence, Opt. Acta, 8 (1961), 105.

Baumeister, P. W., and F. A. Jenkins, Dispersion of the Phase Change for Dielectric Multilayers: Application to the Interference Filter, J. Opt. Soc. Amer., 47 (1957), 57.

Belon, A. E., G. J. Romick, and M. H. Rees, The Energy Spectrum of Primary Auroral Electrons Determined from Auroral Luminosity Profiles, Planet. Space Sci., 14 (1966), 597.

Berger, M. J., S. M. Seltzer, and K. Maeda, Energy Deposition by Auroral Electrons in the Atmosphere, J. Atmos. Terr. Phys., 32 (1970), 1015.

Born, J., and E. Wolf, "Principles of Optics", Permagon Press, Oxford, 4th Ed., 1970.

Borst, W. L., and E. C. Zipf, Cross Section for Electron-Impact Excitation of the (0,0) First Negative Band of N_2^+ from Threshold to 3Kev, Phys. Rev. A., 1 (1970), 1.

Broadfoot, A. L., and K. R. Kendall, The Airglow Spectrum, 3100-10,000Å, J. Geophys. Res., 73 (1968), 426.

Broksenberg, thesis, (unpublished), University of London, 1961.

Budo, A., Uberdie Triplett-Bandentermformel furden allgemeinen intermediaren Fall und Anwendungderselben auf die $B^3\pi$, $C^3\pi$-Terme des N_2-Molekuls, z5. f. Phys., 96 (1935), 219.

Budo, A., Die Rotationskonstanten B, D und Y der 3π-Terme von T_iO, C_2, CO, PH, A1H, NH, zs. f. Phys., 98 (1936), 437.

Budo, A. K, Intensitatsformeln fur die Triplettbanden, zs. f. Phys., 105 (1937), 579.

Chamberlain, J. W., "Physics of the Aurora and Airglow", Academic Press, New York and London, 1961.

REFERENCES (Continued)

Chapman, S., The Absorption and Dissociative or Ionizing Effect of Monochromatic Radiation in an Atmosphere on a Rotating Earth, Proc. Phys. Soc.. 43 (1931), 26.

Dalgarno, A., and M. B. McElroy, The Flourescence of Solar Ionizing Radiation, Planet. Space Sci., 13 (1965), 947.

Dufay, M., Etude Photoelectrique Du Spectre Du Ciel Nocturne, Ann. Geophys., 15 (1959), 134.

Eather, R. H., Latitudinal Distribution of Auroral and Airglow Emissions: The 'Soft' Auroral Zone, J. Geophs. Res., 74 (1969), 153.

Eather, R. H., and D. L. Reasoner, Spectrophotometry of Faint Light Sources and a Tilting-Filter Photometer, J. Applied Optics, 8 (1969), 227.

Eather, R. H., and S. B. Mende, Airborne Observations of Auroral Precipitation Patterns, J. Geophys. Res., 76 (1971), 1746.

Fite, W. L., Positive Ion Reactions, Can. J. Chem., 47 (1969), 1797.

Fite, W. L., and R. T. Brackmann, Ionization of Atomic Oxygen on Electron Impact, Phys. Rev., 113 (1959), 815.

Gerard, J. C., Metastable Oxygen Ions Distribution and Related Optical Emission in the Aurora, Ann. Geophys., 26 (1970), 777.

Green, A. E. S., S. S. Prasad, and L. R. Peterson, Upper Atmospheric Spectroscopy, NASA SP-305, Physics of the Space Environment, Chapter VI, 1972

Hebb, M. H., and D. H. Menzel, Physical Processes in Gaseous Nebulae X. Collisional Excitation of Nebulium, Astrophys. J., 92 (1940), 408.

Henry, R. J. W., P. G. Burke, and A. L. Sinfailam, Scattering of Electrons by C, N, O, N^+, O^+, and O^{++}, Phys. Rev., 178 (1969), 218.

Herzberg, G., "Atomic Spectra and Atomic Structure", Dover Publications, 1944.

Jacchia, L. G., Revised Static Models of the Thermosphere and Exosphere with Empirical Temperature Profiles, Spec. Rep. 332, Smithson. Astrophs. Observ., Cambridge, Mass., 1971.

Jenkins, F. A., and H. E. White, "Fundamentals of Optics", McGraw-Hill, 3rd Edition, 1957.

Jones, A. Vallance, An Analysis of a Spectrogram of the Red Aurora of February 10/11, 1950, in the Wavelength Range 7300-8600Å, Can. J. Phys., 38 (1960), 453.

Jones, A. V., Auroral Spectroscopy, Space Sci. Rev., 11 (1971), 776.

Jones, R. A. and M. H. Rees, Time Dependent Studies of the Aurora – Ion Density and Composition, Planet. Space Sci., 21 (1973), 537.

Kazaks, P. A., P. S. Ganas, and A. E. S. Green, Electron Impact Excitation and Ionization of Atomic Oxygen, Phys. Rev. A, 6 (1972), 2169.

Kieffer, L. J., and G. H. Dunn, Electron Impact Ionization Cross Section Data for Atoms, Atomic Ions, and Diatomic Molecules: I. Experimental Data, Rev. Mod. Phys., 38 (1966), 1.

Lassettre, E. N., Inelastic Scattering of High Energy Electrons by Atmospheric Gases, Can. J. Chem., 47 (1969), 1733.

Lissberger, P. H., Properties of All-Dielectric Interference Filters: I. A New Method of Calculation, J. Opt. Soc. Amer., 49 (1959), 121.

Lissberger, P. H., and W. L. Wilcox, Properties of All-Dielectric Filters. II. Filters in Parallel Beams of Light Incident Obliquely and in Convergent Beams, J. Opt. Soc. Amer., 49 (1959), 126.

Macleod, H. A., "Thin-Film Optical Filters", American Elsevier Publishing Company, Inc., New York, 1969,

Omholt, A., The Red and Near-Infrared Auroral Spectrum, J. Atmos. Terrest. Phys., 10 (1957), 320.

Opal, C. B., W. K. Peterson, and E. C. Beaty, Measurements of Secondary-Electron Spectra Produced by Electron Impact Ionization of a Number of Simple Bases, J. Chem. Phys., 55 (1971), 4100.

Pfister, W., Auroral Investigations by Means of Rockets, Space Sci. Rev., 7 (1967), 642.

Pidgeon, C. R., and S. D. Smith, Resolving Power of Multilayer Filters in Non-Parallel Light, J. Opt. Soc. Amer., 54 (1964), 1459.

Rees, M. H., Auroral Ionization and Excitation by Incident Energetic Electrons, Planet. Space Sci., 11 (1963), 1209.

REFERENCES (Continued)

Rees, M. H., Auroral Electrons, Space Sci. Rev., 10 (1969), 413.

Rees, M. H., and D. Luckey, Auroral Electron Energy Derived from Ratio of Spectroscopic Emissions, 1. Model Computations, J. Geophys. Res., 79 (1974), 5181.

Rees, M. H., J. C. G. Walker, and A. Dalgarno, Auroral Excitation of the Forbidden Lines of Atomic Oxygen, Planet. Space Sci., 15 (1967), 1097.

Rishbeth, H., and O. K. Garriott, "Introduction to Ionospheric Physics", Academic Press, New York and London, 1969.

Rothe, E. W., L. L. Marino, R. H. Nenaber, and S. M. Trujillo, Electron Impact Ionization of Atomic Hydrogen and Atomic Oxygen, Phys. Rev., 125 (1962), 582.

Schlapp, R., Fine Structure in the $^3\Sigma$ Ground State of the Oxygen Molecule, and the Rotational Intensity Distribution in the Atmospheric Oxygen Band, Phys. Rev., 51 (1937), 342.

Schmeltekopf, A. L., F. C. Fehsenfeld, G. I. Gilman, and E. E. Ferguson, Reaction of Atomic Oxygen Ions with Vibrationally Excited Nitrogen Molecules, Planet. Space Sci., 15 (1967), 401.

Seaton, M. J., and D. E. Osterbrock, Relative (OII) Intensities in Gaseous Nebulae, Astrophys. J., 125 (1957), 66.

Seaton, M. J., Electron Impact Ionization of Ne, O, and N, Phys. Rev., 113 (1959), 814.

Sharp, W. E., and P. B. Hays, Optical Emissions from Auroral Secondary Electrons, Transactions A.G.U., 53 (1972), 1072.

Sharp, W. E., and P. B. Hays, Low-Energy Auroral Electrons, J. Geophys. Res., 79 (1974), 4319.

Shemansky, D. E., and A. L. Broadfoot, Excitation of N_2 and N_2^+ Systems by Electrons – I Absolute Transition Probabilities, J. Quant. Spectrosc. Radiat. Transfer, 11 (1971), 1385.

Shemansky, D. E., and N. P. Carleton, Lifetime of N_2 Vegard-Kaplan System, J. Chem. Phys., 51 (1969), 682.

Shemansky, D. E., T. M. Donahue, and E. C. Zipf, Jr., N_2 Positive and N_2^+ Band Systems and the Energy Spectra of Auroral Electrons, Planet. Space Sci., 20 (1972), 905.

Shemansky, D. E., and A. Vallance Jones, Type-B Red Aurora; the O_2^+ First Negative System and the N_2 First Positive System, Planet. Space Sci., 16 (1968), 1115.

Shemansky, D. E., and A. L. Broadfoot, Excitation of N_2 and N_2^+ Systems by Electrons – II Excitation Cross Sections and N_2 1PG Low Pressure Afterglow, J. Quant. Spectrosc. Radiat. Transfer, 11 (1971), 1401.

Shuiskaya, F. K., "Results of Researches on the International Geophysical Projects", Publ. House Nauka, Moscow, 13 (1967), 87.

Shepherd, G. G., C. W. Lake, J. R. Miller, and L. L. Cogger, A Spatial Spectral Scanning Technique for the Fabry-Perot Spectrometer, J. Applied Optics, 4 (1965), 267.

Stebbings, R. F., B. R. Turner, and J. A. Rutherford, Low-Energy Collisions Between Some Atmospheric Ions and Neutral Particles, J. Geophys. Res., 71 (1966), 771.

Stolarski, R. S., V. A. Dulock, Jr., C. E. Watson, and A. E. S. Green, Electron Impact Cross Sections for Atmospheric Species 2. Molecular Nitrogen, J. Geophys. Res., 72 (1967), 3953.

Swenson, G. R., W. E. Sharp, and P. B. Hays, A Study of $O^+(^2P\text{-}^2D)$ Emissions in Electron Aurora, Transactions A.G.U., 55 (1974), 684.

Thelen, A., Equivalent Layers in Multilayer Filters, J. Opt. Soc. Amer., 56 (1966), 1533.

Torr, D. G., Private Communication, 1975.

Walker, J. C. G., D. G. Torr, P. B. Hays, D. W. Rusch, K. Docken, G. Victor, and M. Oppenheimer, Metastable ^2P Oxygen Ions in the Daytime Thermosphere, Submitted to J. Geophys. Res., 1975.

Walker, J. C. G., and M. H. Rees, Ionospheric Electron Densities and Temperatures in Aurora, Planet. Space Sci., 16 (1968), 459.

Wallace, L., An Analysis of a Spectrogram of the Aurora of 11 February, 1958, in the Wavelength Range 3710-4420Å, J. Atmos. Terr. Phys., 17 (1960), 46.

Wiese, W. L., M. W. Smith, and B. M. Glennon, "Atomic Transition Probabilities. Volume I, Hydrogen Through Neon. A Critical Compilation", National Standard Reference Data Series, National Bureau of Standards 4, Lib. Cong. Cat. Card No. 65-60078, 1966.

REFERENCES (Concluded)

Zipf, E. C., The Collisional Deactivation of Metastable Atoms and Molecules in the Upper Atmosphere, Can. J. Chem., 47 (1969), 1863.

*U.S. GOVERNMENT PRINTING OFFICE: 1976 - 635-275/54

191 001 C1 U E 760109 S00903DS
DEPT OF THE AIR FORCE
AF WEAPONS LABORATORY
ATTN: TECHNICAL LIBRARY (SUL)
KIRTLAND AFB NM 87117

> *"The aeronautical and space activities of the United States shall be conducted so as to contribute . . . to the expansion of human knowledge of phenomena in the atmosphere and space. The Administration shall provide for the widest practicable and appropriate dissemination of information concerning its activities and the results thereof."*
>
> —NATIONAL AERONAUTICS AND SPACE ACT OF 1958

NASA SCIENTIFIC AND TECHNICAL PUBLICATIONS

TECHNICAL REPORTS: Scientific and technical information considered important, complete, and a lasting contribution to existing knowledge.

TECHNICAL NOTES: Information less broad in scope but nevertheless of importance as a contribution to existing knowledge.

TECHNICAL MEMORANDUMS: Information receiving limited distribution because of preliminary data, security classification, or other reasons. Also includes conference proceedings with either limited or unlimited distribution.

CONTRACTOR REPORTS: Scientific and technical information generated under a NASA contract or grant and considered an important contribution to existing knowledge.

TECHNICAL TRANSLATIONS: Information published in a foreign language considered to merit NASA distribution in English.

SPECIAL PUBLICATIONS: Information derived from or of value to NASA activities. Publications include final reports of major projects, monographs, data compilations, handbooks, sourcebooks, and special bibliographies.

TECHNOLOGY UTILIZATION PUBLICATIONS: Information on technology used by NASA that may be of particular interest in commercial and other non-aerospace applications. Publications include Tech Briefs, Technology Utilization Reports and Technology Surveys.

Details on the availability of these publications may be obtained from:

SCIENTIFIC AND TECHNICAL INFORMATION OFFICE
NATIONAL AERONAUTICS AND SPACE ADMINISTRATION
Washington, D.C. 20546